University of Concepción
Faculty of Engineering
Department of Chemical Engineering

Theoretical and experimental study of the CO_2 methanation reaction on Ni-Co catalysts

Thesis submitted for the Doctoral Degree in Material Engineering Science, mention in Chemical Engineering

by

Sebastian Adolfo Godoy Gutiérrez

Advisors:	Romel	Jimenez
	Prashant	Deshlahara
	Alejandro	Karelovic

Concepción, Chile
March, 2023

Summary

The $CO_{2(g)}$ methanation reaction on Ni, Co and NiCo catalysts was studied experimentally and theoretically. Supported Ni, Co and NiCo catalyst with narrow particle size distribution were synthetized for kinetic, isotopic and spectroscopic experiments. Monometallic and intermetallic bulk, nanoparticle, (111) and (100) surface models were constructed for DFT simulations.

A single crystalline phase was observed in all the prepared catalysts and near-surface studies for the bimetallic catalysts (EDX and CO-induced segregation) suggest that both, Ni and Co atoms, are present in the catalyst surface. DFT support the stable formation of a Ni-Co phase where Ni draws electronic density from Co, affecting their charges, magnetism and electronic structures. Co/SiO_2 has the highest $CO_{2(g)}$ activity but lower $CH_{4(g)}$ selectivity than Ni/SiO_2, while the $NiCo/SiO_2$ catalysts showed lower $CH_{4(g)}$ formation rates and selectivity compared to both, Ni and Co catalysts. $CO_{(g)}$ formation rates scale linearly with the Co content of the catalysts. Kinetic and isotopic results suggest that $CH_{4(g)}$ is formed through an H-assisted pathway but H is not involved in the $CO_{(g)}$ formation. Direct $CO_{2(g)}$ dissociation to *CO was experimentally observed, Co and NiCo show moderate $^*CO_2$ activation barriers (~ 30 kJ/mol) via DFT and weaker *CO binding compared to Ni, consistent with their higher $CO_{(g)}$ selectivity. FTIR and DFT results suggest that *CO is the most abundant surface intermediate, binding in linear and/or multi-bond modes according to the metal composition. Stronger *C binding on Ni surfaces is consistent with their usual C poisoning while the more oxophilic Co surfaces may also deactivate by oxidation. The binding strength of *C and *O act as descriptors for the adsorption trends of most surface species. These descriptors also reflect highlight their structural sensitivity, different oxophilicities and suggests that bimetallic catalysts behave more similar to the Co catalysts. (111) free energy profiles show a Co<NiCo<Ni trend and lower activation barriers for the assisted HCO route with *CO+*H and HCO dissociation steps as the largest (~148 kJ/mol) and highest (200-240 kJ/mol) barriers, respectively. These barriers are ~50 kJ/mol higher than barriers in the (100) profiles. $^*CH_2/^*CH_3$ hydrogenations are the highest reaction barriers (120-160 kJ/mol) for Ni(100) and Co(100), followed by the *CO direct dissociation and COH barriers, respectively. Both of these activation paths are the highest barriers of the NiCo(111) profile (~160 kJ/mol). These paths produce stable *C and *OH species that may contribute to deactivate (100) surfaces. Both surface geometries show unfavorable $CO_{2(g)}$ adsorptions and activation barriers (>150 kJ/mol) higher than apparent experimental values (60-100 kJ/mol) and the $CO_{(g)}$ desorption energies (~120 kJ/mol), suggesting that other less coordinated surfaces may have larger contributions to the methanation rates and trends experimentally observed.

This work focuses on trends for the geometry and surface composition aiming to provide insight on the fundamental interactions and processes involved on the $CO_{2(g)}$ methanation activity, selectivity and stability of Ni, Co and NiCo catalysts while developing a solid background, workflow and tools for future theoretical studies in heterogeneous catalysts.

Acknowledgments

The author acknowledges the financial support from the Chilean National Agency for Research and Development (ANID), scholarship folio 2018/21180468, and the FONDECYT regular project 1170610. Theoretical results in this work come from 3000+ DFT simulations for which the support of several institutions is acknowledged and deeply appreciated.

- Powered@NLHPC: This research was partially supported by the supercomputing infrastructure of the NLHPC (ECM-02).
- Kultrun Astronomy Hybrid Cluster, University of Concepción, via the projects Conicyt Programa de Astronomía Fondo Quimal 2017 QUIMAL170001
- National Science Foundation (award number 2034911) and computing resources from eXtreme Science and Engineering Discovery environment (project number TG-CTS150005).

On a personal note, the guidance and support of several people has been invaluable in the development of this work. Firstly, thanks to my advisors for their trust and guidance whenever I needed it the most. I must thank professor Beatriz Irigoyen and Agustín Salcedo for receiving me in their research group at the beginning of this work. I would like to express my sincere gratitude to professors Stefan Vogt G., Eduardo Menendez P. and Gerard Alonso B. for the insightful conversations and for having the time and will to answer my endless questions. Thanks to Yilang Liu, Karen Aravena, Verónica Sanhueza, and special thanks to Francisco Villagra-Soza, his work in the laboratory, his insight and our conversations are an integral part of this work. I also need to thank my family and friends for their support, from my grandmother Hilda to my niece Fiorella.

Finally, and most importantly, thanks to Alejandra Irene Gutiérrez Jara (my mother), who read to me and then taught me to read, that was the beginning of all this. She kept me and my curiosity alive all these years.

Copyright statement

Index

List of tables

List of figures

1. Introduction

The constant economic and industrial development of the growing global population in the last decades has been accompanied by the alarmingly hefty production of pollutants and their accumulation in the environment. Atmospheric $CO_{2(g)}$ is one most widely known examples, it is largely produced domestically and from most industries and has been closely related to climate change and global warming. This context fosters great economic, industrial and academic interest in developing more efficient and greener processes that can meet the material and energetic needs of the developing society. A strong focus is on reducing the generation of these pollutants, capturing, removing and convert them to more valuable byproducts. $CO_{2(g)}$ and $CO_{(g)}$, for example, can be used as carbon source for the synthesis of more valuable carbon-containing products such as methane which is a stable and efficient energy carrier that can be easily transported and integrated to power production processes. Besides the convenient utilization of $CO_{2(g)}$ and advantageous $CH_{4(g)}$ production, the methanation reaction may have other industrial purposes such as the removal of small traces of CO and $CO_{2(g)}$ to protect Fe catalyst in ammonia synthesis processes. An important limitation of the CO_x methanation reactions are the kinetic limitations imposed by the high reaction barriers to break the strong C—O bonds, forcing the utilization of specific catalysts and moderately harsh reaction conditions. In the industry, these reactions commonly utilize nickel-based catalysts that are active for $CO_{2(g)}$ and selective towards methane, but prone to deactivation and require to be changed or regenerated periodically. Other metals like cobalt make active and fairly stable catalysts but are less selective to $CH_{4(g)}$ and their scarcity makes them more expensive and less attractive for methanation at the industrial scale.

The development of more widely available experimental and theoretical research techniques has enabled a more fundamental understanding of the molecular processes involved in catalytic reactions. This approach has helped to unveil the specific roles and combined effects of, for example, the metallic phase, nanoparticle size, structure and composition of support, doping and interactions between different metals and with the supports. All these can be combined and carefully engineered for the rational design of catalysts with specifically intended properties. Moreover, alloying some active metals have shown advantageous synergistic effects such as greater catalytic activity and improved stabilities compared to the individual active phases. Combining known active phases like Ni and Co to improve the catalytic performance of the methanation reaction is an interesting and promising approach that requires a fundamental understanding of the reaction mechanism, catalytic properties of the constituents and their electronic interactions.

This work studies the $CO_{2(g)}$ methanation reaction on nickel, cobalt and bimetallic Ni-Co catalysts following a theoretical and experimental approach with focus on the reaction mechanism and on the fundamental chemical interactions that define their activity, selectivity and general behavior as catalysts.

2. Background and theoretical fundaments

2.1 Catalytic $CO_{2(g)}$ methanation

Carbon dioxide, $CO_{2(g)}$, is a highly stable molecule commonly produced in industrial processes and domestically, usually considered a pollutant for the environment and for industrial streams in some productive processes. $CO_{2(g)}$ is also an abundant and cheap source of carbon and its transformation to some more valuable product is thermodynamically favorable as Table 1 exemplifies, making it a good feedstock candidate for the synthesis of process. Of these products, methane is an efficient and stable energy carrier, it is suitable to be produced from $CO_{2(g)}$, can be stored, transported and easily used as combustible. The hydrogenation of $CO_{2(g)}$ to produce $CH_{4(g)}$ was first described in 1902 and is known as the Sabatier reaction.

Table 1 Reaction and enthalpies for products of $CO_{2(g)}$ hydrogenation processes.

Product	Reaction	ΔH_{298K}, kJ/mol	
Methane	$CO_2 + 4H_2 \rightarrow CH_4 + 2H_2O$	−165.0	[1], [2]
Methanol	$CO_2 + 3H_2 \rightarrow CH_3OH + H_2O$	−49.8	[3]
Ethanol	$2CO_2 + 6H_2 \rightarrow C_2H_5OH + 3H_2O$	−172.6	[3]

The high energy barriers to break the strong C-O bonds in $CO_{x(g)}$ molecules impose strong kinetic limitations to the practical implementation of methanation reactions at the industrial scale, which in practices makes necessary the use of catalysts and relatively high reaction temperatures in most cases. The rational selection, design and operation of catalysts that are active at milder reaction conditions, selective to the desired products and can be used uninterruptedly for longer periods leads to greener and more efficient processes, with lower energy requirements and higher productions. To this end it is necessary a fundamental understanding of the elemental reactive processes involved in the hydrogenation of $CO_{2(g)}$ on catalytic surfaces, which is the main purpose of this work. Moreover, other reactive processes may occur under methanation conditions besides the interconversion of $CO_{2(g)}$ to $CH_{4(g)}$, these reactions need to be considered for a proper description of the catalytic system and its macroscopically observed behavior. In particular, carbon monoxide is a commonly undesired byproduct for some catalyst and conditions, the interconversion of CO_2 and CO is known as the reverse water-gas shift reaction (RWGS): $CO_2 + H_2 \rightarrow CO + H_2O$ (ΔH_{298K}=41.1 kJ/mol [1]). Having CO as byproduct and possible intermediate implies that reactive mechanisms common to the $CO_{(g)}$ methanation ($CO + 3H_2 \rightarrow CH_4 + H_2O$, ΔH_{298K}=-206 kJ/mol) may be kinetically relevant for $CO_{2(g)}$. Moreover, the experimental and theoretical study of other processes that may share intermediates or elementary steps with the $CO_{2(g)}$ methanation provide insightful information on fundamental trends, reaction pathways and atomic configurations that help guiding the study of the methanation reaction.

Prominent examples often considered in this work include studies for the Fischer–Tropsch synthesis (FTS), methane reforming using H_2O (steam reforming) or CO_2 (dry reforming of methane, DRM), H_2 production and decomposition of larger hydrocarbons (e.g., ethanol, used as H_2 carrier). For example, the initial stages of DRM processes can be considered sequential dehydrogenations inversely equivalent to last steps of possible methanation routes, the theoretical description of these elementary steps is also useful to discuss how C deposits are eliminated by hydrogenation and the resistance to deactivation by carbon poisoning (sec. 8.4).

2.1.1 Catalyst and fine tuning of catalytic properties

2.1.1.1 Supports

Commercial catalysts for the methanation reaction are usually synthetized by depositing highly dispersed metallic phases that are known to be active for the methanation reaction on less active materials used as supports. Silica (SiO_2), titania (TiO_2), ceria (CeO_2), zirconia (ZrO_2) and alumina (specially γ-Al_2O_3) are some commonly used supports[2], [4], [5] with well-defined structures and high specific areas. Other materials such as zeolites, foams and biochars have also been used as cheaper or environmentally friendlier supports[2]. Carbonaceous and non-reducible supports such as SiO_2 and α-Al_2O_3 are generally considered inactive with little to no effect on the activity or selectivity of the active phases. On the other hand, some catalytic activity may take place on basic supports such as Y_2O_3 and CeO_2 increasing the total CH_4 yield from Ni-based catalysts compared to other supports like Al_2O_3[5]. Reducible oxides such as TiO_2 and Nb_2O_5 may significantly interact with Ni-Co active phases causing surface restructurations[6] and modifying its electronic properties. For these and other strong Metal-Support Interactions (MSI) the support and the metal-support interphase may play a strong role on the overall catalytic activity. However, this work focuses on catalytic differences derived from the composition of active phases; hence, only inert supports are considered.

2.1.1.2 Monometallic active phases

Several transition metals from the 4th-6th periods and 8th-10th groups of the periodic table (including Ni, Ru, Rh, Co, Mo and Fe[2], [4]) have shown catalytic activity for the production of methane from $CO_{x(g)}$. Ru is the most active metal for $CO_{x(g)}$ methanation[2], Ru/TiO_2 catalysts show activity even at room temperature and ambient pressure[5]. Other precious metals also show high activity and selectivity at moderate reaction conditions but its scarcity and high cost makes its industrial utilization inviable. Nickel also has high activity and selectivity towards $CH_{4(g)}$ but is more abundant and usually has a much lower price than other noble metals making it the preferred option for industrial applications. A significant problem with Ni-based catalyst is the activity loss during reaction which forces its recurrent replacement (and concomitant production downtime) or dynamic recuperation schemes. The deactivation of commercial Ni catalysts is usually reversible and most commonly attributed to the formation of carbon deposits and coke (e.g., in presence of heavy hydrocarbons at high temperatures, by polymerization of precursors and intermediates or from the Boudouard reaction: $2CO_{(g)}+{}^*\rightarrow 2CO_{(g)}+{}^*C$) covering the metallic surface and blocking active sites. Other deactivation process common in commercial catalyst are poisoning (e.g., irreversible S adsorption), loss of specific surface by sintering or loss of the active phase by metal gas reactions (e.g., forming volatile organometallics: $Ni_{(s)}+4CO_{(g)}\rightarrow Ni(CO)_{4(g)}$)[2]. Mo has higher resistance to Sulphur poisoning but low selectivity towards methane in favor of long hydrocarbon chains, similar to Fe catalysts commonly used for Fischer-Tropsch Synthesis (FTS). Commercial catalysts with 15-30 %w of cobalt are preferred for low temperature FTS due its stability and high conversion. Cobalt is less abundant than Ni but more abundant than other noble metals (e.g., Ru and Rh), it is cheaper and shows high activity under methanation conditions. More importantly, Co shows a higher resistance to carbon poisoning in methanation conditions[7]. However, it forms carbon deposits (sheets and filaments) in other reactions, such as ethanol dehydrogenation[8], and has been found to deactivate by oxidation DRM and FTS at high temperatures [9], [10].

2.1.1.3 Fine tuning of catalytic properties

Alloying or doping the widely used Ni-based catalysts with transition metals has been shown to affect the resistance to carbon deposition, the activity and selectivity for various reactions including the $CO_{x(g)}$ methanation[7]–[9], [11]–[13]. For example, the carbon resistance and thermal stability of Ni/Al_2O_3 can be improved by MgO promotion, similar to the higher stability observed with CeO_2 doping[4]. This fine-tuning of catalytic (and electronic) properties via alloying has received significant attention in recent experimental and theoretical studies[8], [11], [12], [14] and is a promising area for the development of more active, selective, and stable catalysts for a wide range of reactions. In particular, Co forms homogeneous alloys with nickel over wide composition and temperature ranges[15], [16], making it a good candidate for a bimetallic CoNi that conjugate the higher activity and carbon-resistance of Co with the high CH_4 selectivity of Ni for CO_x methanation at moderate reaction conditions (250-350°C). For example, activity for the decomposition of ethanol on Co-mixed oxides was improved by the formation of active NiCo phases, but began to decrease after 14 h, showing significant deposition of carbonaceous species (carbon nano-filaments and multi-walled nanotubes according to the particle size)[8]. Takanabe et al.[9] experimentally studied $Co\text{-}Ni/TiO_2$ catalysts in DRM conditions, showing that while >80%Ni alloys underwent C formation and >90%Co alloys deactivate by metal oxidation, the intermediate NiCo alloys performed stably with high activity. The higher oxophilicity (affinity to bind O and OH) of Co surfaces has been proposed to propitiate oxidation and removal of surface carbon deposits, making Ni-Co catalysts more resistant to coke poisoning [12], [17]. Tu et al.[12] studied (111) surfaces by DFT and proposed that the higher surface O coverage on Co(111) and CoNi(111) allows an O-assisted dissociative adsorption of CH_4 (not favored on pure Ni surfaces) that enhances methane activation in the DRM conditions. Chen and Yang[18] recently studied NiCo step B_5 sites by DFT, suggesting that higher *C coverage on Ni steps may relate to carbon deposition and higher *O coverage on Co steps may relate to deactivation by oxidation. Ou et al.[11] used DFT to study CH_4 dehydrogenation to surface *C on clean and Co-doped Ni(111) surfaces, finding a negative effect of the Co doping for direct dissociative adsorption of CH_4, which was suggested to be the rate-determining step for DMR. They also reported that the incorporation of Co weakened *C adsorption and lowered the barriers for hydrogenation steps (*C + *H → *CH), which suggested the thermodynamically and kinetically enhanced removal of surface carbon to form CH_4 on Co-doped (111) surfaces.

In summary, Ni-Co alloys show significantly different catalytic properties compared to monometallic Ni and Co catalyst that may be advantageous for the $CO_{2(g)}$ methanation reaction. To understand and exploit these properties it is necessary a more fundamental understanding of the catalytic processes and trends between catalysts.

2.1.1.4 Descriptors and the study of catalytic activity at a fundamental level

Vannice[19] observed a maximum for the CO/H_2 methanation activity across metals of the group VIII of the periodic table (similar to Fig. 1c). The existence of maximum can be understood in terms of the Sabatier principle, which suggest that there is an optimum for the affinity of molecular species on the catalytic surfaces: high enough for their adsorption and activation but low enough to allow the progress of the reaction and release of products. In more general terms, this suggests that it is possible to identify characteristic parameters of some materials and species that are intrinsically related to their catalytic activity. Some classic examples of such relations are the Brønsted acid catalysis relation[1], the Bell-Evans-Polanyi (BEP) principle[2] and the Graselli reactivity pillars for CeO_2. Famously, Norskov and Hammer[20] were able to explain the low reactivity and noble character of gold based on the characterization of its electronic structure, this approach is known as the d-band theory and has been widely applied to explain reactivity trends (see sec. 2.2.2.4).

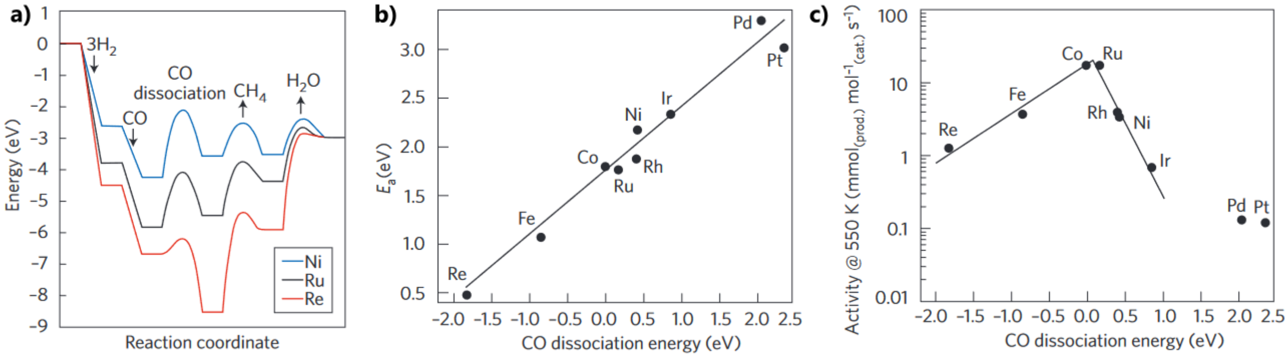

Fig. 1 a) Main CO hydrogenation barriers, b)BEP relation between the CO activation (E_a) and disociation energies and c) disociation energy as activity descriptor (adapted from Nørskov et al. [21]).

---

[1] For a family of acids the equilibrium and rate constant can be related in some reactions by $\log k = \beta_1 \log(K_a) + C$

[2] The energy barrier E_a for a family of reactions is linearly described by the reaction enthalpy ΔE_{rx}, i.e., $E_a = E_0 + \beta_2 \Delta H_{rx}$

From theoretical simulations Nørskov et al.[21] show that the highest reaction barriers for the CO methanation are the C-O dissociation, CH_x hydrogenation and H_2O formation (Fig. 1a). The first of these barriers is well described by a BEP relation with the CO dissociation energy (Fig. 1b), therefore, this dissociation energy can be used as a descriptor of the activity reproducing a volcano trend between metals (Fig. 1c) similar to the early experimental observations of Vannice[19]. It is relevant for this work to note that Ni and Co are in opposite sides of the maximum in Fig. 1c, suggesting again a possible favorable synergy of their alloy.

The CO dissociation energy is related to the stability of *C and *O species, moreover, several studies[22]–[24] coincide in the kinetic relevance of the *C and *O affinity with the surface for the CO methanation rates. Following those kind of relations, Medford et al.[25] constructed maps for CH_4 (Fig. 2a), methanol and ethanol formation rates from CO hydrogenation, which combine in selectivity map for commonly used monometallic catalysts (Fig. 2b). From a similar descriptor analysis Cheng and Hu[24] show that the maximum activity may not correspond to monometallic phases suggesting higher CO hydrogenation activities can be archived by synergic effects on metallic alloys. Chin and Lachkov[22] suggest from experimental results that the relative affinity of *C and *O and the operating ratio of CO and CO_2 pressures determine the most abundant surface species and relative contribution of different mechanisms to the overall reaction rate. These authors relate higher *C affinity of Ni catalysts to *C covered surfaces where the kinetically relevant step is the $*CH_3$+*H addition, while the hydrogenation with *OH species dominates in the more oxophilic Co surfaces and the behavior of NiCo surfaces will depend on the reaction conditions.

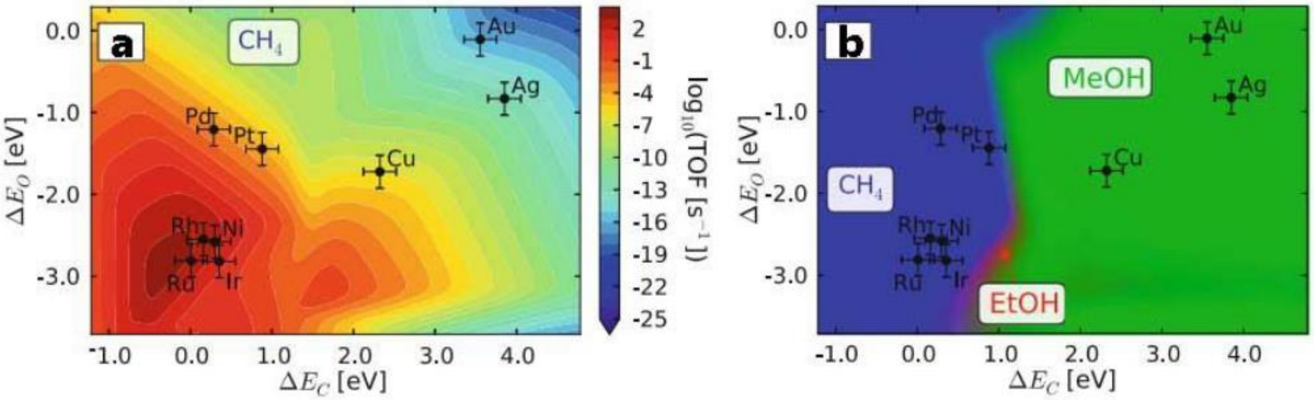

Fig. 2 a) activity and b) selectivity maps for the CO methanation respect to the C and O adsorption energies as descritptors (adapted from Medford et al.[25])

The above discussion only reaffirms that the catalytic activity is determined by intrinsic electronic properties of materials. Therefore, to properly explain trends and differences between catalysts for the $CO_{2(g)}$ (and $CO_{(g)}$) methanation reaction it is necessary to conduct multiscale studies based on the macroscopic and experimentally observable behavior of the catalysts under reaction conditions, but with a focus on the elemental processes, steps, mechanisms and fundamental interactions at the molecular level, for example, studied through (semi) ab-initio simulation techniques.

2.1.2 Reaction mechanisms

The exact mechanism through which $CH_{4(g)}$ is formed from $H_{2(g)}$ and $CO_{2(g)}$ has not been elucidated sufficiently despite numerous experimental and multiscale theoretical studies[22], [26], [27]. Most of these are focused in ideal compact nickel surfaces[1], [28]–[30], fewer works also study Co[31], [32] and bimetallic or doped surfaces[12], [33] with similar mechanisms and obtaining reaction profiles with similar features[3]. These studies often are limited to the (111) surface and only consider electronic or zero-point corrected electronic energies ($E_0 + ZPVE$, see 2.2.3). Also, several works usually consider only specific parts of the reaction (e.g., $*CO_2$ activation[33], *C hydrogenation [34]). A limited set of possible steps connecting several products and intermediates are usually proposed forming large reaction meshes (e.g., [27], [28], [36]) in which the most favorable reaction path will have the highest contribution to the macroscopic experimentally observable catalytic activity. Fig. 3 [30] exemplifies typical steps considered for the CO_x methanation reactions.

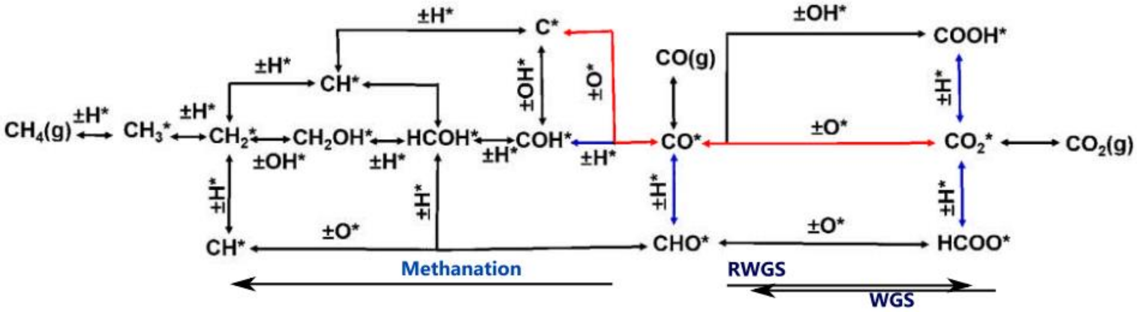

Fig. 3 Proposed elemental steps for the interconversion of $CO_{2(g)}$, $CO_{(g)}$ and $CH_{4(g)}$ including direct C-O dissociation steps (red) and H-assisted steps (blue) for the first and second O remotions (adapted from [30])

A first stage commonly proposed for the $CO_{2(g)}$ methanation is its interconversion with *CO (Fig. 3, right side) through elementary steps common to the RWGS reaction by forming water to eliminate one O atom ($CO_2 + H_2 \rightarrow CO + H_2O$). This stage and the next O elimination require breaking the strong C-O bonds mentioned in sec. 2.1 (and Fig. 1a), which may happen as an unassisted direct dissociation or associatively by H-assistance[4]. Fig. 3, for example, show a direct path (red) along with formate (HCOO*) and carboxyl (*COOH) paths[4]. Vogt et al.[37] showed experimentally that sub-2nm Ni nanoparticles are able to directly dissociate adsorbed $*CO_2$, these nanoparticles were previously thought to be too small to cleave π-bonds. The authors also suggest that the CO_2 activation is not kinetically relevant compared to later *CO hydrogenation steps.

---

[3] That is, for the same surface geometries. Adsorption and reaction profiles are highly sensitive to the surface configuration[32]–[35] while general features of the profiles are preserved between Ni, Co and NiCo[13] as will also be seen later.

[4] These kind of intermediates are more often considered when the formation of oxygenated products such as alcohols[27] or formic acid[29] wants to be included.

Regardless, more favored activations on low coordinated surfaces are reported with lower barriers for Co than Ni surfaces[33]. The activation of the second C-O bond is often found to be one of the most kinetically relevant barriers (Fig. 1a, Fig. 4b) along with the final hydrogenations of $*CH_x$ species mostly depending on the surface geometry in favor of the less coordinated sites [35], [36]. The introduction of Co in Ni surfaces is reported to decrease some relevant barriers as the $*CH_3$ hydrogenation[13] and *C elimination[38].

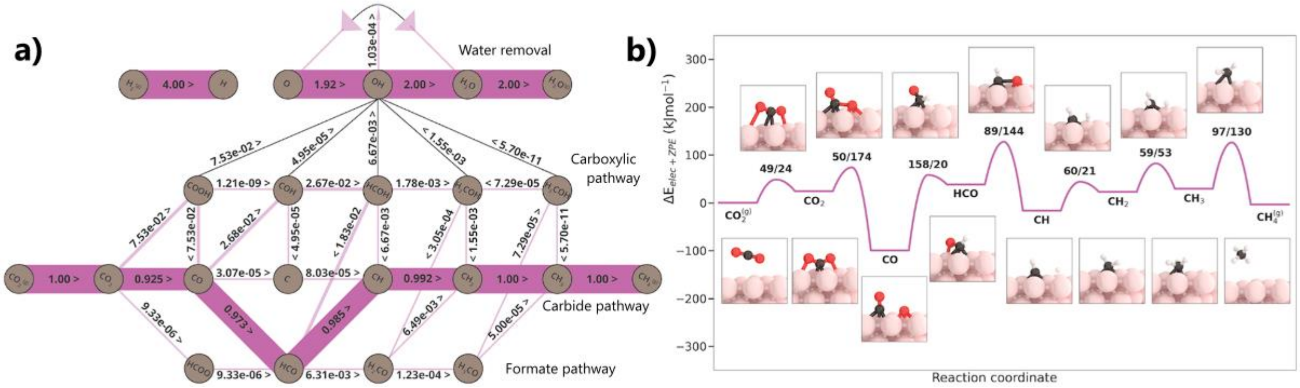

Fig. 4 $CO_{2(g)}$ methanation mechanism on Ni(111). a) Flux diagram from microkinetic simulation, numbers, linedith and symbols show the flux direction and magnitude b) reaction profile.

In a recent study, Sterk et al.[36] performs micro kinetic modeling (MKM) simulations feed with DFT-derived barriers on Ni surfaces including a direct dissociation and hydrogenation or carbide pathway, carboxylic pathway with COOH and COH intermediates and a formate pathway with HCOO and HCO intermediates. They found on Ni(111) (Fig. 4) that the H-assisted HCO path dominates the reaction (~97% of the total flux) and the highest barriers are the *HCO dissociation and $*CH_3$ hydrogenation. On the Ni(100) surfaces a dominant H-assisted COH path (~74% flux) with a smaller contribution of the *CO direct dissociation (~26% flux), with high $*CH_2$ and $*CH_3$ hydrogenation barriers. However, they suggest that the short steps of the Ni(110) facet are the most effective active sites with the highest contribution to the overall $CO_{2(g)}$ methanation rates. These surfaces showed a more diverse contribution of routes with dominant $HCO \rightarrow H_2CO$ pathway (60% flux), highest barrier for the $*H_2C\text{-}O$ dissociation and significant contributions of $*COOH \rightarrow *CO$, direct dissociation, *C-OH dissociation, and $HCO \rightarrow CH+O$ routes. The authors propose this structure sensitivity and the relative abundance of these short step sites may explain activity trends in particle size for small Ni nanoparticles. Notably, these authors (and several other) do not consider the CO desorption. It is also relevant to note that most of these theoretical studies include only electronic or ZPVE-corrected energies largely ignoring the entropic contributions.

Lozano-Reis et al. studied in greater detail[5] the $CO_{2(g)}$ hydrogenation on Ni(111) through a DFT and kinetic MonteCarlo (kMC) approach including the CO desorption and the $CH_3OH_{(g)}$

---

[5] They considered a more diverse reaction mesh and employed the BEEF-vdW functional for their calculations (see sec. 2.2.1) which may be considered more suitable to describe than the PBE functional used in the works of Sterk et al. [36] and Vogt et

formation. Their results agree with Sterk et al.[36] and Vogt et al.[26] about the (111) surface not contributing to the overall methanation rate, but more strictly indicate that the endothermicity of the *CO+*H→*HCO step hinders the progression of the Sabatier reaction in favor of releasing $CO_{(g)}$ performing only a RWGS reaction.

Moreover, other complex factors may come into play as, for example, co-adsorbed species may take an active role in the reaction. Tu et al.[27] points out that the greater oxophilicity of Co and NiCo surfaces promotes higher *O coverages that may enable a more favored reaction paths for the methane activation (reverse last step from perspective of the methanation reaction) through the concerted metallic insertion in the C—H bond and H-abstraction by *O, while cleaner Ni surfaces can only activate methane through three-center $(H_3C—Ni—H)^‡$ transition states. Later Chin and Lachkov[22] showed experimentally two consistent H-assisted HCO mechanisms kinetically limited only by the final reversible $*CH_3$ hydrogenation barrier from *H or *OH species, according to the surface composition (Ni, NiCo or Co) and operating conditions.

2.2 Chemical simulations at the molecular level

According to the first postulate of quantum mechanics, the complete definition of a quantum system of particles i with positions $\underline{r_i}$ is presented as its wavefunction $\Psi(\underline{r_1}, \underline{r_2}, \dots, t)$, commonly described as the ket[6] $|\Psi_i\rangle$. Postulates I-IV associate to every observable property within Ψ of a system an Hermitic operator, for example the total energy of a system (E) is related to its Hamiltonian $\hat{H}$ composed of the kinetic $(\hat{K})$ and potential $(\hat{V})$ energy operators: $\hat{H} = \hat{K} + \hat{V} = \sum_i(\nabla_i^2/2m_i) + \hat{V}$. And the behavior of the wave-function is well described by the Schödinger equation (postulate V):

$$\mathrm{i}\hbar\frac{\partial}{\partial \mathrm{t}}\Psi(\underline{\mathrm{r}}_1, \underline{\mathrm{r}}_2, \dots, \mathrm{t}) = \hat{\mathrm{H}}\Psi(\underline{\mathrm{r}}_1, \underline{\mathrm{r}}_2, \dots, \mathrm{t}) \qquad \text{eq. 2.1}$$

Assuming a time-independent potential field ($\hat{V}\Psi(\underline{r}, t) = f(\underline{r})$) and separability of the time dependency ($\Psi(\underline{r}, t) = \psi(\underline{r}) \cdot f(t)$) leads to solutions of the form $\psi_i(\underline{r}) \cdot \exp(iE_i t/\hbar)$. Here the state $\psi(\underline{r})$ is an eigenvector associated to the eigenvalue E_i as the energy of the system, known as the time independent Schödinger equation, in ket notation:

$$\hat{\mathrm{H}}\,|\psi(\underline{r})\rangle = E|\psi(\underline{r})\rangle \qquad \text{eq. 2.2}$$

Since the mass of nucleons ($m_{p^+}, m_{n^\circ} \approx 10^{-27}$ kg) is several magnitude orders bigger than the mass of electrons ($m_{e^-} \approx 10^{-31}$ kg), an instantaneous arrangement of the electron cloud is suggested when the nuclei positions are specified. For ψ this allows to only consider as variable the position of electrons leaving the nuclei positions as parameters $\underline{r_\alpha}$ (Born-Oppenheimer approximation). Under this assumption:

1) The Hamiltonian operator can be separated in a fixed potential part $\hat{V}_{\alpha-\alpha}$ associated with the inter-nuclei potential energy $E_{\alpha-\alpha}(\underline{r_\alpha})$ and a quantum electronic (electron-electron and

---

al.[26] Their scaling approaches also differ (kMC for Lozano Reis et al. and the direct solution differential system until stabilization for Sterk et al.).

[6] In this context, vectors of a complex Hilbert space.

nuclei-electron) contribution $E_{el}(\underline{r_i})$ to the total energy, defined by the electronic eigenvalue problem:

$$\left(\widehat{H}_{el} - \widehat{V}_{\alpha-\alpha}\right)\psi = E\psi = (E_{el} + E_{\alpha-\alpha})\psi \Rightarrow \widehat{H}_{el}\psi = E_{el}\psi \qquad \text{eq. 2.3}$$

2) The energy of the system is parametric to the set of n nuclei positions ($\mathbb{R}^{3n}$), and can be considered a function $E(\alpha_1, \dots, \alpha_n)\colon \mathbb{R}^{3n} \to \mathbb{R}$ with the energy as a (multi-dimensional) surface known as the potential energy surface (*pes*).

2.2.1 Approximate solution methods and Density Functional Theory (DFT)

For a well-behaved test wavefunction[7] $\varphi(\underline{r})$, its expected energy $E[\varphi]$ is always greater than the expected energy of the real wave-function of the system $E[\psi]$, which is formally known as the variational theorem: $E[\varphi] \geq E[\psi]$. This establishes a method to approximate the exact solutions ψ by minimizing the expected energy of parametric test solutions $\varphi(\underline{r})$.

In the Hartree-Fock (HF) method the ground state of a N-electron system (ψ_0) is approximated as the anti-symmetric product of N spin-orbital one-electron wavefunctions χ_i, i.e., a Slater determinant[8] $|\varphi_0\rangle = |\chi_1, \dots, \chi_N\rangle = |1, \dots, N\rangle$. By minimizing the expected energy of this system ($E[\Phi_0]$) with the restriction that the one-electron wavefunctions remain orthonormal ($\langle\chi_i|\chi_j\rangle = \delta_{ij}$), eq. 2.3 translates to a system of equations $f\,|\chi_i\rangle = \varepsilon_i|\chi_i\rangle$. Here the states $|\chi_i\rangle$ and one-electron orbital energies ε_i are the eigenvectors and eigenvalues of the Fock matrix operator composed of one-electron operators (eq. 2.4 in atomic units).

$$f\,|\chi_i\rangle = \varepsilon_i|\chi_i\rangle \quad ; \quad f_i \coloneqq f(i) = \left[-\frac{\nabla_i^2}{2} - \sum_{a}^{nucl.} \frac{Z_\alpha}{r_{i\alpha}} + \sum_{j}^{N/2} \left(2J_j(i) - K_j(i)\right)\right] \qquad \text{eq. 2.4}$$

The first two terms in the Fock operator are the one-electron Hamiltonian, composed of a kinetic operator ($\nabla_i^2/2$), and electron-nuclei potential ($Z_\alpha/r_{i\alpha}$, nuclei atomic number Z_α with $r_{i\alpha} = \|\underline{r_{i\alpha}}\|$). The $\sum_j J_j(k)$ term contains the Coulomb operator accounting for the interaction from electron j, applied to the one-electron wavefunction $\chi_i(l)$, defined as $\chi_i(l) \int_\infty |\chi_j(k)|^2 r_{ik} dr_k$. Note the $N/2$ limit and the 2 factor, eq. 2.4 as presented is defined for closed shell systems (paired ↑↓ orbitals), an analogous open-shell derivation leads to two analogous systems called the Roothan equations. $K_j(k)$ is a modified exchange (permutation) operator related to the exchange interaction energy for indistinguishable particles that in the case of electrons (fermion particles) relates to the required antisymmetry[9]. Once converged, the algorithm provides an ordered set of one electron approximated wavefunctions and their corresponding energies, these wavefunctions are populated from the lowest energy by the electrons available in the system.

---

[7] Some expected characteristics of the exact wave-function include its normalization ($\langle\psi|\psi\rangle=1$), being anti-symmetric to electron exchange ($\psi(r_1,\dots,r_i,r_j,\dots,rn)=-\psi(r_1,\dots,r_j,r_i,\dots,r_n)$) and higher electron density towards nuclei (cusp condition).

[8] Determinant of the $A_{kl} = \chi_k(l)$ *matrix*, where is a common chemical notation to use the electron index l to represent its spatial and spin coordinates, thus $|\chi_1,\chi_2,\dots\rangle=|1,2,\dots\rangle$.

[9] This is known as Pauli interaction, related to the Pauli exclusion principle and ultimately contributing to our macroscopic notion of volume.

Density Functional Theory: The first Hohenberg-Kohn (HK) theorem establish that (under certain commonly accepted assumptions) there is a unique correspondence between (1) the external potential of a system, (2) its Hamiltonian, (3) the wave-functions that describes it and (4) its electronic density distribution $\rho_e(\underline{r})$. Therefore, all information needed to describe the system is contained in its electron density distribution $\rho_e(\underline{r})$, hence the definition of a functional based on the electron density (Density Functional Theory, DFT).

The second HK theorem is analogous to the variational theorem but for electronic density-derived energies, $E[\rho_e'(\underline{r})] \geq E[\rho_e(\underline{r})]$, allowing us to improve estimations of the real electronic density $\rho_e(\underline{r})$ by minimizing test functions $\rho_e'(\underline{r})$. Analogous to the HF method, the test total electronic density can be composed in a base of one-orbital contributions, i.e., $\rho_e' = \sum_k \phi_{e,k}$. In principle, a bigger basis set for $\rho_e'(\underline{r})$ allows a better representation of the real $\rho_e(\underline{r})$.[10] This derivation leads to a system of equations $h_i^{KS}\phi_{e,k}(\underline{r}) = \varepsilon_i \phi_{e,k}(\underline{r})$. Now, states $\phi_{e,i}$ and their energies ε_i are eigenvectors and eigenvalues for the one-electron KS Hamiltonian operator h_i^{KS}:

$$h_i^{KS}\phi_i(\underline{r}) = \varepsilon_i^{KS}\phi_i(\underline{r}) \quad ; \quad h_i^{KS} := \left[-\frac{\nabla_i^2}{2} - \sum_{a}^{nucl.} \frac{Z_\alpha}{r_{i\alpha}} + \int \frac{\rho_e(\underline{r}')}{\|r_i - r\|} d\underline{r}' + V_{XC}[\rho_e(\underline{r})]\right] \qquad \text{eq. 2.5}$$

analogous to eq. 2.4 with the J term expanded. V_{XC} is potential associated to the exchange and correlation energy contributions ($V_{XC} = \delta E_{XC}[\rho_e]/\delta\rho_e$), its exact form is not known but only approximated by *functionals* of various flavors depending on the intended use of the calculations and computational power available.

Functionals: The simplest taxonomy of functionals considers what kind of information from $\rho_e(\underline{r})$ is considered: including only $\rho_e(\underline{r})$ (local density approximation), $\nabla\rho_e(\underline{r})$ (generalized gradient approximation, GGA, e.g., PBE, BLYP), kinetic energy in meta-GGA functionals (e.g., TPSS), mixed functionals (e.g., B3LYP), parametrized (e.g., optPBE) or statistically corrected functionals for specific applications (e.g., Bayesian Error Estimation Functional, BEEF). Some functionals consider modifications for a better description of long range interactions (e.g., BEEF-vdW[39], optPBE-vdW) and the adaptative combination of results from different functionals has been suggested to improve the accuracy of some calculations [40]. The 1991 Perdew, Wang functional (PW91) and the Perdew, Burke, Ernzerhof (PBE) functionals have been widely used for the simulation of heterogeneous reactions in model surfaces under periodic boundary conditions. The good behavior and popularity of the PBE functional sparked the development of several modified versions for specific applications (e.g., revPBE, RPBE, optPBE). It should be noted that errors in DFT simulations are inherently systematic, which allows the reproducibility and improvement of DFT simulations[41]. An important part of the errors of DFT are characteristic to the formulation of the functional and the kind of system studied, for example

---

[10] Some artifacts may appear, e.g., basis sets from different atoms in close positions may contribute locally for better representations of the electronic structure, this advantage is lost when atoms separate inducing artificial energy differences (Basis Set Superposition Errors, BSSE).

GGA functionals are known to overestimate adsorption energies[35], [42], [43]. Numerous benchmark studies are available to guide the selection of an appropriate functional[40], [44].

2.2.2 Implementation of DFT calculations

2.2.2.1 Iterative electronic and geometric relaxations

The electronic density of a system is computed from the solution of an eigenvalue problem (eq. 2.5) containing the h_i^{KS} operator, which explicitly includes the electronic density. Therefore, the solution needs to be approximated through an iterative process where an initial guess for ϕ_i allows to compute h_i^{KS} and obtain a new set of ϕ_i until a self-consistent electronic density field if obtained. This electronic relaxation (*scf* loop in Fig. 5) is called a *single point* calculation since it considers a fixed set of atomic coordinates (a single point of the *pes*), it provides a set of ϕ_i and their energies allowing to compute the electronic ground state energy and electronic density.

To obtain chemically relevant systems a geometric relaxation needs to be performed on top of the *scf* loop (*geometric* loop in Fig. 5). Minimizing interatomic forces leads to local minima of the *pes* corresponding to stable atomic configurations while restricted search algorithms allows to approximate saddle points usually associated to transition states (see sec. 4.4).

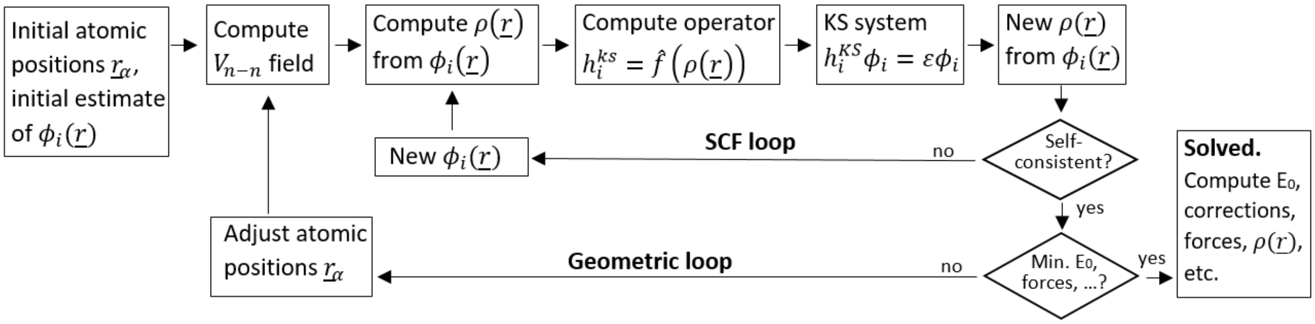

Fig. 5 Electronic and geometric relaxation DFT algorithm to approximate the ground state energy and electronic density of chemically relevant systems.

2.2.2.2 Representative models of large systems

Simulation of relatively small systems (<100 atoms) is computationally demanding even in modern high performing computing centers (HPC). In material science and heterogeneous catalysis, the periodic nature of bulks and extended surfaces can be exploited to compute smaller models representative of the large and more realistic systems. The specific models relevant for this work are described in detail in sec. 4.4 (see Fig. 9) and as they appear in the following sections, only a brief description is provided here.

Bulks: The structure of crystalline materials is represented by the minimal arrangement of atoms that can reproduce the solid by discrete translations $\underline{a}$, $\underline{b}$ and $\underline{c}$. These atoms and vectors define the primitive Wigner-Seitz cell of the material. All possible 3D periodic arrangements can be categorized as one of 14 possible Bravais lattices (e.g., bcc: body centered cubic, *fcc*: face centered cubic and hcp: hexagonal close packed), for instance, cobalt can form *fcc* and *hcp* phases while for nickel only the fcc phase is naturally observed. Bravais lattices do not coincide with primitive cells, for example, *fcc* crystals are constructed with four atoms within an orthogonal cubic cell. Using orthogonal lattice vectors simplifies the definition of directions [i j k] and planes relative to the bulk structure.

Surfaces: The exposed faces of a crystal exhibit the regular patterns of truncating the bulk by a certain plane. These surfaces are identified by Miller index (i j k) associated to the plane of the surface and its orthogonal vector in the direction [i j k] relative to the origin of the Bravais lattice.[11] Surfaces of different miller index have different formation energies and exhibit distinctive site geometries with different intrinsic activity. Surface are usually simulated with one-side slab models where a few layers of the bulk in a cell while leaving a vacuum space (usually <12 Å) on one side of the slab to avoid interaction with periodic images. The surface area of the model will define the coverages that can be simulated.

Therefore, the construction of bulk and surface models as described above requires their computation under periodic boundary conditions (PBC), which introduces some relevant concepts that need to be considered when setting up simulations for heterogeneous catalysis.

2.2.2.3 Periodic boundary conditions

The derivation of the above equations under periodic boundary conditions is far from trivial and only key aspects are discussed here. One-electron wavefunction solutions of the Schrödinger Equation in periodic potentials take the form of the Blöch functions $\psi_{\underline{k}} = \exp(i\underline{k} \cdot \underline{r}) u_{\underline{k}}(\underline{r})$ where $\underline{r}$ is the position, $u_{\underline{k}}$ is a periodic function and the exponential is a plane wave associated with the crystal momentum and wave vector $\underline{k}$. Therefore, approximated electronic states can be expanded in a basis set of Blöch functions. Low energy states have the highest contributions to the converged electronic structure, so basis sets are truncated to include functions only up to certain cut-off energy. Typical cut-off energies in modern calculations for heterogeneous catalysis are in the 350-500 eV range. In practice, the convergence of core orbitals is difficult due to their rapid oscillations, but the outer valence orbitals are responsible of most of the interactions between atoms. Using effective pseudopotentials to represent the contribution of core orbitals strongly alleviate the computational effort required.[12] Pseudopotentials provided for this work were constructed by smoothing the core wavefunction according to the Projector Augmented Wave (PAW[45]) method as implemented in the VASP code[46].

---

[11] Formally, the (i j k) surface is defined as the plane that intersects the three base vectors of the Bravais lattices at 1/i, 1/j and 1/k fractions from the origin, respectively (or 0 if the plane does not intersect the vector). For lattices with hexagonal symmetry (i.e., *hcp*) a fourth linearly dependent parameter is added defining (i j k l) surfaces just for mnemonic and visual convenience.

[12] This is a common approach for both, PBC and non-periodic boundary conditions but through different methods.

Given the periodicity of crystalline bulks and surfaces, the vector space representation of the periodic atomic arrangements and cell model is dual[13] to the reciprocal space mapped by the Fourier transform. Computations are routinely performed in the reciprocal space and, specifically, integrals of functions $g(\underline{k})$ in its irreducible zone[14] (Brillouin zone, BZ) are estimated by the weighted summation over a set of $\underline{k}_j$ points representative of its translational symmetry, i.e.,

$$I = \left(\frac{V_{cell}}{2\pi^3}\right)\int_{BZ} g(\underline{k})d\underline{k} \approx \sum_{j=1}^{n} c_j g(\underline{k}_j) \qquad \text{eq. 2.6}$$

In principle, denser k-point meshes provide better descriptions of the periodic nature of the models being computed, but the inverse scaling between real and reciprocal vectors implies that larger (real) cells require less k-points. Special choice of collocation and weight of these k-points allows to reduce the amount needed and computational effort, the Monkhorst-Pack[47] colocation scheme is used in this work.

2.2.2.4 Electronic structure and properties of atoms in materials

Electronic structure methods allow to estimate molecular orbitals and well-defined energies for isolated (non-periodic) chemical systems. These are rationalized through the Molecular Orbital (MO) theory as electronic states to be occupied for the available electrons in the system. In close arrangements of atoms several electronic states tend to coincide, this degeneracy of states is avoided by distributing the available states in the energy axis producing a density distribution $g(E)$ instead of localized individual states (as in MO)[15], $g(E)$ is the density of states (DOS). States are populated from the lowest energy by the available electrons up to the fermi level ε_f. In periodic systems, like extended metallic surfaces the analysis of the DOS, allows to study conductivity, polarization, band gaps and has been related to the chemical activity and reactivity of metals[20], [48].

<u>Band centers:</u> A classical descriptor of catalytic activity is mathematically defined as the ratio of the first and zeroth moment of the $g(E)$ distribution, i.e.,

$$e_d = \left(\int_{\infty} E \cdot g(E)dE\right)\left(\int_{\infty} g(E)dE\right)^{-1} \qquad \text{eq. 2.7}$$

A higher band center is usually related to a higher density of states close to the fermi level (ε_f), these states are involved in chemical reactions. Breaking the degeneracy of interacting states pushes occupied (unoccupied) states to lower (higher) energies, thus more states close to ε_f can be related to lower energies of resulting systems after reactive interactions [20].

Instead of directly analyzing electronic density distributions $\rho_e(\underline{r})$ or its field properties it is often more useful to assign contributions to the individual atoms. This approach is generally

---

[13] In the mathematical sense in which a vector space is defined to have a dual vector space.

[14] The Brillouin zone in the reciprocal space and the Wigner-Seitz in the real spare are equivalent irreducible (minimal) representations of the periodic arrangements in their respective vector spaces.

[15] Fig. S11 provides a good example comparing $CO_{2(g)}$ MO states (a) with the adsorbed extended surface (d).

known as atoms in materials (AIM) and is widely employed to assign atomic charges, atomic magnetic moments, project density of states and other properties through various partition methods.

Bader charges: Partitions based on a Voronoi division of the charge density following the surfaces of minimum electronic density ($\nabla\rho_e = \theta$) naturally occurring between atoms. Integration of the electronic density $\rho_e(\underline{r})$ inside the Bader volumes provides electronic charges for the atom within, integration of the spin densities $\rho_\uparrow(\underline{r}) - \rho_\downarrow(\underline{r})$ also provides a good estimation of the atomic spin moments. The public code by the Henkelman group is used in this work[49].

DDEC schemes: The Density Derived Electronic Charge (DDEC) partitions focus on a representation of the chemical potential, this provides more conservative estimates of atomic charges, allows to compute magnetization and bond orders between atoms. The DDEC6 Chargemol code[50]–[52] is used for clean surfaces in this work to confirm Bader trends.

DOS partitions: The total DOS can be projected onto atomic orbitals (PDOS) to analyze the individual atomic contributions and interactions. All PDOS in this work considered spin up and down, *s*, *p* and *d* projections directly obtained from VASP, escalated to integrate the number of electrons up to the fermi level (ε_f) correcting the numerical inaccuracies of the projection.

2.2.2.5 Atomic frequencies

Atoms in stable configurations still oscillate within their positions. Analysis of the vibrational modes of a chemical system is useful to (1) check its stability and (2) compute vibrational contributions to thermodynamic quantities. The simplest approach is to assume that the set $\underline{r_\theta}$ of $3n_a$ spatial coordinates represent a stable geometry for the system of n_a atoms, i.e., a *pes* minima where $\nabla E(\underline{r_\theta}) = \theta$. For a small distortion $\underline{r} = \underline{r_i} - \underline{r_\theta}$ of the geometry, the Taylor expansion of the *pes* is

$$E(r) = E(r_\theta) + \frac{1}{2}\left[\underline{r}\cdot\underline{\underline{\hat{H}}}_\theta\cdot\underline{r}^T\right] = E(\theta) + \sum_i^{3n_\alpha}\sum_j^{3n_\alpha} H_{ij} r_i r_j \qquad \text{eq. 2.8}$$

where $H_{ij} = \partial^2/\partial r_i \partial r_j E(\underline{r})$ are the elements of the Hessian matrix $\nabla^2 E$ at $\underline{r_\theta}$. The corresponding force field would be $\underline{F} = -\nabla E(\underline{r}) = -\sum_i^{n_a} r_i H_{ki}$, for the coordinate *k*, the second law of Newton is

$$\frac{d^2 r_k}{dt^2} = -\sum_i^{3n_a}\left(\frac{H_{ki}}{m_A}\right) r_i = \sum_i^{3n_a}\left(H_{ki}^{(m)}\right) r_i \qquad \text{eq. 2.9}$$

where m_A is the mass of the atom associated with the coordinate k, $H_{ki}^{(m)}$ are all the Hessian matrix elements i for the coordinate k (i.e., H_{ki}/m_i) over the mass of the atom associated with the coordinate k. And for the whole system

$$\frac{d^2}{dt^2}\left(\underline{r}^T\right) = \begin{pmatrix} -\sum_{i}^{n}\left(H_{1i}^{(m_1)}\right) r_i \\ \vdots \\ -\sum_{i}^{n}\left(H_{3n_a i}^{(m_1)}\right) r_i \end{pmatrix} = -\underline{\underline{H}}^{(m)} \cdot \underline{r}^T \qquad \text{eq. 2.10}$$

which is an *eigenvalue* equation for the mass weighted (by rows) Hessian matrix. The $3n_a$ eigenvectors $\underline{r}_{(k)}$ and corresponding eigenvalues λ_k are solutions in the form $\underline{r}^{(k)}(t) = \cos\left(\sqrt{\lambda_k}t + \varphi\right)\underline{r}^{(k)}(t)$ and together build up the solution space of harmonic vibrational motions of the system. The square root of the eigenvalues λ_k correspond to the vibrational frequencies, and their respective eigenvectors are the directions associated with those movements. For a well-defined transition state, a single imaginary frequency ($\lambda_k < 0$) is associated with an eigenvector in the direction of the reaction coordinate.

Various DFT codes compute the Hessian matrix from at least two finite differences for every degree of freedom, that is a total of $6n_a + 1$ single point evaluations for n_a atoms with 3 degrees of freedom. The computation of high vibrational frequencies is generally robust to numerical inaccuracies but low frequencies (absolute value < 100 cm^{-1}) are usually unreliable and may introduce large errors to thermodynamic quantities (see sec. 4.4 and annex A1.1).

Experimentally, incident infrared (IR) radiation of specific wavelengths can excite vibrational modes, some of these movements deform more significantly the local electron density affecting the dipolar moment. IR radiation is partly absorbed in these interactions (IR-active modes), which allows the experimental identification and quantification of some species according to the frequency and adsorbed fraction of the incident radiation. Formally, the intensity of IR active vibrational modes is related to the squared change of the electronic dipolar moment ($\underline{\mu}$, hereafter referred to simply as dipolar moment) and has a weak inverse dependence on the vibrational frequency usually ignored [53], [54].

2.2.3 Thermodynamic contributions

The DFT derived energies represent only the ground state electronic contributions to the energy of the chemical systems under study. For a better representation of the energy of the systems under study is necessary to statistically consider the available system configurations, pressure and temperature effects. Statistical mechanics allows computations of thermodynamic quantities for collectives of the DFT-derived systems that better represent the temperature dependent real systems. The most commonly contributions derived from statistical molecular thermodynamics[55] are used in this work and presented here.

The ensemble of molecular systems is completely represented by its partition function Q for which the electronic q_e, vibrational q_v, rotational q_r and translational q_t contributions can be considered: $Q = q_e q_v q_r q_t$. Their individual contributions to energy and entropy are:

$$E_i = N_{av} k_b T^2 (\partial \ln q_i / \partial T)_V \qquad \text{eq. 2.11}$$

$$S_i = N_{av} k_b (\ln(q_i) + T(\partial \ln(q_i) / \partial T)_V) \qquad \text{eq. 2.12}$$

Here and offing N_{av} is Avogadro's number, k_b the boltzmann constant and h the Planck constant.

Translational: For free particles in 3D spaces $q_t = (2\pi m k_b T h^{-2})^{3/2} V$, where $V = k_b T/P$ under ideal gas assumptions at moderate temperature. Applying eq. 2.11 and eq. 2.12 leads to the translational energy contribution of $E_t = (3/2) N_{av} k_b T$ and entropic contributions of $S_t = N_{av} k_b (\ln(qt) + 5/2)$.

Rotational: for a free system of N atoms with fixed relative positions (e.g., gas molecules), the principal rotation axis are defined as the eigenvectors of the inertia tensor $I_{ij} = \sum_k^N m_k(\|r_k\|^2 \delta_{ij} - r_i r_j)$. The three corresponding eigenvalues $I_{r,i}$ are the inertia moments that characterize rotation around the principal axis and define the rotational temperatures $\theta_{r,i} = h^2/8\pi I_{r,i} k_b$. The general form of the partition function is $q_r = (\pi^{1/2} \sigma_r^{-1})(T^3/\theta_{r,1}\theta_{r,3}\theta_{r,3})$ where σ_r or rotational symmetry is the number of indistinguishable geometries obtained by partial rotations (<360°)[16]. Contribution to the total energy is $E_r = (3/2) N_{av} k_b T$ and to entropy is $S_r = N_{av} k_b (\ln(q_r) + 3/2)$. For linear molecules a new derivation resolves $E_r = N_{av} k_b T$ and $S_r = N_{av} k_b (\ln(q_r) + 1)$.

Vibrational: each frequency ν_i defines a vibrational temperature[17] $\theta_{\nu,i} = h\nu_i/k_b$ that contributes to the vibrational partition function $\prod_i \exp(-\theta_{\nu,i}/2T)(1 - \exp(-\theta_{\nu,i}))^{-1}$. Applying eq. 2.11, a temperature independent Zero Point Vibrational Energy (ZPVE)

$$ZPVE = N_{av} k_b \sum_{\nu i} \frac{\theta_{\nu i}}{2} \qquad \text{eq. 2.13}$$

can be separated from the temperature-dependent vibrational contribution

$$E_v(T) = N_{av} k_b \sum_{\nu i} \frac{\theta_{\nu i}}{\exp(\theta_{\nu i}/T) - 1} \qquad \text{eq. 2.14}$$

And from eq. 2.12 the contribution to entropy is

$$S_v = N_{av} k_b \sum_{\nu i} \left[\frac{\theta_{\nu i}/T}{\exp(\theta_{\nu i}/T) - 1} - \ln\left(1 - \exp\left(-\frac{\theta_{\nu i}}{T}\right)\right) \right] \qquad \text{eq. 2.15}$$

Electronic: the states of quantized energy ε_k, each one of degeneracy (multiplicity) ω_k, compose the electronic partition function: $q_e = \sum_k \omega_k \exp(-\varepsilon_k/k_b T)$. For this work (and chemical reactions in general) is usually considered that no excited states are populated, leaving only the DFT-derived ground state without degeneracy ($\omega_0 = 1$), that is $q_e = \exp(-\varepsilon_0/k_b T)$, the energetic contribution is simply $N_{av}\varepsilon_0$ and the entropic contribution reduces to zero.

---

[16] e.g., 1 for CO, 2 for H_2, O_2 and 12 for CH_4.

[17] Frequencies ν_i in s^{-1}, $\nu_i = 100 \cdot c \cdot f$ (c speed of light in vacuum) for frequencies f in cm^{-1}.

__For the DFT models:__ As in the classical treatment enthalpy is $H = U + PV = E_0 + E_v + ZPVE + E_r + E_t$ and entropy is $S = S_t + S_r + S_v + S_e$ and the Gibbs free energy is simply $G = H - TS$. For the free species (gases) all contributions are considered (but $S_e = 0$). For all models including metallic slabs any phononic contribution is neglected[18] and for adsorbed surface slab models translation (2D migration) and rotation of adsorbed species are disregarded leading to $E_t = E_r = 0$ and $S_t = S_r = 0$, though low frequencies are interpreted as hindered translations and rotations through equivalent vibrational contributions, as discussed before (section 2.2.2.5 and in literature[56]). With these simplifications for the clean surfaces $G = E_0$ and for adsorbed surfaces $G = E_0 + E_v + ZPVE - TS_v$.

2.2.4 Transition State Theory: reaction rate and equilibrium constants

Rate constants can be estimated from Statistical Thermodynamics. For the simple case A→B going through the transition state $A^{\ddagger}$ under steady state (pseudo steady state hypothesis, *pssh*) the rate equation is $-r_A = k_A[A] = k_{\ddagger}[A^{\ddagger}]$. Solving for k_A leads to the ratio of concentrations for the TS and initial state, that can be described by the equilibrium constant $K^{\ddagger}$ and related to the free energy changes, that is $[A^{\ddagger}]/[A] = K^{\ddagger} = \exp(-(G_{\ddagger} - G_A)/k_bT) = \exp(-\Delta G_{A\ddagger}/k_bT)$.

When computing $\Delta G_{A\ddagger}$ from partition functions, the imaginary frequency ν_i is not a vibrational degree of freedom and its contribution to the partition function is separated as the factor $(1 - \exp(-h\nu_i/k_bT))^{-1}$. Therefore from $k_A = k_{\ddagger}\exp(-\Delta G_{A\ddagger}/k_bT)$

$$k_A = \frac{k_{\ddagger}}{1 - \exp(-h\nu_i/k_bT)} \cdot \frac{Q'_{\ddagger}}{Q_A} \exp\left(-\frac{\Delta U_{A\ddagger}}{k_bT}\right) \approx \frac{k_bT}{h} \cdot \frac{k_{\ddagger}}{\nu_i} \cdot \frac{Q'_{\ddagger}}{Q_A} \exp\left(-\frac{\Delta U_{A\ddagger}}{k_bT}\right) \qquad \text{eq. 2.16}$$

As a simple approach the factor $k_{\ddagger}/\nu_i$ can be eliminated under the assumption that both terms represent the frequency of the system evolving through the transition state. The partition functions can be reintegrated to $-\Delta U_{A\ddagger}$ to get $-\Delta G_{A\ddagger}$ which is estimated as discussed in section 2.2.3. Rewriting G=H-TS and grouping (eq. 2.17) facilitates the physical interpretation.

$$k_A = \left[\frac{k_bT}{h} \exp\left(\frac{\Delta S^{A\ddagger}}{k_b}\right)\right] \exp\left(\frac{-\Delta H^{A\ddagger}}{RT}\right) = k_0 \exp\left(-\frac{\Delta H^{A\ddagger}}{RT}\right) \qquad \text{eq. 2.17}$$

Equilibrium constants are defined as $K_{AB}=k_A/k_B$, where the forward (k_A) and backwards (k_B) rate constants can be estimated from the above equations. Computation of rate and equilibrium constants is included in the VASP toolset package developed for this work. For experimental data, linearizing eq. 2.17 allows the quick interpretation of slope and intercepts of 1/T plotted against $\ln k_A$ (*Arrhenius Plots*) or $\ln K_A$ (*Van't Hoff Plots*) in terms of enthalpy and entropy changes.

---

[18] Formally, phonon (excitation of the periodic arrangement) contributions are considered systematic and unperturbed by surface activity, thus not appearing in any energy difference of interest.

3. Guidelines and outlook

3.1 Hypothesis and objectives

The approach of this work follows the **hypothesis** that there are nickel-cobalt bimetallic phases with higher reactivity, selectivity and/or stability for the $CO_{2(g)}$ methanation reaction compared to monometallic Ni and Co catalysts.

General objective: Study through experimentation and theoretical simulations the activity, selectivity, and stability of Ni-Co catalysts for the $CO_{2(g)}$ hydrogenation under methanation conditions.

Specific objectives:

SO1. Evaluate activity, selectivity, and stability of supported Ni-Co catalyst for the $CO_{2(g)}$ hydrogenation reaction through kinetic, isotopic, and spectroscopic experiments under methanation conditions.

SO2. Apply Density Functional Theory (DFT) simulation techniques to estimate energy barriers of the preferred methanation routes for $CO_{2(g)}$ on Ni-Co surfaces, depending on the surface metallic composition and coverage of reaction intermediates.

SO3. Suggest and evaluate theoretical descriptors that explain or give fundamental support to the reactivity, selectivity, and stability trends for Ni-Co phases in the $CO_{2(g)}$ methanation reaction.

3.2 Organization of the study

These objectives translate into an experimentally guided simulation of model reactive Ni, Co and bimetallic Ni-Co surfaces for the hydrogenation of $CO_{2(g)}$. Experimental and theoretical methods are detailed in sec. 4. First, the structure of the synthetized catalyst and NiCo alloy models are studied experimentally and theoretically addressing their stability and electronic properties (sec. 5). A kinetic study addresses activity and selectivity trends in sec. 6. A detailed analysis of the reaction requires insight on the reactive surface, for which sec. 7 discuss the experimental characterization of the reactive surface and theoretical adsorption strength trends of relevant species. With this insight, a detailed analysis on the reaction is conducted in sec. 8 through isotopic and kinetic experiments (sec. 8.1-8.2.1), and the simulation of the reactive steps (sec. 8.2.2-8.4) for the construction and discussion of reactive profiles (sec. 8.5).

4. Methodology

Mono and bimetallic Ni-Co catalysts for the $CO_{2(g)}$ methanation reaction were studied experimentally and theoretically. The following sections details first the catalysts preparation and characterization techniques (sec. 4.1), kinetic studies (sec. 4.2), spectroscopic analysis (4.3) and the theoretical simulations (4.4) included in this work.

4.1 Catalysts preparation and characterization

Synthesis: To synthetize the studied catalysts, metallic nanoparticles were deposited on SiO_2 support (Saint-Gobain NorPro, SS61138) following the Incipient Wetness Impregnation (IWI) method as described by Villagra-Soza[7] and summarized below.

The support was sifted between 150-380μm and dried at 105°C (12 hours), total pore volume was estimated by N_2 chemisorption (77K) in a Micromeritic Gemmini VII 2390t equipment. The hexa-hydrated nitrate precursors $Ni(NO_3)_2{\cdot}6H_2O$ and $Co(NO_3)_2{\cdot}6H_2O$ (from Merck) were used to prepare solutions for the impregnation of pure Ni, pure Co, Ni:Co=1:1 and Ni:Co=4:6 catalysts. The support was impregnated for a 5% weight metal charge. The produced catalysts were dried in oven at 105°C (24 hours) and finally reduced in 50ml/min H_2 stream with a slow heating ramp (1°C/min for Co/SiO_2, 2°C/min for every other) up to 400°C for Ni/SiO_2 and 500°C for every other. These reduction temperatures allow the elimination of residual nitrates (confirmed by thermogravimetric analysis coupled to mass spectrometer) and the slow heating ramp prevents thermal sintering of the metallic nanoparticles. Milder reductions were routinely done in situ prior any experiment, as described in the following sections. This methodology produced mono and bimetallic catalysts with narrow nanoparticle size distribution between 3-5 nm, based on the following characterization techniques.

TEM micrography: Transmission Electron Microscopy (TEM) is an imaging technique based on the transmission of a beam of electron through a sample. The small de-Broglie wavelength of electrons (compared to photons) allows to obtain near atomic resolution images. Fig. 6 shows bright-field TEM micrographs of supported metallic nanoparticles from the catalyst used in this work obtained using a JEOL JEM-1200 EX II electron microscope from the Center of Spectroscopy and Electronic Microscopy (CESMI, Universidad de Concepción). The different scattering and adsorption of the electron beam through the sample portraits in shades the structure of the support and the metallic nanoparticles (dark spots) allowing its identification, counting and sizing. By standard, the individual counting of about 500 nanoparticles from different TEM images of a catalyst sample are generally used to statistically estimate the average particle diameter $\langle d_{TEM} \rangle$ as

$$\langle d_{TEM} \rangle = \frac{\sum_i n_i d_i^3}{\sum_i n_i d_i^2} \qquad \text{eq. 4.1}$$

a surface weighted average of the diameter d_i of every measured particle, which is estimated from its equivalent oval area in the micrograph. TEM analysis in this work used the *ImageJ* open source code[57]. The dispersion index (DI, eq. 4.2) describes the scattering of nanoparticle sizes, values below 1.5 indicate a narrow distribution appropriately represented by the average values.

$$DI = \frac{(\sum_i n_i d_i^3 \sum_i n_i)}{(\sum_i n_i d_i^3 \sum_i n_i d_i)}$$

eq. 4.2

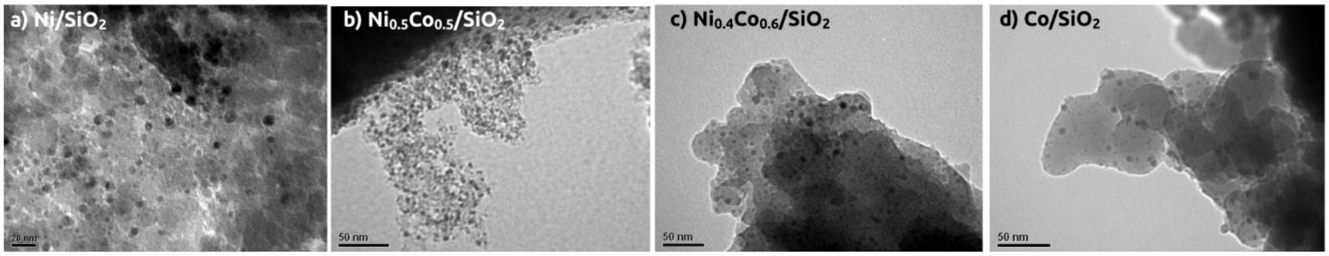

Fig. 6 Bright field TEM micrographs of a)Ni/SiO_2, b)$Ni_{0.5}Co_{0.5}/SiO_2$, c)$Ni_{0.4}Co_{0.6}/SiO_2$ and d) Co/SiO_2

TEM-EDX: Under vacuum conditions, electron beams produced with accelerations >50 kV can interact with different atoms producing x-rays of specific energies. Matching the produced x-ray energies to the corresponding atomic types allows to map their distribution in a sample at the resolution of a typical TEM micrography. A representative $Ni_{0.5}Co_{0.5}$ sample was studied (see Fig. 11 in sec. 5) using a FEI TECNAI F2o XT transmission electron microscope from the Department of Chemical & Petroleum Engineering, University of Kansas, coupled with a field emission gun operated at 200 kV to obtain TEM micrographs with EDX mapping of Ni and Co atoms.

XRD diffractograms: Diffraction of incident X-rays in a crystalline particle will interfere constructively at certain angles (*Bragg condition* in *Laue equations*) depending on the lattice morphology. The presence of identifiable X-ray diffraction patterns for a sample allows the identification of crystal structures within. Surface index, lattice spacing and even average size of the crystalline domain may be identified or estimated from XRD diffractograms. For metal-supported catalysts, the well-ordered compact crystalline structure of metallic nanoparticles usually produces identifiable peaks associated to metallic facets with well-defined Miller index. Average size of those nanoparticles can be estimated from the XRD peaks associated to representative facets of the main crystalline domain using the Scherrer equation:

$$d_{XRD} = K\lambda/\beta \cos\theta$$

eq. 4.3

where K is an adimensional factor (around 0.9 for some materials and usually ignored in catalysis), λ is the X-Ray wavelength, β (radians) is the broad of the peak at half its maximum, and θ is the diffraction angle (peak position or Bragg angle). XRD diffractograms in this work were obtained using CuK_α radiation (λ=0.154 nm) in a X D4 ENDEAVOR X-Ray diffractometer from the Institute of Applies Economic Geology (GEA, University of Concepción).

Dispersion of the catalysts: Under the reasonable assumption of supported metallic nanoparticles having an average hemispherical shape (see discussion in sec. 5.1), the dispersion of the catalysts (D) can be estimated from the diameter d_p of the nanoparticle, eq. 4.4.

$$D = n_s/n_t = 6v_m/d_p a_m \qquad \text{eq. 4.4}$$

Here D represents the ratio of surface/total metal atoms (n_s/n_t) in the average nanoparticle, where v_m and a_m are the average estimated area of surface atom and volume of bulk atom. Reaction rates are usually expressed as intensive turnover frequencies, i.e., rates normalized to the number of exposed atoms approximated by the dispersion of the catalysts.

4.2 Kinetic studies

Reaction kinetics and isotopic effects were studied in differential reactors working in low conversion conditions and free of transport limitations (confirmed by Weisz-Prater and Mears criteria). Fig. 7 shows the schematic experimental setup installed in the Carbon and Catalysis Laboratory (CarboCat, University of Concepción). The differential reactor consists of a stainless-steel tube of ¾ in. inner diameter where a small sample (20-40 mg, particle sizes 150-360 µm) of the prepared catalyst diluted with inert SiO_2 (1:1 mass ratio) is deposited between small quartz wool plugs. The tube is encased in an electric ceramic split open oven; a type K thermocouple is placed along the tube with its tip at about the height of the catalyst bed. The thermocouple is connected to a PID temperature controller that regulates the oven to reach and maintain the desired temperatures.

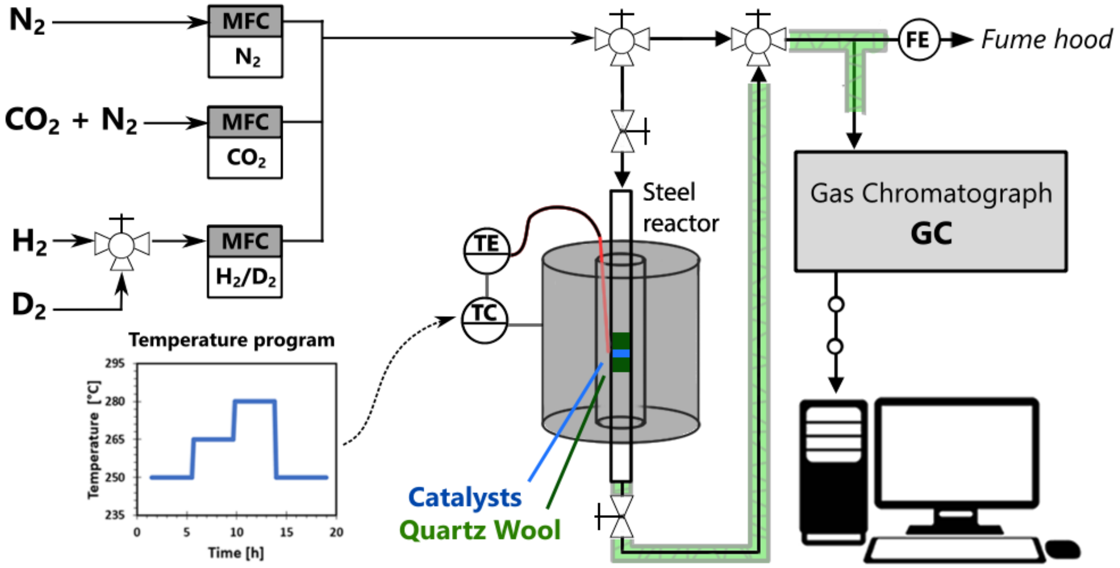

Fig. 7 Experimental setup for kinetic analysis using a differential reaction cell (steel reactor) and gas chromatograph. Each feed configuration was studied in a temperature program as presented.

Once mounted, the catalysts were reduced in situ in H_2 stream by slowly heating (1°C/min ramp for Co samples, 2°C/min for all others) up to 350°C, maintaining for two hours and then letting it cool down to 250°C. The reactive gas mixture is then feed to the system, its composition was regulated with individual Kofloc 8500 mass flow controllers for the reactive (H_2, CO_2) and inert (N_2) gases. The effluent gases are derived to a fume hood open to the atmosphere, therefore the reaction is considered to take place at atmospheric pressure. A temperature program is used to keep the reaction for three hours at 250°C, then 265°C, then 280°C and finally goes back to 250°C (Fig. 7, inset). The temperature program allows to reach steady state and analyze three effluent samples at each temperature, explore the effect of temperature (compute activation energies), and assess the activity loss (deactivation) comparing the initial and final catalytic performances at 250°C. The small mass of catalyst and careful choice of reaction conditions keep conversion below 10%, allowing to consider the computed rates as initial reaction velocities (mostly) free of the effect of product concentration. The dilution with SiO_2 helps avoiding channeling of the reactant flow in the catalyst bed and the formation of hot spots. Results presented in this work were obtained under a strict kinetic regime where mass and heat transfer limitations were discarded using the Weisz-Prater and Mears criteria.

The composition of effluent gases is analyzed in a gas chromatograph Perkin-Elmer 8700. In this equipment, an aliquot of the effluent gases is injected to a Porapak-Q packed column and pushed with He as carrier. Different species exit the column after different times depending on their size, polarity and the column specifications. After calibration, the different exit times allows identification and quantification of relevant species (CO, CO_2, CH_4). Relevant species at the exit of the column are detected using a Thermal Conductivity Detector (TCD). The aliquot and carrier are then feed to a Ni methanizer that converts carbonated species to CH_4, which is detected in a Flame Ionization Detector (FID). Integrated intensity of signals from the TCD and FID at specific times correspond to the concentration of a specific gas in the effluent (determined by calibration). The three-way valves in Fig. 7 allow to bypass the reactor to directly check the feed composition in the GC or its total flow using the final bubble flow meter (FE in Fig. 7), which is routinely done at the beginning and end of every experiment.

Isotopic effect: The same setup and standard procedure of the kinetic studies was employed but using D_2 instead of H_2 to study the isotopic H_2/D_2 effect on the CO and CH_4 formation rates. Effluent gases were analyzed in the gas chromatograph now equipped with a Carboxen 1000 packed column.

4.3 In-situ spectroscopic and operando analysis

Specific IR radiation excites specific vibrational modes and its absorption in IR active modes allows the identification of molecular structures (sec. 2.2.2.5). In practice, in infrared spectroscopy varying proportions of different incident wavelengths go through a sample simultaneously and the raw absorption data is processed using Fourier transforms to generate an absorbance spectrum. Position and intensity of IR absorbance peaks in the spectra allows the identification of specific bonds or atomic structures present in the sample. This technique is known as Fourier Transform

Infrared Spectra (FTIR) and is widely used to characterize catalytic surfaces *in-situ*, *ex-situ* and even under *operando* conditions.

FTIR results shown in this work were obtained in the experimental setup schematized in Fig. 8a, which is installed in the Carbon and Catalysis Laboratory (CarboCat, Universidad de Concepción) using a Nicolet iS-10 FTIR spectrometer (Thermo Scientific) equipped with a FTIR reaction cell provided by In-Situ Research & Instruments (Fig. 8b). Powder catalyst (~30 mg) is pressed for 10 minutes at 3000 psi to form a thin wafer which is placed inside the FTIR cell, in the middle between the two CaF_2 windows. The cell is aligned between the emissor and receptor of the spectrometer so the incident IR beam can enter and exit the reaction chamber going through the wafer. The temperature of the cell is measured with integrated thermocuples (K type) and maintained at the desired level using embedded electric heater bars connected to a temperature controller. The block of the reactor cell is continuously water cooled.

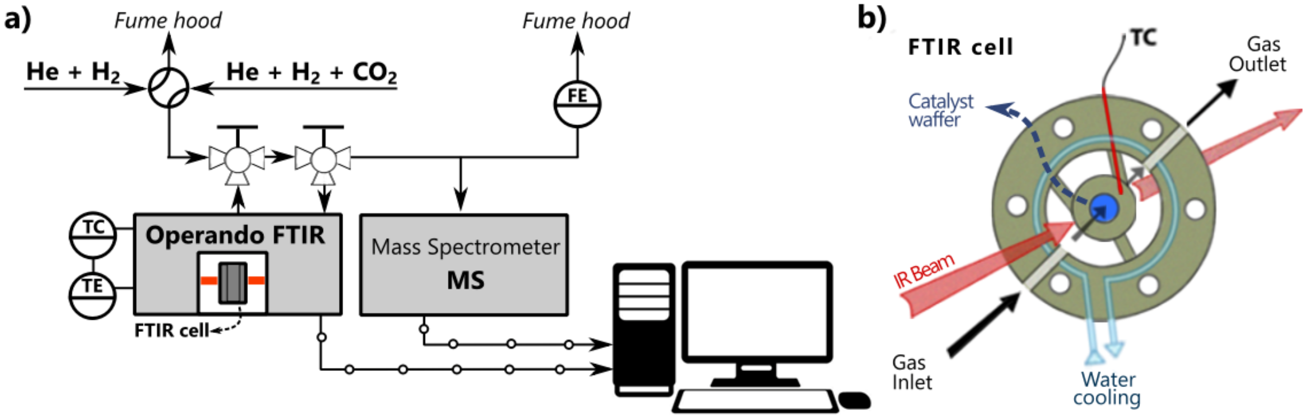

Fig. 8 a)General experimental setup for operando FTIR in situ experiments coupled to a mass spectrometer and b) schematic detail of the FTIR differential reactor cell.

For the kinetic-surface studies: Reactive (CO_2 and H_2) and inert (Ar, He) gases are passed through oxygen-traps to remove any unexpected O_2 content and feed to the reaction cell in different proportions as needed using Kofloc 8500 mass flow controllers (Kojima Instruments). Starting any experiment, the catalysts was reduced in-situ by heating up to 350°C in H_2 flow (with 1°C/min ramp for Co samples, 2°C/min for all others), maintaining for 2 hours and then letting it cool down to the desired reaction temperature (usually 250-280 °C). FTIR spectra were obtained between 1300-3500 cm^{-1} at a $4cm^{-1}$ resolution averaging 32 scans, background spectra are obtained at the reaction conditions (but before feeding reactive gases) and substracted to the FTIR spectra obtained during the reaction.

The four-way valve in Fig. 8a allows fast switching from feeding the reactive gas mix (H_2+CO_2+ inert) to an H_2+He, which allows to suddenly eliminate one reactive and study the evolution of the surface species (via FTIR) upon its decreasing concentration. The three-way valves allow by-passing the FTIR cell to check for leaks, check the feed composition or any other task.

Effluent gases are analyzed in a bench-top mass spectrometer (MS) Omnistar GSD 320 (Pfiffer Vacuum). This equipment fragments and separate species according to their mass-to-charge ratio. Signal channels detecting different atomic masses (*amu*) allow the identification and quantification of some species, though some channels may not be directly interpreted, e.g., the total 28 *amu* signal is mostly attributed to CO ($m_C+m_O=28$ *amu*) but has a 10% contribution from fragmented CO_2 species (redundant from the 44 *amu* signal). Other relevant signals are H_2 (2 amu), H_2O (18 amu) and CH_4 that is quantified using the 15 *amu* signal (m_C+3m_H) since its natural 16 *amu* signal (m_C+4m_H) is detected along with 16 *amu* signal of O atoms. Heat and transfer limitations in kinetic studies in this system were ruled out by replicating kinetic results from the differential steel reaction at some test reaction conditions.

4.4 Molecular simulations

The formation of $CH_{4(g)}$ from $CO_{2(g)}$ was simulated on Ni, Co and a bimetallic NiCo surfaces according to the DFT formalism (sec. 2) using the VASP 5.4 code[58]–[61]. Simulations were performed in the National Laboratory of High-Performance Computing (NLHPC) and the Astronomy Hybrid Cluster Kultrun (see A1.2). Small calculations and data analysis were performed with open source or homemade code in local machines. The revised version of the PBE functional (RPBE [62]) was selected for its better representation of CO adsorption energies. Spin polarized and non-symmetrized calculations were carried out using a 460eV plane wave basis set with core interaction described by the PAW (Protector Augmented Wave) method[45], [46]. Electronic relaxations were considered converged with differences between steps less than 10^{-5} eV though higher precisions were often requested (10^{-6} eV in relaxations, 10^{-7} eV in frequency and dimmer). Geometric relaxations minimized interatomic forces through force-based algorithms. A 0.05 Methfessel-Paxton[63] smearing was employed to accelerate the electronic convergence of calculations, all energies are then extrapolated to 0 K. Initial atomic magnetic moments of 0.6 and 1.6 μB were used for Ni and Co atoms to accelerate electronic convergence and avoid high energy electronic configurations (see sec. 5.2). Electronic charges and atomic magnetic moments were computed using the Bader and DDEC6 codes (sec. 2.2.2.4). Projected density of states was computed for some models, a fermi smearing with a 0.1 factor was used for these calculations to obtain positive and less noisy DOS curves. The selection and construction of models and their analysis is described in detail as they appear in the following sections, only a general description is provided here. Geometric and parametric files for every calculation are available in the digital repository of the Carbon and Catalysis Laboratory (CarboCat), University of Concepción.

Bulk materials: The fcc bulk of monometallic Ni, Co and equimolar intermetallic NiCo (1:1) are represented by cubic cells with four atoms (e.g., Fig. 9a) and computed with a 12x12x12 Monkhorst-Pack (MP)[47] k-point mesh (see 5.2). The lattice parameter were adjusted by fitting the cell volume (V) and electronic energy (E_b)according to the Murnaghan Equation of State

(EoS, [64]), eq. 4.5 where V_0 (equilibrium volume), B_0, B_0' and C_b (other physical properties) are used as fitting parameters (see Fig. 12 in sec. 5.2).

$$E_b(V) = \frac{B_0 V}{B_0'(B_0'-1)}\left[B_0'\left(1-\frac{V_0}{V}\right)+\left(\frac{V_0}{V}\right)^{B_0'}-1\right] \qquad \text{eq. 4.5}$$

Nanoparticles: The ideal shapes of monometallic Ni and Co nanoparticles were constructed by minimizing the total surface formation energy according to the Wulff methodology, using the WulffPack python package [65] and surface energies taken from reference (Table S5, ref. [66]). Models of nanoparticles of different sizes were obtained by truncating the bulk material inside Wulff polyhedral envelopes of different sizes. In bimetallic nanoparticles the atom positions were randomly assigned to fixed ratios of Ni and Co atoms. The average coordination degree of Ni and Co atom types were computed by counting the nearest neighbors[19] of each atom, lower average coordination implies more surface positions for that atom type. Varying segregation degrees were obtained by switching atom positions to maximize or minimize the average coordination degrees through a homemade genetic algorithm. The nanoparticles were placed in cubic cells with 7.5Å clearance in every direction for a total separation of 15Å between periodic images (e.g. Fig. 9b). A single k-point was used and all but one atom positions were relaxed until atomic forces were below 0.05 eV/A. Dipolar corrections centered in the nanoparticle showed negligible effect. Formation energies for the Ni_xCo_{n-x} nanoparticles (mono and bimetallic) were computed taking the atomic bulk energies ($E_{Ni,\text{bulk}}$ and $E_{Co,\text{bulk}}$, 4 atoms each) as reference (eq. 4.6).

$$E_{form}(Ni_xCo_{n-x}) = E_0 - (x/4)E_{Ni,\text{bulk}} - \big((1-x)/4\big)E_{Co,\text{bulk}} \qquad \text{eq. 4.6}$$

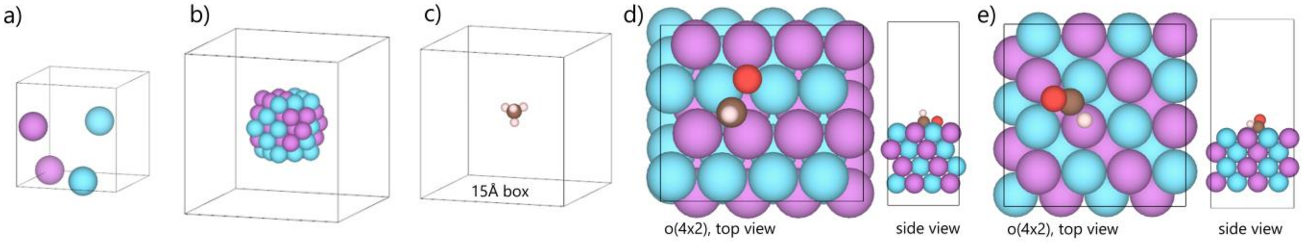

Fig. 9 Example DFT model types (not in common scale): a) NiCo fcc bulk, b) $Ni_{27}Co_{28}$ (n_{55} nanoparticle), c) gas phase CH_4, and adsorbed species on the slab models d) NiCo(111) and e) NiCo(100). Color code is purple: Ni, cyan: Co, black: C, red: O and white: H.

Gases: Models for gases and other isolated atomic and molecular species were placed in the center of a 15^3 Å^3 cubic cells (e.g., Fig. 9c) and computed using a single k-point. All but one atomic coordinates are relaxed and the three coordinates for each atom are considered degrees of freedom for vibrational computations but only real frequencies are considered further.

---

[19] Automatic counting before relaxation considered atoms within 5% of the first envelope according to the bulk lattice parameter. Average coordination of Ni and Co atoms were obtained, as well as the average Ni-Ni, and Co-Co coordination degree.

Surface models: Surfaces are represented by metallic slabs constructed by rotation, multiplication and truncation of the bulk models. The constructed (111) and (100) surface models (see Fig. 15) contain four metallic layers with 16 atoms each for a total of 64 atoms in an orthogonal periodic cell[20]. Models with large surface were chosen to focus on the interaction of adsorbed species with the surface and the electronic effects of the Ni-Co alloy, this also minimizes adsorbate-adsorbate interactions and achieves a better electronic description with a smaller k-point mesh. A 4x4x1 k-point MP mesh is used. The slab is centered at about a quarter height (z~0.25) of the cell leaving at least a 15Å vacuum between periodic slab images (see Table S2). Adsorption and reaction steps are simulated on one of the surfaces (e.g., Fig. 9d,e, respectively). Dipolar corrections to the energy for the one-sided adsorbed models accounted in most cases for <1kJ/mol ($\lesssim$0.01 eV) and are generally considered negligible. The atomic position of the bottom two metallic layers was frozen to their bulk positions, only the top two layers and adsorbed species were allowed to relax. Surface formation energies (eq. 4.7) compare the energy of a clean surface (E_S, slab with n atoms) with the average energy of its atoms in the bulk phase (E_{bulk})

$$\Delta E_{surf} = (E_S - nE_{bulk})/2 \qquad \text{eq. 4.7}$$

The binding strength adsorbed species can be described by their adsorption energy (eq. 4.8) comparing its energy on the surface ($E_{S\text{-}X}$) to the energy of the clean surface (E_S) and the free adsorbate (E_X). Alternatively, the energy of the constituent atoms in their most stable positions on the surface (E_{*C}, E_{*O} and E_{*H}) can be used as reference to compute a surface recombination energy (eq. 4.9). Lower values indicate more stable species on the surfaces.

$$\Delta E_{ads-X} = E_{S-X} - (E_S + E_X) \qquad \text{eq. 4.8}$$

$$\Delta E_{form-C_xO_yH_z} = E_{S-C_xO_yH_z} + (x + y + z - 1)E_S - (xE_{*C} - yE_{*O} - zE_{*H}) \qquad \text{eq. 4.9}$$

Vibrational frequencies: All three degrees of freedom for every atom of the adsorbed species were considered to construct a hessian matrix using the finite difference method with symmetric displacements of 0.01Å and assuming that the potential energy surface (*pes*) is locally well described by a harmonic potential. The rows of the hessian matrix are weighted by the atomic masses as detailed in in sec. 2.2.2.5, vibrational directions and frequencies are obtained as eigenvectors and eigenvalues of the mass-weighted hessian matrix (respectively) and vibrational contributions to thermodynamic functions are computed as described in 2.2.3. Every frequency calculation in this work was accompanied by the computation of the dipolar moment perpendicular to the surface, for vibrational modes in this direction the $(d\mu_z/dz)^2$ is easily computed and used to discuss relative experimental IR intensities[53], [54].

Flat zones of the *pes* are poorly described by the finite difference method and harmonic assumption, leading to artificially low or undesired imaginary frequencies (absolute value <100 cm^{-1}) that may be more representative of hindered rotations or translations. Calculations of higher precision, tighter relaxations and varying the finite step-size were tested in such cases (see A1.1).

---

[20] Formally, monometallic models are o(4x4) and the intermetallic are o(2x2) due its periodicity. The orthogonal arrangement reduced the number of k-point required by the Monkhorst-Pack method to 8, compared to 24 for the primitive ∢60° cell.

These frequencies induce large errors in the computation of vibrational entropies and temperature-dependent vibrational contributions to the enthalpy. A common approach to avoid this artifact is to truncate these inaccurate low frequencies to a fixed value (100 cm^{-1} in this work) whose harmonic vibrational contribution is more representative of the hindered translations and rotations in those directions of the *pes* [56].

Transition state search: Possible initial and final geometries of an elementary step are relaxed at a lower precision (smaller k-point mesh, higher convergence criteria). A set of 6-8 configurations are interpolated between the initial and final geometries and adjusted manually to represent the reaction path. The set of intermediate images is relaxed simultaneously using the nudged elastic band (neb) method for a few steps (15-20), to identify and reduce high forces, and then relaxed using the Climbing-Image neb method[67] to push one of the images to the transition state (TS) until its forces are below 0.2 eV/Å. The TS candidate is relaxed towards the saddle point of the pes using the dimer method [68] and taking the reaction coordinate from the neighboring neb images. When all forces are below 0.02 eV/Å, the new configuration and the dimer-corrected reaction coordinate are used in a final dimer calculation at the standard precision used in this study (4x4x1 k-point mesh). A frequency calculation with a single imaginary frequency (>100 cm^{-1}) associated to the reaction coordinate confirms that the converged dimer is a saddle point connecting the proposed initial and final configurations. In cases where the connection between the TS and initial or final geometries was unclear, a fall test was performed by displacing the TS geometry in the direction of the dimmer-corrected reaction coordinate and performing a geometry relaxation at a lower precision. This sequential procedure allowed to explore and discard several reaction routes at a low computational cost before performing transition state relaxations at high precision.

The methanation reaction is studied in three stages: the adsorption and activation of $CO_{2(g)}$ (sec. 8.2.2), activation of the *C-O bond (sec. 8.3) and finally, the sequential hydrogenation of $*CH_x$ (sec. 8.4). Elementary steps were proposed and discussed for each stage (Scheme S1) considering experimental evidence and mechanisms from literature. DFT-derived rate and equilibrium constants are estimated through classic transition state theory (eq. 2.17) as described in sec. 2.2.4. For an elementary step, the activation Gibbs free energy barriers (ΔG_a, eq. 4.10) and reaction energies (ΔG_r, eq. 4.11) are computed as

$$\Delta G_a = G_{TS} - G_i \qquad \text{eq. 4.10}$$

$$\Delta G_{rx} = G_f - G_i \qquad \text{eq. 4.11}$$

Where the energy of the transition (G_{TS}) or the final state (G_f), respectively, are compared to the energy of the initial state of the step. Reaction energy profiles are constructed by carefully concatenating reaction energies while ensuring a geometrically consistent progression of the adsorbed species (see A7.1). Reaction barriers are more often discussed in relation to the reference energy of the reaction profiles.

Data handling: A python package (*stego*) was written to help organize and analyze results from the hundreds of simulations presented in this work. The energetic and vibrational information are paired in objects of different classes (e.g., gases, clean surfaces, adsorbed surfaces) allowing the construction of databases and the systematic computation of thermodynamic contributions, functions and kinetic parameters as described in sec. 2.2.3-2.2.4. The code is directly compatible with other widely used python packages and is publicly available under a MIT license (*stego* and utilities in *VASP_tools*, repositories in https://github.com/sebagodoy), together with several other utilities to . All reaction profiles in this work were constructed using built in modules of the *stego* package. Several more utilities to ease working with DFT simulations were also written[21] including a DOS module (*stego.dedos*) that was used for all PDOS plots and data analysis in this work.

---

[21] Including computation of thermodynamic contributions, inertia moments, generating relaxation reports, constructing neb paths, extracting reaction coordinates from neb paths, re-computing vibrational frequencies and isotopic exchange effect on vibrations (for KIE and TIE).

5. Characterization of catalysts

For all catalysts samples a single peak was identified in the powder XRD spectrum (Fig. 10a) which was associated to the (111) surfaces. The absence of two different peaks for the bimetallic samples suggests that a single mixed crystalline phase was formed instead of two separated monometallic phases. The close position of the (111) peak between the samples implies there are no strong differences in the lattice spacing and crystalline structure between the samples, though a small shift to higher 2Θ values consistent with the fractional Ni content (Fig. 10b) as reported in earlier works[9]. The peak position corresponds to coherent scattering angles (Bragg condition) and is inversely related to the lattice spacing, the Co < NiCo < Ni order in 2θ implies that the lattice spacing increases from Ni to the bimetallic to Co. This trend is consistent with early reports from Pearson and Thompson[16] showing the lattice spacing increases from Ni when the Co fraction is increased in NiCo solutions. The average nanoparticle diameters estimated from the peak widths in Fig. 10 and are included in Table 2, though a precise implementation of the Scherrer equation to estimate average particle size of nanoparticles from XRD is difficult given the broad peaks observed and high noise/signal ratio.

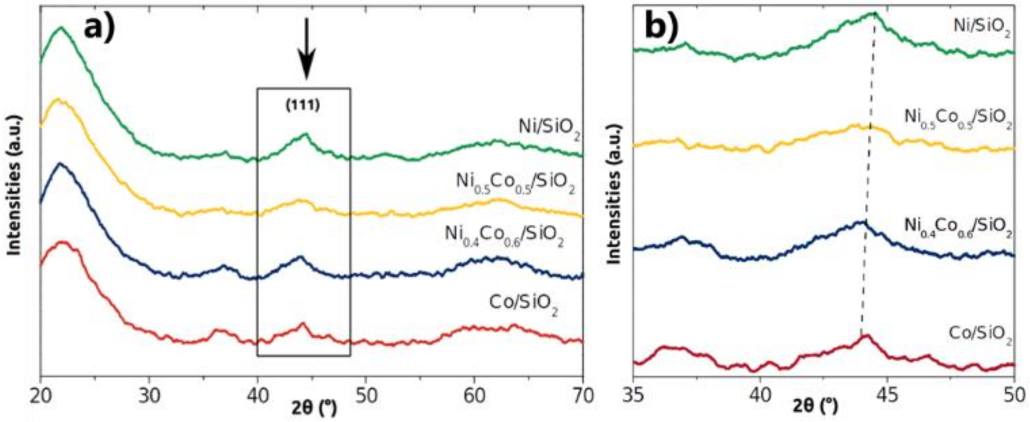

Fig. 10 a) X-ray difraction (XRD) of prepared catalysts and b) close up to the (111) peak position.

Energy dispersive X-ray Spectroscopy (EDX) was be used to map the distribution of different metallic species. Similar distribution patterns are identified for Ni and Co metals in Fig. 11b,c for a $Ni_{0.5}Co_{0.5}/Al_2O_3$ sample, which further supports XRD results about a single bimetallic phase being formed. Average nanoparticle size and its variability was also estimated from sample TEM micrographs of the prepared catalyst. TEM diameters in Table 2 show similar sizes for all catalysts around 5.0 nm with a low (<1.5) dispersion index (DI, eq. 4.2), which indicates similar structures and suggests the comparative analysis between catalysts is not significantly affected by structural sensitivity of the studied reactions. Histograms of the particle analysis in the TEM micrographs show for most catalysts a majoritarian population between 3nm and 6nm.

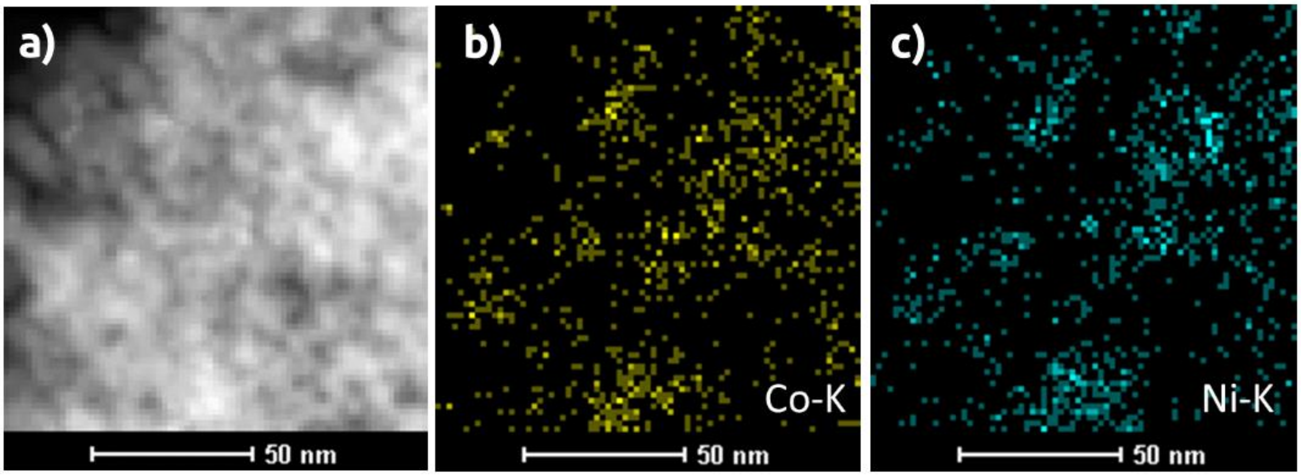

Fig. 11 a)TEM micrograph of a $Ni_{0.5}Co_{0.5}/Al_2O_3$ sample with EDX mapping of b)Ni (in yellow) and c)Co (in blue).

Table 2: Mean nanoparticle diameter from TEM and XRD (in nm), with DI the dispersion index.

Catalysts	d_{XRD}	d_{TEM}	DI
Co/SiO_2	3.7	5.0	1.16
$Ni_{0.4}Co_{0.6}/SiO_2$	3.1	5.4	1.21
$Ni_{0.5}Co_{0.5}/SiO_2$	5.0	4.8	1.21
Ni/SiO_2	4.3	5.0	1.24

5.1 Crystal structure of supported nanoparticles

Nickel is experimentally observed to form *fcc* (face centered cubic) phases in large bulks and big nanoparticles (~100nm) of high anisotropy[69]. Cobalt is reported to form either *fcc* or *hcp* (hexagonal close packed) phases, which may have significant effects on its catalytic properties[32]. For Co nanoparticles the observed phase may depend on the preparation technique and particle size[70] with predominant *hcp* phases for nanoparticles with diameters >40nm but *fcc* structure for smaller nanoparticles (<20nm) like the ones in Table 2. Nickel and cobalt are known to form homogeneous alloys in a wide range of compositions with a small effect in the lattice spacing[16]. The Ni-Co phase diagram shows thermally induced martensitic transformations to the *hcp* phase for high Co content at low temperatures but a predominant *fcc* phase when the Ni content is greater 35% wt[15]. These antecedents, the small particle diameter from TEM and XRD (<20nm), and the identification of (111) planes in Fig. 10 indicate a predominant *fcc* phase in all the prepared catalyst. This led to the selection of *fcc* phases for all computational models (Ni, Co and NiCo), which also allows to comparatively focus on the differences between monometallics, effects of the Ni-Co alloy and surface geometry while disregarding crystallographic bulk differences.

Lattice constants from simulations were obtained by fitting the RPBE-derived bulk energies for different volumes of a 4-atom *fcc* cubic cell to the Murnaghan equation of state[64] (eq. 4.5) as shown in Fig. 12 (details in Table S3). The resulting RPBE lattice parameters are 3.5542 Å, 3.5519Å and 3.5509Å (Table 3), associated with bulk modulus of 174.22 GPa, 179 GPa and 186

GPa for Ni, NiCo and Co, respectively (Table S3). The close lattice parameters are in agreement with the reported small effect of alloying Ni-Co in the lattice spacing[16] and the close peak positions in Fig. 10. The fit values are close to experimentally reported lattice parameters between 3.52Å to 3.54Å for Ni, Co and alloyed Ni-Co phases[15], [16], [71] and bulk modulus of 186GPa for Ni and 191GPa for Co[72]. The differences are attributed to the choice of functional and computational methods, Table 3 shows fit lattice parameters obtained with RPBE (chosen functional for this work) and classic PBE, with and without long range dispersion corrections (D3BJ, Grimme's third correction with Becke-Johnson damping function). Similar differences for different methods are reported by others[18], [27], [40], [73], [74]. Adding the D3BJ dispersion correction led to significantly larger errors in the lattice parameter but also suggested increased lattice spacing for higher Co content in agreement with Fig. 10 and early experimental reports[16]. Effects of the dispersion correction are further discusses in A1.4. Though PBE results offer a better description of the lattice parameters, RPBE is the functional of choice in this work for its better description of chemisorption energies[40], [62] as discussed in detail later. The effect of the small differences between the DFT-derived and experimental lattice parameter (0.8% in this work for RPBE) is usually neglected in catalytic studies[18] and only showed negligible differences upon testing (e.g., *C-O stretching frequencies change <4cm^{-1} using the experimental lattice parameter).

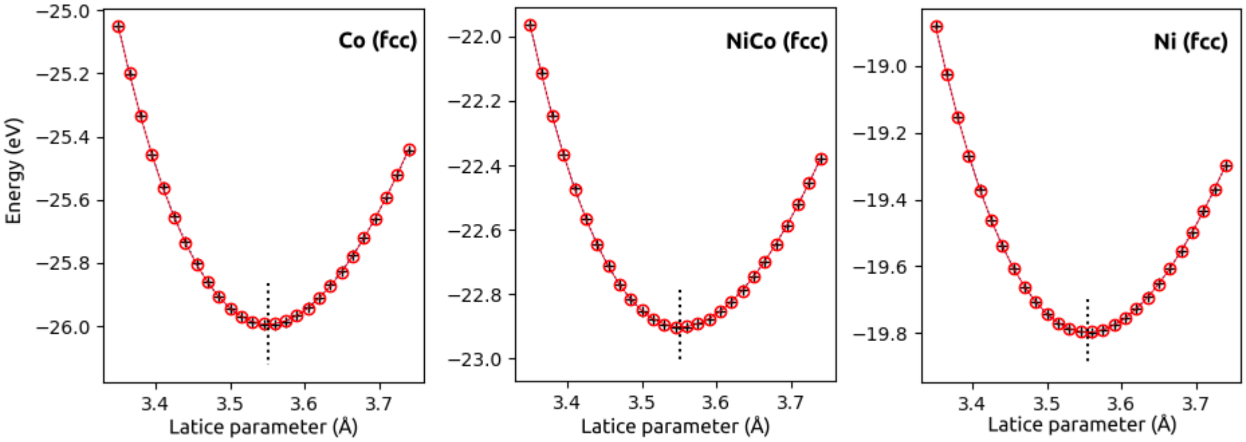

Fig. 12 RPBE-derived energies (o) fit to the Murnaghan equation of state (-), vertical dotted segment show the fitted lattice parameter.

Table 3 Lattice parameters fit to the Murnaghan equation of state (in Å) and experimental values.

Functional	PBE	PBE-D3BJ	RPBE	RPBE-D3BJ	Experimental values
Ni	3.518	3.476	3.554	3.368	3.516 [16]
NiCo	3.517	3.479	3.552	3.379	3.527 [16]
Co	3.516	3.481	3.551	3.389	3.544 [71]

To approximate the geometry of nanoparticles in the prepared catalyst, ideal Wulff polyhedron of minimal surface energy were constructed for *fcc* Ni and Co nanoparticles using the WulffPack python package[65] and surface energies taken from reference (Table S5, ref. [66]). The Wulff polyhedron in Fig. 13 shows for both metals predominant low index (111) and (100) surfaces, as expected from their orientations (matching compact lattice planes) and significantly lower surface formation energies compared to surfaces of higher Miller index. The abundance of (111) and (100) surfaces have also been reported for Ni[75] and Co[32] in previous DFT studies. Moreover, predominant (111) and (100) surfaces, along with (110) facets, have also been experimentally observed for large Ni nanoparticles (>100nm)[69] while multiply twined icosahedrons with (111) facets and Wulff Polyhedron with (111) and (100) facets have been used to describe the experimental size dependency of Co nanoparticles on the crystal phase[70].

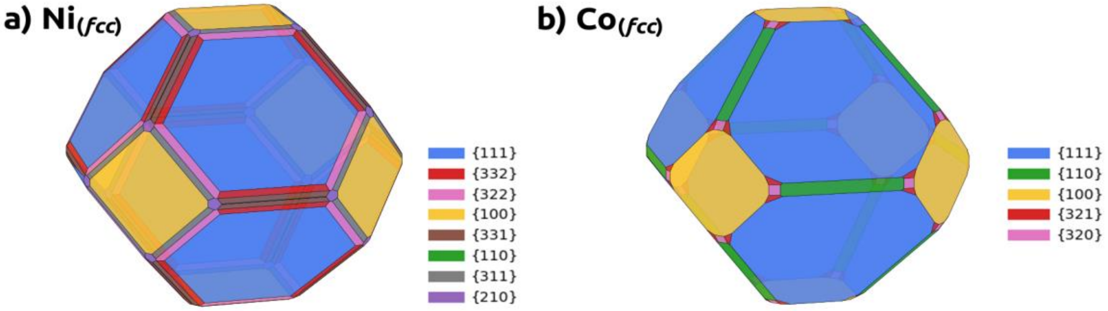

Fig. 13 Wulff polyhedron for a)Ni and b) Co ideal (and “large”) fcc nanoparticles. Facets are color coded as each legend specifies.

Close packed low index surfaces are also the most used in theoretical studies exploring surface reactions on metals. The (111) surface in particular has been systematically used in DFT studies of methanation[26], [76], [77], RWGS[27], [30], [78] and DMR[77], [79] reactions, though its ability to represent experimental observations has been questioned recently[27]. The (re)activity differences between sites on the large compact terraces and on surfaces of higher Miller Index (e.g., steps and kinks) have been theoretically compared [35], [37], [80]–[84] for monometallic surfaces but few studies probe these surfaces of for mixed metals and are limited to a single type surface surface[18] and pure surfaces with a single doping atom[85].

Sites with different local geometries may have different activities in forming or cleaving σ and π bonds related to the CO methanation reaction, therefore the relative abundance of these sites may affect the experimentally observed intrinsic activity of catalyst. These kinds of structural effects for CO and CO_2 reactions have been studied in relation to the size of Ni[37], [86] and Co[87] nanoparticles. For example Vogt et al showed $CO_{(g)}$ formation from $CO_{2(g)}$ for sub 2nm Ni particles previously thought to be unable to cleave the π bonds of CO_2 [37] and higher $CO_{(g)}$ production for smaller nanoparticles[26] suggesting a significant structure sensitivity of the competing *CO hydrogenation reactions. Though, it has also been suggested that the methanation TOF of larger Ni nanoparticles (5-91nm) is insensitive to the particle size[88].

The ideal Wulff polyhedron in Fig. 13 does not explicitly considers the different energetic contribution of edges between the ideal planes, therefore it describes better the geometry of only large nanoparticles (compared to the lattice parameter) where the number of atoms in ideal extended planes is proportionally much larger than the number of atoms in edges and corners.

For the small nanoparticle sizes experimentally prepared the edge/flat face proportion of atoms is larger and the contribution energetic contribution of those atoms with lower coordination degree may be significant, therefore the shape of the nanoparticle may differ from the ideal Wulff polyhedron near the edges and corners. A more detailed study of the nanoparticle morphology at the experimental sizes is outside the scope of this work, but a general idea of these nanoparticles still provide some insight on the site diversity, proportional abundance and predominant facets. As a simplified approach, nanoparticles for Ni and Co of diameters between 3.5nm and 6.0nm were generated (Fig. 14) using the Atomic Simulation Environment[89], [90] to truncate the *fcc* lattice to the Wulff polyhedron. Fig. 14 show for both metals the expected apparition of well-defined low index (111) and (100) facets becoming more predominant in the larger nanoparticles.

It is suggested from Wulff polyhedron in Fig. 14 that the low index facets connect in bands of lower coordination degree similar to (110) facets (e.g., Co$_{6931}$, Co$_{9045}$ in Fig. 14a) and long steps (more predominant for Ni, e.g., Ni$_{3247}$, Ni$_{4633}$ in Fig. 14b) whose area (and number of sites) may be more significant compared to the area of compact facets (e.g., Co$_{6931}$, Co$_{9045}$ and most Ni NPs). These areas may contribute to activity offering a wide range of different kinds of sites (e.g., upper/lower steps, B$_5$ sites and kinks) whose abundance on monometallic particles in reaction conditions will strongly depend on the interaction with the support and gas environment. For bimetallic particles this variability is even higher considering not only geometry but also local composition and gas-induced segregation, this high variability makes impractical their consideration for systematic comparisons between Ni, Co and NiCo. This conduced to the selection of the two predominant (111) and (100) facets of different coordination degree but common to Ni, Co to represent the active surfaces of Ni, Co and NiCo catalysts in this study.

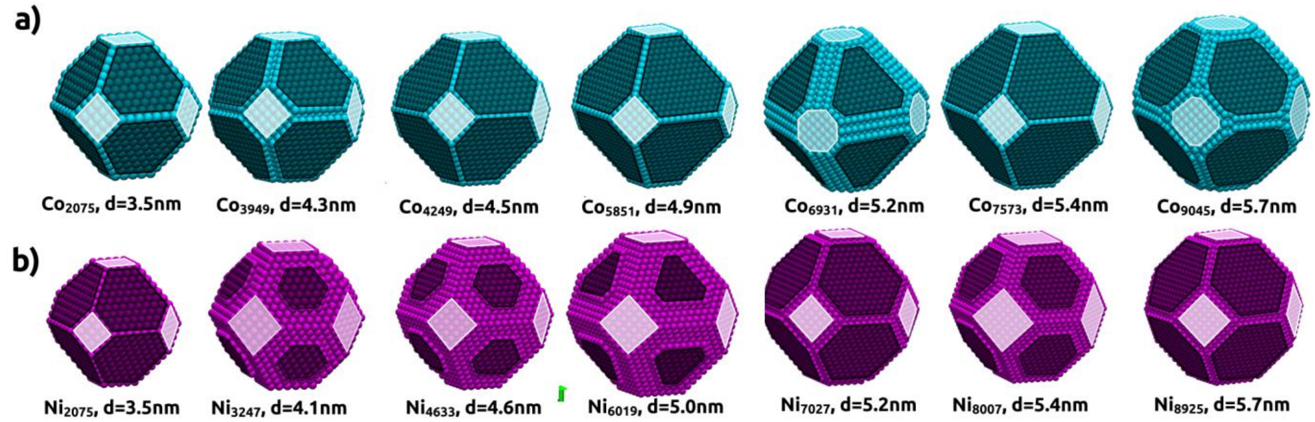

Fig. 14 fcc nanoparticles of a)Ni and b)Co constructed by truncation of bulk lattice according to the Wulff polyhedron. Black and white highlight (111) and (100) zones respectively.

5.2 Electronic properties of Ni, Co and NiCo bulk and surfaces

The slab models in Fig. 15 were constructed by repetition, rotation and truncation of the bulk models with RPBE lattice parameters and computed as described in sec. 4.4. The slab models were used to explore the electronic properties of the mono and bimetallic surfaces, and to simulate the adsorptions and reactions of interest for this work.

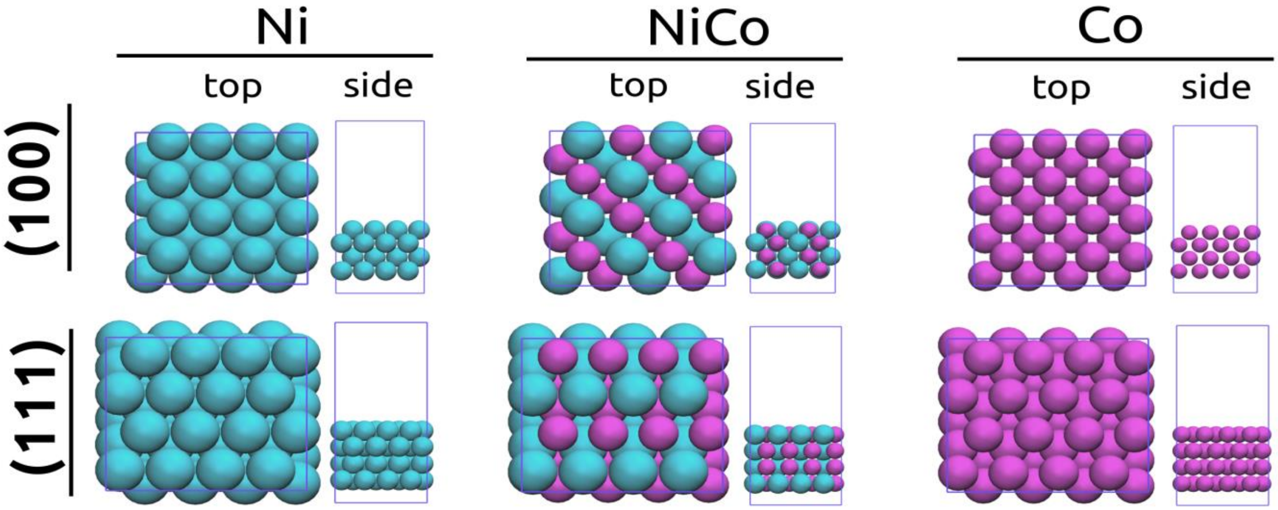

Fig. 15: Slab models of (111) and (100) surfaces of Co, NiCo and Ni.

The relaxed surfaces show the expected slight compression between the surface and subsurface layer and consequent separation between the second and third layer.[22] Lower formation energies are obtained from the slab models used in this work ($\gamma_{Ni(111)}$=1.7 J/m^2, $\gamma_{Ni(100)}$=2.0 J/m^2, $\gamma_{Co(111)}$=1.8 J/m^2 and $\gamma_{Co(100)}$=2.2 J/m^2) compared to reference values (Table S5, ref. [66]). Such differences were expected considering that models in this work are intended for the exploration of surface reactions, thus include fewer layers and only two layers on one side are relaxed. However, these values accurately reproduce the ratio $\gamma_{(111)}/\gamma_{(100)}$ for the monometallics (0.86 on Ni and 0.82 on Co) and the similar ratio for NiCo (0.84), which suggest similar surface proportions of (111) and (100) surfaces for the monometallic and intermetallic Wulff ideal nanoparticle shape.

Table 4 shows the average spin magnetic moments of atoms derived from the DDEC6 partition schemes of the electronic density. Bulk monometallic values for Ni and Co are 0.65 μ_B and 1.66 μ_B, respectively, coincident with Bader (Table S4) and with previously reported values[10], [29], [33]. This suggest an appropriate representation of the electronic structure and those values were used as initial estimates in all calculations.[23]

---

[22] A closer first and second layer compensate for the lower coordination of the surface atoms. Both layers are pushed away from the third layer (and bulk) since the atoms in the second layer are destabilized by their greater interaction with the first layer.

[23] this showed to avoid the eventual spontaneous convergence to magnetic layered slab configurations (layers with spins +/-/+/-) with higher energies which are not considered representative of the nanoparticle surfaces. This also probed to speed up computations with fewer *scf* iterations.

Table 4 DDEC6 atomic (average) electronic charges and spin magnetic moments.

	Electronic charges (e)			Spin magnetic moment (μ_B)		
	bulk	$(111)_{\text{surf.}}$	$(100)_{\text{surf.}}$	bulk	$(111)_{\text{surf.}}$	$(100)_{\text{surf.}}$
Co	0	-0.01	+0.01	1.66	1.72	1.82
$\text{Co}_{(@\text{ NiCo})}$	+0.04	+0.04	+0.10	1.72	1.81	1.89
$\text{Ni}_{(@\text{ NiCo})}$	-0.04	-0.05	-0.09	0.65	0.64	0.65
Ni	0	-0.01	+0.01	0.65	0.67	0.70

From Table 4, surface atoms in monometallic (111) and (100) surfaces remain essentially neutral (charges ~±0.01e) but exhibit higher magnetic moments than the bulk atoms (0.67 and 0.70 μ_B for Ni, 1.72 and 1.78 μ_B for Co). The intermetallic DDEC6 charges show electron density is drawn from Co atoms ($\text{Co}_{@\text{NiCo}}$) to the more electronegative Ni atoms ($\text{Ni}_{@\text{NiCo}}$) in the bulk and surface models. The magnetic moment of $\text{Ni}_{@\text{NiCo}}$ for the bulk and surfaces remains essentially the same as bulk Ni, but the corresponding magnetic moment of $\text{Co}_{@\text{NiCo}}$ is higher than bulk Co. The extent of charge donation and magnetic moment change in Co is higher for the less coordinated (100) surfaces than the (100) surface. This increase in magnetic moment of Co upon alloying but essentially change for Ni is not explained by simple electronic donation and requires consideration of their corresponding density of states.

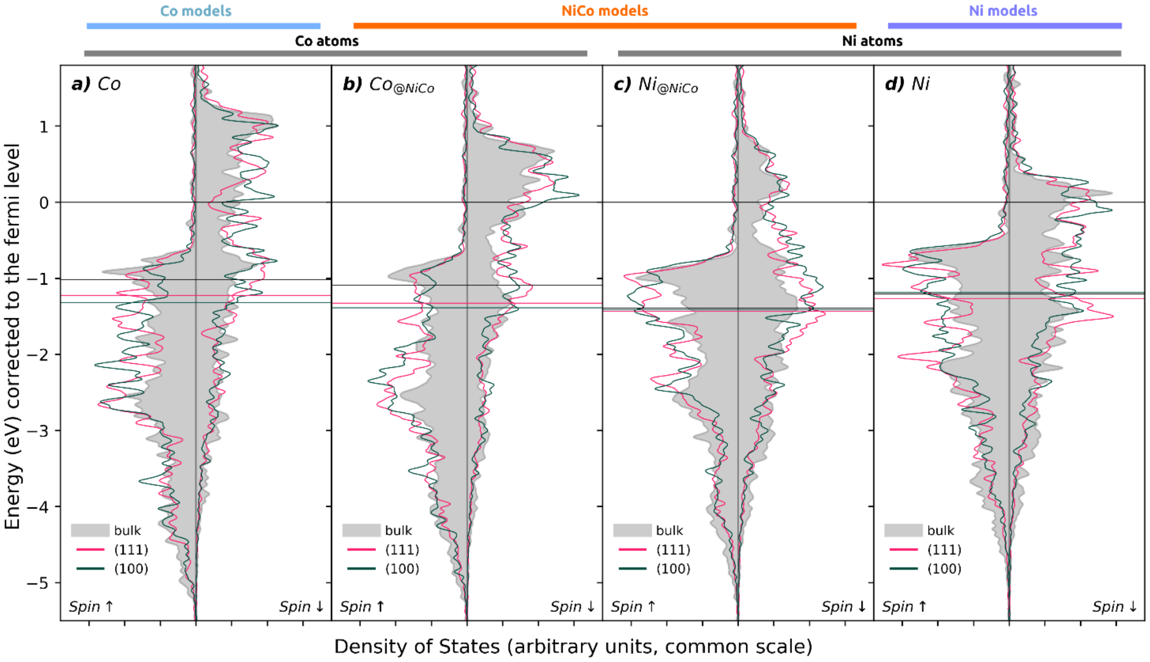

Fig. 16 d-band Projected Density of States (PDOS) in bulk, (100) and (111) surfaces for a) Co, b)Co in NiCo, c) Ni in NiCo and d)Ni. Fermi level at the zero line (Fermi-corrected PDOS), non-zero horizontal lines show the corresponding d-band centers (e_d).

The d-band PDOS of Co and Ni atoms in mono and intermetallic bulks, (111) and (100) surfaces are shown in Fig. 16. The spin-up components of Co atoms (Fig. 16a,b) appear at significantly lower energies than the spin-down component. Spin-up bands are completely filled while the spin-down bands extend across the fermi level with empty states at higher energies than monometallic Ni. The Ni atoms (Fig. 16c,d) contain more symmetric spin-up and spin-down components at the low energy end with the spin-up also completely filled but fewer unoccupied states above the Fermi level for the spin-down component compared to the Co atoms. These differences in d-bands are consistent with the higher magnetization of Co than Ni in the alloy and monometallics.

For bulk metals and surfaces the Co → Ni electron donation in the alloy increases the amount of Co empty states just above the Fermi level with only a slight reduction of occupied states around -0.5eV. A similar reduction around that energy is also observed for the Ni atoms in the alloy, but in this case the density of unoccupied states is also reduced around the Fermi level and spread to higher energies while occupied states concentrate at lower energies (~-1.2eV) compared to the monometallic Ni.

These changes in band and filled states distributions can be represented by the Fermi corrected *d*-PDOS centers (e_d; sec. 2.2.2.4) shown in Table 5 and as vertical lines in Fig. 16. For monometallics surfaces, higher e_d values have been reported for Ni(100) than Ni(111)[80], conversely, lower e_d values for Co(100) compared to less coordinated surfaces[91]. These trends agree with values in Table 5 and are attributed to the polarization of Co (asymmetry of up and down bands). For Ni and $\mathrm{Ni}_{@\mathrm{NiCo}}$ atoms there is little difference in e_d between bulk and both surfaces, which is consistent with the small geometric effects on Table 4 compared with Co atoms. More importantly, the overall effect of the Ni-Co interaction is a reduction of the *d*-band centers for both, Co and Ni in all, bulk, (111) and (100) surfaces. Ni atoms also show a larger downwards shift from mono to bimetallic. However, in the case of Co the shift o lower energy is due to loss of high energy filled occupied states that move above the fermi level upon donation to Ni. In contrast, in the alloy Ni atoms gain electronic density in similar proportions for he spin-up and spin-down components. This analysis suggests that the electronic structure of Ni atoms is more affected by alloying although it is not appropriate to stablish a direct relation to catalytic activity as in the classical d-band theory[48], [92].

Table 5 Average d-band centers (e_d in eV) for bulk, (111) and (100) surfaces.

	Bulk	$(111)_{\mathrm{surf.}}$	$(100)_{\mathrm{surf.}}$
Co	-1.01	-1.23	-1.32
Co@ NiCo	-1.08	-1.32	-1.38
NiCo (average)	-1.24	-1.38	-1.40
Ni @ NiCo	-1.39	-1.43	-1.41
Ni	-1.21	-1.26	-1.18

5.3 Composition and segregation

Surface segregation of one or the other metal in NiCo alloys have been reported experimentally with opposite results depending on the support and preparation conditions. Hernandez-Mejía et al.[6] reports Co enriched surfaces on reducible oxides (TiO_2 and Nb_2O_5) but their results suggest

Ni migrates to the surface on α-Al_2O_3 supports. EXAFS[24] from Cheng and Guo[93] shows Ni-rich surfaces for small (3-8 nm) NiCo nanoparticles on carbon supports. The surface formation energies (sec. 5.2 and Table S5) suggest naturally more stable formation of low index nickel surfaces than the cobalt surfaces in monometallic particles ($\gamma_{Ni(i,j,k)} < \gamma_{Co(i,j,k)}$). These results and observations show the necessity to study the surface composition of NiCo phases.

5.3.1 Experimental study of the CO-induced segregation

The CO-induced segregation of $Ni_{0.5}Co_{0.5}/SiO_2$ catalysts was studied following the experimental procedure shown in Fig. 17,a. The bimetallic catalyst was placed in the FTIR-cell, heated with a low temperature ramp (<2°C/min), reduced *in situ* with H_2 for two hours, and cooled to 20°C in He. IR spectra were taken before (Fig. 17, s_0) and after (s_1) saturating the surface with CO(1%)+He for 40 minutes.

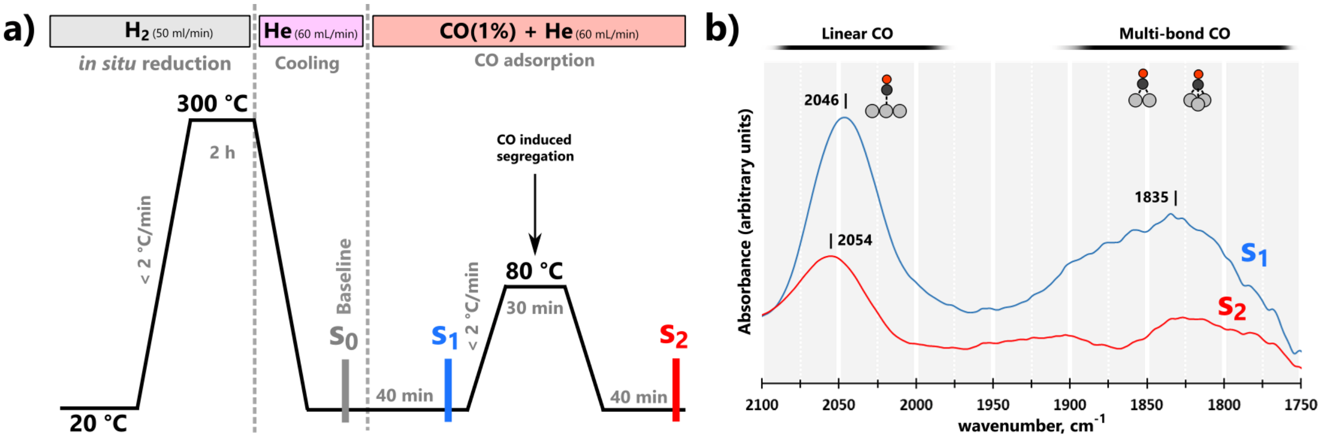

Fig. 17 Thermal and CO-induced segregation experiments with $NiCo/SiO_2$. a) procedure for in situ reduction, low-temperature CO saturation and obtaining of spectrum baseline (s_0), before (s_1) and after (s_2) exposure to high temperature $CO_{(g)}$ environment and b) the resulting spectrum.

The sample was heated with a slow ramp up to 80°C and kept for 30 min. before lowering the temperature to 20°C. The final spectra (Fig. 17, s_2) was taken after 40 min. at the same conditions used for the initial spectra. $CO_{(g)}$ bands in a SiO_2 sample previously taken at the experimental conditions were also subtracted. Two peaks are identified in the 2100-1750 cm^{-1} range and assigned to high-coverage linearly bond CO (~2050 cm^{-1}) and multi-bond CO (~1830 cm^{-1}). For the later spectra (Fig. 17b, s_2) lower intensities and areas are observed for both adsorption modes. Moreover, the linearly bounded peaks shows a blue-shift from 2046cm^{-1} to 2054cm^{-1} while the multi-bond peak almost disappears. These observations indicate that surface changed upon heating in a CO environment, possibly by varying the fractions of Ni and Co near the surface. Therefore, varying effects of both (Ni and Co) are involved on the surface chemistry instead of, for example, a multilayer core-shell configuration where only one metal is exposed and behaves as its monometallic form. The lower intensity in the later spectra (Fig. 17b, s_2) also suggest less

---

[24] extended X-ray absorption fine structure spectroscopy

abundant and less stable carbonyl species (*CO) after the thermal-CO treatment, which may be a relevant feature of the bimetallic surface (considering $CO_{(g)}$ is a byproduct) and will be discussed later (sec. 7.1-7.2.1).

5.3.2 Simulating segregation and composition

For some insight on the relative stability of segregated surfaces the position exchange of Ni and Co atoms in slab and nanoparticle models were tested (Fig. 18a,b, sec. A2.4). Effects of the interaction with support are not represented by these the DFT models, but are also not expected for the non-reducible support (SiO_2) of the catalysts in this study.

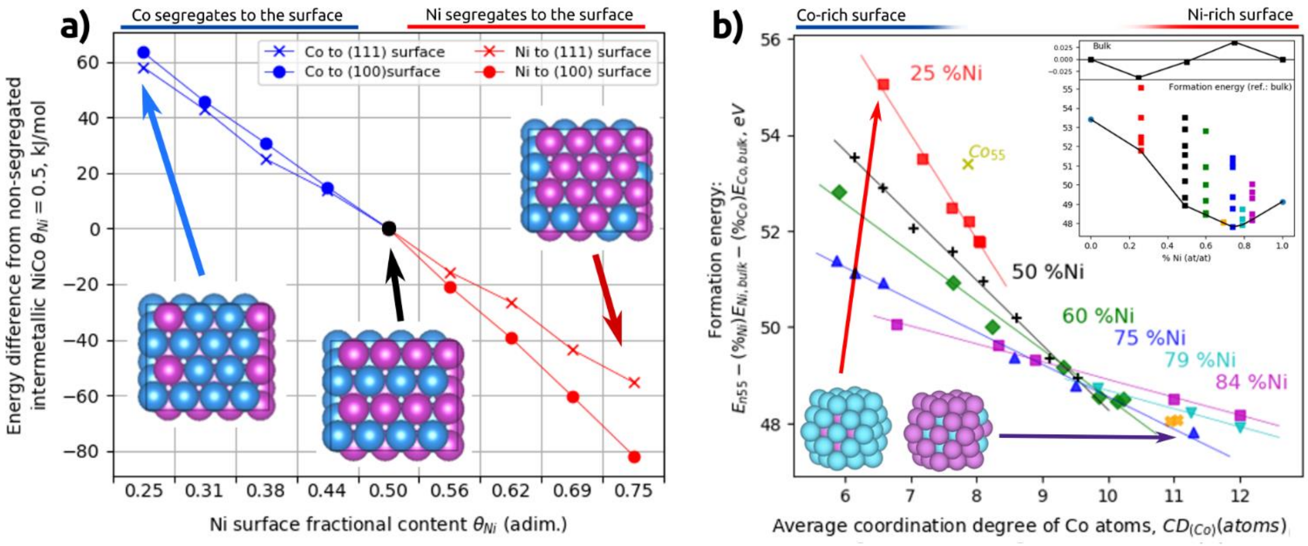

Fig. 18 a) Relative stability of segregated $Ni_{0.5}Co_{0.5}$ slab models, symbols: × for (111) and • for (100) surfaces, b) Formation energies for Ni_xCo_{55-x} nanoparticles (relative to bulk monometallic phases) and coordination degree of Co atoms, inset shows the convex hull in composition for the Ni-Co bulk (upper) and Ni_xCo_{55-x} nanoparticles (lower). Color code, purple: Ni, cyan: Co.

<u>**Segregation on surfaces (Fig. 18a):**</u> the two top layers of the intermetallic slab in Fig. 15 were reorganized and relaxed to produce models of different Ni surface fractions. Up to four atoms from the top layer were replaced with atoms from the second layer, in this way the fraction of Ni atoms in the surface ($\theta_{Ni} = n_{Ni}/(n_{Ni} + n_{Co}) = 0.5$) varied between $\theta_{Ni} = 0.25$ for a Co-rich surface to Θ_{Ni}= 0.75 for a Ni-rich surface[25]. Fig. 18a compares the energy of these segregated models to the intermetallic surfaces ($E_{\theta_{Ni}} - E_{\theta_{Ni}=0.5}$) showing that (111) and (100) surfaces become more stable forming an exposed layer more rich on Ni and moving Co to the bulk. The segregation difference becomes bigger for the less coordinated (100) Ni-rich surfaces, as expected

---

[25] Note that in this exchange a x% Ni-rich surface has a 1-x% Co subsurface

from greater difference between $\gamma_{(100)}$ for Ni and Co, compared to the $\gamma_{(111)}$ difference for Ni and Co.[26]

Segregation in nanoparticles (Fig. 18b): Ni_xCo_{55-x} nanoparticle[27] were used to explore low coordination corners and edges. The nanoparticles were constructed as described before (sec. 5.1), the average coordination degree of Co atoms ($CD_{(Co)}$) were computed and atom labels were exchanged through a genetic algorithm to minimize and maximize $CD_{(Co)}$ spanning from a Co-rich surface to a Ni-rich surface, respectively. Formation energies are computed relative to the monometallic bulk phases: $E_{Ni_xCo_{1-x}} - xE_{Ni,\text{bulk}}/55 - (1-x)E_{Co,\text{bulk}}/55$. Fig. 18b shows that a Ni outer layer is favored in all metal compositions with an almost linear relation to CD_{Co}. Moreover, the convex hull for the composition (Fig. 18, lower inset) shows more stable nanoparticles are formed with a higher Ni composition. This is exclusively attributed to the stability of Ni in the surface and the high surface atoms/bulk atoms ratio of the small nanoparticles studied (n_{55}, ~1 nm). It is expected for larger nanoparticles that the most stable global composition shifts to higher Co compositions closer to Ni:Co=3:1, the most stable bulk composition (Fig. 18, upper inset).

---

[26] The position exchange within the top layer forming of Ni or Co patches was also studied, though these reorganizations are also favored suggesting coalescence of similar atoms in the surface, but the energy of the system is only slightly reduced (<4kJ/mol) compared to the exchange between layers.

[27] n=55 fcc clusters consist two shells surrounding a central atom in an icosahedron structure with I_h symmetry forming fairly stable nanoparticles, n=55 is one of the “magic numbers” and n=55 nanoparticles are widely used in literature[94]

6. Kinetic studies

6.1 Reaction rates and selectivity

A kinetic study of the $CO_{2(g)}$+$H_{2(g)}$ reaction was conducted using the differential reactor setup and procedure described in sec. 4.2. Only $CO_{(g)}$ and $CH_{4(g)}$ were identified as products and carbon balances >95% including $CO_{2(g)}$, $CO_{(g)}$ and $CH_{4(g)}$ indicated no other species were produced in significant amounts. Fig. 19a,b shows the intrinsic rates for the $CH_{4(g)}$ and $CO_{(g)}$ formation, Table 6 shows the corresponding apparent activation energies (E_{app}) and annex A5.1 shows similar trends for other feed conditions. Higher temperatures increase all rates, but the trend in catalyst composition remains approximately the same for the three temperatures suggesting that the dominant reaction pathways for both reactions do not change within the studied temperature range.

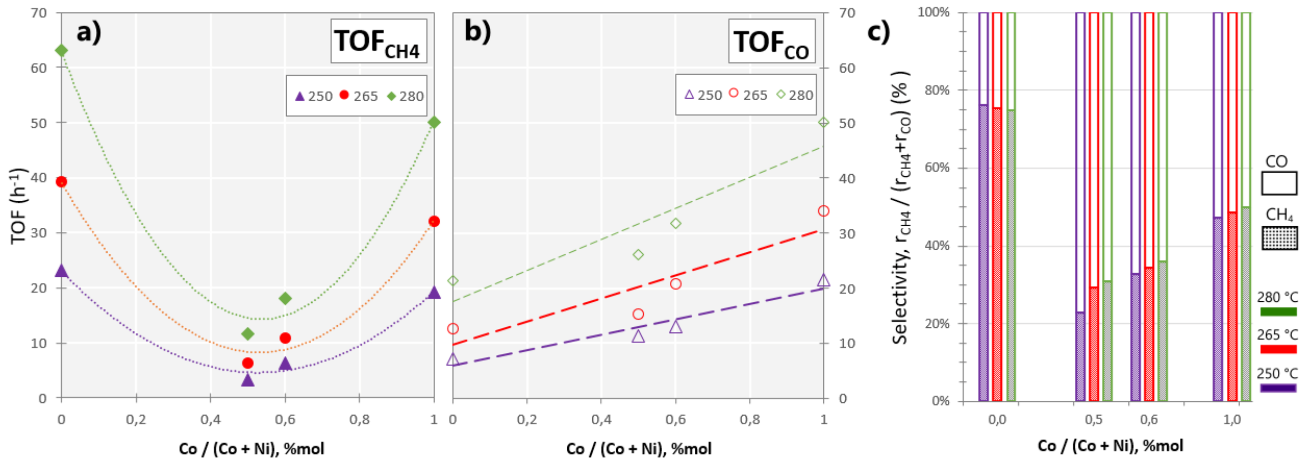

Fig. 19 Effect of the catalyst Ni-Co molar composition on the intrinsic reaction rates (TOF) for (a) $CH_{4(g)}$, (b) $CO_{(g)}$ formation and (c) their selectivities ($TOF_x/(TOF_{CO}+TOF_{CH4})$) from 1 kPa $CO_{2(g)}$ + 25 kPa $H_{2(g)}$ (He balance for 1 atm) at 250 °C (purple), 265 °C (red) and 280 °C (green).

Table 6 Apparent activation energies (E_{app}, kJ/mol) for the $CH_{4(g)}$ and $CO_{(g)}$ formation from 1 kPa $CO_{2(g)}$ + 25 kPa $H_{2(g)}$ (He balance for 1 atm) on the studied catalysts.

E_{app}, kJ/mol	Ni/SiO_2	$Co_{0.5}Ni_{0.5}/SiO_2$	$Co_{0.6}Ni_{0.4}/SiO_2$	Co/SiO_2
$CH_{4(g)}$ formation	81	99	84	77
$CO_{(g)}$ formation	87	66	72	68

For the bimetallic catalysts, $TOF_{CH4(g)}$ is significantly lower (Fig. 19a) and has higher E_{app} (Table 6) compared to both monometallic catalysts at the same temperature. This anti-synergistic effect on the $CH_{4(g)}$ formation also evidences the formation of a bimetallic Ni-Co phase where Ni and/or Co atoms behave significantly different from their monometallic surfaces as was suggested in sec. 5.2. E_{app} for the methane formation is slightly lower than for the $CO_{(g)}$ formation on Ni/SiO_2, indicating a higher selectivity towards $CH_{4(g)}$ that decreases with increasing temperature[28] as observed in Fig. 19c (for Co/(Co+Ni)=0). For all other catalyst $E_{app}(CO) < E_{app}(CH_4)$ which is consistent with their higher CO selectivity, with the observed promotion of the methane formation by increasing temperature, and suggest that bimetallic catalysts behave more similar to Co rather than Ni catalysts. On the other hand, Fig. 19b shows that the $CO_{(g)}$ formation rate increases linearly following the Co molar content (weighted average between the monometallics), consistent with the higher CO formation rates on Co/SiO_2 catalysts. This suggest that, unlike the methane formation, the interaction of Ni and Co atoms in the bimetallic catalyst has little effect on the production of $CO_{(g)}$.

In summary, for the methanation reaction alloying Ni and Co has the counterproductive effect of lowering the methane production (hereafter referred to as the anti-synergic effect) but has almost no effect on the $CO_{(g)}$ formation which increases linearly with the Co content. These effects make bimetallic catalysts less active for the $CO_{2(g)}+H_{2(g)}$ reaction (lower $CO_{2(g)}$ consumption rates, Fig. S7) and less selective towards methane. More generally, these differences suggest that the formation of CO and CH_4 are hindered in different kinetically relevant pathways.

6.2 Apparent reaction orders

A simple power law $r = k_0 P_{CO_2}^{n_{CO_2}} P_{H_2}^{n_{H_2}}$ was fit to explore the effect reactant concentration in the methane and CO formation. The apparent reaction orders in Table 7 do not change considerably with temperature, supporting that the reaction pathways with the highest contribution to the CO and CH_4 formation reactions does not change significantly within the studied temperature range. The H_2 apparent order for CH_4 are slightly lower (~ 0.28) on $Ni_{0.5}Co_{0.5}/SiO_2$ compared to the other catalysts (~ 0.4), otherwise H_2 and CO_2 apparent orders are fairly similar on the monometallic and bimetallic catalyst: n_{H2} ~ 0.4 and n_{CO2} ~ 0.0 for the CH_4 formation, n_{H2} ~ 0.0 and n_{CO2} ~ 0.5 for the CO formation. This suggest that similar pathway contributions or preferred mechanisms take place in the mono and bimetallic catalyst surfaces.

The methane formation rate shows a significant effect of the H_2 partial pressure with apparent orders ~ 0.5, suggesting hydrogen (probably *H) is directly involved in the rate limiting for the main reaction paths in the CH_4 formation route. Conversely, the CH_4 formation shows little effect of the CO_2 partial pressure ($|n_{CO_2}| < 0.15$) suggesting either, CO_2 is not related to the rate determining steps or the CO_2 direct contribution to the surface occupancy outweighs its contribution to the rate determinant step in the rate equation. A significant CO_2 surface population is unlikely considering the weak binding of CO_2 to the metallic surfaces (discussed further in sec. 8.2) and FTIR results (sec. 7.1). H-assisted dissociation of the *C-O bond has been suggested as the main pathway in recent DFT-microkinetic studies on Ni(111) and Ni(100)[36].

---

[28] This is the expected usual behavior; higher temperatures favor the reaction with higher E_{app} increasing their selectivity.

Table 7 Apparent reaction orders of H_2 and CO_2 partial pressures in the CH_4 and CO intrinsic formation rates

	TOF_{CH4} (h^{-1})						TOF_{CO} (h^{-1})					
	n_{H2}			n_{CO2}			n_{H2}			n_{CO2}		
Temperature, °C	250	265	280	250	265	280	250	265	280	250	265	280
Ni/SiO_2	0.44	0.43	0.42	-0.05	-0.07	-0.09	-0.06	-0.05	0.03	0.63	0.60	0.57
$Ni_{0.5}Co_{0.5}/SiO_2$	0.24	0.27	0.32	0.04	-0.14	-0.04	-0.08	-0.04	0.00	0.44	0.49	0.53
$Ni_{0.4}Co_{0.6}/SiO_2$	0.41	0.44	0.43	-0.03	-0.02	-0.02	-0.03	0.00	0.03	0.47	0.51	0.52
Co/SiO_2	0.51	0.45	0.52	-0.08	-0.03	0.03	0.01	-0.01	0.08	0.52	0.54	0.59
	~ 0.41			~ -0.04			~ -0.01			~ 0.53		

Apparent orders for the CO formation rate show the opposite behavior compared to the CH_4 formation, orders ~0.5 for the CO_2 partial pressure but almost no effect of H_2. This is consistent with carbon monoxide being formed without H assistance through a direct dissociation of $CO_{2(g)}$, which also explains the high CO coverage observed in FTIR (sec. 7.1). Vogt et al.[26] showed experimentally than CO_2 direct dissociation towards *CO is possible even on small Ni nanoparticles, this step was considered the main source of *CO but kinetically irrelevant compared to later hydrogenation for the CH_4 formation pathways[37] in agreement with the previous observations about the n_{H_2} and n_{CO_2} orders for both products.

7. Species on the reactive surfaces

The identification and study of molecular species on the catalysts surfaces provides key insight for 1) proposing chemically consistent reaction mechanisms and 2) their later exploration through theoretical methods. The identity and evolution of surface species is experimentally studied at a macroscopic level in sec. 7.1, from those results, trends in surface geometry and composition are theoretically studied in detail for possible reaction intermediates (7.2).

7.1 Surface species under reaction conditions from MS/FTIR analysis

An operando FTIR study was conducted with the experimental setup and procedure described in section 4.3 and refs.[7], [95] to assess the identity of surface species on the prepared Ni/SiO_2, $Ni_{0.5}Co_{0.5}/SiO_2$ and Co/SiO_2 catalysts under reaction conditions. The steady state FTIR results allow the identification of surface species, their relation to the reactive pathway is discussed considering their dynamic evolution upon feed changes (reactive mixture and pure H_2).

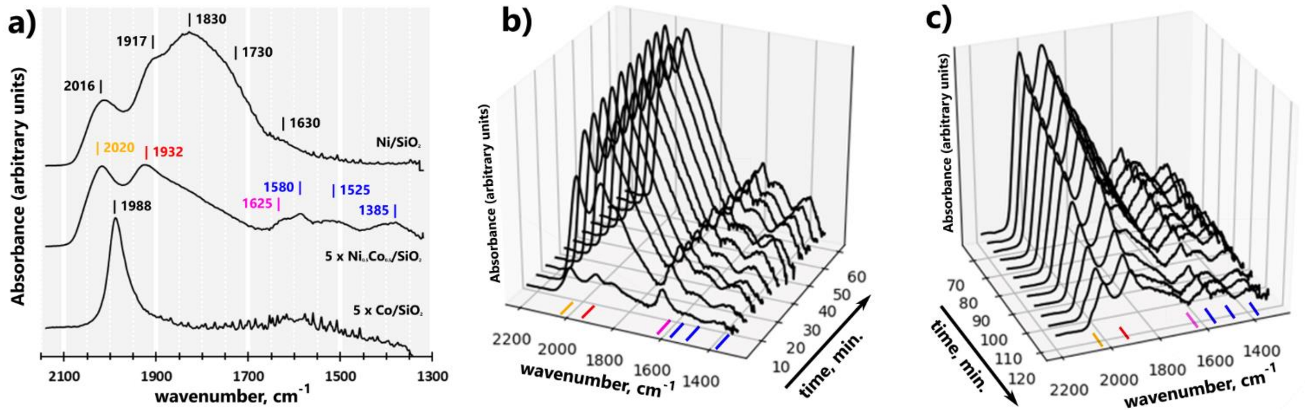

Fig. 20 a) Steady state (200°C, 1kPa CO_2 + 25 kPa H_2 + He balance) FTIR absorption spectra and b) dynamic evolution of the FTIR spectra on $Ni_{0.5}Co_{0.5}/SiO_2$ spectra at 200°C switching from b) He to 1kPa CO_2 + 25 kPa H_2 and c) from 1kPa CO_2 + 25 kPa H_2 to 25 kPa H_2 (He balance) feeds.[7]

Fig. 20a shows the absorption spectra for the catalyst at steady state for CO_2+H_2 feed under reaction conditions. Note the scaling factors in Fig. 20a, since the adsorption intensities for each catalyst depend on several experimental factors (e.g., width of the wafer) and comparison between catalysts is only qualitative. For all catalysts the most relevant features of the spectra were identified in the 2200-1200 cm^{-1} range and associated to carbonyl (surface CO), formyl (surface HCOO) and carbonate (surface HCO_3) species[7], [95].

For Co/SiO_2 the main feature identified is single peak at 1988 cm^{-1} associated to the C-O stretching frequency of linearly adsorbed carbonyl species, i.e., *CO on top of a Co surface atom. The asymmetry of the peak extending to lower frequencies can be associated to the contribution of different surface geometries where *CO adsorbs linearly (see Table 8 below[29]) and a small proportion of bidentate carbonyl species (**CO in bridge positions).

The absorption spectra for Ni/SiO_2 shows peaks at 2016 cm^{-1}, 1918 cm^{-1} and 1824 cm^{-1}. The highest frequency is again associated to linearly bonded carbonyl and the band at 1918 cm^{-1} to bidentate (bridge) carbonyl. The peak at 1824 cm^{-1} gives the highest contribution to the absorption spectra and extends asymmetrically to lower frequencies (until ~1675 cm^{-1}) thanks to a contribution at about 1730cm^{-1} (evidenced in the dynamic IR profiles, Fig. 20b), this zone is associated to multi-dentate (three- and four-fold) carbonyl species. The higher peaks for the bridge and multi-bonded species suggest their greater abundance compared to the linearly adsorbed *CO, though different modes have different intrinsic contributions to the absorbance (see section 2.2.2.5) and the relation between intensity and concentration of the species is not direct. The small shoulder around 1630 cm^{-1} is associated to the asymmetric stretching of a proportionally small population of bicarbonate species (surface HCO_3).

Carbonyl species are also identified for the bimetallic $Ni_{0.5}Co_{0.5}/SiO_2$ catalysts in the 2200-1650 cm^{-1} range. The peak at 2020 cm^{-1} is associated to linearly bonded *CO, at slightly higher frequency than on Ni/SiO_2 (2016 cm^{-1}) but significantly higher than on Co/SiO_2 (1988 cm^{-1}). This blue-shift (shift to higher frequencies) may be directly related to the electronic effect of the bimetallic Ni-Co interaction or attributed to higher CO coverages on the bimetallic surface. Regardless, the closer frequency to the linear adsorption on Ni/SiO_2 suggests a higher population of *CO linearly bonding on top of Ni atoms on the bimetallic catalyst. This would be consistent with a segregated Ni-rich surface on the bimetallic catalyst (discussed in section 5.3 and later in sec. 7.2.1.2). A peak at 1927 cm^{-1} and a smaller shoulder at 1825 cm^{-1} are associated to the presence of carbonyl species adsorbed in bridge and multi-dentate modes, respectively. The closer heights of the linear and multi-bonded peaks suggest a lower proportional abundance of the multi-bonded carbonyl species on the bimetallic catalyst, compared to the Ni/SiO_2 surface, but still significantly higher than on the Co/SiO_2 catalyst where no significant multi-bonded contribution is observed[30]. The dynamic evolution of the $Ni_{0.5}Co_{0.5}/SiO_2$ spectra (Fig. 20b,c) shows the early apparition of a peak at 1625 cm^{-1} associated to bicarbonate species, followed by the apparition of peaks at 1580 cm^{-1} and 1385 cm^{-1} associated to symmetric and asymmetric vibrations of bidentate formate and a peak at 1525cm^{-1} associated to monodentate formate.

The normalized integral areas of the identified FTIR bands[31] are shown in Fig. 21a for $Ni_{0.5}Co_{0.5}/SiO_2$, along with the normalized intensities of the effluent CO, CO_2 and CH_4 from the mass spectrometer (MS, Fig. 21b). The areas of linear and multi-bonded carbonyl species rapidly increased at about the same rate while feeding CO_2+H_2 (He balance) approaching a stabilized level at ~40min. MS signals for effluent CO, CH_4 (products) and CO_2 (unreacted) increase rapidly reaching steady state. When the feed is replaced by H_2+He the MS signals for CO and CO_2 rapidly

---

[29] Compared to (111), a surface with lower coordination degree as (100) appear to lower the vibrational frequency of linearly bonded carbonyl species.

[30] A proper comparison need to consider the intrinsic IR absorptions of the different adsorption modes, see sec. 7.2.1.2.

[31] Contributions to the total spectrum are deconvoluted to Gaussian contributions associated to the identified species.

decay to zero within the first 10 min. The CH_4 signal shows a lower descent rate with persistent production of methane even after the CO and CO_2 signals disappear. The FTIR areas for CO for linear and multi-bonded carbonyl species decay at the same rate, suggesting that there is a rapid exchange between linear and multi-bonded adsorption modes, but slower than the CO MS signal suggesting that those carbonyl species do not significantly contribute to the CO production. The equally fast dynamic evolution of CO and CO_2 MS signals is consistent with a rather simple (or direct) production of CO from the CO_2 feed, compared to the slower decay for CH_4 that could be explained by the hydrogenation of the remaining surface carbonyl species observed in the FTIR. Similar results were observed for the monometallic catalysts[7].

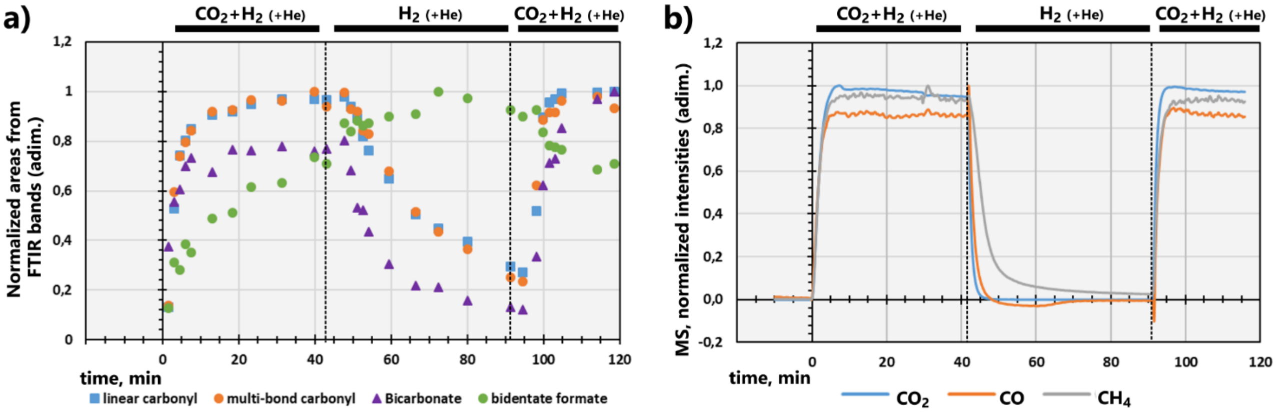

Fig. 21 Normalized a) integral areas for FTIR bands and b) mass spectrometer signals, for $Ni_{0.5}Co_{0.5}/SiO_2$ at 200°C cycling 1kPa CO_2 + 25 kPa H_2 and 25 kPa H_2 (He balance) from Fig. 20b,c.[7]

The bicarbonate areas evolve similar to the carbonyl species but with a faster rise and stabilization during the CO_2+H_2+He feed and faster elimination under H_2+He feed, possibly dissociating and releasing CO_2. Following the evolution of formate species (surface HCOO) is also relevant since many authors have propose H-assisted dissociations of CO_2 through formate intermediate. The FTIR areas for the bidentate formate begin increasing with the CO_2+H_2+He feed and continue increasing the first 30 min. even after only H_2+He is feed. This behavior does not seem to be related to the feed composition, the evolution of surface carbonyl (FTIR) or the CH_4 and CO production (MS). Therefore, formate may only appear as a stable expectator, probably not involved in the reaction mechanism or even blocking active methanation sites.

In summary, the results above suggest that surface *CO is one of the most relevant and abundant surface species and its evolution is closely related to the progression of the reaction. Therefore, the following sections study in detail the adsorption and stability of CO and other possible reaction intermediates with emphasis on trends for the geometry and composition of the model surfaces.

7.2 Adsorbed species on surface models

The adsorption of CO and other relevant reaction intermediates on the Ni, Co and NiCo, (111) and (100) slab models (Fig. 15) was studied using the RPBE functional. The unique adsorption sites identified in Fig. 22 were considered, including linear (t, top), bidentate (b, bridge), threefold sites (*fcc* or *hcp* with different sublayers) on (111) surfaces and fourfold or hollow sites on (100) surfaces. For the intermetallic (111) surface (Fig. 22c), three-fold *fcc* and *hcp* sites can be distinguished according to their local composition in Ni-rich $CoNi_2$ sites and Co-rich Co_2Ni sites. Four-fold sites on NiCo(100) (Fig. 22d) have the same local surface composition (Co_2Ni_2) but are open to a single Ni or Co subsurface atom that defines them as Ni-rich or Co-rich, respectively.

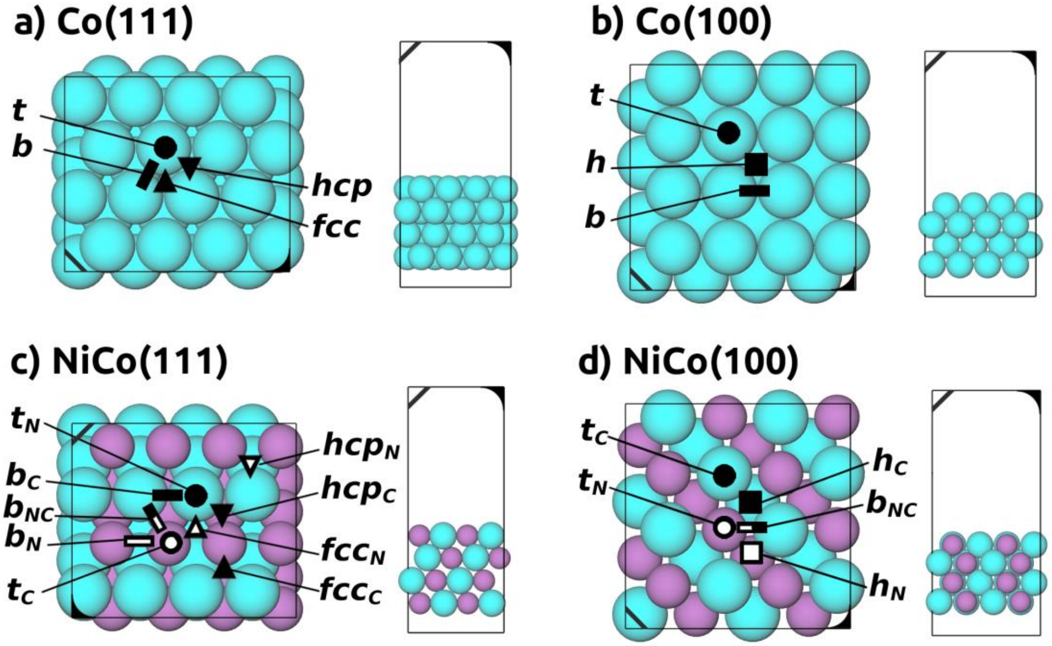

Fig. 22 Unique adsorption sites on monometallic and bimetallic (111) and (100) surfaces. Sites on Ni surfaces are equivalent to the Co surfaces depicted.

Possible surface intermediates were relaxed on several sites and configurations (sec. A6). Fig. 23 compares their stability on the surface taking the most stable atomic species on the surface as reference (recombination energy, eq. 4.9, refs. [26], [36]), lower energies indicating more stable species. Positive energies on the (100) surfaces (red) directly result from the highly stable adsorption of the atomic C, O and H species. CO shows the lowest energy on (111) surfaces and moderately positive on (100) surfaces, suggesting a high stability of *CO species in all catalysts and consistent with the pool of surface carbonyl experimentally observed (sec. 7.1). Higher energies on Co(100) and Co(111), compared to the corresponding Ni and bimetallic surfaces, suggest a weaker binding of *CO, consistent the higher selectivity towards $CO_{(g)}$ of Co/SiO_2 catalysts (Fig. 19c). Conversely, CO_2 higher recombination energies are consistent with its weak chemisorption[32]. The stability of formate (HCOO) on (111) surfaces also agrees with their experimental identification in sec. 7.1, though its dynamic evolution ruled it out of the dominant pathway for the CO or CH_4 formation. HCOH species show some of the highest recombination energies on all surfaces and higher than HCO and COH, which is consistent with methanation pathways including the first hydrogenates but not HCOH species as suggested by Sterk et al.[36]. Carbonate species (CO_3) were experimentally identified but appear to be less stable than most other species in Fig. 23, suggesting that $*CO_3$ tends to decompose quickly without contributing to the reaction mechanism (e.g., $*CO_3$ may form from *O and $CO_{2(g)}$ species that can be easily released back to the gas phase, see sec. 8.2.1 and A6.3). The following sections discuss in detail trends in surface geometry and local site composition for the most relevant surface species.

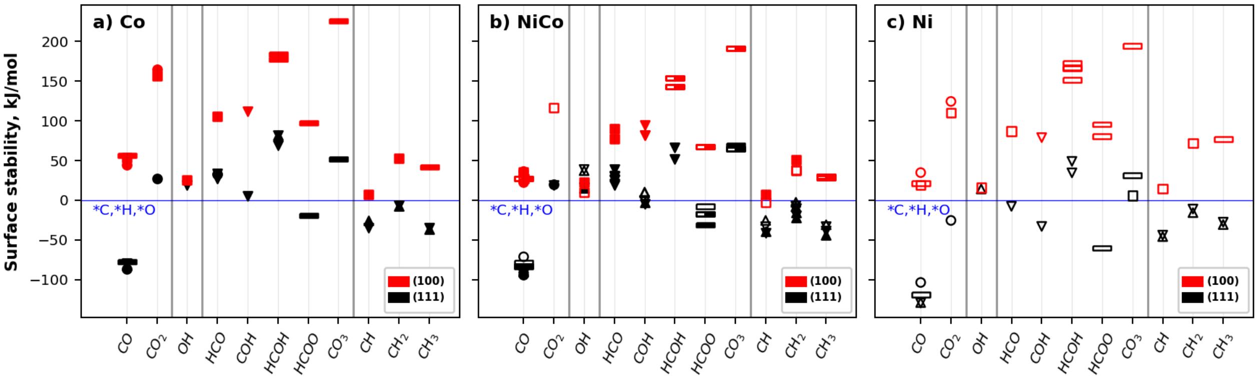

Fig. 23 Surface stability of possible intermediates on a) Co, b) NiCo and c) Ni, black : (111) and red : (100) surfaces, symbols denote approximate adsorption site geometry as in Fig. 22, close symbols for Co or Co-rich sites, open symbols for Ni or Ni-rich sites.

7.2.1 Carbonyl species

The stability of carbonyl species on the model surfaces are compared through the $CO_{(g)}$ adsorption enthalpies[33] shown in Fig. 24, higher values indicate weaker *CO binding and can be associated to an easier release of $CO_{(g)}$ species. Geometries and energies are included in in A6.1, Table 9 shows electronic adsorption energies for reference. Six vibrational frequencies were computed considering all degrees of freedom for the C and O atoms and tracking the changes in the normal dipole moment ($\underline{\mu_z}$). For all surface geometries and compositions, the *C-O stretching is the highest vibrational frequency ($\nu_{*C-O} > 1500\ cm^{-1}$), all other frequencies represent *CO oscillations within the binding site with frequencies lower than 500cm^{-1}. Table 8 shows ν_{*C-O} and the $(\partial\mu/\partial z)^2$ as surrogate of the IR intensities (sec. 2.2.2.5). Accuracy, the effect of coverage and possible corrections are discussed before comparing to the experimental results from section 7.1.

---

[32] CO_2 chemisorption is discussed in detail in the context of the reaction in sec. 8.2.2

[33] Most studies consider only electronic or ZPVE corrected energies (e.g., [44], [96]), given the poor stimation of low frequencies. Enthalpies are presented here for comparison with experimental values, though ZPVE and thermodynamic corrections have little effect on the electronic adsorption energy and preserve the electronic trends as detailed in Table 9.

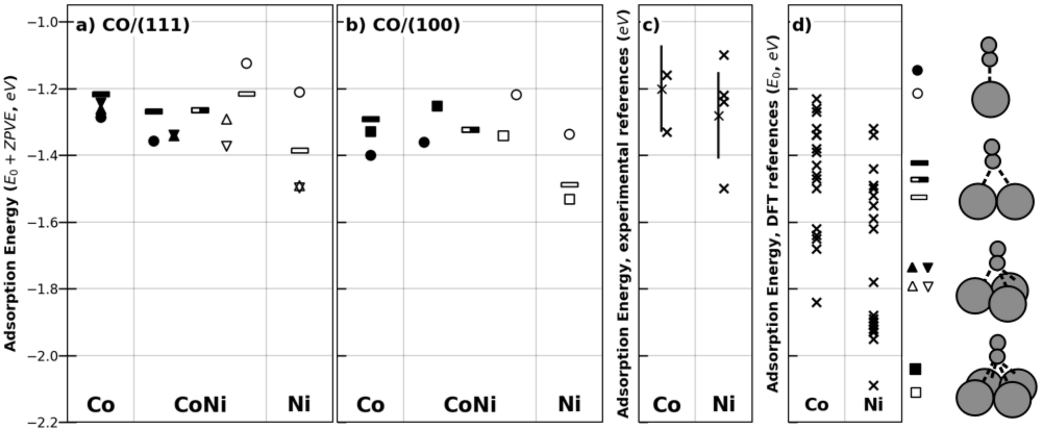

Fig. 24 CO adsorption enthalpies (200°C) on a) (111) and b) (100) Co, NiCo and Ni surfaces. Symbols: ▲ fcc, ▼ hcp, top, ▬ bridge and ■ four-fold hollow, as schematized (right). Open symbols for Ni or Ni-rich sites, close symbols for Co or Co-rich sites. c)Experimental and d) DFT values (Table S8, Table S9 and references within).

Table 8: *C-O stretching frequencies ($\nu_{*C\text{-}O}$ mode, cm-1) and $(\partial\mu/\partial z)^2$ (μ_B^2/Å^2, in parentheses)

		(111) surfaces		
Co	1938 (8.1) , *top*	1764 (6.8), *bridge*	1727 (5.3), *fcc*	1708 (5.4), *hcp*
NiCo	1937 (8.2), top_{Co} 1970 (7.8), top_{Ni}	1767 (6.7), $bridge_{Co\text{-}Co}$ 1799 (6.9), $bridge_{Co\text{-}Ni}$ 1803 (6.8), $bridge_{Ni\text{-}Ni}$	1726 (5.1), fcc_{Co} 1747 (5.3), fcc_{Ni}	1721 (5.0), hcp_{Co} 1735 (5.1), hcp_{Ni}
Ni	1978 (9.1), *top*	1801 (6.6), *bridge*	1738 (5.0), *fcc*	1736 (5.0), *hcp*
		(100) surfaces		
Co	1914 (8.1), *top*	1783 (6.5), *bridge*	1565 (3.1), *h*	
NiCo	1921 (8.2), top_{Co} 1959 (7.8), top_{Ni}	1814 (5.9), $bridge_{Co\text{-}Ni}$	1602 (3.4), h_{Co} 1591 (3.6), h_{Ni}	
Ni	1970 (8.3), *top*	1817 (6.0), *bridge*	1597 (3.5), *h*	

7.2.1.1 Accuracy and corrections

First, the reaction enthalpy and free energy of the gas phase $CO+H_2 \rightarrow CH_4+H_2O$ were computed in the 25°C-280°C with <1kJ/mol difference from reference values (see A3, Fig. S2) showing an excellent agreement for the reaction energies, thus no corrections to the free molecules were considered. Adsorption energies are in the same range for (111) and (100) surfaces, are close to experimental values (Fig. 24c) and in range with theoretical studies (Fig. 24d, from Table S8, Table S9 and references within). A known problem of DFT with GGA functionals is the systematic overestimation of $CO_{(g)}$ adsorption energies favoring of multi-bonded adsorption modes, in some cases over the experimentally determined preferred linear mode (e.g., Pt and Co[96]). This error comes from the poor description of a LUMO $2\tilde{\pi}^*$ molecular orbital for CO at too low energy and overestimating its interaction with the metallic *d*-band of surfaces upon adsorption[42].

The exchange part of the RPBE functional chosen for this work was specifically adjusted to provide more accurate adsorption energies[62] and is one of the best performing functionals for strongly chemisorbed systems[40], [44], it also describes a stronger CO adsorption for the top site on Co, suggesting a preferred linear adsorption more consistent with the experimental observations (sec. 7.1). Adsorption free energies on Co(111) still show threefold sites ~4kJ/mol more stable than the linear adsorption but this calculation is also affected by the truncation of the poorly estimated low frequencies. This is particularly problematic for linear carbonyl where *CO sits in a rather flat zone of the PES[34] poorly mapped by numerical methods. Exploration of numerical solutions is possible[35] but a case-to-case treatment is impractical and generally unnecessary.

Table 9: Electronic adsorption energies (eV) directly deribed from RPBE-DFT calculations and extrapolated according tho the E_{S-T} difference to experiments (in parentheses).

		(111) surfaces		
Co	-1.35 (-1.08) , *top*	-1.27 (-0.87), *bridge*	-1.31 (-0.88), *fcc*	-1.29 (-0.85), *hcp*
NiCo	-1.42 (-1.15), *top* $_{Co}$ -1.19 (-0.96), *top* $_{Ni}$	-1.32 (-0.92), *bridge* $_{Co\text{-}Co}$ -1.32 (-0.94), *bridge* $_{Co\text{-}Ni}$ -1.27 (-0.90), *bridge* $_{Ni\text{-}Ni}$	-1.39 (-0.96), *fcc* $_{Co}$ -1.34 (-0.93), *fcc* $_{Ni}$	-1.39 (-0.96), *hcp* $_{Co}$ -1.42 (-1.00), *hcp* $_{Ni}$
Ni	-1.28 (-1.05), *top*	-1.44 (-1.06), *bridge*	-1.54 (-1.12), *fcc*	-1.55 (-1.12), *hcp*
		(100) surfaces		
Co	-1.46 (-1.18), *top*	-1.36 (-0.82), *bridge*	-1.34 (-0.95), *h*	
NiCo	-1.42 (-1.15), *top* $_{Co}$ -1.28 (-1.04), *top* $_{Ni}$	-1.38 (-1.01), *bridge* $_{Co\text{-}Ni}$	-1.38 (-0.78), *h* $_{Co}$ -1.29 (-0.86), *h* $_{Ni}$	
Ni	-1.40 (-1.16), *top*	-1.57 (-1.06), *bridge*	-1.54 (-1.18), *h*	

Singlet-Triplet correction: Mason et al.[42] proposed a simple extrapolation scheme with reasonable results[53], [96] using the computed and experimental values of the singlet-triplet (E_{S-T}) excitation for $CO_{(g)}$ to correct the CO adsorption energies. In this work $E_{S-T} = 5.53$ eV, closer to the experimental value (6.095 eV) than others (5.33 - 5.35 eV [42], [96]) already suggesting better estimations of energies and electronic structures. Following the method from [53], carbonyl models were relaxed using soft PAW pseudopotentials for C and O atoms (E_{S-T}=5.23 eV) and adsorption energies (and frequencies) were extrapolated to the experimental E_{S-T} value (see details in A4.2). Table 9 shows electronic adsorption energies with and without the E_{S-T} extrapolation. This correction increased the preference for the linear adsorption on Co atoms (on Co and NiCo surfaces) but increased the adsorption energies over the experimental values. This leads to positive free adsorption energies even at the low 1/16 ML coverage which conflicts the experimentally

---

[34] Linear adsorptions occupy a small zone on top of atoms, closely surrounded by small barriers that prevent the adsorbate from "falling" to neighboring multifold sites. Hence their poor description and hindered translator character. See sec. 2.2.2.5.

[35] e.g., mapping the PES in 4 instead of 2 points per degree of freedom, increasing numerical integration meshes, tighten convergence parameters (geometric and electronic), all this at significantly larger computational cost, or fiddling with the finite difference step length, at risk of falling outside the valid zone for harmonic approximations. See discussion in A1.1.

observed pool of carbonyl species on Fig. 20 (and Fig. 21, where remnant *CO rather to hydrogenate than to desorb). The E_{S-T} extrapolation also increases the *C-O stretching frequencies (see Fig. S4) closer experimental observed values (e.g., 2016 cm^{-1} vs. 2018 cm^{-1} on Ni) though lower frequencies should be expected due the lower coverage in DFT models.

Therefore, the correction has the qualitative desired effect on adsorption energies and site preferences, and helps to explain the experimentally observed population of linear carbonyl. However, the E_{S-T} method (as applied here) overestimates the corrections, which is not unexpected considering it is an extrapolation about two times outside the probed E_{S-T} range (see A4.2). Considering also that no similar corrections are available for H_XCO_Y (intermediates in methanation mechanisms), the values in the following sections do not include this correction.

Coverage and frequencies: From experiments[6] and simulations[43], [97] it is known that increasing the *CO coverage weakens the average adsorption energy of $CO_{(g)}$ and increases the *C—O stretching frequency [97]. For the models in this work a single *CO represents a low coverage of 1/16=0.06 ML, compared to other commonly used slab models (2x2 and 3x3 slabs, coverages from 0.25 to 0.11 ML) and high coverages observed experimentally. In fact, DFT frequencies for all adsorption modes in Table 8 are lower than the experimental (sec. 7.1) and some theoretical values reported[6], which is partially attributed to the lower coverage.[36] This coverage effect was confirmed by increasing the *CO coverage to θ_{CO}=1/4=0.25 ML[37] which led to a blueshift in ν_{*C-O} for CO/Ni(111) increasing from 1978cm^{-1} to 1998cm^{-1}. Another common approach is the simple application of scaling factors (~1.0) that can be used to bring average errors in the 30-60cm^{-1} range below 20cm^{-1} [98] without changing the obtained trends.

Ma et al.[98] (vdW-DF2, θ_{CO}=1/4) and Gajdos et al.[43] (PW91 and RPBE, θ_{CO}=1/4) also report *C–O stretching frequencies lower than experimental values, but agree with results in Table 8 for higher stretching frequencies on Ni than on Co from DFT calculations and experimental results. As a general trend, they report higher stretching frequencies with increasing d-band filling in the periodic table (e.g., Co→Cu and Ru→Ag). It is more relevant for the purpose of this work to compare and analyze this kind of trends in site composition and coordination and the effects of the Ni-Co intermetallic rather than more precise species-specific corrections.

7.2.1.2 Insight on the carbonyl population and activity

Fig. 24 shows for (111) and (100) surfaces a stronger binding on the monometallic Ni surfaces, compared to the intermetallic and Co surfaces (by >15kJ/mol), consistent with several previously reported DFT results [44], [96], [98], [99] though experimental results usually show closer values between monometallics (within 10kJ/mol [44], [96]). Adsorption enthalpies on both NiCo surfaces are higher (weaker binding) than on Ni, closer to the adsorption on Co surfaces and slightly lower

---

[36] Though part of the error is not related to coverage but inherent to DFT and the RPBE functional, for example, note that the computed $CO_{(g)}$ frequency (2104 cm^{-1}) is also lower than the experimental values (2100-2200 cm^{-1}).

[37] by reducing the slab size from *o*(4x4) to *o*(2x2) (4 surface metal atoms instead of 16) and increasing k-mesh to 5x5x1

on (111) but higher on (100) surfaces. This evidences the structure sensitivity of the anti-synergic effect of alloying Ni-Co. The stronger CO binding on Ni surfaces suggests higher coverages, which is consistent with the more than three times higher FTIR bands in Fig. 20a[38] for Ni/SiO_2 compared to the other catalysts. Increasing CO coverage on Ni surfaces is also known to favor the stable apparition of linearly bonded carbonyl species[97] which were also identified in Fig. 20a.

On Co and the Co-rich sites of the NiCo, CO shows stronger bonding on the top position, conversely, Ni and Ni-rich sites on NiCo surfaces show a stronger preference for the multi-bonded adsorption on three and fourfold sites. This site preference is observed for the (111) and (100) surfaces, it would be enhanced by the E_{S-T} correction and is consistent with the experimental identification of mostly linear carbonyl on Co/SiO_2 and $Ni_{0.5}Co_{0.5}$/SiO_2 but mainly multi-bonded *CO on Ni/SiO_2 (Fig. 20a).

Stretching frequencies in Table 8 show that ν_{*C-O} is characteristic to the local coordination of *CO species with little difference between (111) or (100) for top and bridge modes. The DFT-derived wavenumbers follow the order *top* > *bridge* > three-fold *hollow* (*fcc*, *hcp*) > tetra-fold hollow. The extension of the *C−O bond (Table S11) and the total Bader charge of the carbonyl (Table S12) are also characteristic of the site coordination and, in general, slightly larger for the Co surface and Co-rich multi-bond sites, compared to Ni-rich sites or surfaces. Moreover, *CO Bader charges in Table S11 suggest that multi-bonded carbonyl species (more abundant on Ni surfaces) could drain more electron density from the surfaces.[39] The larger Bader charges can be associated to longer *C-O bonds, lower ν_{*C-O} and greater activation of the C-O bond but again, weaker the *CO binding on Co and NiCo surfaces suggest a more facile desorption from those surfaces.

The $(\partial\mu/\partial z)^2$ values in Table 8 are also characteristic to the site coordination, higher for linear modes (~8.0-9.0 $\mu_B^2/Å^2$) than for bidentate (~7.0 $\mu_B^2/Å^2$) and multifold modes (~5.0-3.0 $\mu_B^2/Å^2$). These values suggest intrinsically higher IR signals for the linear mode compared to the other adsorption sites (especially for the Ni(111) surface). Consequently, for Ni/SiO_2 in Fig. 20 the height or area proportion between the linear carbonyl peak at 2018 cm^{-1} and the multi-bonded bands is likely to overestimate the relative abundance of linear *CO. The proportional abundance of linear *CO on $Ni_{0.5}Co_{0.5}$/SiO_2 (compared to multi-bond) may also be overestimated but it is still expected to be lower compared to Co/SiO_2 and higher than for Ni/SiO_2. DFT results in Table 8 agree with higher frequencies for linear ν_{*C-O} on Ni surfaces than on Co surfaces (by ~40-55 cm^{-1}), in good agreement with the FTIR spectra in Fig. 20a with the linear CO band for Ni/SiO_2 at about 30 cm^{-1} higher wavenumber than on Co/SiO_2. NiCo DFT stretching frequencies on (111) and (100) surfaces show a similar difference (~30 cm^{-1}) when CO binds linearly to a Ni or a Co atom, again higher for the top-Ni site and closer to the frequency of *CO on the top site of Ni(111) and Ni(100) models. These results also suggest similar intrinsic IR intensities for both linear

---

[38] Note that Co/SiO_2 and $Ni_{0.5}Co_{0.5}$/SiO_2 are shown with a 5x factor, though recall that direct numerical comparison between catalysts is not possible without careful calibration due experimental factors.

[39] Bader charges need to be considered with caution given the geometric nature of the partition. The DDEC partition scheme showed not to be reliable to the addition, thus DDEC *CO charges are not presented.

adsorptions on NiCo (111) and (100) surfaces ($(\partial\mu/\partial z)^2 \sim 7.8-8.2\mu_B^2/\text{Å}^2$, Table 8), thus there is not a significant underestimation of the population of one or another from their observed contribution to the FTIR spectra.

The FTIR peak with the highest frequency on $Ni_{0.5}Co_{0.5}/SiO_2$ (Fig. 20a) is close to the band assigned to linear carbonyl on Ni/SiO_2, from this and the discussed DFT trends the 2020 cm^{-1} peak on $Ni_{0.5}Co_{0.5}/SiO_2$ is attributed to the linear adsorption of CO on top of a Ni atom. No similar peak within 70 cm^{-1} at lower frequencies is directly observed in Fig. 20 suggesting there is no significant population of carbonyl species linearly bonded to Co atoms on $Ni_{0.5}Co_{0.5}/SiO_2$. This is unexpected considering the top-Co sites are more stable than the top-Ni sites according to the discussed adsorption energies and the $E_{S\text{-}T}$ extrapolation (by about 20 kJ/mol, in both scenarios). Several factors may play a role in inhibiting the CO linear adsorption. The segregation of Ni to the catalyst surface (sec. 5.3) entails a lower proportion of surface Co atoms available for CO adsorption. Also, Ni atoms are prone to occupy corners and edges positions in small nanoparticles (sec. 5.3.2, Fig. 18), sites of lower coordination that are expected to offer strong adsorption sites for carbonyl species while Co surface atoms available may also form sites with greater strength for other of the identified species[40] effectively blocking the linear *CO adsorption. Similarly, atomic species may strongly bind in multi-bond sites or interstitial sublayer sites near surface the Co atoms, inhibiting the adsorption of $CO_{(g)}$.

For the monometallic surfaces the weaker *CO binding in Co surfaces is consistent with the significant $CO_{(g)}$ production of Co/SiO_2 (sec. 6.1) while the stronger adsorption on Ni surfaces favors the hydrogenation towards methane explaining its higher CH_4 selectivity of Ni/SiO_2. As discussed for the clean surfaces (sec. 5.2), Ni and Co atoms behave considerably different in pure surfaces than as part of the NiCo alloy. Indeed, the adsorption on top-Ni and Ni-Ni bridge sites on the NiCo surfaces in Fig. 24 (sites solely composed by Ni atoms) is weaker than on the equivalent sites of the monometallic Ni models, evidencing the electronic effect of forming the NiCo alloy for the Ni atoms. All these NiCo sites are less stable for *CO and more prone to desorb $CO_{(g)}$ than the monometallic Ni surface, which is consistent with the experimental lower methane selectivity of the bimetallic surfaces.

In summary, the identity and different stabilities of carbonyl species may be a key differentiating factor between the monometallic Ni, Co and the bimetallic catalyst, directly related to the selectivity towards the undesired product.

7.2.2 Atomic H and C, C_n chains, and CH_x species

Previous DFT studies have shown that C, H and CH_x (x=1-3) species preferentially bind to three- and four-fold sites of (111) and (100), Ni and Co surfaces, with the exception of CH_3 that prefers a bidentate bridge site on (100) surfaces[100], [101]. Fig. 25 shows the electronic adsorption energies (eq. 4.8) for the most stable geometries of adsorbed H, C, CH, CH_2 and CH_3 species on

---

[40] e.g., HCOO**, *OH or other O-binding species, considering the greater oxophilicity of Co atoms discussed later in sec. 7.2.3

surface (symbols as in Fig. 22, images, energies and geometric parameters in 0). Formation of C deposits (sec. 7.2.2.1) and a descriptor approach (sec. 7.2.2.2) are also discussed.

7.2.2.1 Atomic species and C_n chains

Fig. 25 shows that C and H atoms exhibit similar binding strengths on Ni(111) and Co(111) surfaces (Fig. 25a,b), but both bind significantly more strongly on Ni(100) than Co(100) (Fig. 25f,g). Moreover, while H binds more strongly on the (111) fcc sites than on the four-fold sites of (100) surfaces, C binds over 100 kJ/mol more strongly on the (100) surface than on the (111) hcp sites. For C on (111) surfaces, Co and the Co-rich intermetallic sites show similar binding energies, close to Ni and significantly stronger than the Ni-rich intermetallic site. For the intermetallic, less stable adsorptions are found for H in both surfaces and for C in (100), which is qualitatively consistent with the lower band centers (sec. 5.2) according to the d-band model[48]. This anti-synergistic effect is more clear and significantly greater on the (100) surface than on the more studied (111) surfaces[13], [79], especially for C on NiCo(100) (9kJ/mol less stable than on Co(100) and 30kJ/mol than on Ni(100)). Weaker C and H binding also suggests a higher surface mobility that can promote hydrogenation, lessen carbon deposits and render the intermetallic less prone to poisoning by carbon.

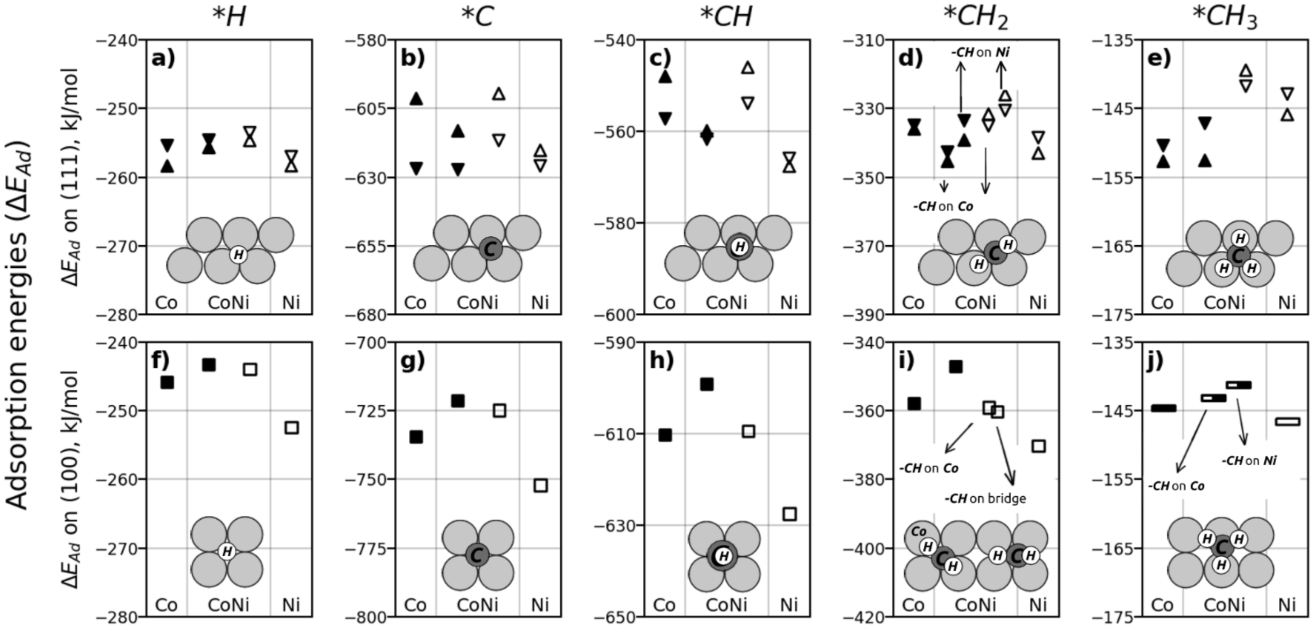

Fig. 25 Adsorption energies (ΔE_{ad}) on Co, NiCo, and Ni for H (**a,f**), C (**b,g**), CH (**c,h**), CH_2 (**d,i**) and CH_3 (**e,f**) on (111) and (100) surfaces (respectively). Sites ▲fcc,▼hcp, ▬ bridge and ■ hollow, filled symbols on Co and Co-rich sites and open symbols on Ni and Ni-rich sites (as in Fig. 22). Top views of geometries are shown as insets.

The strong binding of C is consistent with the well reported deactivation due formation of surface C deposits, especially for Ni-based catalysts. Such deactivation is also observed for Co, for example, in DMR conditions [83] but it is not usually reported under the milder conditions of methanation reactions. The build-up of a small amount of C was studied through formation of C-chains from atomic *C (Fig. 26; annex A6.6, Table S14), that are reported to be thermodynamically stable, to have higher mobility than adatoms and serve as a precursor of star-like formations, rings and then graphitic over layers[102].

On (111) surfaces the C-chains become more stable with increasing chain length (Fig. 26a), compared to surface C species. In contrast, on (100) surfaces the longer chains are less stable (Fig. 26b), which suggests that the high stability of C adsorbed on the four-fold M_4 sites hinders the formation of C-C bonds in favor or more dispersed *C. This distribution of *C blocks more sites than more compact C-deposits and may favor other reconstruction or deactivation processes[103], [104]. For the (111) intermetallic two chain directions, one along and other across the Co-Ni interface lines (Fig. 26a, insets l- and t-) exhibit some differences in the energies of C_2 and C_3 chains but give similar energies for longer chains. For (100) C_5 chains are similar or more stable than C_4 chains, and C_3 are more stable than C_2. On both, C_2 and C_4 chains one terminal C ends on a less stable bridge site. Thus, the position of terminal C-atoms instead of the direction of chains appears to dominate formation energy of short linear C_n.

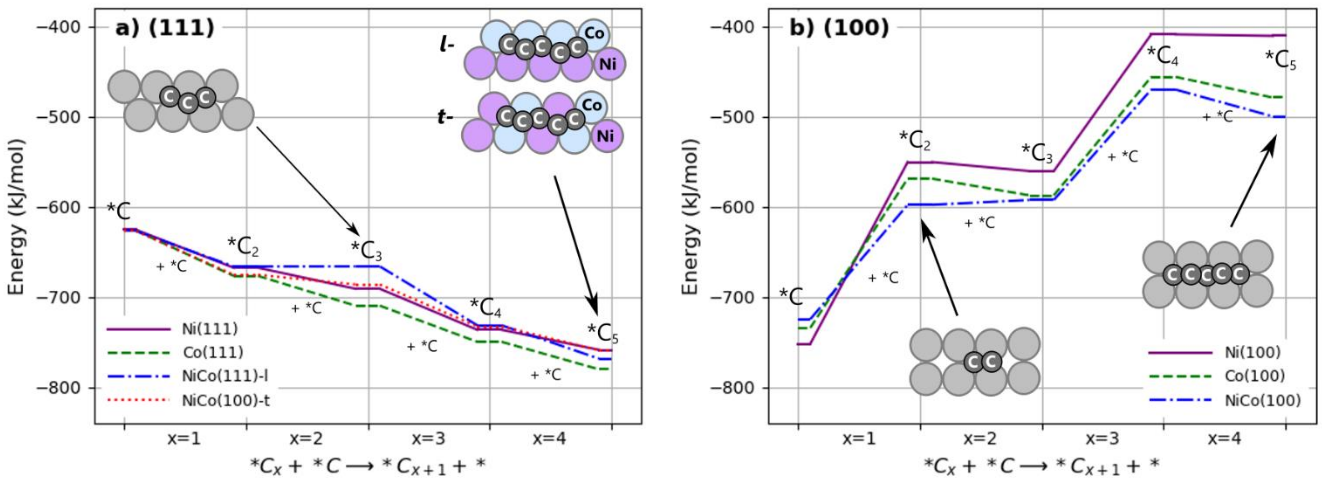

Fig. 26 Reaction energies of surface C additions forming linear C_n chains, precursors of C deposits, on a) (111) and b) (100) surfaces

7.2.2.2 Stability and geometry of CH_x species on the surface

<u>CH:</u> From Fig. 25c, on (111) surfaces the hcp sites are preferred on monometallic Co and the NiCo alloy, but fcc sites are preferred on Ni(111). The CH species binding is strongest on Ni, followed by Co-rich NiCo sites, Co(111) and lastly Ni-rich NiCo, for their respective preferred sites. These energy differences span a range of about 10 kJ/mol from the strongest binding Ni(111) and weakest binding Ni-rich NiCo(111). From Fig. 25h, all (100) sites bind CH species at least 30 kJ/mol more strongly than the (111) sites of similar composition. Among the (100) sites, the CH binding is the strongest on Ni(100), followed by Co(100) and the Ni-rich NiCo(100) sites (17kJ/mol weaker). In this case, the energy difference between the strongest binding Ni and weakest binding Co-rich NiCo sites is over 30kJ/mol. Compared to pure Ni and Co surfaces, both NiCo sites appear less effective to stabilize C-containing surface species.

<u>CH_2:</u> CH_2 species adsorbs with an H atom above the C atom and the second H (with longer C-H bond) in a top or bridge position (Fig. 25d,i insets and SI.7, M-H distances between 1.7-1.8Å) . The fcc sites are preferred on Co(111), Ni(111) and the Co-rich NiCo(111) sites. The Co-rich NiCo(111) site adsorbs CH_2 most strongly, followed by Ni(111), Co(111), and 10 kJ/mol more strongly the Ni-rich NiCo(111) sites. On NiCo(111), $^*CH_2$ orientations with the second H on top of a Co atom are preferred over that on top of Ni atoms by at least 5 kJ/mol, suggesting that (C-H)-Co agostic interactions (i.e., interactions of C-H bonds with metal atoms[105], [106]) are stronger than (C-H)-Ni interactions. Adsorption of CH_2 on Ni(100) is about 12 kJ/mol stronger than on Co(100) and the Ni-rich NiCo(100) sites but 27kJ/mol stronger than the Co-rich sites on NiCo(100). On the NiCo(100) surfaces. The preference of Ni-rich sites suggests a predominant effect of the more stable Ni-C interaction, as observed for C and CH (Fig. 25g,h), rather than the (C-H)-Co agnostic interactions that exist in (111) surfaces.

<u>CH_3:</u> On (111) surfaces CH_3 sits in a three-fold site with its three H atoms on top of surface metal atoms (inset in Fig. 25.e and annex 0, distance M-H between 2.0-2.1Å). The fcc sites binds CH_3 more strongly than the hcp sites by about 3 kJ/mol on both monometallics and by 5.6 kJ/mol on the NiCo(111) Co-rich sites. The Co and Co-rich (111) fcc sites exhibit the strongest binding, 6.7 kJ/mol stronger than Ni(111) and over 11kJ/mol stronger than the hcp Ni-rich site on NiCo(111). On (100) surfaces CH_3 species binds preferentially through C on a bridge site and one of the three H atoms over a surface metal (inset Fig. 25j). The binding on Ni(100) is slightly stronger than on Co(100) (2kJ/mol) but both monometallics bind CH_3 more strongly than the NiCo(100) surface. In contrast to other CH_x species, the Co-rich NiCo(100) sites bind CH_3 more strongly than the Ni-rich NiCo(100) also, all (100) surfaces bind CH_3 weaker than the (111) surfaces and the Co-rich NiCo(100) site is preferred to the Ni-rich NiCo(100) site. The preferred multi-bonded adsorption mode on both surfaces is unexpected considering C valence but may be explained by the stability of the suggested agostic M-(C-H) interactions. The role these interactions in stabilizing adsorbed species and transition states is evidenced and further discussed in sec. 8.4.3 (Fig. 41).

In summary, adsorption energies of H, C and CH_x species exhibit complex trends resulting from geometric and electronic factors. Geometric effects are evidenced by the differences between (111) and (100) surfaces, while electronic factors determine differences between the local site compositions. The adsorption energy of CH_x species on (100) and (111) surfaces increases about 200 kJ/mol with the number of Hydrogens in the species (i.e., from CH to CH_2 and from CH_2 to CH_3). On the (100) surface all species exhibit similar trends for composition effects on adsorption energy, with bimetallic surfaces binding species less strongly than monometallics. Similar regularities have been exploited before to use the adsorption energy of the central atoms of CH_x, NH_x, OH_x species as descriptors on several other (111) surfaces[107]. Fig. 27 shows linear fit for CH_x adsorption energies in Fig. 25 with *C. The (100) surfaces show larger slope and with a better fit[41] than (111) surfaces, a single linear fit may describe well (111) and (100) surfaces for CH and CH_2 but not CH_3 (see Fig. S9). The diminishing slopes in Fig. 27 with increasing hydrogenation (*CH > *CH_2 > *CH_3) indicate that other interactions besides the strength of the M-C bond (e.g., M-(C-H) interactions) become more relevant in the stabilization of CH_2 and CH_3 species.

For the three-fold sites on NiCo, adsorption of C and CH_x species is stronger on the Co-rich sites than on the Ni-rich sites regardless of the distinction between fcc and hcp geometries. In contrast, on the four-fold NiCo(100) sites C, CH and CH_2 show a preferred adsorption on Ni-rich NiCo sites that is consistent with the stronger adsorption on Ni(100) compared to Co(100). For CH_2 on (111) and CH_3 on both surfaces, the preferred adsorption configuration allows favorable alignment of H atoms with surface metal atoms at short distances (1.7-2.1Å), suggesting a role of agostic interactions between electron-deficient metal and C-H σ-bonds. The (C-H)-Co agostic interactions are stronger than (C-H)-Ni interactions, which accounts for stronger adsorption on Co(111) than on Ni(111), contrary to other CH_x species. It also may help explaining the preferred multi-bonded adsorption mode of CH_3 for both surface geometries of the three metals.

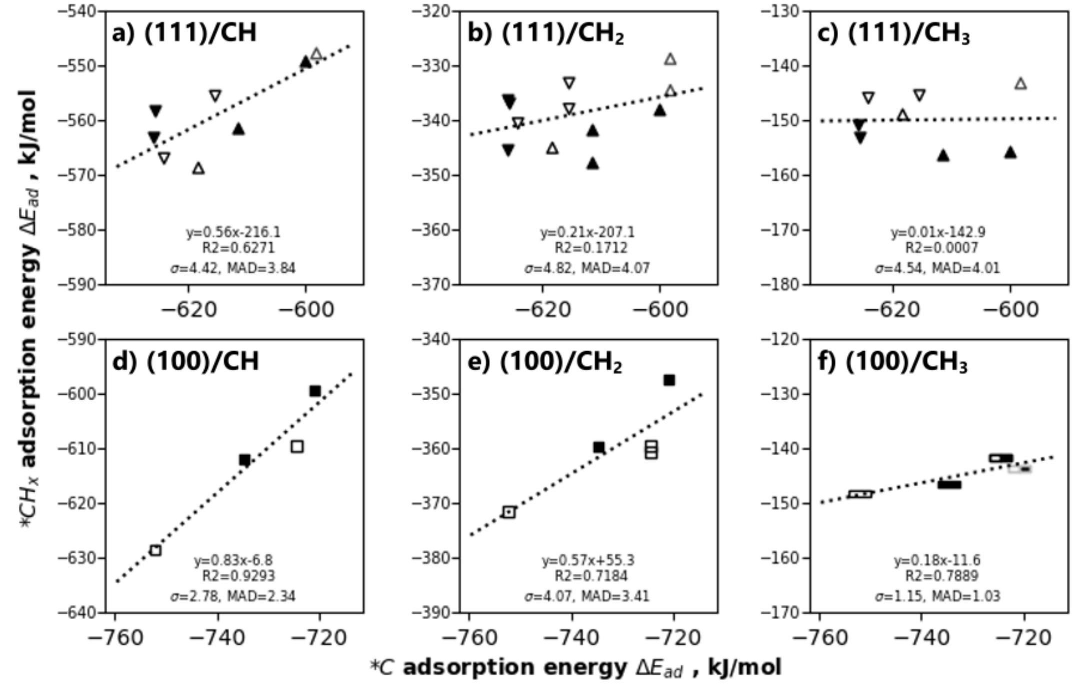

Fig. 27 *C bindind strength as a descriptor of the *CH_x adsorption energies in Fig. 25. Open symbols for Ni or Ni-rich sites, closed symbols for Co or Co-rich sites. Linear fit as dotted lines, equation, and fit wellness parameters (R2:coefficient of determination, σ: standard deviation of the error, MAD: medium absolute difference).

For the (100) surfaces, the Ni(100) is preferred to Co(100) and the Ni-rich sites are preferred on NiCo(100), which suggests that the strong interaction with Ni atoms in four-fold sites is the predominant effect. Weaker adsorption on Ni-rich sites is observed for all species and surfaces

---

[41] See σ, R2 and MAD (medium absolute difference $\sum_n |x_{\text{data}} - x_{\text{fit}}|/n$, same units as the data) in Fig. 27 but mind that R2 is ill defined to describe fit wellness when the slope approaches zero (here for CH_3 plots).

compared to the monometallic Ni and also weaker than monometallic Co in most cases, which suggest a strong anti-synergy from alloying Ni and Co in the less coordinated surface. From the Co→Ni electronic donation, the slightly more negative Ni atoms (also with fewer states near the fermi level) form weaker binding sites for CH_x. In turn, the more electronically unsaturated Co atoms offer stronger binding sites and are able to further stabilize C-H σ-bonds through agostic interactions. These Co atoms in the alloy provide more stable M-(C-H) centers that also may function as transition states for hydrogenation / dehydrogenation reactive steps (see sec. 8.4.3).

7.2.3 Stability of O and OH and the oxophilicity of Co

The electronic adsorption energy of atomic O and OH species was computed (eq. 4.8) on relevant sites of the (111) and (100) surfaces (Fig. 28). Geometries and energies are detailed in A6.2. As for C and most CH_x species (Fig. 25), the four-fold sites on (100) surfaces (Fig. 28c,d) show stronger binding compared to the three-fold sites on (111) surfaces (Fig. 28a,b). Contrary to C and CH_x species, O and OH adsorb at least 20 kJ/mol stronger on monometallic Co surfaces rather than Ni surfaces. The adsorption energies of O and OH on NiCo(111) surfaces (Fig. 28a,b) are almost the same between *hcp* and *fcc* sites showing a negligible effect of the sublayer. Adsorption energies on NiCo(111) Co-rich sites are similar to the adsorption energies on the Co(111) surface but also about 20 kJ/mol stronger than on the Ni-rich NiCo(111) or the Ni(111) sites, i.e., no significant differences are observed between A_3 and A_2B three-fold sites, though this may be a compensation from the effects of the alloy on Ni and Co atoms as discussed below. The four-fold sites on NiCo(100) show adsorption energies for O and OH (Fig. 28c,d) between the monometallics but stronger binding on the Ni-rich sites which implies a relevant interaction of adsorbed species with the metal in the second layer but opposite to the trend between monometallics and NiCo(111) sites (i.e., stronger for Co atoms). Fig. 28e shows that the adsorption of OH is well described by the O adsorption energy as previously suggested[107], moreover, a single linear fit describes well both, (111) and (100) surfaces (MAD<3 kJ/mol).

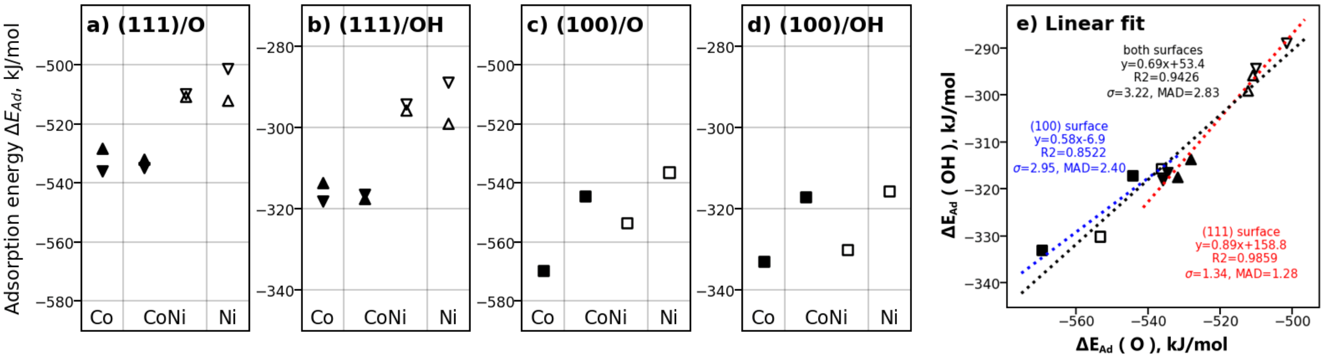

Fig. 28 Adsorption energy of O (a,c) and OH (b,d) on (111) and (100) surfaces (respectively) and linear fit with O as descriptor (e). Sites ▲fcc,▼hcp and ■ hollow, filled symbols on Co and Co-rich sites and open symbols on Ni and Ni-rich sites (as in Fig. 22).

A greater stabilization of *O (from $CO_{2(g)}$ dissociation on the surface) but not for *CO is consistent with a higher selectivity towards $CO_{(g)}$ rather than hydrogenated products, which is in line with the greater activity but lower CH_4 selectivity of Co catalysts (sec. 6.1). More generally, this suggest that the stabilization of *O plays an important role on the $CO_{2(g)}$ activation and $CO_{(g)}$ production for the mono and bimetallic catalysts (see sec. 8.2.2). The stronger adsorption of O and OH species on Co (and bimetallic) surfaces also suggests a higher population of O-binding species on the surface that may, for example, block sites or allow alternative pathways[12]. It is also consistent with oxidative deactivation processes reported for Co-based catalysts[9], [10] and the higher reduction temperatures required for Co/SiO_2 in this work (sec. 4.1). Finding opposite trends in adsorption energy for the mixed sites in NiCo(111) (three-fold) and NiCo(100) (four-fold) is consistent with an stabilization of the Ni-O interaction and destabilization of the Co-O interaction[42] by the electronic Co→Ni electronic donation in the alloy.

Considering the electrophilic nature of O atoms, Bader charges for *O models were computed to study O and OH trends in detail. Surface O atoms show about the same Bader charge on both monometallic surfaces (−1.14e on Ni(100) and Co(100), −1.00e on Ni(111) and Co(111)) suggesting electronic density is similarly drawn from Ni and Co surfaces. The greater oxophilicity of Co surfaces is then attributed to a greater stability of electronically deficient Co, compared to electronically deficient Ni atoms. *O draws electronic density in similar magnitude from the bimetallic than from the monometallic surfaces (see A6.7, Fig. S8). The greater stability of (111) Co-rich sites (threefold $NiCo_2$) is consistent with its higher Co composition, additionally, the Co→Ni donation of the alloy (sec. 5.2) provides electronic density to Ni atoms helping the stabilization of the $Ni^{\delta+}$ atom interacting with O (Fig. S8a,b). Fourfold (100) sites have the same surface composition (Ni_2Co_2) and similar surface Bader charges upon O adsorption but different sublayer atoms. The Ni-rich sites are likely to remain more stable while serving as electron density reservoirs[103] for the adsorbed electrophilic species thanks to the sublayer Ni atom being stabilized by the Co→Ni donation in the bulk (and remaining as $Ni^{\delta-}$ upon adsorption, Fig. S8c,d), which explains the greater stability of Ni-rich sites compared to Co-rich sites.

7.2.4 Stability of other $C_xO_yH_z$ species

The adsorption energies of some relevant oxygenated species are detailed in Fig. 29 for several sites and configurations. All species adsorb stronger on the (100) surfaces and prefer multi-dentate adsorption modes[26]. Direct hydrogenation of *CO results in *HCO or *COH, depending on the addition site, therefore these species may be a relevant in the preferred reaction pathway. Both species bind through C to the surface and follow the $CH_{x<3}$ trend of adsorbing more strongly (by ~10 kJ/mol) on monometallic Ni rather than Co surfaces. On NiCo(100) surfaces both species exhibit a significant anti-synergy binding more weakly than on Ni(100). On NiCo(111) these species show adsorption energies between the Ni(111) and Co(111) but still strongly affected by

---

[42] and *O-binding species in general (see sec. 7.2.4). Note this smaller effect for Co atoms in the alloy is consistent with the greater effect on the electronic restructuration of Ni atoms rather than Co observed from their DOS in sec. 5.2.

the local site composition and configuration. HCOH species prefer to adsorb in a *trans* configuration linking to the surface with C in a bridge position that preserves the tetra-valence of the carbon atoms, the cis configuration is about 10 kJ/mol less stable due steric interactions.

Formate (HCOO) and carbonate (CO_3) bind through O atoms and follow the described trend for O and OH by binding stronger on Co rather than Ni surfaces. Both species were identified experimentally under reaction conditions but ruled out from the kinetically dominant pathways in sec. 7.1. HCOO binds preferably bidentate in a short bridge (Fig. 29i, inset), more strongly on Co than Ni surfaces and about intermediate binding energies on the bimetallic (100) surface. The Ni-bridge and Co-bridge positions on NiCo(111) (Fig. 29d) show higher and lower adsorption energies (respectively) than on monometallic surfaces evidencing that alloying stabilized Co but destabilized Ni upon interaction with electrophilic fragments[43]. Carbonate (CO_3) binds bidentate occupying a top and three-fold sites on (111) surfaces and two top sites in a short bridge on (100) surfaces (Fig. 29e,j insets), similar to HCOO though a less stable species (Fig. 23) more prone to dissociate before desorbing. Carbonate may be temporarily formed from surface *O and $CO_{2(g)}$ which is then released as suggested before (sec. 7.1).

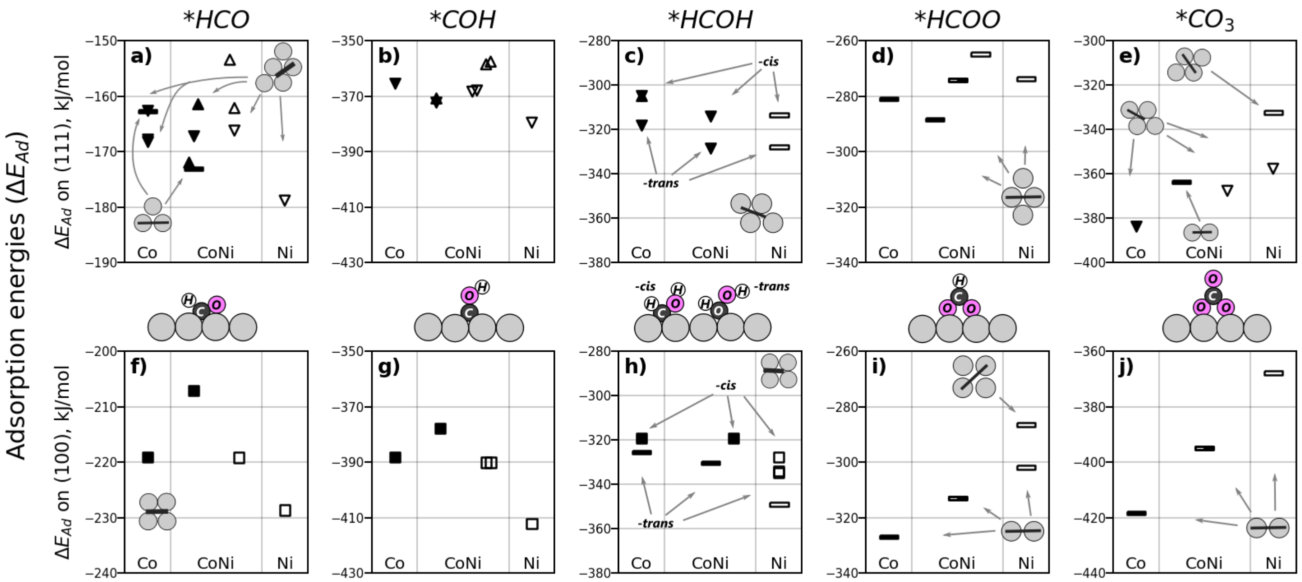

Fig. 29 Adsorption energy for (a,f) HCO, (b,g) COH, (c,h) HCOH, (d,i) HCOO and (e,j) CO_3 on (111) and (100) (respectively) Co, NiCo and Ni surfaces. Symbols specify site geometry as in Fig. 22, filled symbols on Co or Co-rich sites and empty symbols on Ni or Ni-rich sites. Models and insets show configurations and orientations

Therefore, species linking through C to the surface (i.e., *CO, *HCO, COH*, HCOH*) bind more strongly to the monometallic Ni surfaces similar to the $CH_{x<3}$ trends, conversely O, OH and O-binding species are significantly more stable on Co atoms and surfaces. Bimetallic surfaces show a significant effect of the local composition and site geometry on the adsorption energies, close to the monometallic surfaces for the (111) facet but showing with a more anti-synergistic effect on NiCo(100) for HCO, COH and the $CH_{x<3}$ species. Linear relationships with the *C and *O

---

[43] Note the same behavior for *O and *OH on NiCo(111) in Fig. 28

adsorption energies (similar to Fig. 27 and Fig. 28e) can be stablished for *HCO, *COH, *HCOO and $^*CO_3$ (Fig. S10), which further supports the *O and *C descriptor analysis used by Medford et al.[25] for large catalysts screening of (211) metal surfaces and the experimental approach of Lachkov and Chin[22] with C and O chemical potentials. Fig. 30 entails most of the discussed trends by showing all the *C and *O adsorption energy pairs for the studied surfaces, i.e., the zones in the chemical space of the *C and *O as descriptors mapped by the Ni, Co and NiCo surfaces. The horizontal positions of (100) surfaces in Fig. 30 describe the strong Ni(100)-C bond (left purple x) and anti-synergy of the NiCo(100) surface (right orange patch) for the stabilization of C-binding species while showing intermediate adsorptions energies for NiCo(100) for O-binding species (vertical positions). The (111) surfaces are positioned in the upper right corner showing weaker adsorbate-surface interactions compared to the (100) surfaces. More interestingly, Co(111) almost entirely overlaps with NiCo(111) but is completely separated from Ni(111) by their relative oxophilicity, the close representative averages (x in Fig. 30)[44] of Co(111) and NiCo(111) are consistent with the more similar experimental behavior of the bimetallic catalyst to the monometallic Co catalyst described in sec. 6. The descriptor analysis in Fig. 30 also evidences a greater structure sensibility (~100 kJ/mol difference) for *C than for *O adsorption (~20-30 kJ/mol). This also affects *HCO, *COH, and other C-binding species that are possible intermediates of the methanation pathway further supporting its structure sensibility. Fig. 30 also shows that Ni, Co and bimetallic surfaces are differentiated by their oxophilicities, which has been proposed as a determinant factor in activity and reactivity[22]. The oxophilicity of the surfaces directly increases with the Co content and agrees with the $CO_{(g)}$ formation trend (Co > NiCo > Ni) suggesting that the O stabilization also has a significant role in the $CO_{2(g)}$ activation and $CO_{(g)}$ formation.

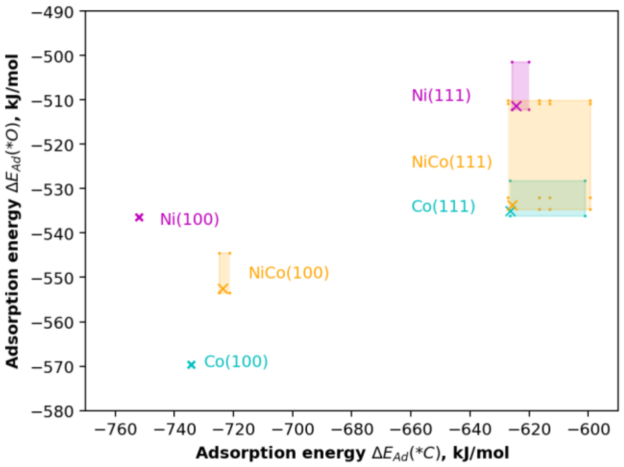

Fig. 30 *C and *O adsorption energy zones for surfaces studied in this work. Dots map all the (ΔE_{*C}, ΔE_{*O}) combinations for a given surface, x marks the representative Boltzmann average (265°C).

---

[44] (a,b) coordinates are computed as the Boltzmann averages (a.k.a. thermal averages) at 265°C of the *C and *O adsorption energies, i.e., ($\langle \Delta E_{*C} \rangle$, $\langle \Delta E_{*C} \rangle$) with $\langle \Delta E_{*x} \rangle = \sum_i (\Delta E_{*x}) \exp(-\Delta E_{*x}/k_b T) \, / \sum_i \exp(-\Delta E_{*x}/k_b T)$

8. Detailed study of the reaction mechanism

8.1 Kinetic isotopic experiments

An H_2/D_2 kinetic isotope effect study was conducted to confirm the involvement of H atoms in the kinetically relevant steps for the CO and CH_4 formation, KIE are shown in Table 10 (extended in A8 and further discussed in ref.[7]).

Table 10 Experimental KIE (1kPa $CO_{2(g)}$, 25 kPa $H_{2(g)}$, He balance, 250 °C)

KIE	Co/SiO_2	$Ni_{0.5}Co_{0.5}/SiO_2$	Ni/SiO_2	
$CO_{(g)}$ formation	1.01	1.06	1.02	~ 1.0
$CH_{4(g)}$ formation	0.79	0.90	0.79	< 1.0

Close to unity KIE values for the $CO_{(g)}$ formation strongly support that hydrogen bonds are not involved in the kinetically relevant steps for the formation of $CO_{(g)}$ in good agreement with the close to zero apparent orders of $H_{2(g)}$ for the TOF_{CO} (sec. 6.2). Though not the only possible pathway without H-assistance[45], this further supports that a direct dissociation of CO_2 on the metallic surfaces is the main source of $CO_{(g)}$ as discussed previously, suggested by the DFT calculations, and literature[37]. Lower (inverse) KIE values are observed for the $CH_{4(g)}$ formation (~0.8 on Ni/SiO_2 and Co/SiO_2, ~0.9 on $Ni_{0.5}Co_{0.5}/SiO_2$), evidencing that the kinetically relevant steps to produce methane somehow involve the formation or breaking of hydrogen bonds. Such H-assisted route is consistent with the non-zero apparent order of H for the $CH_{4(g)}$ formation discussed before (sec. 6.2). Moreover, a double-site Langmuir-Hinshelwood model at high *CO coverage obtained from this data supports the H-assisted methanation via HCO intermediates[95].

Therefore, both results are consistent with a direct dissociation of $*CO_2$ on the surface forming the pool of *CO species observed by FTIR (7.1) and main source of C for the reaction, followed by H-assisted kinetically relevant steps involved in the pathway to break second C-O bond and/or hydrogenating intermediates.

8.2 Adsorption and activation of CO_2

8.2.1 Experimentally observed direct dissociation

The isotopic study (8.1), apparent reaction orders (sec. 6.2), abundance of surface *CO under reaction conditions (FTIR in sec. 7.1) and previous studies[37] support that CO_2 can adsorb and dissociate without assistance of H on the monometallic and bimetallic catalyst. The ability of the

---

[45] e.g., dissociation assisted by the support with the reaction taking place in the metal-support interphase or being assisted by *O species initially produced in small quantity by direct dissociation in specific low coordination sites.

Ni/SiO_2 and $Ni_{0.5}Co_{0.5}/SiO_2$ catalysts to directly dissociate $CO_{2(g)}$ to without $H_{2(g)}$ was tested experimentally by feeding pure $CO_{2(g)}$ and following the FTIR spectra (system in Fig. 8). The catalysts were mounted in the FTIR cell and reduced in situ, the system was purged using He at 350°C for 3 hours to eliminate most *H species before cooling down to 200°C and feeding pure $CO_{2(g)}$.

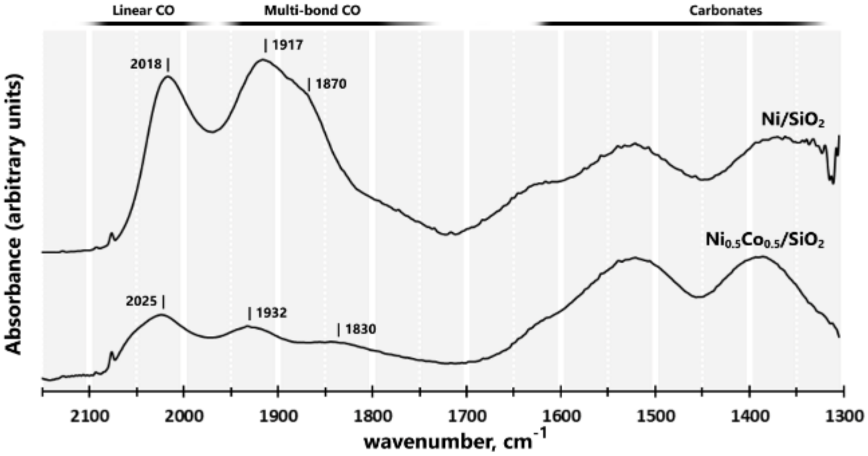

Fig. 31 FTIR spectrum when pure $CO_{2(g)}$ is feed (200°C, 1atm) to the Ni/SiO_2 and $Ni_{0.5}Co_{0.5}/SiO_2$ catalysts after cleaning for surface H.

Fig. 31 shows that carbonyl species of all adsorption modes (linear and multi-bond) are formed on the Ni and bimetallic catalyst surfaces supporting that *CO can be produced directly from $CO_{2(g)}$ without H assistance. Linearly bonded CO appears with similar intensity and at slightly higher wavenumbers (Ni/SiO_2: 2018 cm^{-1}, $Ni_{0.5}Co_{0.5}/SiO_2$: 2025 cm^{-1}) that under reaction conditions (Ni/SiO_2: 2016 cm^{-1} and $Ni_{0.5}Co_{0.5}/SiO_2$: 2020 cm^{-1} in Fig. 20), again slightly higher for the bimetallic than on Ni/SiO_2. The smaller carbonyl signal (compared to the carbonate bands) for the bimetallic in Fig. 31 can be associated to a lower population of carbonyl species and weaker binding of CO compared to the Ni surface. Bridge and multi-bonded bands for CO on Ni are significantly lower and closer to the linear bands suggesting a smaller total population of carbonyl species. Conversely, bands in the section assigned to carbonates (>1700cm^{-1}) are proportionally larger in intensity, closer to the carbonyl bands for Ni/SiO_2 and almost double the carbonyl bands on the bimetallic. This is partly explained by the higher $CO_{2(g)}$ pressure promoting the formation of carbonates in the metallic surface and/or support. Mass Spectroscopy (MS) of effluent gases shows no $O_{2(g)}$ being released from the system, therefore all the *O species that under reaction conditions (when *H is available) form $H_2O_{(g)}$ must remain in the surface. These *O may help capturing $CO_{2(g)}$ and forming carbonates on the metallic surface ($*O+CO_{2(g)}+*\rightarrow**CO_3$) or even be strongly incorporated to the upper layers oxidizing the metallic surfaces. The higher oxophilicity of Co atoms (sec. 7.2.3) is consistent with the proportionally higher population of carbonate species on the bimetallic surface. The higher abundance of carbonate species and strongly bonded *O occupying multi-atom surface sites may partly explain the lower population of multi-bonded carbonyl (compared to Fig. 20) with little effect on the ability of some sites to linearly bind $CO_{(g)}$. The interaction with carbonate species may also weaken the *CO binding and activation of the C-O bond increasing the stretching frequency for *CO, similar to the effect of increasing the *CO coverage (sec. 7.2.1.1), which may contribute to the observed redshift of carbonyl bands compared to the reaction conditions (Fig. 20). Is has also been suggested than under reaction conditions the abundant *H contributes electronic density to the surface decreasing the back-donation interaction for *CO which would strengthen the C-O bond and increase its vibrational frequency [6].

8.2.2 Simulating the direct *CO_2 dissociation

The activation of $CO_{2(g)}$ is now studied in detail using theoretical methods. First, it was found that adding a +0.3712eV correction to the CO_2 electronic energy fits the experimental reaction enthalpy and free energy of the CO_2 methanation reaction within the studied temperature range (see annex A3). Similar static corrections are often used for CO or CO_2 [36], [108], [109], and have been associated to the O-C-O backbone or C-O group contributions. Note that this correction lowers the $CO_{2(g)}$ chemisorption energies but do not affect the discussed trends between surface composition and geometries.

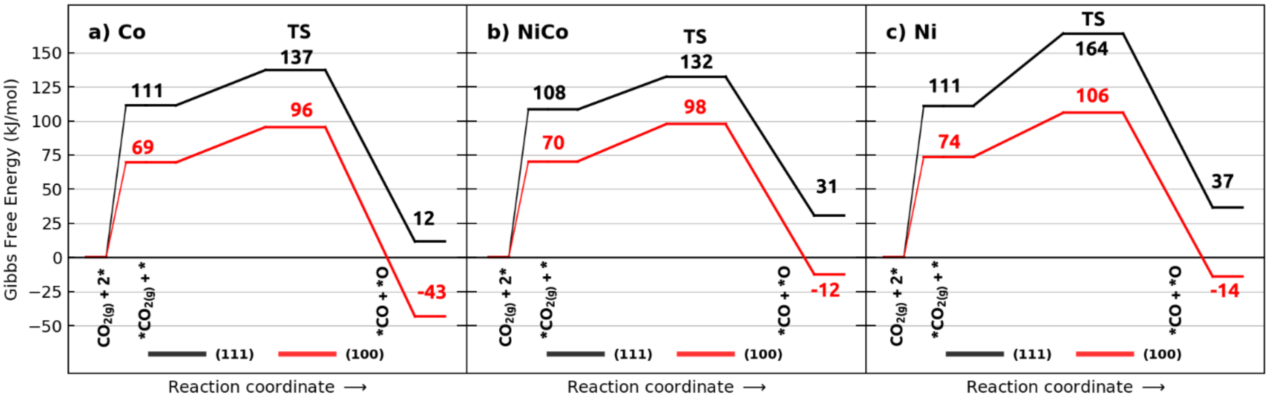

Fig. 32 CO_2 adsorption and activation (1kPa, 265°C), black: (111), red: (100) surfaces.

Fig. 32 shows the chemisorption and dissociation free energy profile for the $CO_{2(g)}+2^* \rightarrow {}^*CO+{}^*O$ reaction pictured in Fig. 33, Table 11 shows the $CO_{2(g)}$ adsorption, *CO_2 activation and dissociation energy. Chemisorption is found to be endoergic (positive) even after the correction, suggesting an unfavorable adsorption of $CO_{2(g)}$ species, consistent with a low *CO_2 population. Positive chemisorption energies are often reported [29], [33], [36], [110], suggesting a preferred and only slightly favored ($E_{ads} \sim -0.05$ eV) physisorbed configuration where CO_2 stays parallel about 3.5Å over the surfaces in its gas phase geometry ($\sphericalangle_{O\text{-}C\text{-}O}$~180°, $d_{C\text{-}O}$~1.18Å). It is reported that using dispersion corrections or vdW-corrected functional lowers physisorption and chemisorption energies, even making the $CO_{2(g)}$ chemisorption exothermic [108], [111]. These corrections have a systematic effect on the adsorption energies but little effect on structural parameters of the chemisorbed *CO_2 geometry that precedes the C-O bond activation[111]. While adsorption energies may be systematically overestimated, energy differences on the surface are expected to be well behaved.

For all slab compositions the CO_2 chemisorption on (100) surfaces is 38-40 kJ/mol stronger than on (111) surfaces, in excellent agreement with published values on Ni [26], [33], [111] with different DFT methods. Differences by surface composition are small, the $^*CO_2$ chemisorption follows the order NiCo(111) < Co(111) < Ni(111) and Co(100) < NiCo(100) < Ni(100) within <5 kJ/mol. This suggest that differences in $CO_{2(g)}$ binding strength are not a relevant factor differentiating the reaction kinetics between the catalysts.

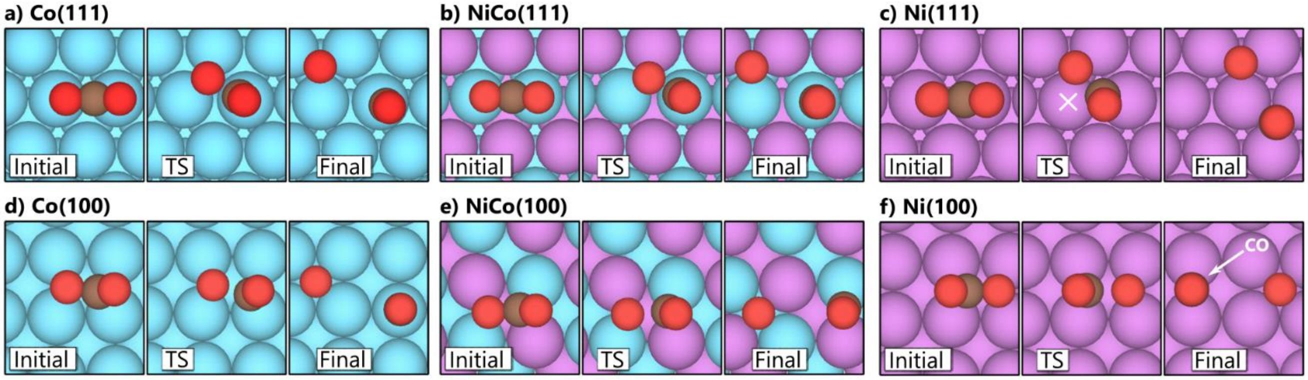

Fig. 33 Direct $^*CO_{2(g)}$ dissociation on Co (q,d), NiCo (b,e) and Ni (c,f) (111) and (100) surfaces (respectively). Atom colors: Cyan - Co, purple - Ni, gray - C, red - O. White X on c) Ni(111) marks the shared Ni atom.

The direct dissociation barrier ($^*CO_2+^*\rightarrow^*CO+^*O$) is about 60kJ/mol higher on Ni(111) than on Ni(100), which is ~20kJ/mol higher than the chemisorption energy difference suggesting an intrinsically less active (111) surface Ni surface and consistent with previous reports [33], [36], [111]. Such structural difference is not found for the Co or NiCo surfaces,[46] both barriers are lower than the barrier Ni barrier by ~30 kJ/mol on (111) and ~10kJ/mol on (100) surfaces. Therefore, bimetallic and Co surfaces appear to behave more similar and more active than Ni for the direct $^*CO_2$ dissociation. Dissociative adsorption (from $CO_{2(g)}$) appears to be only favored on the (100) surfaces ($\Delta G_{rx}<0$) but again, $CO_{2(g)}$ adsorption may be overestimated by RPBE-DFT. Reaction energies for $^*CO_2+^*\rightarrow^*CO+^*O$ (Table 2, parenthesis) show that the activation of $^*CO_2$ is thermodynamically favored ($\Delta G_{rx}<0$) on all surface geometries and compositions, and significantly lower on the Co surfaces (by >20kJ/mol on (111) and >30 kJ/mol on (100)). Considering the $^*CO$ and $^*O$ stability trends (sec. 7.2.1, 7.2.3) this is attributed to the strong oxophilicity of the Co surface stabilizing better the co-adsorbed species and, conversely, Ni and Ni-rich sites on (111) showing less stable interactions with O atoms. The slightly lower barrier on NiCo amongst (111) surfaces can be attributed to the favorable stabilization by Co atoms of $^*O$ (compared to Ni(111)) and $^*CO$ (compared to Co(111)). In summary, (100) surfaces may contribute more to the $CO_{2(g)}$ direct dissociation than (111) surfaces while the Co and bimetallic surfaces show lower activation

---

[46] For the step barrier, without considering the chemisorption difference between (111) and (100) surfaces

barriers and more favorable reaction energies appearing to be more effective in splitting $CO_{2(g)}$ compared to monometallic Ni surfaces regardless of surface geometry.

Table 11 $CO_{2(g)}$ adsorption (ΔG_{ads}), $^*CO_2$ activation (ΔG_a) and dissociation (ΔG_{rx}) free energies (kJ/mol).

Surface	Co		NiCo		Ni	
	ΔG_{ads}	ΔG_a (ΔG_{rx})	ΔG_{ads}	ΔG_a (ΔG_{rx})	ΔG_{ads}	ΔG_a (ΔG_{rx})
(111)	111	25.97(-99.72)	108	24.15(-77.53)	111	52.93(-74.65)
(100)	69	26.02(-112.72)	70	27.40(-82.62)	74	32.23(-87.81)

The activation of $^*CO_2$ was studied in detail to gain insight on the differences between mono and bimetallic catalysts. Upon interaction with metallic surfaces, CO_2 receives electronic charge that bends the molecule, moves the in-plane contribution of the $2\Sigma u$ molecular orbital (LUMO) to lower energies and lengthen one of the C-O bonds[26], [111], [112]. $^*CO_2$ species in Fig. 33 (initial) show $O_{(1)}$-C-$O_{(2)}$ angles of 123-139° (similar to [33]) with C-$O_{(2)}$ bonds extended to 1.37-1.24Å on (100) and (111) surfaces, respectively. PDOS of the $CO_{2(g)}$ molecule bending and extending the C-$O_{(2)}$ bond confirms that this activation moves of the $2\Sigma_u$ MO closer to the Fermi level and increases the proportional contribution from the $O_{(2)}$ atom (see A7.2).

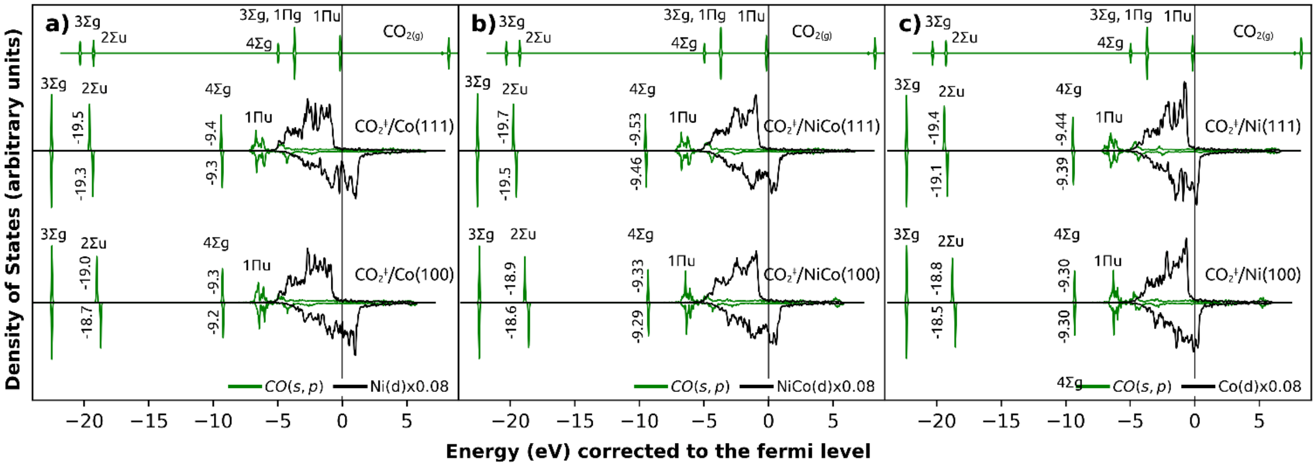

Fig. 34 PDOS (Fermi-corrected) of the transition state configurations for the activation of $^*CO_2$ (Fig. 33) on (a) Ni, (b) NiCo and (c) Co surfaces

Lui et al.[33] suggest that activation of the bend chemisorbed $CO_2^{\delta-}$ (Fig. 33, initial) on the surface is related to the Bader charge donation from the surface for a wide range of transition metals and surface geometries, Bader charges in this work show little difference between the (100) surfaces (<0.02 e) and do not explain differences between Ni and Co. On the other hand, Vogt[26] relates CO_2 activation on Ni surfaces to the coupled effects of the activation of the $2\Sigma_u$ molecular orbital (MO) and the Bond Order Conservation principle (BOC[47]), i.e., a more stable transition state on Ni(100) where no metal atoms are shared than on Ni(111) where there is a common Ni

---

[47] In this case, fewer shared Ni atoms in (100) than in (111) yield more stable transition states [26].

atom (Fig. 33c, marked atom). Applying BOC to explain differences in surface composition is less clear, linearly binding *CO on Co atoms of Co(111) and NiCo(111) (Fig. 33a,b) suggest there are no shared atoms in the transition state, which helps explaining the larger differences in activation energy between (111) surfaces but not for the (100) surfaces of different composition.

Fig. 34 shows the PDOS for the transition states for the *CO_2 activation, position of $2\Sigma_u$ MO is closer to the fermi level for (100) compared to (111) surfaces agreeing with its higher activity, as suggested by Vogt et al. [26], but does not explains by itself the differences between Ni, NiCo and Co surfaces. Integration of the $2\Sigma_u$ MO in Fig. 34 shows 83-86% contribution of the leaving *O atom on (111) and (100) surfaces, respectively, which suggest a transition state closer to the products and the relevance of stabilizing *O. In that case, the lower barriers on Co and the bimetallic surface can be attributed to the favorable interaction with the leaving O atom by Co atoms and the geometric effects described by BOC. As discussed (sec. 7.2.3), some bimetallic sites maintain the strong oxophilicity of the Co atoms, explaining the similar barriers on Co and NiCo surfaces and both lower than Ni.

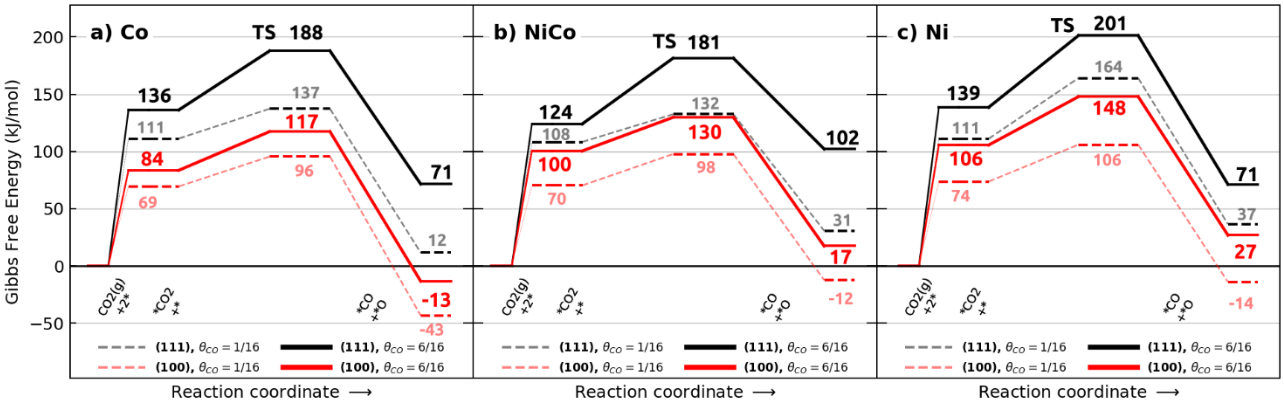

Fig. 35 Adsorption and activation of $CO_{2(g)}$ on (1kPa, 265°C), black: (111), red: (100) surfaces. Solid lines: surfaces pre-covered with six *CO nearby (Θ_{CO}=0.46 ML), segmented lines: clean surfaces (Θ_{CO}=1/16=0.06 ML).

Under reaction conditions high populations of *CO species were observed (sec. 7.1). It is expected those co-adsorbed species drawn electronic density from the surface affecting the stability of the intermediates, *$CO_2^{\ddagger}$ and other activated species. To emulate this effect the *CO_2 activation was studied on a surface pre-covered with six *CO spectators[48] for a coverage of Θ_{CO}=0.43 ML (after dissociation) closer to the expected occupancy under reaction conditions. Geometries and methods are detailed in annex A7.3, Fig. 35 shows the reaction profiles at high and low *CO coverage. Adsorption energies increase ~20 kJ/mol on (111) and ~30 kJ/mol on (100) covered surfaces (regardless of surface composition) due the interaction with spectators and a more electronically depleted surface. Activation barriers from *CO_2 (Table S16, step barriers) increase around 10 kJ/mol on (100) surfaces, 26kJ/mol on Co(111), 33 kJ/mol on NiCo(111) but only

---

[48] The number of atoms increases to 79. To keep a reasonable computational cost the k-point mesh was reduced to 3x3x1 and convergence criteria increased to 10-5 eV (electronic) and -0.05 eV/Å (relaxation), see details in A7.3.

10kJ/mol on Ni(111), though Fig. 35 shows both Ni surfaces still have the highest barriers for the adsorption and dissociation. Reaction energies (ΔG_{rx}, Table S16) on Co(111) and NiCo(111) increase significantly more than on Ni surfaces (35 kJ/mol, 56 kJ/mol and ~8 kJ/mol, respectively). Both observations suggest that compact Ni surfaces are less affected by higher *CO coverages while compact Co and NiCo surfaces stabilize less the activated and coadsorbed *O and *CO species, which is consistent with the more stable adsorption of $CO_{(g)}$ on Ni (sec. 7.2.1).

8.3 Preferred *C-O dissociation pathways

Direct CO_2 dissociation is agreed to be the main source of *CO species and not kinetically relevant to the methanation reaction. A significant population of those carbonyl species were identified in FTIR (sec. 7.1) and observed to evolve with the reaction conditions. Therefore, it is kinetically relevant to study the evolution of the carbonyl species and how the remaining C-O bond is broken to later form the methane molecule. The three possible reaction pathways in Scheme 1 are explored to break the second C-O bond: (1) the direct dissociation or carbide pathway, (2) H-assisted dissociation through HCO intermediate and (3) H-assisted through COH intermediate. These three simple routes have been previously proposed for Ni and Co and recently found to be kinetically relevant contributions to the overall methanation rate on the studied Ni surfaces [36]. The routes also include species with distinctively different adsorption strength trends on Ni and Co surfaces (*O, *C, *CH, *OH), making its study representative of the main differences between the studied metals. Only steps after *CO are relevant for this discussion, therefore $CO_{(g)}$ (1kPa), $H_{2(g)}$ (25 kPa) and the clean surfaces at 265°C are used as convenient energy reference[49]. The remaining hydrogenation steps are discussed later (sec. 8.4).

Scheme 1 Reaction steps in C-O bond breaking routes for $CO_{(g)} + H_{2(g)} + 2* \rightarrow *CH + *OH$.

(1) Direct route	(2) H-assisted: HCO route	(3) H-assisted: COH route
$CO_{(g)} + * \rightarrow *CO$	$CO_{(g)} + * \rightarrow *CO$	$CO_{(g)} + * \rightarrow *CO$
$*CO + * \rightarrow *C + *O$	$*CO + ½ H_{2(g)} \rightarrow *HCO$	$*CO + ½ H_{2(g)} \rightarrow *COH$
$*C + ½ H_{2(g)} \rightarrow *CH$	$*HCO + * \rightarrow *CH + *O$	$*COH + * \rightarrow *C + *OH$
$*O + ½ H_{2(g)} \rightarrow *OH$	$*O + ½ H_{2(g)} \rightarrow *OH$	$*C + ½ H_{2(g)} \rightarrow *CH$

Fig. 36 shows the free energy reaction profiles for the direct dissociation ($*CO + * \rightarrow *C + *O$, in red) and H-assisted pathway through HCO (green) and through COH (purple). For the HCO route, breaking the HC-O bond forms *CH+*O, while the COH route forms *C+*OH and the direct dissociation only forms the atomic species *O+*C. For a more consistent comparison, $*C + *H \rightarrow *CH$ and $*O + *H \rightarrow *OH$ hydrogenation steps were added at the end of each path so all routes end up with *CH and *OH. Therefore, each profile section represents the $CO_{(g)} + H_{2(g)} + 2* \rightarrow *CH + *OH$ excerpt of a catalytic cycle.

---

[49] This only adds the molecular $CO_{(g)}$ and dissociative $H_{2(g)}$ adsorption steps without overloading the profiles in Fig. 36, in addition, the accuracy of the simulated *CO species has already been discussed thoroughly.

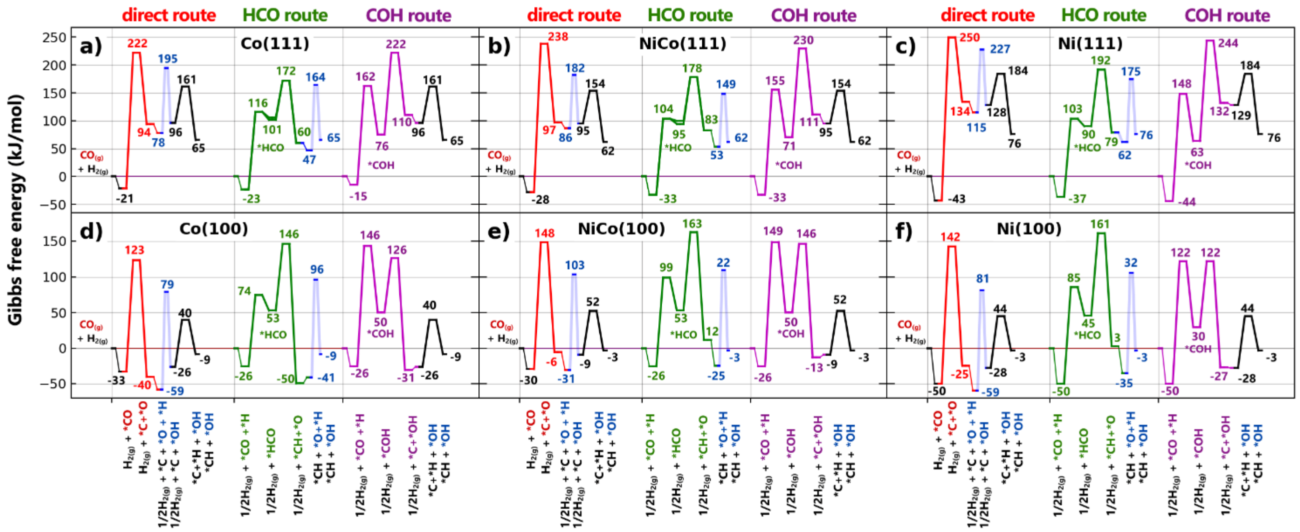

Fig. 36 Free energy profiles for the C-O breaking routes: direct (red), HCO (green) and COH (purple) on Co, NiCo and Ni, (111) and (100) surfaces (1kPa CO, 25kPa H_2 , 265°C). Molecular adsorption of CO, dissociative adsorption of H_2 and hydrogenation steps of *C (black) and *O (blue) are included for consistency.

8.3.1 Routes on the (111) surface

For all (111) surfaces the formation of *CH and *OH from the gas species is thermodynamically unfavorable ($\Delta G_{rx}>0$) by about 64 kJ/mol on Co(111) and NiCo(111) but up to 76 kJ/mol on Ni(111). This difference comes from the weaker stabilization of co-adsorbed *CH and *OH species by Ni(111), attributed to the electronically demanding stabilization of the OH species (sec. 7.2.3, 7.2.4). Consistent with the operando IR results (sec. 7.1) and CO adsorption energies (sec.7.2.1), *CO is the lowest point for all the profile segments on the (111) surface, agreeing with *CO being the most abundant surface species. For all surface compositions the direct dissociation (Fig. 36a,b,c, red) is the highest barrier at 222 kJ/mol for Co(111), 238kJ/mol for NiCo(111) and 250 kJ/mol for Ni(111). The prohibitively low rate constants (k ~10^{-12} s^{-1} for Co on NiCo, ~10^{-16} s^{-1} on Ni) indicate that the direct dissociation does not contribute significantly to the C-O bond breaking on extended (111) surfaces regardless of the surface composition.

For the H-assisted paths, the formation of the *COH intermediate (Fig. 36a,b,c purple) is thermodynamically favored and 25-30 kJ/mol more stable than the *HCO intermediate (Fig. 36a,b,c green). On the other hand, the H-addition barrier of the HCO paths are 46-50 kJ/mol lower than the COH path, similar for Ni(111) and NiCo(111) (~100 kJ/mol) and only slightly higher on Co(111) (116 kJ/mol). This first hydrogenation in the HCO route has lower direct barriers (k~$10^{-1}$$s^{-1}$) and low *HCO+*↔*CO+*H dehydrogenation barriers (<15 kJ/mol, k > 10^{11} s^{-1}), suggesting *CO and *H interconvert more with *HCO than *COH. The following C-O bond breaking are the highest barriers for the COH and HCO routes, and higher barrier than the first H-addition of the COH path suggesting *COH may form and contribute to the reaction rates.

The C-O breaking barrier is at least 50 kJ/mol lower for *HCO than for *COH and the formation of *CH+*O species from the HCO route is thermodynamically more favored than the

*C+*OH species resulting from the COH route. The *C and *O hydrogenation steps added at the end of the COH and HCO routes have low step barriers and therefore little kinetic effect. Overall, the HCO route is considered the most favorable both, kinetically and thermodynamically, on the (111) extended surfaces, and is expected to contribute more to the methanation reaction and the HCO dissociation towards *CH+*O the kinetically relevant step. The HCO pathway is also found to be relevant in the methane reforming on Ni(111)[113] and methanol steam reforming on Co(0001) and Co(100)[3]. A preferred HCO route is consistent with proposed mechanism with the KIE results[95]. Recent DFT-microkinetic results[36] agree with the almost exclusive prevalence of the HCO route for the CO_2 methanation on Ni(111).

The effect of a higher *CO coverage was studied for the main barrier of the HCO route as in sec. 8.2.2. Fig. 37 shows the CO adsorption, HCO intermediate and the HC-O bond breaking barrier (highest barrier) in a 6/16 *CO coverage (see Fig. 37). Free energy of the HCO intermediate increased moderately on Ni(111) and NiCo(111) but shows no significant change on Co(111). Similarly, the HC-O dissociation barrier had almost no change on Co(111) but increased significantly on Ni(111) (~50 kJ/mol). More importantly, the $CO_{(g)}$ adsorption energy increases to be endothermic on Co(111) and NiCo(111), displacing the CO equilibrium towards the gas phase. Regardless the accuracy of the specific value, this evidences again the lower capacity of Co and bimetallic surface to retain carbonyl species, which is consistent with the lower FTIR carbonyl signals in sec. 7.1 (Fig. 20a, compared to Ni/SiO_2) and explains the higher release of $CO_{(g)}$ and concomitant lower selectivity towards $CH_{4(g)}$ of these catalysts (Fig. 19c). Therefore, the ability to retain *CO on the surface (allowing its hydrogenation) appears to be a deciding factor on the selectivity of the studied materials.

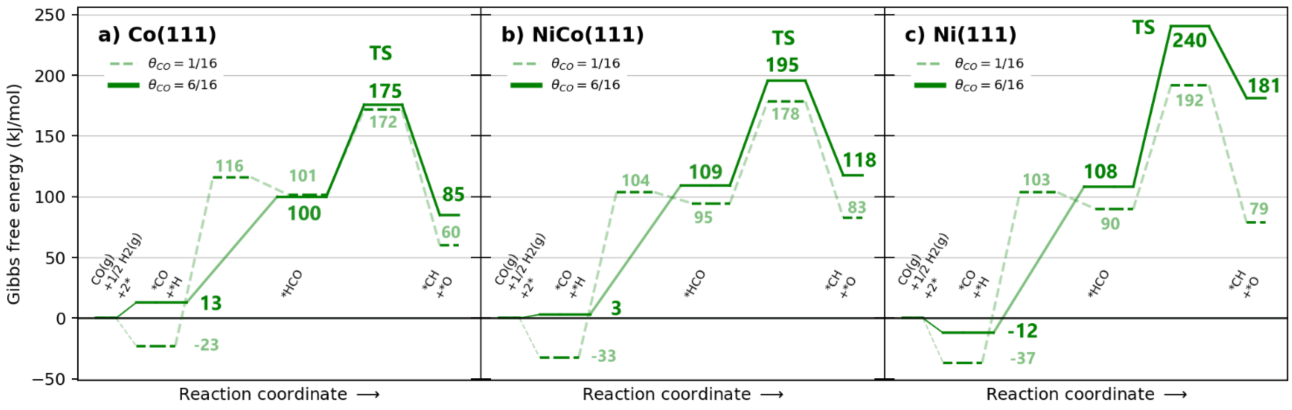

Fig. 37 Free energy profile for CO adsorption, HCO intermediate and highest barrier in the HC-O bond breaking route (1kPa CO, 25kPa H_2 , 265°C). Solid lines: surfaces pre-covered with six *CO nearby (Θ_{CO}=0.46 ML), segmented lines: clean surfaces (Θ_{CO}=1/16=0.06 ML).

8.3.2 Routes on the (100) surface

On (100) surfaces (Fig. 36d,e,f) adsorption and reaction of $CO_{(g)}+H_{2(g)}$ forming *CH+*OH is considered thermodynamically neutral for all surface compositions with ΔG_{rx}=-3 kJ/mol on

Ni(100) and NiCo(100) and only slightly more negative (ΔG_{rx}=-9 kJ/mol) on Co(100). The lower reaction energies on Co(100) are consistent with the greater stabilization of *OH species by Co atoms (sec. 7.2.3). Unlike the (111) surface, *CO is not the unique most stable part for all the profiles but *C, *O and *H for Co(100) and NiCo(100), these species are difficult to identify experimentally so their possible high abundance is not necessarily inconsistent the FTIR results (sec. 7.1).

All steps show smaller barriers on the (100) surface, as expected from the stronger stabilization of adsorbed species. The direct C-O dissociation (Fig. 36d,e,f, red) is again the highest single barrier (k~10^{-3} on Co(100), ~10^{-5}-10^{-6} on NiCo(100) and Ni(100)) but closer to the highest barriers for the H-assisted paths, making it a more competitive pathway than on the (111) surfaces (in good agreement with published results[36], [76]) and the preferred on Co(100) between the studied routes (by ~20 kJ/mol). The first H-addition barrier is smaller forming *HCO than *COH (by >60kJ/mol) with a moderate reverse barrier (~20kJ/mol on Co(100), ~30 kJ/mol on Ni(100) and ~45 kJ/mol) suggesting that *CO interconverts more with *HCO than *COH. Both intermediates are similarly stable on Co(100) and NiCo(100) but *COH is more stable on Ni(100) (by ~15 kJ/mol) favoring its higher population. The *COH→*C+*OH dissociation has a lower barrier on Ni(100) than the CO and HCO dissociations (by 20 kJ/mol and 40 kJ/mol, respectively), probably attributed to the greater stabilization of *C in four-fold Ni sites. This suggest the COH path is expected to contribute more to the methanation reaction on Ni(100) between the studied routes and in agreement with previous studies[35], [36]. In particular, DFT-microkinetic results from Sterk et al.[36] agree with the preferred COH route but also report a significant contribution of the direct dissociation (26%) to the overall methanation rate.

In summary, the direct dissociation appears to be more competitive on Co(100) (compared to the other routes and surfaces) and the COH route is preferred on Ni(100). For the bimetallic the activation barriers for the CO and COH pathways are close (~148 kJ/mol), thus both are considered kinetically relevant and further microkinetic simulations may be necessary to address their contributions to the methanation rate. Now comparing the metallic compositions, the greater stabilization of O by Co atoms (sec. 7.2.3) is consistent with the lower barriers for the CO direct route[31] and the *HCO→*CH+*O dissociation on Co(111) and Co(100) compared to Ni(111) and Ni(100). The stronger adsorption of *O and *OH on Co surfaces also facilitates O-H reactions facilitating formation and activation of H_2O[3]. The strong *CH (and *C) adsorption on Ni_4 sites is consistent with the greater stabilization of the *COH→*C+*OH dissociation on Ni(100) compared to Co(100) and NiCo(100). Therefore, the proposed reaction steps capture some of the key differences between Ni and Co surfaces previously discussed (sec. 7).

From the experimental results and literature review it is considered that the direct CO dissociation should not contribute significantly to the overall reaction rate[36] though above results show it as an available pathway on Co(100) and competitive to the H-assisted routes on the other (100) surfaces. Three possibilities are that a different reaction route is preferred (see A8.2), that the abundance of *HCO species allow the activation HCO route contribute more significantly to the overall rate despite the higher HC-O dissociation barrier (for which a microkinetic study is necessary) or that (100) facets are not available or do not contribute significantly to the overall reaction rate. Going back to the roughly estimated nanoparticles in Fig. 14 (sec. 5.1), the abundance of well defined (100) surfaces in 3-5nm nanoparticles is less than the ideal Wulff polyhedral suggest (Fig. 13), furthermore, fourfold sites close to the edges may behave significantly different than what the extended (100) DFT surfaces studied here. Recently Sterk et al.[36] suggested that (110) sites and not (111), (100) or (211) contribute the most to the overall CO_2 methanation rate on Ni nanoparticles, though small near-edge sites were represented by extended (110) slab models. Additionally, fourfold sites may be blocked by the strong adsorption of some atomic species (*C, *O) and small intermediates (*CH, *OH). In particular, the direct CO dissociation and COH routes form surface *C, which is known bind strongly on the fourfold sites (sec. 7.2.2), promoting surface restructuration and formation of larger C deposits (sec. 7.2.2.1). However, the hydrogenation sequence of *C is of interest not only as part of the methanation reaction but more generally as a mechanism for the elimination of surface C deposits that may form other industrially relevant reactions such as Fischer-Tropsch, methane reformate and alkane decomposition to produce H_2.

8.4 Hydrogenation of surface *C

The sequential hydrogenation of an adsorbed C atom to methane was studied through the elementary steps in Scheme 2. Fig. 38 shows the free energy reaction profile on the (111) and (100) surfaces. Free energies, electronic energies and electronic profile are shown in annex A9.2. The free energy for dissociative H_2 co-adsorption is slightly positive, suggesting absence of a pool of bound H-atoms.[50] Therefore, H-atoms are added sequentially for each hydrogenation and referenced to gas-phase H_2 free energy. Fig. 39 and Fig. 40 show the geometries of steps R1-R4 on the (111) and (100) surface of the alloy (other surfaces in SI.10, geometric parameters in Table S20 and Table S19), the exploration of different reaction paths for the kinetically relevant steps converged to the paths presented here.

Scheme 2. Hydrogenation steps to eliminate *C forming $CH_{4(g)}$

R1)	$^*C + \frac{1}{2} H_2(g)$	$\rightarrow$	$^*CH$
R2)	$^*CH + \frac{1}{2} H_2(g)$	$\rightarrow$	$^*CH_2$
R3)	$^*CH_2 + \frac{1}{2} H_2(g)$	$\rightarrow$	$^*CH_3$
R4)	$^*CH_3 + \frac{1}{2} H_2(g)$	$\rightarrow$	$^*CH_{4(phys)}$
D)	$^*CH_{4(phys)}$	$\rightarrow$	$^* + CH_{4(g)}$

---

[50] Even considering this positive value as part of the innacuracies of the functional it suggests a close to zero free energy dissociative adsorption which supports the absece of an *H pool or at least the

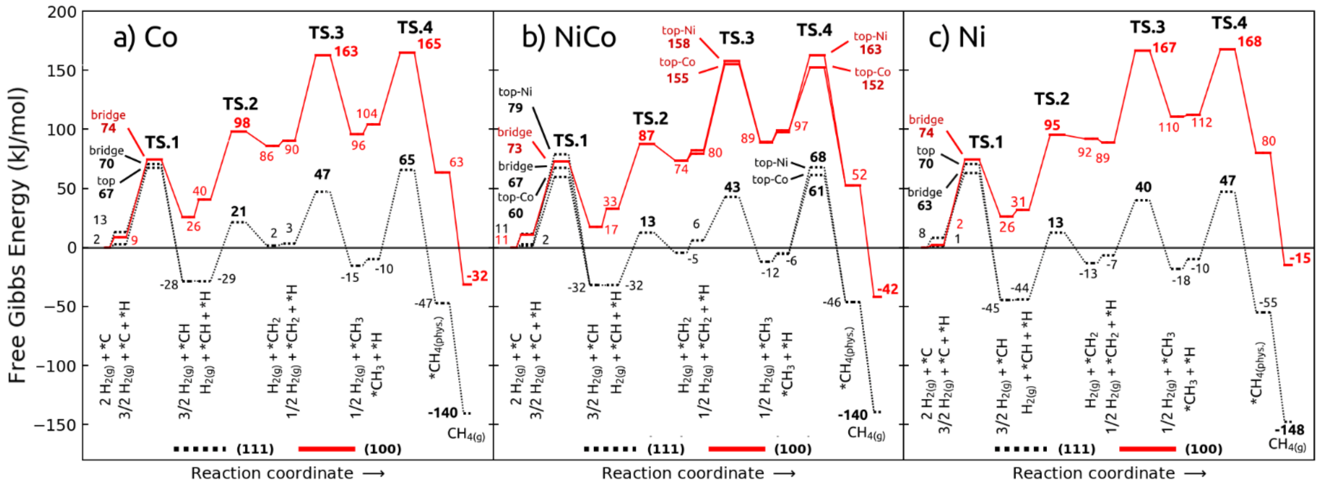

Fig. 38 Gibbs free energy profiles for the hydrogenation of *C to $CH_{4(g)}$ on (111)(dotted lines) and (100) (solid lines) surfaces (265 °C, 25kPa H_2, 1kPa CH_4).

8.4.1 *C hydrogenation on the (111) surface

The sequential hydrogenation of *C species requires a H_2 dissociation at an empty site and migration of a *H species close to a CH_x species. H_2 dissociation and migration steps exhibit low barriers[28], [76], [78], [114], leading to their rapid rates and kinetic irrelevance. The transition states for the H_2 dissociation are therefore not shown in Fig. 38 for simplicity. The *H formation for most H addition step is slightly endoergic (positive free energy ~10kJ/mol; Fig. 38). The C-H bond formation transition state for the first H addition (step R1, Scheme 2), can involve H-atom atop a surface metal atom or in bridge position between two metal atoms (Fig. 39a,b,c). The transition states with H atoms on top of metal atoms are more stable on Co(111) and NiCo(111) surfaces, consistent with the importance of (C-H)-metal agostic interactions observed in sec. 7.2.2.2. In the case of NiCo(111), transition stated with H atop a Co atom are more stable than those atop Ni atoms. Subsequent H additions (steps R2-R4) also involve similar interactions involving H-atoms in top positions and favoring Co atom over Ni in the intermetallic surfaces.

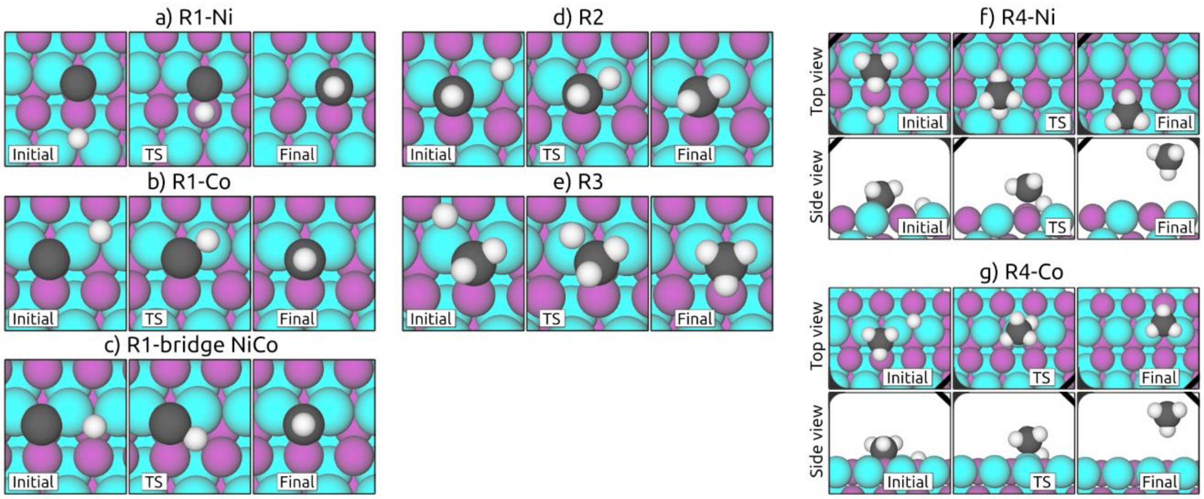

Fig. 39 Hydrogenation steps on the NiCo(111) surface. Atom colors: Cyan - Co, purple - Ni, gray - C, white - H.

On all (111) surfaces, the first hydrogenation step R1 (Scheme 2) is exoergic (dotted lines; $\Delta G_r<0$; Fig. 38), favoring the formation of *CH from *C. The *CH is the lowest free energy CH_x species on the (111) surface for Co(111), NiCo(111), and Ni(111), making it the most abundant surface species. The transition states for the second (R2; TS.2) and third hydrogenations (R3; TS.3) on all (111) surfaces exhibit lower free energy than the first hydrogenation (TS.1). Thus, interconversion between *CH, $*CH_2$ and $*CH_3$ can occur more frequently than between *C and *CH. The transition state for the hydrogenation of $*CH_3$ to form methane (TS.4) has higher free energy than the hydrogenation of *CH (TS.2) and $*CH_2$ (TS.3) on all (111) surfaces, close to the free energy barrier for the first hydrogenation (TS.1) on Co(111) and NiCo(111) but 16kJ/mol lower on Ni(111). This suggest that the first (R1) and last (R4) hydrogenations are similarly kinetically relevant on Co(111) and NiCo(111) surfaces but essentially solely the first hydrogenation limits the rate on Ni(111) at the simulated conditions. Note that conditions that inhibit the H_2 dissociative adsorption (higher ΔG_r, e.g., lower H_2 pressure or higher temperature) will push the later hydrogenation barriers (TS.2, TS.3 and TS.4) to higher energies, thus making more relevant the last hydrogenation. At the reaction conditions, the complete hydrogenation of *C towards $CH_{4(g)}$ is thermodynamically favored on all (111) surfaces ($\Delta G_r<-100$kJ/mol), similar on Co(111) and NiCo(111) and slightly more negative on Ni(111). The free energies of *CH, $CH_{4(g)}$ and the TS.4 transition state on NiCo(111) are similar to Co(111) (e.g., TS.4 ΔG 65, 61, and 47 kJ/mol in Co, NiCo and Ni; Fig. 38), suggesting that the equimolar intermetallic behaves kinetically more similar to the monometallic Co(111) than Ni(111). Ni catalysts are experimentally known to deactivate by C poisoning more than Co catalysts, but the TS.1 barriers are slightly lower on Ni(111) than on Co(111) and the TS.4 barriers (that may also be relevant, as discussed) for Ni(111) are 14 kJ/mol lower than for Co(111) or NiCo(111), suggesting a more facile elimination of *C through hydrogenation on Ni(111) surfaces. Therefore, even though combination of *C in *Cn chains is favored on (111) surfaces (sec. 7.2.2.1), the flat (111) surfaces are not the primary responsible of deactivation processes by C poisoning.

8.4.2 *C hydrogenation on (100) surfaces

The transition states for sequential hydrogenation of *C involve a bridging position of the first and second added H atoms (R1, R2; Fig. 40). The third and the fourth H-atoms are near the top of a metal atom in their respective hydrogenation transition states (R3, R4). The free energy of the first hydrogenation transition states (TS.1;Fig. 38) on (100) surfaces is within 5 kJ/mol of values on corresponding (111) surfaces. However, on (100) surfaces, the first hydrogenation step R1 is endoergic ($\Delta Gr > 17$ kJ/mol) and all TS.2 free energies are higher than TS.1. This suggests a favored equilibrium towards *C rather than *CH. Moreover, for all (100) surfaces the transition state energies are in the order TS.1 < TS.2 < TS.3 ~ TS.4. Thus all $*CH_x$ species favor further dehydrogenation and *C is the most abundant surface species. In particular, the small TS.2 (reverse) barriers compared to $*CH_2$ suggest an equilibrium entirely displaced towards the dehydrogenation and any $*CH_2$ formed quickly dissociates to *CH, especially on the Ni(100) surface. TS.4 presents the highest barrier for methane formation on all Ni(100) and Co(100) surfaces, but within 5kJ/mol the *CH_2 hydrogenation barrier (TS.3). The significant dehydrogenation barriers for *CH_3 (>57kJ/mol, with TS.3 as reverse barrier) suggest *CH_3 species may also be relevant for other reaction conditions. For instance, previous studies of the DMR process on (100) monometallic surfaces[80], [115] coincide with the dissociative adsorption of $CH_{4(g)}$ as the highest barrier towards *C.

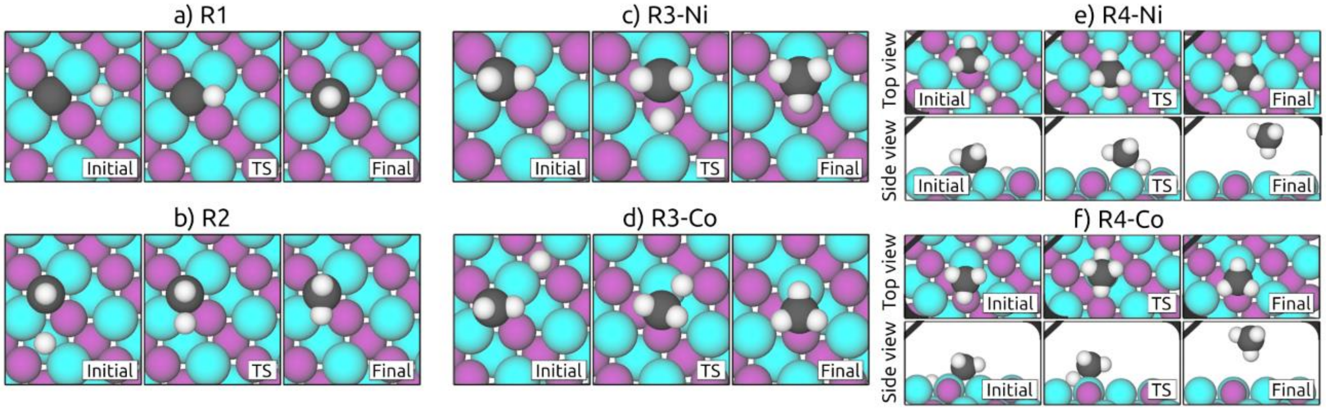

Fig. 40 Hydrogenation steps on the NiCo(100) surface. Atom colors: Cyan - Co, purple - Ni, gray - C, white - H.

The TS.1 free energies are similar on all (100) surfaces (~74kJ/mol), but the values for TS.2, TS.3 and TS.4 are lower on NiCo(100) than on monometallic (100) surfaces, suggesting a more facile hydrogenation of *C on NiCo(100) surfaces consistent with the experimentally observed C poisoning resistance of NiCo catalysts[116]. In particular, the higher TS.4 barrier on Ni(100) compared to Co(100) and NiCo(100) suggest a more difficult elimination of *C from the four-fold sites by hydrogenation on Ni(100). These *C do not recombine favorably to C_n chains (sec. 7.2.2.1) but are hard to eliminate by hydrogenation (specially on the Ni(100) surface), this suggests *C species may distribute on (100) surfaces blocking four-fold sites. The accumulation of *C on four-fold sites is related to deactivation near step edges[104] and propitiates surface restructuring of flat surfaces[103] (though such reconstructions are easier on Co than Ni surfaces). These results suggest that (100) surfaces are more relevant for explaining deactivation phenomena and the greater resistance of NiCo bimetallics to C poisoning.

The formation of $CH_{4(g)}$ from *C is thermodynamically more favored on NiCo(100) than on Co(100) and significantly less favored on Ni(100). This trend is consistent with the trends in adsorption energy discussed in sec. 7.2.2 , with all species (specially *C) binding more strongly on Ni(100) and significantly weaker on the NiCo(100) surface.

8.4.3 Evidence of the transition state stabilization from the density of states

Transition states on (111) and (100) surfaces involving C-H bonds are stabilized more on top of Co rather than Ni atoms (sec. 8.4.1-8.4.2) and CH_x species with agostic interactions with Co are more stable than that with Ni (sec. 7.2.2). The oxophilicity of Co atoms can be related to the stabilization of transition states involving O atoms but does not explain barrier and reaction trends for $*CH_x$ species. PDOS for metal (Ni or Co), C, and H atoms was computed to analyze the difference between top-Co and top-Ni transition states on NiCo surfaces (Fig. 41). Interaction of the forming bond with the metal, i.e., M-(C-$H_{(1)}$), is observed between -7.3 and -6.3eV while the non-interacting $H_{(3)}$ and $H_{(4)}$ only have a peak in the same position as the C atoms near -5.6eV. On the (100) surfaces, position of the reacting peaks (-6.78 eV for Co, -6.83 eV for Ni; Fig. 41b,d) are closer to the Fermi level than on (111) surfaces (-7.16 eV for Co, -7.22 for Ni; Fig. 41a,c). On both (111) and (100) surfaces these peaks are slightly closer to the Fermi level for the top-Co transition states, in agreement with reports for (111) bimetallic surfaces[11]. The $H_{(2)}$ atom in TS.4 is near the metal surface in the opposite position to the forming C-$H_{(1)}$ bond. This $H_{(2)}$ atom shows populations overlapping with the M-$H_{(1)}$ populations and the non-reactive $H_{(3)}$ and $H_{(4)}$ populations, suggesting some interaction of $H_{(2)}$ with the metal that is consistent with the M-(C-H) interactions proposed in 7.2.2.2 and would further differentiate the stability of the Co and Ni transition states. Therefore, the electronic and binding effects of alloying Ni and Co translate to kinetic effects that differentiate NiCo surfaces from the expected average of monometallic Ni and Co surfaces.

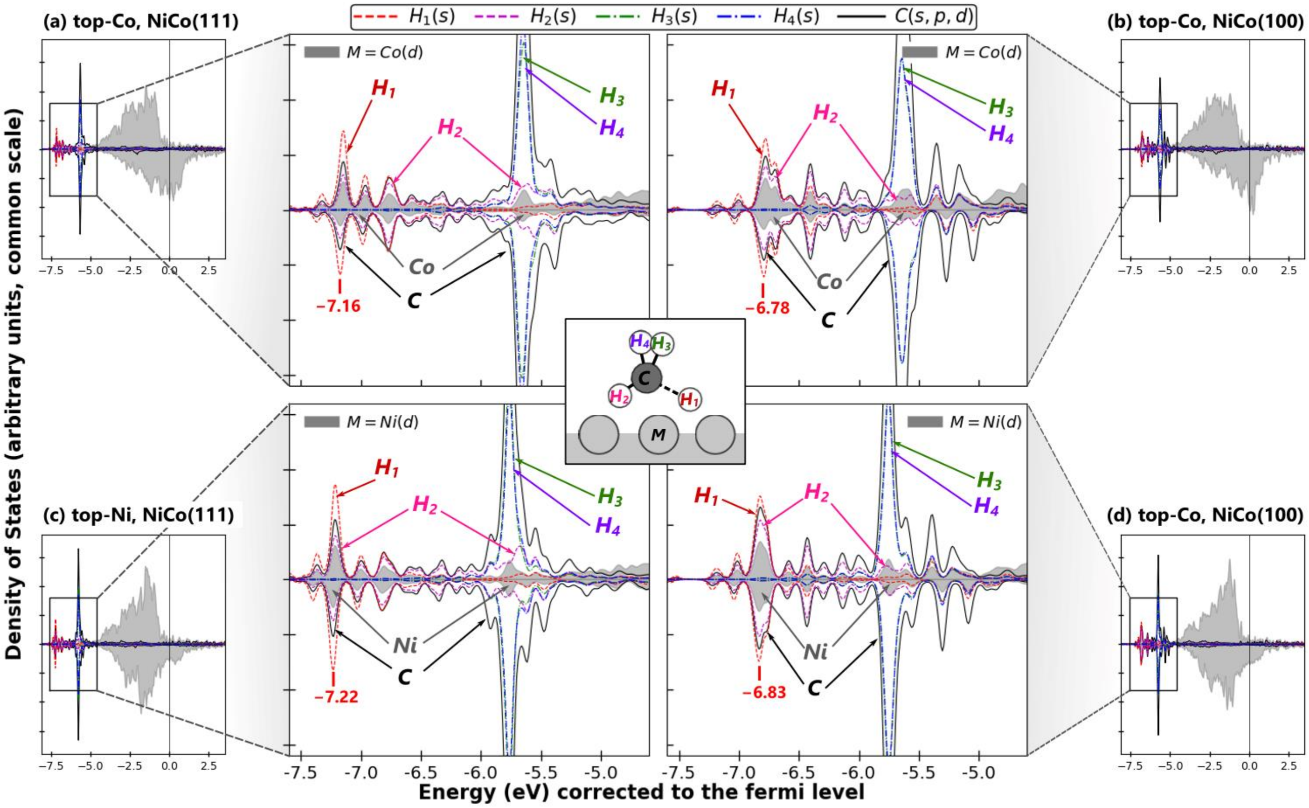

Fig. 41 PDOS (corrected to the fermi level) for the transition state $*CH_3+*H \rightarrow CH_{4(phys.)}+2*$ a) top-C path on NiCo(111), b)top-Co path on NiCo(100), c)top-Ni on NiCo(111) and d) top-Ni on NiCo(100).

The electronic adsorption energies of *C, *H and $*CH_x$ species (sec. 7.2.2), the reaction energies to form key intermediates and transition states barriers suggest the intermetallic surfaces behave more similar to monometallic Co than Ni. Although it should be noted that the effect of the Ni-

Co interaction discussed here are specific to the local coordination degree, specific reaction path and are strongly related to the site composition, with Ni atoms in the alloy providing generally less stable adsorption and reaction sites compared to Co atoms in the alloy and monometallic Ni surfaces.

8.5 Complete reaction profile

Fig. 42 and Fig. 43 compile the preferred Gibbs free energy reaction profiles for the (111) and (100) surfaces, respectively, following the energetics of carbonated species from $CO_{2(g)}$ to $CH_{4(g)}$ (energies in Table S18). For simplicity, only the routes with the lowest barriers are included for the (100) surface (Fig. 43). Hydrogen is added to the surface from $H_{2(g)}$ as required but parallel steps like *O/*OH eliminations are omitted for simplicity and similar to published profiles [36] (see Fig. S18 for a profile including all steps).

For the (111) surfaces (Fig. 42) *CO is the lowest point in the free energy profiles and its desorption is endergonic ($\Delta G > 0$, Fig. 42 dashed lines) indicating a *CO/$CO_{(g)}$ equilibrium displaced to the surface. This leads to the experimentally observed formation of a carbonyl pool on the surface under $CO_{2(g)}$ methanation conditions (sec. 7.1) with *CO being the most abundant surface intermediate. The *CO_2 direct dissociation barriers are relatively low and not kinetically relevant compared to the later hydrogenations of CH_x species. However, lower *CO_2 dissociation barriers on Co(111) and NiCo(111) promote the formation of *CO species more than on Ni(111) but these carbonyl are more weakly bound to the Co and bimetallic surfaces and more prone to desorb (Fig. 42, dashed lines). Moreover, these lower barriers and poorer retention of *CO species on Co and NiCo explain the higher $CO_{(g)}$ formation rates for Co/SiO_2 and $Ni_{0.5}Co_{0.5}/SiO_2$, compared to Ni/SiO_2 (sec. 6.1, A5.1). On the other hand, the Ni surface retains *CO more strongly promoting higher carbonyl coverages (see 7.1) that could undergo hydrogenation towards methane while *O and O-binding species are more weakly bound and more prone to be eliminated from the Ni(111) surface vacating active sites than from Co(111) or NiCo(111). These observations are consistent with the higher activity of Co/SiO_2 for $CO_{2(g)}$ but lower selectivity towards methane of Co/SiO_2 and $Ni_{0.5}Co_{0.5}/SiO_2$, compared to Ni/SiO_2. The lower activity of the NiCo/SiO_2 catalyst for the $CO_{2(g)}$ consumption could be attributed to the stronger binding of *CO compared to Co surfaces but also stronger binding of oxygenated species occupying active sites compared to Ni surfaces resulting in a smaller exchange rate on the surface. This complex interplay is ultimately related to the competing binding strengths of surface species as described in sec. 7.2.4 and the experimental approach described by Lachkov and Chin[22].

For the hydrogenation towards methane, the largest step barrier is the H addition to *CO forming *HCO (Ni(111), Co(111) ~140 kJ/mol > NiCo(111) ~135 kJ/mol, $k \sim 10^{-1}\ s^{-1}$), followed by the HC-O bond breaking in the order Co(111) < NiCo(111) < Ni(111) (70-100 kJ/mol barriers, $k \sim 10^{6}$-$10^{3}\ s^{-1}$).[51] This HC-O bond breaking is the highest barrier in all surfaces, 40 kJ/mol higher

---

[51] Note all these barriers are lower with $CO_{(g)}$ as reference (Fig. 36), a more representative approach for its adsorption equilibrium.

on Ni(111) than on Co(111) and 20kJ/mol higher on the bimetallic surface and followed by the $*CH_3$ hydrogenations ~ 30 kJ/mol lower. Therefore, the hydrogenation of *CO and activation of the C-O bond are the most kinetically relevant steps for the $CO_{2(g)}$ methanation on (111) surfaces.

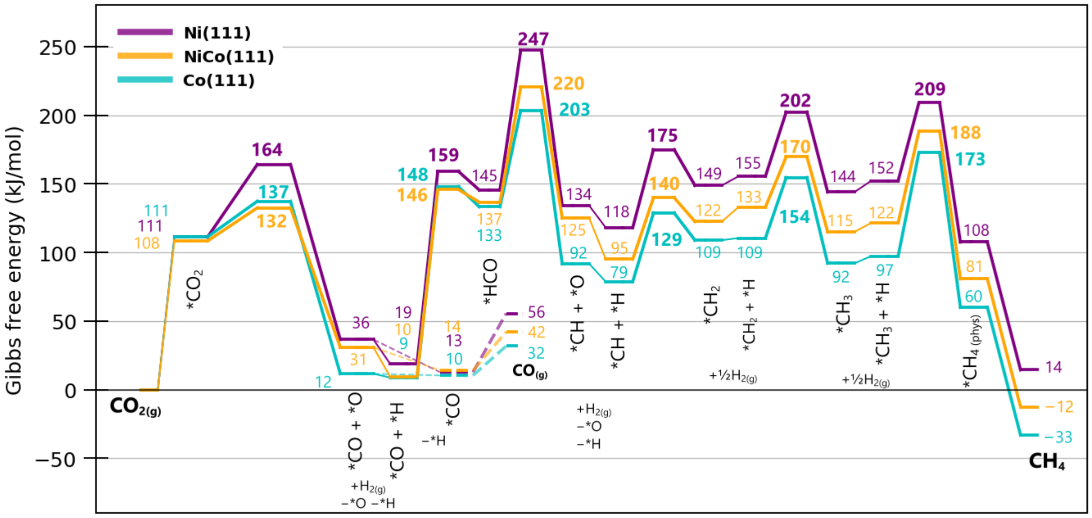

Fig. 42 Gibbs free energy reaction profile for the $CO_{2(g)}$ hydrogenation to methane (solid lines, 1 kPa $CO_{2(g)}$, 25 kPa $H_{2(g)}$, 265 °C, $CH_{4(g)}$ at 1kPa) on (111) surfaces. Cyan: Co(111), orange: NiCo(111) and purple: Ni(111).

On the (100) profiles (Fig. 43) the highest barriers are the dissociation of C-O bonds and the $*CH_2$ and $*CH_3$ hydrogenations, within ~14 kJ/mol for each surface. Monometallics have slightly higher $*CH_x$ hydrogenation barriers (~157 kJ/mol for Ni(100) and ~127 kJ/mol for Co(100)), while NiCo(100) has a higher *CO dissociation barrier (161 kJ/mol) and the highest barrier in the (100) profiles. Regardless of surface composition, all these are significantly lower than the (111) barriers (in part thanks to the lower $CO_{2(g)}$ adsorption energy) suggesting an intrinsically higher reactivity on the (100) surfaces that is consistent with their lower coordination degree and more stable four-fold sites. The (100) profiles also show highly stable carbonyl species not prone to desorb as $CO_{(g)}$ (Fig. 43, dashed lines) and more strongly bonded on Ni(100) than on NiCo(100) or Co(100). These *CO are favorably formed from $*CO_2$ through moderate activation barriers (slightly higher for Ni(100) but within ~10 kJ/mol from Co(100) and NiCo(100)). *C and *OH are also shown within the lowest points in the profiles and close to carbonyl, these intermediates are surrounded by the highest reaction barriers of the profiles inhibiting either, the formation and release of $CO_{(g)}$ or that these species continue their hydrogenation towards $CH_{4(g)}$. This feature of the profile and the low abundance of (100) surfaces in small nanoparticles (Fig. 14) suggest that these surfaces do not to contribute significantly to the macroscopic methanation rates despite their lower activation barriers.

In summary, (111) and (100) surfaces show adsorption and activation trends consistent higher $CO_{(g)}$ formation rates as the Co content increases (Ni < NiCo < Co), in good agreement with the experimentally observed $CO_{(g)}$ formation rates ($Ni/SiO_2 < Ni_{0.5}Co_{0.5}/SiO_2 < Co/SiO_2$) and with an unassisted CO_2 dissociation mechanism. While (111) surfaces show a clear preference for the

HCO activation route as the rate determining step with barriers following the trend Ni(111) > NiCo(111) > Co(111), the (100) surfaces exhibit competing activation routes with significantly lower barriers than the highest (111) barriers (by >50 kJ/mol), suggesting more reactive (100) surfaces. Higher activation barriers on NiCo(100) are consistent with the experimentally observed anti-synergy of NiCo catalyst for the methanation rates. Furthermore, this also evidences the significantly different behavior and contribution of reaction mechanism on the NiCo alloy depending on the surface geometry. However, for the methanation reaction both surface geometries have steps with high activation energies (> 120 kJ/mol) and barriers compared to the experimental apparent activation barriers (76-100 kJ/mol, sec. 6) and $CO_{(g)}$ desorption energies. This suggests low methanation rates and selectivities on (111) and (100) surfaces that are not entirely consistent with the experimental performance of the three catalyst, as discussed recently for Ni surfaces[27], [36]. Other less coordinated and less abundant topographic features such as kinks and steps (sec 5.1) may have larger contributions to the $CH_{4(g)}$ formation rates on Ni, Co and bimetallic NiCo catalysts that better explain their experimental performance. This study provides insight on the most relevant characteristics and differences of Ni, Co and alloyed Ni-Co surfaces, structural sensitivity, electronic effects of the alloy and catalytic consequences but further studies with less coordinated mono and bimetallic surfaces is recommended to fully explain the catalytic performance, activity and selectivity for the methanation reaction on bimetallic surfaces.

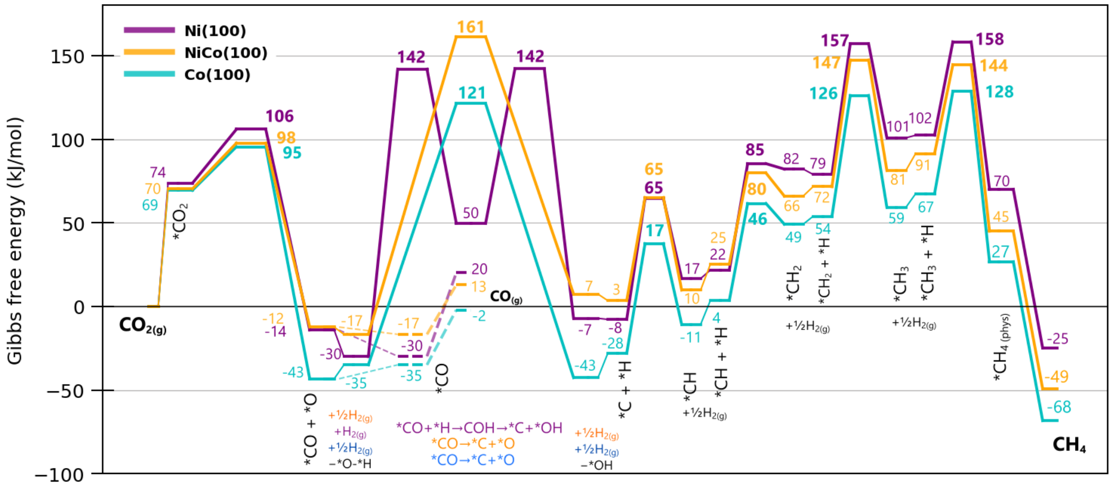

Fig. 43 Gibbs free energy reaction profile for the $CO_{2(g)}$ hydrogenation to methane (solid lines, 1 kPa $CO_{2(g)}$, 25 kPa $H_{2(g)}$, 265 °C, $CH_{4(g)}$ at 1kPa) on (100) surfaces. Cyan: Co(100), orange: NiCo(100) and purple: Ni(100).

9. Concluding remarks

9.1 Outcome from objectives and hypothesis validation

Experimental and theoretical techniques were applied to study the catalytic performance of monometallic Ni and Co, and bimetallic NiCo catalysts, in accordance to the **general objective** of this work. The specific objectives previously defined (SO in sec. 3.1) guided the experimental and theoretical approaches taken through all sections in this work (sec. 5-8), more specifically:

SO1. Kinetic, isotopic and spectroscopic studies were performed for the synthetized mono and bimetallic catalysts under methanation conditions, fulfilling the experimental specific objective of this work (SO1, sec. 3.1). The kinetic study confirmed the stability of the catalysts and provided a direct characterization of their catalytic performance in which the bimetallic catalysts were found to exhibit lower activity and selectivity towards the formation of $CH_{4(g)}$ compared to monometallic Ni and Co supported catalysts. On the other hand, the isotopic and spectroscopic studies provided insight on the reaction mechanism and relevant surface species. Isotopic H_2/D_2 exchange evidenced the participation of H in the rate determinant steps for the methanation reaction but not for the undesired $CO_{(g)}$ formation. Spectroscopic FTIR results indicated that the direct dissociation of $*CO_2$ species is possible, under methanation conditions FTIR results showed the abundance of carbonyl as a reaction intermediate with distinctive adsorption modes according to the surface composition and helped to rule out the participation of other surface species (e.g., *HCOO). Analysis of these results also provided valuable insight to direct the theoretical simulation.

SO2. A complete catalytic cycle including three possible *CO activation routes was simulated using Density Functional Theory and six model surfaces: Ni, Co and NiCo compositions, with (111) and (100) surface geometries. Reaction energies and activation barriers were computed for every reaction step under consideration, fulfilling the specific objective for the simulation of reaction pathways (SO2, sec. 3.1) and allowing the construction of reaction energy profiles. These profiles suggested an abundance of carbonyl intermediate (in agreement with SO1 results) and the kinetic relevance of the *CO activation and final hydrogenations towards methane. Profiles for the (111) surfaces showed similar features for all surface compositions but higher barriers (by >50kJ/mol) and distinctively different features than the (100) profiles. Methanation barriers in both profiles are significantly greater (>40 kJ/mol) than the experimental apparent reaction barriers. Higher methanation barriers compared to the carbonyl desorption energies in the (111) and (100) profiles suggests high $CO_{(g)}$ selectivities that are not consistent with experiments. Possible explanations to take into consideration are, for example, that reaction routes not considered in this study may have greater contributions to the macroscopic reaction rates, that modifications to the theoretical approach may be necessary, or the reaction may take place on a different surface geometry.

SO3. Catalytic performance descriptors such as the d-band center and adsorption energy of key surface species were analyzed for the theoretically studied surfaces. d-band center shifts for Ni and Co atoms in their alloy (compared to monoatomic forms) evidence electronic differences with the monometallic surfaces and derived from the surface geometry. These descriptors are suitable for large scale screening but lack resolution for comparing the similar surfaces under study. Adsorption energies of C and O species are proposed as descriptors for the binding strength trends of most of the possible reaction intermediate species. More importantly for the focus of this work (and fulfilling SO3 in sec. 3.1), these descriptors are able to depict key features related to the catalytic performance from the surface composition and geometry such as (1) the greater oxophilicity of Co compared to Ni, (2) stronger binding of most adsorbed species to (100) rather than (111) surfaces and (3) the weaker interaction of adsorbates with NiCo(100) surfaces compared to the (100) monometallic surfaces, which evidences the structural sensitivity of the descriptor for the effects of the bimetallic alloy. These features were related theoretically suggested trends for the activity and stability and to experimentally observed trends of the catalytic performance of the studied catalysts.

Finally, the **hypothesis** that nickel-cobalt bimetallic phases have better catalytic performance for the $CO_{2(g)}$ methanation reaction compared to monometallic Ni and Co catalysts is probed to be **not correct**. Kinetic studies (SO1) directly shows for the bimetallic catalysts a lower intrinsic activity and selectivity towards the formation of $CH_{4(g)}$ under methanation conditions, compared to the monometallic phases.

9.2 Conclusions

Kinetic studies for the $CO_{2(g)}$ methanation reaction on Ni/SiO_2, Co/SiO_2 and Ni_xCo_{1-x}/SiO_2 showed that Co catalysts have the highest activity but lower selectivity towards $CH_{4(g)}$ compared to the Ni catalysts. $CO_{(g)}$ formation rates scale linearly with the Co content of the catalyst. Ni_xCo_{1-x}/SiO_2 catalysts are less active under CO_2 methanation conditions than the monometallic Ni/SiO_2 and Co/SiO_2 catalyst and showed the highest selectivity towards $CO_{(g)}$ (undesired product), contradicting the hypothesis of this work. Similar activation energies and reaction orders show that the reaction mechanism does not change within the studied reaction conditions for each catalysts. Apparent reaction orders and H_2/D_2 kinetic isotope effects indicate that $H_{2(g)}$ is involved in the rate determining steps for the $CH_{4(g)}$ formation while only $CO_{2(g)}$ is involved in the $CO_{(g)}$ formation indicating a route not assisted by H for $CO_{(g)}$. $CO_{2(g)}$ was observed to form *CO on the catalysts surfaces without $H_{2(g)}$ feed, further supporting a direct $CO_{2(g)}$ dissociation as the main source of carbonyl. Spectroscopic experiments (MS coupled FTIR) showed a predominant population of *CO directly related to the reaction rates under methanation conditions, other identified species are considered to act as spectators (*HCOO) or to rapidly dissociate (*CO_3). Different adsorption modes for *CO are characteristic of the surface composition, multi-bond modes on Ni/SiO_2, linear on Co/SiO_2 and similar proportions of linear and multi-bonded *CO interconverting on $Ni_{0.5}Co_{0.5}/SiO_2$.

DFT studies provided insight about possible descriptors of the catalytic performance and on the effects of the Ni-Co alloy, which are significantly dependent on the specific site geometries and their local composition. DFT confirms that *CO binds multi-bonded and more strongly to Ni (111) and (100) surfaces compared to bimetallic and Co surfaces where linear modes are preferred. Compared to (111), (100) surfaces bind most reaction intermediates more strongly due to the low coordination of four fold sites, in particular, a stronger binding of *C inhibits its hydrogenation and migration rendering (100) surfaces more susceptible to C poisoning. Ni surfaces adsorb *C and other C-binding species more strongly than Co and NiCo surfaces, and are commonly deactivated by C poisoning, but Co surfaces stabilize better *O and O-binding species, which explains their usual deactivation by oxidation and requiring harsher reduction conditions. NiCo surfaces show significant differences in adsorption strength related to the site geometry and local composition. Co atoms help to stabilize adsorbates and transition states by interacting with O atoms and C—H bonds (agostic interactions), though NiCo(100) shows a weaker adsorption of C-binding species compared to other (100) surfaces. These differences in surface geometry and composition for the adsorption energy of most surface species is well represented by the adsorption strength of *C and *O, which are suggested as activity and selectivity descriptors. Mapping these descriptors evidences the structural sensibility and oxophilicity differences (key factors for the catalytic performance) and suggests a similar behavior of NiCo and Co (111) surfaces consistent with experimental observations.

Studying the reaction mechanism via DFT, RPBE calculations overestimate $CO_{2(g)}$ adsorption energies but show moderate *CO_2 activation energies supporting its direct dissociation. Lower *CO_2 activation barriers on Co and NiCo surfaces are associated to geometric factors and the stabilization of *O in activated and final states, consistent with their higher $CO_{(g)}$ formation activity. *CO activates on (111) surfaces via H-assisted pathways. The HCO route shows lower barriers than the COH and direct routes, with the *CO hydrogenation and *HC—O dissociation as the most kinetically relevant steps and the highest reaction barriers. NiCo(111) shows lower barriers than Ni(111) but higher than Co(111). Reaction profiles show *CO as the most stable and probably most abundant surface intermediate in all (111) surfaces, but more weakly bound and prone to desorb as $CO_{(g)}$ on Co and NiCo than on Ni(111). Conversely, the HCO route has the highest barriers on (100) surfaces but still at least 40 kJ/mol lower than the (111) barriers. The COH and direct CO dissociation routes show the lowest CO activation barriers on Ni(100) and Co(100), respectively. Both of these routes have similarly high barriers on NiCo(100), though the *CH_2 and *CH_3 hydrogenations are the highest barriers for the (100) monometallics. *C and *OH species appear as highly stable intermediates (close to *CO) but are inhibited to reform and desorb as $CO_{(g)}$ or further hydrogenate towards $CH_{4(g)}$ by their high activation barriers. (111) and (100) surfaces show adsorption and activation trends consistent with the experimental $CO_{(g)}$ formation, but also show unfavorable $CO_{2(g)}$ adsorptions and high *C-O activation barriers compared to the $CO_{(g)}$ desorption and the experimental apparent activation energies for the methanation reaction. This suggests that the methane formation is mostly inhibited on the simulated surfaces and that other surface geometries may have larger contributions and better explain the observed trends for the methanation rates on Ni, Co and bimetallic Ni-Co catalysts.

This work disproves the hypothesis of an enhanced catalytic performance (activity and selectivity) of NiCo catalysts compared to Ni and Co catalysts for the $CO_{2(g)}$ methanation reaction, but offers insight on fundamental aspects of Ni, Co and NiCo surfaces that define their catalytic performance and provides a detailed workflow for theoretical-experimental studies in heterogeneous catalytic systems. Further studies focused on the structural sensitivity and the role of less coordinated surfaces are recommended for a better understanding of the behavior of mono and bimetallic Ni-Co catalysts under $CO_{2(g)}$ methanation conditions.

10. References

[1] D. Schmider, L. Maier, and O. Deutschmann, “Reaction Kinetics of CO and CO2 Methanation over Nickel,” *Ind. Eng. Chem. Res.*, vol. 60, no. 16, pp. 5792–5805, Apr. 2021, doi: 10.1021/acs.iecr.1c00389.

[2] S. Rönsch *et al.*, “Review on methanation – From fundamentals to current projects,” *Fuel*, vol. 166, pp. 276–296, Feb. 2016, doi: 10.1016/j.fuel.2015.10.111.

[3] W. Luo and A. Asthagiri, “Density Functional Theory Study of Methanol Steam Reforming on Co(0001) and Co(111) Surfaces,” *J. Phys. Chem. C*, vol. 118, no. 28, pp. 15274–15285, Jul. 2014, doi: 10.1021/jp503177h.

[4] B. Miao, S. S. K. Ma, X. Wang, H. Su, and S. H. Chan, “Catalysis mechanisms of CO2 and CO methanation,” *Catal. Sci. Technol.*, vol. 6, no. 12, pp. 4048–4058, Jun. 2016, doi: 10.1039/C6CY00478D.

[5] H. Muroyama *et al.*, “Carbon dioxide methanation over Ni catalysts supported on various metal oxides,” *J. Catal.*, vol. 343, pp. 178–184, Nov. 2016, doi: 10.1016/j.jcat.2016.07.018.

[6] C. Hernández Mejía, J. E. S. van der Hoeven, P. E. de Jongh, and K. P. de Jong, “Cobalt–Nickel Nanoparticles Supported on Reducible Oxides as Fischer–Tropsch Catalysts,” *ACS Catal.*, vol. 10, no. 13, pp. 7343–7354, Jul. 2020, doi: 10.1021/acscatal.0c00777.

[7] F. Villagra-Soza, “Aspectos Mecanísticos de la Metanación de CO2 sobre Catalizadores Bimetálicos Ni-Co,” University of Concepción, Concepción, Chile, 2022.

[8] A. Ashok, A. Kumar, R. Bhosale, M. A. Saleh Saad, F. AlMomani, and F. Tarlochan, “Study of ethanol dehydrogenation reaction mechanism for hydrogen production on combustion synthesized cobalt catalyst,” *Int. J. Hydrog. Energy*, vol. 42, no. 37, pp. 23464–23473, Sep. 2017, doi: 10.1016/j.ijhydene.2017.01.175.

[9] K. Takanabe, K. Nagaoka, K. Nariai, and K. Aika, “Titania-supported cobalt and nickel bimetallic catalysts for carbon dioxide reforming of methane,” *J. Catal.*, vol. 232, no. 2, pp. 268–275, Jun. 2005, doi: 10.1016/j.jcat.2005.03.011.

[10] S. Kocić, M. Corral Valero, J.-M. Schweitzer, and P. Raybaud, “Surface speciation of Co based Fischer-Tropsch catalyst under reaction conditions: Deactivation by coke or by oxidation?,” *Appl. Catal. Gen.*, vol. 590, p. 117332, Jan. 2020, doi: 10.1016/j.apcata.2019.117332.

[11] Z. Ou *et al.*, “Effect of active site and charge transfer on methane dehydrogenation over different Co doped Ni surfaces by density functional theory,” *Int. J. Hydrog. Energy*, vol. 45, no. 56, pp. 31849–31862, Nov. 2020, doi: 10.1016/j.ijhydene.2020.08.187.

[12] W. Tu, M. Ghoussoub, C. V. Singh, and Y.-H. C. Chin, “Consequences of Surface Oxophilicity of Ni, Ni-Co, and Co Clusters on Methane Activation,” *J. Am. Chem. Soc.*, vol. 139, no. 20, pp. 6928–6945, May 2017, doi: 10.1021/jacs.7b01632.

[13] K. Li, M. Jiao, Y. Wang, and Z. Wu, “CH4 dissociation on NiM(111) (M = Co, Rh, Ir) surface: A first-principles study,” *Surf. Sci.*, vol. 617, pp. 149–155, Nov. 2013, doi: 10.1016/j.susc.2013.08.004.

[14] L. H. Sprowl, B. M. Adam, J. D. Tucker, and L. Arnadottira, “First-principles study of the products of CO2 dissociation on nickel -based alloys: Trends in energetics with alloying element,” *Surf. Sci.*, vol. 677, pp. 219–231, Nov. 2018, doi: 10.1016/j.susc.2018.06.011.

[15] Y. Liu, H. Yang, Y. Liu, B. Jiang, J. Ding, and R. Woodward, “Thermally induced fcc to hcp martensitic transformation in Co–Ni,” *Acta Mater.*, vol. 53, no. 13, pp. 3625–3634, Aug. 2005, doi: 10.1016/j.actamat.2005.04.019.

[16] W. B. Pearson and L. T. Thompson, “The Lattice Spacings of Nickel Solid Solutions,” *Can. J. Phys.*, vol. 35, no. 4, pp. 349–357, Apr. 1957, doi: 10.1139/p57-040.

[17] A. Leba and R. Yıldırım, “Determining most effective structural form of nickel-cobalt catalysts for dry reforming of methane,” *Int. J. Hydrog. Energy*, vol. 45, no. 7, pp. 4268–4283, Feb. 2020, doi: 10.1016/j.ijhydene.2019.12.020.

[18] S. Chen and B. Yang, “Activity and stability of alloyed NiCo catalyst for the dry reforming of methane: A combined DFT and microkinetic modeling study,” *Catal. Today*, vol. 400–401, pp. 59–65, Sep. 2022, doi: 10.1016/j.cattod.2021.11.016.

[19] M. A. Vannice, “The catalytic synthesis of hydrocarbons from H2CO mixtures over the Group VIII metals: V. The catalytic behavior of silica-supported metals,” *J. Catal.*, vol. 50, no. 2, pp. 228–236, Nov. 1977, doi: 10.1016/0021-9517(77)90031-8.

[20] B. Hammer and J. K. Nørskov, “Why gold is the noblest of all the metals,” *Nature*, vol. 376, no. 6537, Art. no. 6537, Jul. 1995, doi: 10.1038/376238a0.

[21] J. K. Nørskov, T. Bligaard, J. Rossmeisl, and C. H. Christensen, “Towards the computational design of solid catalysts,” *Nat. Chem*, vol. 1, no. 1, pp. 37–46, Apr. 2009, doi: 10.1038/nchem.121.

[22] P. T. Lachkov and Y.-H. (Cathy) Chin, “Influence of Carbon and Oxygen Chemical Potentials on the Hydrogen Donor Identity During Methanation on Ni, Co, and Ni-Co Clusters,” *ChemCatChem*, vol. 11, no. 4, pp. 1244–1255, 2019, doi: https://doi.org/10.1002/cctc.201801545.

[23] M. P. Andersson *et al.*, “Toward computational screening in heterogeneous catalysis: Pareto-optimal methanation catalysts,” *J. Catal.*, vol. 239, no. 2, pp. 501–506, Apr. 2006, doi: 10.1016/j.jcat.2006.02.016.

[24] J. Cheng and P. Hu, “Utilization of the Three-Dimensional Volcano Surface To Understand the Chemistry of Multiphase Systems in Heterogeneous Catalysis,” *J Am Chem Soc*, vol. 130, no. 33, pp. 10868–10869, Aug. 2008, doi: 10.1021/ja803555g.

[25] A. J. Medford *et al.*, “Activity and Selectivity Trends in Synthesis Gas Conversion to Higher Alcohols,” *Top Catal*, vol. 57, no. 1, pp. 135–142, Feb. 2014, doi: 10.1007/s11244-013-0169-0.

[26] C. Vogt *et al.*, “Understanding carbon dioxide activation and carbon–carbon coupling over nickel,” *Nat. Commun.*, vol. 10, no. 1, Art. no. 1, Nov. 2019, doi: 10.1038/s41467-019-12858-3.

[27] P. Lozano-Reis, H. Prats, P. Gamallo, F. Illas, and R. Sayós, “Multiscale Study of the Mechanism of Catalytic CO2 Hydrogenation: Role of the Ni(111) Facets,” *ACS Catal.*, Jun. 2020, doi: 10.1021/acscatal.0c01599.

[28] Y.-A. Zhu, D. Chen, X.-G. Zhou, and W.-K. Yuan, “DFT studies of dry reforming of methane on Ni catalyst,” *Catal. Today*, vol. 148, no. 3, pp. 260–267, Nov. 2009, doi: 10.1016/j.cattod.2009.08.022.

[29] G. Peng, S. J. Sibener, G. C. Schatz, S. T. Ceyer, and M. Mavrikakis, “CO2 Hydrogenation to Formic Acid on Ni(111),” *J. Phys. Chem. C*, vol. 116, no. 4, pp. 3001–3006, Feb. 2012, doi: 10.1021/jp210408x.

[30] M. Zhou and B. Liu, “DFT Investigation on the Competition of the Water–Gas Shift Reaction Versus Methanation on Clean and Potassium-Modified Nickel(1 1 1) Surfaces,” *ChemCatChem*, vol. 7, no. 23, pp. 3928–3935, 2015, doi: 10.1002/cctc.201500547.

[31] J. Wang, Y. Kawazoe, Q. Sun, S. Chan, and H. Su, “The selectivity and activity of catalyst for CO hydrogenation to methanol and hydrocarbon: A comparative study on Cu, Co and Ni surfaces,” *Surf. Sci.*, vol. 645, pp. 30–40, Mar. 2016, doi: 10.1016/j.susc.2015.10.035.

[32] J.-X. Liu, H.-Y. Su, D.-P. Sun, B.-Y. Zhang, and W.-X. Li, “Crystallographic Dependence of CO Activation on Cobalt Catalysts: HCP versus FCC,” *J. Am. Chem. Soc.*, vol. 135, no. 44, pp. 16284–16287, Nov. 2013, doi: 10.1021/ja408521w.

[33] X. Liu, L. Sun, and W.-Q. Deng, “Theoretical Investigation of CO2 Adsorption and Dissociation on Low Index Surfaces of Transition Metals,” *J. Phys. Chem. C*, vol. 122, no. 15, pp. 8306–8314, Apr. 2018, doi: 10.1021/acs.jpcc.7b12660.

[34] H. Huang, Y. Yu, and M. Zhang, “Structure sensitivity of CH4 formation from successive hydrogenation of C on cobalt: Insights from density functional theory,” *Chem. Phys. Lett.*, vol. 737, p. 136824, Dec. 2019, doi: 10.1016/j.cplett.2019.136824.

[35] M. P. Andersson *et al.*, “Structure sensitivity of the methanation reaction: H2-induced CO dissociation on nickel surfaces,” *J. Catal.*, vol. 255, no. 1, pp. 6–19, Apr. 2008, doi: 10.1016/j.jcat.2007.12.016.

[36] E. B. Sterk *et al.*, “Structure Sensitivity of CO2 Conversion over Nickel Metal Nanoparticles Explained by Micro-Kinetics Simulations,” *JACS Au*, Oct. 2022, doi: 10.1021/jacsau.2c00430.

[37] C. Vogt *et al.*, “Unravelling structure sensitivity in CO 2 hydrogenation over nickel,” *Nat. Catal.*, vol. 1, no. 2, Art. no. 2, Feb. 2018, doi: 10.1038/s41929-017-0016-y.

[38] X. Guo, H. Liu, B. Wang, Q. Wang, and R. Zhang, “Insight into C + O(OH) reaction for carbon elimination on different types of CoNi(111) surfaces: a DFT study,” *RSC Adv.*, vol. 5, no. 26, pp. 19970–19982, Feb. 2015, doi: 10.1039/C4RA15555F.

[39] F. Studt, F. Abild-Pedersen, J. B. Varley, and J. K. Nørskov, “CO and CO2 Hydrogenation to Methanol Calculated Using the BEEF-vdW Functional,” *Catal. Lett.*, vol. 143, no. 1, pp. 71–73, Jan. 2013, doi: 10.1007/s10562-012-0947-5.

[40] A. J. R. Hensley *et al.*, “DFT-Based Method for More Accurate Adsorption Energies: An Adaptive Sum of Energies from RPBE and vdW Density Functionals,” *J. Phys. Chem. C*, vol. 121, no. 9, pp. 4937–4945, Mar. 2017, doi: 10.1021/acs.jpcc.6b10187.

[41] K. Lejaeghere *et al.*, “Reproducibility in density functional theory calculations of solids,” *Science*, Mar. 2016, doi: 10.1126/science.aad3000.

[42] S. E. Mason, I. Grinberg, and A. M. Rappe, “First-principles extrapolation method for accurate CO adsorption energies on metal surfaces,” *Phys. Rev. B*, vol. 69, no. 16, p. 161401, Apr. 2004, doi: 10.1103/PhysRevB.69.161401.

[43] M. Gajdo, A. Eichler, and J. Hafner, “CO adsorption on close-packed transition and noble metal surfaces: trends from ab initio calculations.,” *J. Phys. Condens. Matter*, vol. 16, no. 8, pp. 1141–1164, Feb. 2004, doi: 10.1088/0953-8984/16/8/001.

[44] J. Wellendorff *et al.*, “A benchmark database for adsorption bond energies to transition metal surfaces and comparison to selected DFT functionals,” *Surf. Sci.*, vol. 640, pp. 36–44, Oct. 2015, doi: 10.1016/j.susc.2015.03.023.

[45] P. E. Blöchl, “Projector augmented-wave method,” *Phys. Rev. B*, vol. 50, no. 24, pp. 17953–17979, Dec. 1994, doi: 10.1103/PhysRevB.50.17953.

[46] G. Kresse and D. Joubert, “From ultrasoft pseudopotentials to the projector augmented-wave method,” *Phys. Rev. B*, vol. 59, no. 3, pp. 1758–1775, Jan. 1999, doi: 10.1103/PhysRevB.59.1758.

[47] H. J. Monkhorst and J. D. Pack, “Special points for Brillouin-zone integrations,” *Phys. Rev. B*, vol. 13, no. 12, pp. 5188–5192, Jun. 1976, doi: 10.1103/PhysRevB.13.5188.

[48] B. Hammer and J. K. Nørskov, “Electronic factors determining the reactivity of metal surfaces,” *Surf. Sci.*, vol. 343, no. 3, pp. 211–220, Dec. 1995, doi: 10.1016/0039-6028(96)80007-0.

[49] W. Tang, E. Sanville, and G. Henkelman, “A grid-based Bader analysis algorithm without lattice bias,” *J. Phys. Condens. Matter*, vol. 21, no. 8, p. 084204, Jan. 2009, doi: 10.1088/0953-8984/21/8/084204.

[50] T. A. Manz and N. G. Limas, “Introducing DDEC6 atomic population analysis: part 1. Charge partitioning theory and methodology,” *RSC Adv.*, vol. 6, no. 53, pp. 47771–47801, May 2016, doi: 10.1039/C6RA04656H.

[51] N. G. Limas and T. A. Manz, “Introducing DDEC6 atomic population analysis: part 2. Computed results for a wide range of periodic and nonperiodic materials,” *RSC Adv.*, vol. 6, no. 51, pp. 45727–45747, May 2016, doi: 10.1039/C6RA05507A.

[52] T. A. Manz, “Introducing DDEC6 atomic population analysis: part 3. Comprehensive method to compute bond orders,” *RSC Adv.*, vol. 7, no. 72, pp. 45552–45581, 2017, doi: 10.1039/C7RA07400J.

[53] P. Deshlahra, J. Conway, E. E. Wolf, and W. F. Schneider, “Influence of Dipole–Dipole Interactions on Coverage-Dependent Adsorption: CO and NO on Pt(111),” *Langmuir*, vol. 28, no. 22, pp. 8408–8417, Jun. 2012, doi: 10.1021/la300975s.

[54] D. Steele, “Infrared Spectroscopy: Theory,” in *Handbook of Vibrational Spectroscopy*, John Wiley & Sons, Ltd, 2006. doi: 10.1002/0470027320.s0103.

[55] D. A. McQuarrie and J. D. Simon, *Molecular Thermodynamics*. University Science Books, 1999.

[56] L. H. Sprowl, C. T. Campbell, and L. Árnadóttir, “Hindered Translator and Hindered Rotor Models for Adsorbates: Partition Functions and Entropies,” *J. Phys. Chem. C*, vol. 120, no. 18, pp. 9719–9731, May 2016, doi: 10.1021/acs.jpcc.5b11616.

[57] C. A. Schneider, W. S. Rasband, and K. W. Eliceiri, “NIH Image to ImageJ: 25 years of image analysis,” *Nat. Methods*, vol. 9, no. 7, Art. no. 7, Jul. 2012, doi: 10.1038/nmeth.2089.

[58] G. Kresse and J. Furthmüller, “Efficiency of ab-initio total energy calculations for metals and semiconductors using a plane-wave basis set,” *Comput. Mater. Sci.*, vol. 6, no. 1, pp. 15–50, Jul. 1996, doi: 10.1016/0927-0256(96)00008-0.

[59] G. Kresse and J. Furthmüller, “Efficient iterative schemes for ab initio total-energy calculations using a plane-wave basis set,” *Phys. Rev. B*, vol. 54, no. 16, pp. 11169–11186, Oct. 1996, doi: 10.1103/PhysRevB.54.11169.

[60] G. Kresse and J. Hafner, “Ab initio molecular dynamics for liquid metals,” *Phys. Rev. B*, vol. 47, no. 1, pp. 558–561, Jan. 1993, doi: 10.1103/PhysRevB.47.558.

[61] G. Kresse and J. Hafner, “Ab initio molecular-dynamics simulation of the liquid-metal--amorphous-semiconductor transition in germanium,” *Phys. Rev. B*, vol. 49, no. 20, pp. 14251–14269, May 1994, doi: 10.1103/PhysRevB.49.14251.

[62] B. Hammer, L. B. Hansen, and J. K. Nørskov, “Improved adsorption energetics within density-functional theory using revised Perdew-Burke-Ernzerhof functionals,” *Phys. Rev. B*, vol. 59, no. 11, pp. 7413–7421, Mar. 1999, doi: 10.1103/PhysRevB.59.7413.

[63] M. Methfessel and A. T. Paxton, “High-precision sampling for Brillouin-zone integration in metals,” *Phys. Rev. B*, vol. 40, no. 6, pp. 3616–3621, Aug. 1989, doi: 10.1103/PhysRevB.40.3616.

[64] V. G. Tyuterev and N. Vast, “Murnaghan’s equation of state for the electronic ground state energy,” *Comput. Mater. Sci.*, vol. 38, no. 2, pp. 350–353, Dec. 2006, doi: 10.1016/j.commatsci.2005.08.012.

[65] J. M. Rahm and P. Erhart, “WulffPack: A Python package for Wulff constructions,” *J. Open Source Softw.*, vol. 5, no. 45, p. 1944, Jan. 2020, doi: 10.21105/joss.01944.

[66] R. Tran *et al.*, “Surface energies of elemental crystals,” *Sci. Data*, vol. 3, no. 1, Art. no. 1, Sep. 2016, doi: 10.1038/sdata.2016.80.

[67] G. Henkelman, B. P. Uberuaga, and H. Jónsson, “A climbing image nudged elastic band method for finding saddle points and minimum energy paths,” *J. Chem. Phys.*, vol. 113, no. 22, pp. 9901–9904, Dec. 2000, doi: 10.1063/1.1329672.

[68] G. Henkelman and H. Jónsson, “A dimer method for finding saddle points on high dimensional potential surfaces using only first derivatives,” *J. Chem. Phys.*, vol. 111, no. 15, pp. 7010–7022, Oct. 1999, doi: 10.1063/1.480097.

[69] H. Meltzman, D. Chatain, D. Avizemer, T. Besmann, and W. Kaplan, “The equilibrium crystal shape of nickel,” *Acta Mater.*, vol. 59, pp. 3473–3483, 2011.

[70] O. Kitakami, H. Sato, Y. Shimada, F. Sato, and M. Tanaka, “Size effect on the crystal phase of cobalt fine particles,” *Phys. Rev. B*, vol. 56, no. 21, pp. 13849–13854, Dec. 1997, doi: 10.1103/PhysRevB.56.13849.

[71] E. A. Owen and D. M. Jones, “Effect of Grain Size on the Crystal Structure of Cobalt,” *Proc. Phys. Soc. Sect. B*, vol. 67, no. 6, p. 456, Jun. 1954, doi: 10.1088/0370-1301/67/6/302.

[72] J. M. Wills and W. A. Harrison, “Interionic interactions in transition metals,” *Phys. Rev. B*, vol. 28, no. 8, pp. 4363–4373, Oct. 1983, doi: 10.1103/PhysRevB.28.4363.

[73] F. Chiter, V. B. Nguyen, N. Tarrat, M. Benoit, H. Tang, and C. Lacaze-Dufaure, “Effect of van der Waals corrections on DFT-computed metallic surface properties,” *Mater. Res. Express*, vol. 3, no. 4, p. 046501, Apr. 2016, doi: 10.1088/2053-1591/3/4/046501.

[74] J. Klimeš, D. R. Bowler, and A. Michaelides, “Van der Waals density functionals applied to solids,” *Phys. Rev. B*, vol. 83, no. 19, p. 195131, May 2011, doi: 10.1103/PhysRevB.83.195131.

[75] W.-B. Zhang, C. Chen, and S.-Y. Zhang, “Equilibrium Crystal Shape of Ni from First Principles,” *J. Phys. Chem. C*, vol. 117, no. 41, pp. 21274–21280, Oct. 2013, doi: 10.1021/jp404569m.

[76] J. Ren, H. Guo, J. Yang, Z. Qin, J. Lin, and Z. Li, “Insights into the mechanisms of CO2 methanation on Ni(111) surfaces by density functional theory,” *Appl. Surf. Sci.*, vol. 351, pp. 504–516, Oct. 2015, doi: 10.1016/j.apsusc.2015.05.173.

[77] Z. Han, Z. Yang, and M. Han, “Comprehensive investigation of methane conversion over Ni(111) surface under a consistent DFT framework: Implications for anti-coking of SOFC anodes,” *Appl. Surf. Sci.*, vol. 480, pp. 243–255, Jun. 2019, doi: 10.1016/j.apsusc.2019.02.084.

[78] R. C. Catapan, A. A. M. Oliveira, Y. Chen, and D. G. Vlachos, “DFT Study of the Water–Gas Shift Reaction and Coke Formation on Ni(111) and Ni(211) Surfaces,” *J. Phys. Chem. C*, vol. 116, no. 38, pp. 20281–20291, Sep. 2012, doi: 10.1021/jp302488f.

[79] H. Liu, R. Zhang, R. Yan, B. Wang, and K. Xie, “CH4 dissociation on NiCo (111) surface: A first-principles study,” *Appl. Surf. Sci.*, vol. 257, no. 21, pp. 8955–8964, Aug. 2011, doi: 10.1016/j.apsusc.2011.05.073.

[80] J. Li, E. Croiset, and L. Ricardez-Sandoval, “Methane dissociation on Ni (100), Ni (111), and Ni (553): A comparative density functional theory study,” *J. Mol. Catal. Chem.*, vol. 365, pp. 103–114, Dec. 2012, doi: 10.1016/j.molcata.2012.08.016.

[81] T. Jiang *et al.*, “Trends in CO Oxidation Rates for Metal Nanoparticles and Close-Packed, Stepped, and Kinked Surfaces,” *J. Phys. Chem. C*, vol. 113, no. 24, pp. 10548–10553, Jun. 2009, doi: 10.1021/jp811185g.

[82] J.-X. Liu, H.-Y. Su, and W.-X. Li, “Structure sensitivity of CO methanation on Co (0001), (1 0 $\bar{1}$ 2) and (1 1 2 0) surfaces: Density functional theory calculations,” *Catal. Today*, vol. 215, pp. 36–42, Oct. 2013, doi: 10.1016/j.cattod.2013.04.024.

[83] S. Chen, J. Zaffran, and B. Yang, “Dry reforming of methane over the cobalt catalyst: Theoretical insights into the reaction kinetics and mechanism for catalyst deactivation,” *Appl. Catal. B Environ.*, vol. 270, p. 118859, Aug. 2020, doi: 10.1016/j.apcatb.2020.118859.

[84] Y. Wong *et al.*, “Dry Reforming of Methane on Cobalt Catalysts: DFT-Based Insights into Carbon Deposition Versus Removal,” *J. Phys. Chem. C*, vol. 125, no. 40, pp. 21902–21913, Oct. 2021, doi: 10.1021/acs.jpcc.1c04819.

[85] K. Yang, M. Zhang, and Y. Yu, “Effect of transition metal-doped Ni(211) for CO dissociation: Insights from DFT calculations,” *Appl. Surf. Sci.*, vol. 399, pp. 255–264, Mar. 2017, doi: 10.1016/j.apsusc.2016.12.073.

[86] J. Gao, C. Jia, M. Zhang, F. Gu, G. Xu, and F. Su, “Effect of nickel nanoparticle size in Ni/α-Al2O3 on CO methanation reaction for the production of synthetic natural gas,” *Catal. Sci. Technol.*, vol. 3, no. 8, pp. 2009–2015, Jul. 2013, doi: 10.1039/C3CY00139C.

[87] V. Iablokov *et al.*, “Size-Controlled Model Co Nanoparticle Catalysts for CO2 Hydrogenation: Synthesis, Characterization, and Catalytic Reactions,” *Nano Lett.*, vol. 12, no. 6, pp. 3091–3096, Jun. 2012, doi: 10.1021/nl300973b.

[88] D. Beierlein *et al.*, “Is the CO2 methanation on highly loaded Ni-Al2O3 catalysts really structure-sensitive?,” *Appl. Catal. B Environ.*, vol. 247, pp. 200–219, Jun. 2019, doi: 10.1016/j.apcatb.2018.12.064.

[89] A. H. Larsen *et al.*, “The atomic simulation environment—a Python library for working with atoms,” *J. Phys. Condens. Matter*, vol. 29, no. 27, p. 273002, 2017.

[90] S. R. Bahn and K. W. Jacobsen, “An object-oriented scripting interface to a legacy electronic structure code,” *Comput Sci Eng*, vol. 4, no. 3, pp. 56–66, Jun. 2002, doi: 10.1109/5992.998641.

[91] H. Huang, Y. Yu, and M. Zhang, “Mechanistic insight into methane dry reforming over cobalt: a density functional theory study,” *Phys. Chem. Chem. Phys.*, vol. 22, no. 46, pp. 27320–27331, Dec. 2020, doi: 10.1039/C9CP07003F.

[92] M. T. Gorzkowski and A. Lewera, “Probing the Limits of d-Band Center Theory: Electronic and Electrocatalytic Properties of Pd-Shell–Pt-Core Nanoparticles,” *J. Phys. Chem. C*, vol. 119, no. 32, pp. 18389–18395, Aug. 2015, doi: 10.1021/acs.jpcc.5b05302.

[93] G. Cheng and T. Guo, “Surface Segregation in Ni/Co Bimetallic Nanoparticles Produced in Single-Walled Carbon Nanotube Synthesis,” *J. Phys. Chem. B*, vol. 106, no. 23, pp. 5833–5839, Jun. 2002, doi: 10.1021/jp025530r.

[94] M. J. Piotrowski *et al.*, “Theoretical Study of the Structural, Energetic, and Electronic Properties of 55-Atom Metal Nanoclusters: A DFT Investigation within van der Waals Corrections, Spin–Orbit Coupling, and PBE+U of 42 Metal Systems,” *J. Phys. Chem. C*, vol. 120, no. 50, pp. 28844–28856, Dec. 2016, doi: 10.1021/acs.jpcc.6b10404.

[95] F. Villagra-Soza, S. Godoy, A. Karelovic, and R. Jiménez, “Scrutinizing the mechanism of CO2 hydrogenation over Ni, CO and bimetallic NiCo surfaces: Isotopic measurements, operando-FTIR experiments and kinetics modelling,” *J. Catal.*, vol. 414, pp. 1–15, 2022, doi: https://doi.org/10.1016/j.jcat.2022.08.018.

[96] F. Abild-Pedersen and M. P. Andersson, “CO adsorption energies on metals with correction for high coordination adsorption sites – A density functional study,” *Surf. Sci.*, vol. 601, no. 7, pp. 1747–1753, Apr. 2007, doi: 10.1016/j.susc.2007.01.052.

[97] A. Eichler, “CO adsorption on Ni(111)––a density functional theory study,” *Surf. Sci.*, vol. 526, no. 3, pp. 332–340, Mar. 2003, doi: 10.1016/S0039-6028(02)02682-1.

[98] X. Ma, A. Genest, L. Spanu, and N. Rösch, “Structures and vibrational frequencies of CO adsorbed on transition metals from calculations using the vdW-DF2 functional,” *Comput. Theor. Chem.*, vol. 1069, pp. 147–154, Oct. 2015, doi: 10.1016/j.comptc.2015.07.013.

[99] B. E. Nieuwenhuys, “Adsorption and reactions of CO, NO, H2 and O2 on group VIII metal surfaces,” *Surf. Sci.*, vol. 126, no. 1, pp. 307–336, Mar. 1983, doi: 10.1016/0039-6028(83)90726-4.

[100] R. M. Watwe, H. S. Bengaard, J. R. Rostrup-Nielsen, J. A. Dumesic, and J. K. Nørskov, “Theoretical Studies of Stability and Reactivity of CHx Species on Ni(111),” *J. Catal.*, vol. 189, no. 1, pp. 16–30, Jan. 2000, doi: 10.1006/jcat.1999.2699.

[101] S.-G. Wang, D.-B. Cao, Y.-W. Li, J. Wang, and H. Jiao, “CH4 dissociation on Ni surfaces: Density functional theory study,” *Surf. Sci.*, vol. 600, no. 16, pp. 3226–3234, Aug. 2006, doi: 10.1016/j.susc.2006.06.008.

[102] D. Cheng, G. Barcaro, J.-C. Charlier, M. Hou, and A. Fortunelli, “Homogeneous Nucleation of Graphitic Nanostructures from Carbon Chains on Ni(111),” *J. Phys. Chem. C*, vol. 115, no. 21, pp. 10537–10543, Jun. 2011, doi: 10.1021/jp2028092.

[103] A. Nandula, Q. T. Trinh, M. Saeys, and A. N. Alexandrova, “Origin of Extraordinary Stability of Square-Planar Carbon Atoms in Surface Carbides of Cobalt and Nickel,” *Angew. Chem. Int. Ed.*, vol. 54, no. 18, pp. 5312–5316, 2015, doi: 10.1002/anie.201501049.

[104] K. Fei Tan, J. Xu, J. Chang, A. Borgna, and M. Saeys, “Carbon deposition on Co catalysts during Fischer–Tropsch synthesis: A computational and experimental study,” *J. Catal.*, vol. 274, no. 2, pp. 121–129, Sep. 2010, doi: 10.1016/j.jcat.2010.06.008.

[105] J. E. Mueller, A. C. T. van Duin, and W. A. Goddard, “Structures, Energetics, and Reaction Barriers for CHx Bound to the Nickel (111) Surface,” *J. Phys. Chem. C*, vol. 113, no. 47, pp. 20290–20306, Nov. 2009, doi: 10.1021/jp810555y.

[106] J. Robinson and D. P. Woodruff, “The local adsorption geometry of CH3 and NH3 on Cu(111): a density functional theory study,” *Surf. Sci.*, vol. 498, no. 3, pp. 203–211, Feb. 2002, doi: 10.1016/S0039-6028(01)01769-1.

[107] F. Abild-Pedersen *et al.*, “Scaling Properties of Adsorption Energies for Hydrogen-Containing Molecules on Transition-Metal Surfaces,” *Phys. Rev. Lett.*, vol. 99, no. 1, p. 016105, Jul. 2007, doi: 10.1103/PhysRevLett.99.016105.

[108] O. Mohan, Q. T. Trinh, A. Banerjee, and S. H. Mushrif, “Predicting CO2 adsorption and reactivity on transition metal surfaces using popular density functional theory methods,” *Mol. Simul.*, vol. 45, no. 14–15, pp. 1163–1172, Oct. 2019, doi: 10.1080/08927022.2019.1632448.

[109] A. A. Peterson, F. Abild-Pedersen, F. Studt, J. Rossmeisl, and J. K. Nørskov, “How copper catalyzes the electroreduction of carbon dioxide into hydrocarbon fuels,” *Energy Environ. Sci.*, vol. 3, no. 9, pp. 1311–1315, Aug. 2010, doi: 10.1039/C0EE00071J.

[110] S.-G. Wang *et al.*, “Factors Controlling the Interaction of CO2 with Transition Metal Surfaces,” *J. Phys. Chem. C*, vol. 111, no. 45, pp. 16934–16940, Nov. 2007, doi: 10.1021/jp074570y.

[111] K. Czelej, K. Cwieka, and K. J. Kurzydlowski, “CO2 stability on the Ni low-index surfaces: van der Waals corrected DFT analysis,” *Catal. Commun.*, vol. 80, pp. 33–38, May 2016, doi: 10.1016/j.catcom.2016.03.017.

[112] A. Álvarez *et al.*, “CO2 Activation over Catalytic Surfaces,” *ChemPhysChem*, vol. 18, no. 22, pp. 3135–3141, 2017, doi: 10.1002/cphc.201700782.

[113] D. W. Blaylock, T. Ogura, W. H. Green, and G. J. O. Beran, “Computational Investigation of Thermochemistry and Kinetics of Steam Methane Reforming on Ni(111) under Realistic Conditions,” Feb. 2009, doi: 10.1021/jp806527q.

[114] J. Greeley and M. Mavrikakis, “Surface and Subsurface Hydrogen: Adsorption Properties on Transition Metals and Near-Surface Alloys,” *J. Phys. Chem. B*, vol. 109, no. 8, pp. 3460–3471, Mar. 2005, doi: 10.1021/jp046540q.

[115] X. Hao, Q. Wang, D. Li, R. Zhang, and B. Wang, “The adsorption and dissociation of methane on cobalt surfaces: thermochemistry and reaction barriers,” *Rsc Adv.*, vol. 4, no. 81, pp. 43004–43011, 2014, doi: 10.1039/c4ra04050c.

[116] Z. Bian and S. Kawi, “Highly carbon-resistant Ni–Co/SiO2 catalysts derived from phyllosilicates for dry reforming of methane,” *J. CO2 Util.*, vol. 18, pp. 345–352, Mar. 2017, doi: 10.1016/j.jcou.2016.12.014.

[117] H. S. Bengaard *et al.*, “Steam Reforming and Graphite Formation on Ni Catalysts,” *J. Catal.*, vol. 209, no. 2, pp. 365–384, Jul. 2002, doi: 10.1006/jcat.2002.3579.

[118] X. Hao, B. Wang, Q. Wang, R. Zhang, and D. Li, “Insight into both coverage and surface structure dependent CO adsorption and activation on different Ni surfaces from DFT and atomistic thermodynamics,” *Phys. Chem. Chem. Phys.*, vol. 18, no. 26, pp. 17606–17618, Jun. 2016, doi: 10.1039/C6CP01689H.

[119] M. Zhou and B. Liu, “First-Principles Investigation of Adsorbate–Adsorbate Interactions on Ni(111), Ni(211), and Ni(100) Surfaces,” *Ind. Eng. Chem. Res.*, vol. 56, no. 20, pp. 5813–5820, May 2017, doi: 10.1021/acs.iecr.7b00447.

[120] G. T. K. K. Gunasooriya, A. P. van Bavel, H. P. C. E. Kuipers, and M. Saeys, “CO adsorption on cobalt: Prediction of stable surface phases,” *Surf. Sci.*, vol. 642, pp. L6–L10, Dec. 2015, doi: 10.1016/j.susc.2015.06.024.

11. Appendix

A1 Additional methodology information

A1.1 Treating low vibrational frequencies

The default displacement is 0.015 Å and is generally assumed to map a harmonic-like region of the potential energy surface around relaxed or transition states. In some problematic cases, secondary small or extra imaginary frequencies are produced (absolute value > 100 cm^{-1}). Instead of representing atomic vibrations, these frequencies were attributed to numerical uncertainties or an inappropriate mapping of the PES outside the harmonic region more associated to hindered translational or rotational movements. Reducing or increasing the distance for the finite displacements helped in some cases to eliminate the extra imaginary frequencies, with little effect on the larger real frequencies ($>$150 cm^{-1}) and on the large imaginary frequency associated with the reaction coordinate ($<-$150cm^{-1}). The small frequencies, conversely, are strongly affected by the step size. While too-large displacements may fall outside the harmonic region, too-small displacements may not be long enough to map the harmonic region, and there is not a way to determine the appropriate distance in every case for every degree of freedom a priori besides trial and error. Values of the small frequencies are therefore an important source of uncertainty that most DFT studies must consider.

It is outside the scope of this work to accomplish an accurate estimation of small frequencies, but those frequencies constitute a major contribution to the vibrational entropy of the system used to estimate free energy (see next section). In this work, the approach taken for troubling cases was to test larger ($<$0.02 Å) and smaller step distances (0.005–0.002 Å) and then simply to replace the ill-estimated low, real, or imaginary frequencies with a frequency of 100 cm^{-1}. This simple approach has been thoroughly discussed elsewhere[56] and is effective to avoid artificially high entropy contributions for the free energy calculations, correcting hindered translations/rotations with the equivalent harmonic oscillator contributions.

Table S1 Example effect of finite displacement on the vibrational frequencies.

System	Finite displacement (Å)	Computed frequencies (cm−1)
Transition state on Co(111) for $CH_3+H \rightarrow CH_4$	0.015	(…), 344, 121, 89, −45, −919 (reaction)
	0.003	(…), 338, 70, 50, 16, −915 (reaction)
Transition state on NiCo(111) for $CH_3+H \rightarrow CH_4$	0.015	(…), 307, 126, 103, −63, −904 (reaction)
	0.003	(…), 311, 145, 138, 71, −901 (reaction)
Transition state on Ni(111) for $CH_3+H \rightarrow CH_4$	0.015	(…), 325, 132, 95, −30, −928 (reaction)
	0.003	(…), 327, 154, 145, −31, −906 (reaction)

A1.2 High Performance Computing (HPC)

DFT calculations ran in three HPC infrastructures, the majority in the National Laboratory of High-Performance Computing (NLHPC) and Kultrun-Astronomy Hybrid Cluster (Astronomy department, University of Concepción), for which some parameters are provided below. Performance was tuned and checked through a tracking script (Tracker.py, in the VASP tools), the relevant parameter is the total computational time per electronic iteration, i.e., time*# of cores/# of scf iterations (in seconds, s_t/scf). When possible, k-point parallelization was implemented with an integer divider of the total number of k-points, e.g., 4x4x1 MP-meshes with 8-points total (see IBZKP file) allow 2, 4 and 8 partitions with increasing memory requirements.

- **NLHPC:** Most pre-convergence and exploratory calculations ran in the "slims" partition (nodes with 2x Intel Xeon E5-2660v2 processors, 2.2 GHz, 20 cores/node) between 100-300 s_t/scf. Final relaxations and frequency calculations ran in the "general" partition (Intel nodes, 44 cores each, 2xIntel Xeon Gold 6152 CPU, 2.1 GHz, 187 GB) using a full node (44 cores) for 2 k-points in parallel (KPAR=2) and 2 bands in parallel (NPAR=2), i.e., 22 cores/k-point and 11 cores/band at around 400-600 s_t/scf. Exploratory neb with 8 images used 4 slim nodes (80 cores, 10 cores/node) for 1-2 k-points with 2 bands in parallel (NPAR=2, 2 cores/band).
- **Kultrun (Kutral_AMD partition):** 2 AMD nodes, 32 cores each, 2xAMD Naples (Epyc) 2.2 GHz, 64 GB RAM, 4 TB HDD. Relaxation and frequency calculations ran in a full node (32 cores) parallelizing 2 k-points (KPAR=2) and 2 bands within (NPAR=2), i.e., 16 cores/ k-point and 8 cores/band. A full calculation run between 900-1300 s_t/scf, that is an observed time of <1 min per iteration. Exploratory neb calculations used a single point (two at most) and 8 images (4 cores per image) with no more than two bands in parallel (NPAR=2, 2 cores/band).

A1.3 Cut-off energy and vacuum convergence test

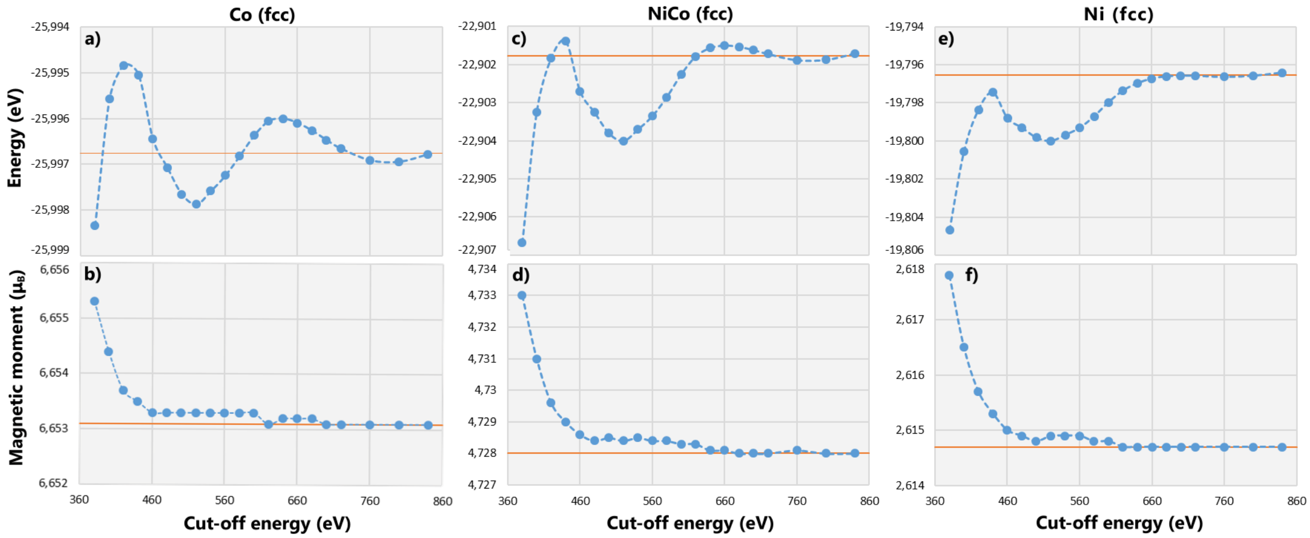

Fig. S1 Convergence of the total energy (a,c,e) and magnetic moment (b,d,f) of Co, Ni and NiCo fcc models with the cutoff energy. Orange lines show average of last five values with highest cutoff energies

Fig. S1 shows an appropriate convergence of the total energy and magnetic moments with respect to the cut-off energies used in this work. Table S2 shows the difference in electronic energy for a clean and CO_t adsorbed Co(111) surfaces with different vacuum spaces between slabs to test the sufficiency of the ~15Å vacuum used in this work. Co surfaces were conservatively selected for this test for the larger volume of the Co atoms. Table S2 shows differences smaller than 0.01 eV (~ 1 kJ/mol), without consistent sign and in the range of expected differences from the geometric convergence criteria (forces < 0.02 eV/Å) used in this work indicating a negligible effect of adding more vacuum in the context of the exploration of reaction profiles.

Table S2 Convergence test for the vacuum in relaxed slab models (clean and adsorbed). Differences in electronic energy with respect to a 20.18Å vacuum (considered the least affected by slab interaction of the studied cases)

	Electronic energy differences (eV) with respect to a 20.18 Å vacuum			
Vacuum	10.18 Å	12.68 Å	16.18 Å	17.68 Å
Clean Co(111) surface	+0.00153733	-0.00055190	+0.00114686	-0.00235325
Co(111)/CO_t	+0.00441604	-0.00054618	+0.00474777	-0.00158727

A1.4 Dispersion corrections

Dispersion corrections deal with long range interaction poorly described by DFT calculations alone and become a relevant contribution to the energy and forces in the description of loosely interacting structures (e.g., graphitic layers) weak chemisortions or the interaction between close adsorbates. For the large surface model (unless explicitly defined) low coverages are simulated for which adsorbate-adsorbate long range interaction are expected to be minimal. However, the effects of including dispersion corrections were tested on Ni(111) surfaces for some key computations, besides the lattice parameter fitting discussed in sec. 5.1. The third iteration of the Grimme dispersion corrections with a Becke-Johnson damping function (D3BJ) was used as implemented in the VASP code. Unlike more complex options such as Tkatchenko-Scheffter methods (dependent on the charge density), Grimme corrections are only dependent on the geometry and only add a negligible computational time to the calculations.

Relaxation of clean surfaces with dispersion corrections further compressed the free top layers towards the bulk which in turn increased the estimated magnetic moment of surface Ni atoms to 0.75 μ_B. Testing the effect on reaction barriers, the forward (backward) activation barrier for the *CO direct dissociation on Ni(111) goes from 2.98 eV to 2.73 eV (from 1.24 eV to 1.20) when computed with D3BJ dispersion corrections, these differences suggest a significant stabilization particularly for the *CO. Dispersion corrections decreased the adsorption energy of *CO on hcp sites to -2.35 eV (from -1.54 eV without dispersion corrections) significantly overestimating the adsorption strength as discussed in sec. 7.2.1.1. The appropriate simulation of *CO species, their adsorption energies and trends was considered critical at the beginning of this work, and the significant difference from the D3BJ corrections led to not considering it further in the study.

Finally, note that D3BJ energy corrections can be quickly computed for the geometries relaxed without the dispersion corrections and added to their energies as a kind of "static dispersion correction". For Ni(111) surface used as example, this approach with static corrections result in a forward barrier of 2.72eV and backward barrier of 1.10 eV for the *CO activation and adsorption energy of -2.13. This indicates small differences (≲10 kJ/mol) for the surface reaction energies and moderate (≲22 kJ/mol) for the adsorption energy despite the geometrical differences of models relaxed with and without D3BJ force dispersion corrections.

A2 Catalyst structures

A2.1 Fitting of Murnaghan equation of state

Table S3 Fitting of RPBE bulk energies and volume to the Murnaghan equation of state.

Bulk	Fitted parameters				Lattice parameter (Å)		Bulk Modulus, B_0 (GPa)	
	V_0 (Å^3)	B_0 (eV/Å^3)	B_0' (-)	C_b (eV)	Fit	Exp.	Fit	Exp.
Ni	44.899556	1.087432	4.717617	-19.7979	3.5542	3.516 [16]	174.22	186 [72]
NiCo	44.810797	1.121328	4.986190	-22.9017	3.5519	3.527 [16]	179.66	-
Co	44.773515	1.161023	4.718196	-25.9935	3.5509	3.544 [71]	186.02	191[72]

A2.2 Bader atomic charges and magnetic moments

Table S4 Bader atomic average electronic charges and spin magnetic moments.

	Electronic charges (e)			Spin magnetic moment (μ_B)		
	bulk	$(111)_{surf.}$	$(100)_{surf.}$	bulk	$(111)_{surf.}$	$(100)_{surf.}$
Co	0	−0.02	0.00	1.66	1.73	1.84
$Co_{(@ NiCo)}$	0.16	+0.07	+0.10	1.72	1.82	1.91
$Ni_{(@ NiCo)}$	−0.16	−0.12	−0.11	0.64	0.65	0.67
Ni	0	−0.03	−0.01	0.65	0.67	0.71

A2.3 Construction of Wulff polyhedral and nanoparticles

Table S5 Surface energies from the Crystallium database (Materials Project) [66].

Surface	(111)	(100)	(221)	(110)	(321)	(211)	(210)	(332)	(322)	(320)	(310)	(331)	(311)
Ni	1.92	2.21	2.17	2.29	2.32	2.24	2.40	2.09	2.12	2.56	2.40	2.23	2.30
Co	2.04	2.48	2.33	2.42	2.49	2.52	4.36	3.19	3.05	2.56	3.43	3.64	3.28

A2.4 Segregation test for surfaces and nanoparticles

Segregation of Ni or Co atoms to the surface was studied in slab and nanoparticle models. As example, Table S6 shows the segregated slab models on the (111) surface and their surface Ni coverage while Table S7 exemplifies the segregated sequence studied for the $Ni_{27}Co_{28}$ (n=55) nanoparticle according to the average coordination degree of Co atoms.

Table S6 Slab surface segregated models, energies (E_0, eV) and surface Ni fraction ($\theta_{Ni\text{-}sup}$, adim.)

	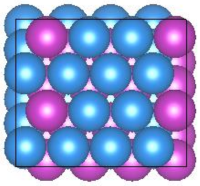	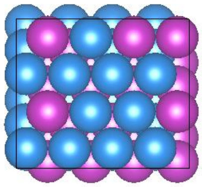	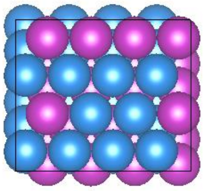	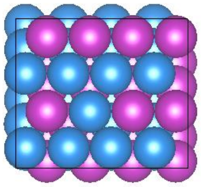	● Ni atoms ● Co atoms
$\theta_{Ni\text{-}sup}$=	0.25	0.3125	0.3750	0.4375	
E_0=	-346.39273230	-346.55105271	-346.73601079	-346.85351666	
	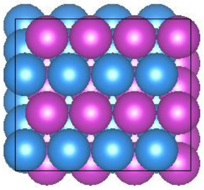	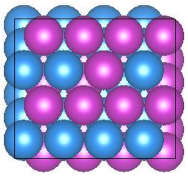	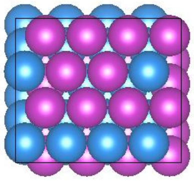	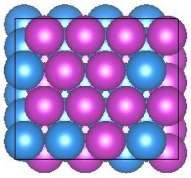	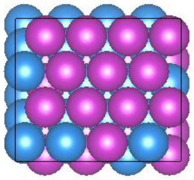
$\theta_{Ni\text{-}sup}$=	0.5	0.5625	0.6250	0.6875	0.75
E_0=	-346.99558518	-347.15753110	-347.27073802	-347.44793534	-347.57008497

Table S7 Nanoparticle $Ni_{27}Co_{28}$ models (n=55), energies (E_0, eV) and average coordination degree of Co atoms ($CD_{(Co)}$, atoms). Smaller $CD_{(Co)}$ means Co is more present in the surface.

	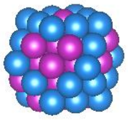	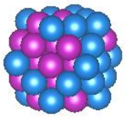	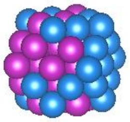	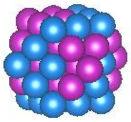	● Ni atoms ● Co atoms
$CD_{(Co)}$=	6.1	6.6	7.0	7.6	
E_0=	-262.09287334	-262.72024217	-263.56990704	-264.04335535	
	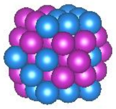	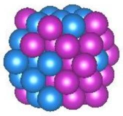	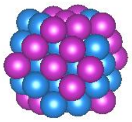	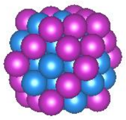	
$CD_{(Co)}$=	8.1	8.6	9.1	9.5	
E_0=	-264.65133630	-265.42371483	-266.27934277	-266.68401654	

A3 Gas phase reaction energies

The gas phase methanation of CO and CO_2 were computed and compared to experimental data and values from reference (Fig. S2, and NIST as reference using the parametrized Shomate equation, in good agreement with published values[1], [5]). The DFT-RPBE methodology was found to properly reproduce the energetics of the $CO + 3H_2 \rightarrow CH_4 + H_2O$ reaction adding a correction factor to the electronic energy of CO of only 0.009127 eV. Conversely, a correction factor of 0.37116421 eV needed to be applied to the electronic energy of CO_2 to fit the energetics of the $CO_2 + 4H_2 \rightarrow CH_4 + 2H_2O$ reaction.

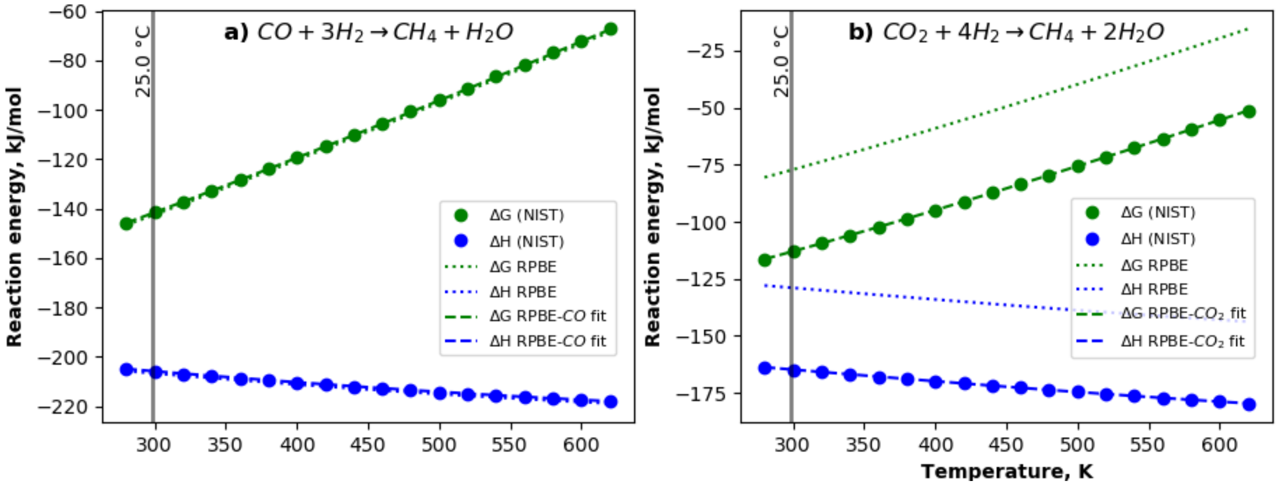

Fig. S2 Gas phase reaction of a) CO methanation and b) CO_2 methanation (1 atm).

A4 Surface species – DFT studies

A4.1 Reference values for CO adsorption energies

Table S8 and Table S9 show the experimental and DFT-derived CO adsorption energies on Ni and Co surfaces included in Fig. 24c,d in the main text (section 7.2.1).

Table S8 Reference values for the adsorption of CO on Ni surfaces.

Surface	E_{ads} (eV)	Comments	Ref.
Ni(111)	-1.1~-1.5	Exp., compiled from ref. within	[117]
Ni(111)	-1,22	Exp.	[108]
Ni(111)	-1.28±0.13	Exp. (Hollow)	[96]
Ni(111)	-1.49 ~ -2.	Theoretical, compiled from ref. within	[117]
Ni(111)	-1.92 (hcp)	VASP-PBE	[28]
Ni(111)	-1.5	Dacapo	[113]
Ni(111)	-2.09 (hcp)	SIESTA	[78]
Ni(111)	-1.88 (hcp)	VASP, PBE	[78]
Ni(111)	-1.95 (hollow)	VASP-PW91(450eV)	[43]
Ni(111)	-1.90 (hollow)	VASP-PW91(700eV)	[43]
Ni(111)	-1.44 (hollow)	VASP-RPBE(700eV)	[43]
Ni(111)	-1.93 (hcp), -1.91 (fcc), -1.78 (b), -1.49 (t)	VASP-PBE-D	[118]
Ni(111)	-1.34 (t), -1.52 (b), -1.62 (hcp), -1.59 (fcc)	DACAPO-RPBE	[96]
Ni(111)-t	-1.20 (t), -1.24 (b), -1.26 (fcc), -1.29 (hcp)	DACAPO-RPBE +ZPVE+$E_{S\text{-}T}$ corrections	[96]
Ni(111)	-1.89	VASP-PBE	[31]
Ni(111)	-1.93 (h), -1.92 (f), -1.55 (t)	VASP, PBE	[119]
Ni(111)	-1,32 (fcc)	Dmol^3, PW91	[76]
Ni(111)	-1.93 (hcp)	VASP, PBE (385eV)	[30]

Table S9 Reference values for the adsorption of CO on Co surfaces

Surface	E_{ads} (eV)	Comments	Ref.
Co(0001)	-1.20±0.13	Experimental (top-preferred)	[96]
Co(0001)	-1.33	Experimental (low coverage enthalpy)	[120]
Co(0001)	-1.65 (t)	VASP-PW91(450eV)	[43]
Co(0001)	-1.62 (t)	VASP-PW91(700eV)	[43]
Co(0001)	-1.32 (t)	VASP-RPBE(700eV)	[43]
Co(0001)	-1.34 (t), -1.34 (b), -1.38 (fcc), -1.39 (hcp)	DACAPO-RPBE	[96]
Co(0001)	-1.16 (t), -1.05, -1.03 (fcc), -1.05 (hcp)	DACAPO-RPBE +ZPVE+E_{S-T} corrections	[96]
Co(0001)-t	-1.34 (t), -1.23 (b), -1.27 (hcp), -1.26 (fcc)	VASP-RPBE-D	[120]
Co(0001)-t	-1.50 (t), -1.43 (b), -1.46 (hcp), -1.47 (fcc)	VASP-RPBE	[120]
Co(111)	-1.84	VASP-PBE	[31]
Co(111)-f	-1.68	VASP-PBE	[3]
Co(111)-f	-1.64	VASP-PBE+ZPVE	[3]

A4.2 Singlet-Triplet extrapolation for *CO

The $CO_{(g)}$ singlet-triplet excitation energy ($E_{S\text{-}T}$) is used as surrogate of how well a functional and method estimates the $2\pi^*$ orbital, Table S10 shows $E_{S\text{-}T}$ for the experimental (E_{S-T}^{E}), standard (E_{S-T}^{N}), soft (E_{S-T}^{S}) and hard pseudopotential (E_{S-T}^{H}). Soft and normal calculations use 460 eV cut-off energy but the hard pseudopotential required a 700eV cutoff, the calculation is significantly more expensive with little improvement of $E_{S\text{-}T}$ thus hard pseudopotentials were not employed further. The relaxed models for all adsorbed sites were relaxed again using the soft pseudopotential for C and O atoms to obtain soft electronic adsorption energies E_{ad}^{S}. The standard adsorption energies (E_{ad}^{N}) were linearly extrapolated using the according to the observations of Mason et al.[42] and the procedure detailed by Deshlara et al.[53] using eq. S1 as shown in Fig. S3. Corrected and uncorrected adsorption energies are shown in Table 9 from the main text.

$$E_{ad} = E_{ad}^{N} + (E_{S-T}^{E} - E_{S-T}^{N})(E_{ad}^{N} - E_{ad}^{S})/(E_{S-T}^{N} - E_{S-T}^{S}) \qquad \text{eq. S1}$$

Table S10 Singlet-Triplet extrapolation energy from different pseudopotential

	Soft	Standard	High	Experimental
$E_{S\text{-}T}$, eV	5,23231958	5,52743142	5,58883434	6,095

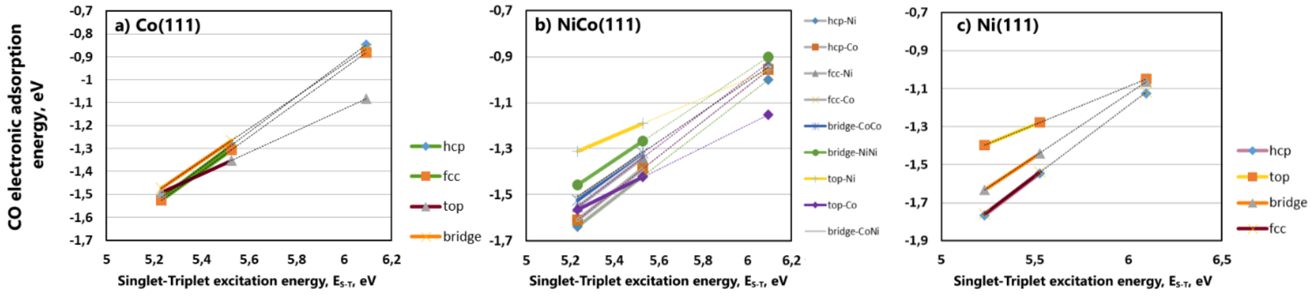

Fig. S3 Extrapolation to the electronic adsorption energy based on the singlet-triplet excitation energy on a) Co(111), b) NiCo(111) and c)Ni(111)

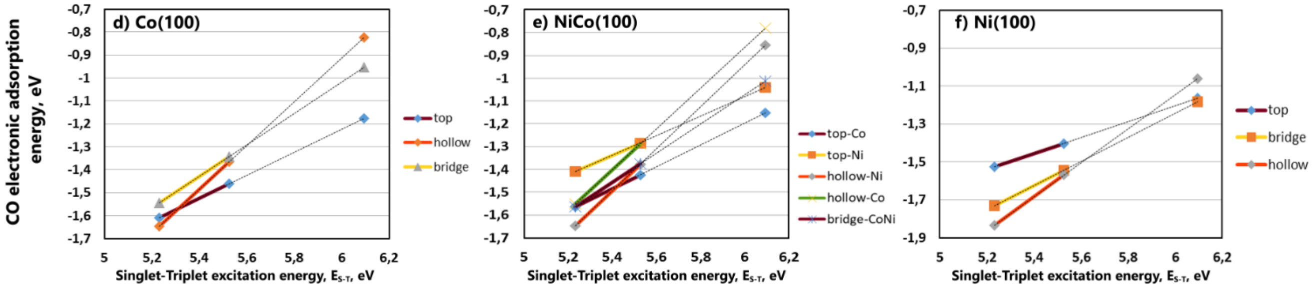

Fig. S3(cont.) Extrapolation to the electronic adsorption energy based on the singlet-triplet excitation energy on d) Co(100), e) NiCo(100) and f)Ni(100)

A4.3 *CO vibrational frequencies, bond lengths and Bader charges

*C-O stretching frequencies from Table 8 in the main text are plotted in Fig. S4 with their corresponding singlet-triplet linear extrapolation (analog to eq. S1) as discussed in section 7.2.1.1 (the main) text and detailed in sec. A4.2. Table S11 shows the *C—O bond length evidencing its stretching upon adsorption and Table S12 shows the total Bader charges for the carbonyl species.

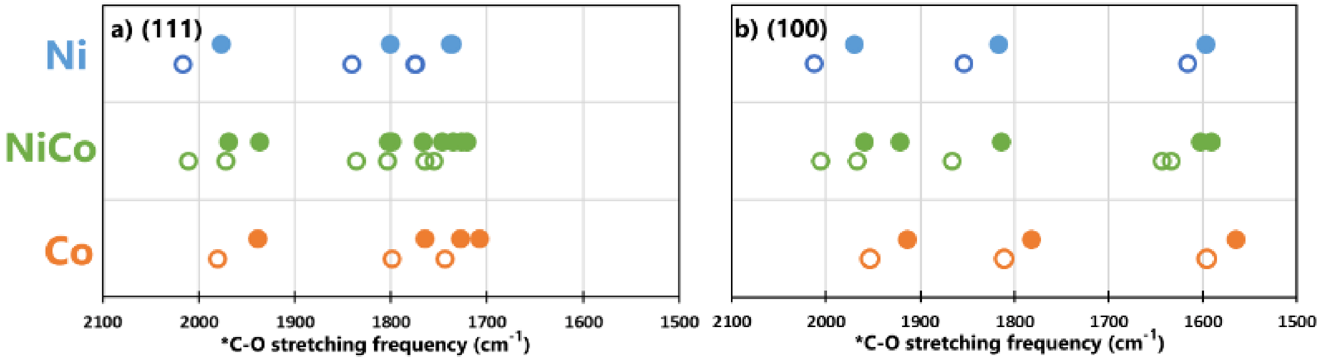

Fig. S4 *C-O stretching frequencies on Ni, Co and NiCo a) (111) and b) (100) surfaces for all the adsorption defined in Fig. 22. Close symbols mark the directly DFT-derived frequencies and open symbols mark the $E_{S\text{-}T}$ extrapolation.

Table S11 Adsorbed *C–O bond lengths (in Å)

(111) surfaces				
Co	1.173 (*top*)	1.195 (*bridge*)	1.200 (*fcc*),	1.203 (*hcp*)
NiCo	1.173 (top_{Co}) 1.168 (top_{Ni})	1.195 ($bridge_{Co\text{-}Co}$) 1.191 ($bridge_{Co\text{-}Ni}$) 1.190 ($bridge_{Ni\text{-}Ni}$)	1.201 (fcc_{Co}) 1.198 (fcc_{Ni})	1.202 (hcp_{Co}) 1.200 (hcp_{Ni})
Ni	1.168 (*top*)	1.191 (*bridge*)	1.200 (*fcc*)	1.200 (*hcp*)
(100) surfaces				
Co	1.176 (*top*)	1.194 (*bridge*)	1.227 (*h*)	
NiCo	1.174 (top_{Co}), 1.170 (top_{Ni})	1.188 ($bridge_{Co\text{-}Ni}$)	1.219 (h_{Co}), 1.222 (h_{Ni})	
Ni	1.169 (*top*)	1.189 (*bridge*)	1.219 (*h*)	

Table S12 Bader charges for the adsorbed *CO species (e)

		(111) surfaces		
Co	-0.32 (*top*),	-0.54 (*bridge*)	-0.62 (*fcc*),	-0.64 (*hcp*)
NiCo	-0.29 (top_{Co}), -0.30 (top_{Ni}),	-0.51 ($bridge_{Co\text{-}Co}$) -0.49 ($bridge_{Co\text{-}Ni}$) -0.48 ($bridge_{Ni\text{-}Ni}$)	-0.59 (fcc_{Co}), -0.54 (fcc_{Ni}),	-0.60 (hcp_{Co}), -0.58 (hcp_{Ni})
Ni	-0.24 (*top*),	-0.48 (*bridge*)	-0.58 (*fcc*),	-0.55 (*hcp*)
		(100) surfaces		
Co	-0.31 (*top*)	-0.50 (*bridge*)	-0.89 (*h*)	
NiCo	-0.27 (top_{Co}), -0.34 (top_{Ni})	-	-0.72 (h_{Co}), -0.72 (h_{Ni})	
Ni	-0.25 (*top*)	-0.46 (*bridge*)	-0.77 (*h*)	

A5 Kinetic data

A5.1 Effect of catalyst composition on the TOF and selectivity for different feed compositions

Fig. S5 and Fig. S6 (analog to Fig. 19 main text) show for $H_{2(g)}:CO_{2(5)}=1:15$ and $H_{2(g)}:CO_{2(5)}=2:25$ feeds (respectively) nearly the same trends discussed in sec. Fig. 19 for a $H_{2(g)}:CO_{2(5)}=1:25$ feed. Fig. S7 shows the combined formation rates of $CO_{(g)}$ and $CH_{4(g)}$ (roughly equivalent to $CO_{2(g)}$ consumption since C balance >95%) at the different feed ratios evidencing the lower activity of the bimetallic catalysts.

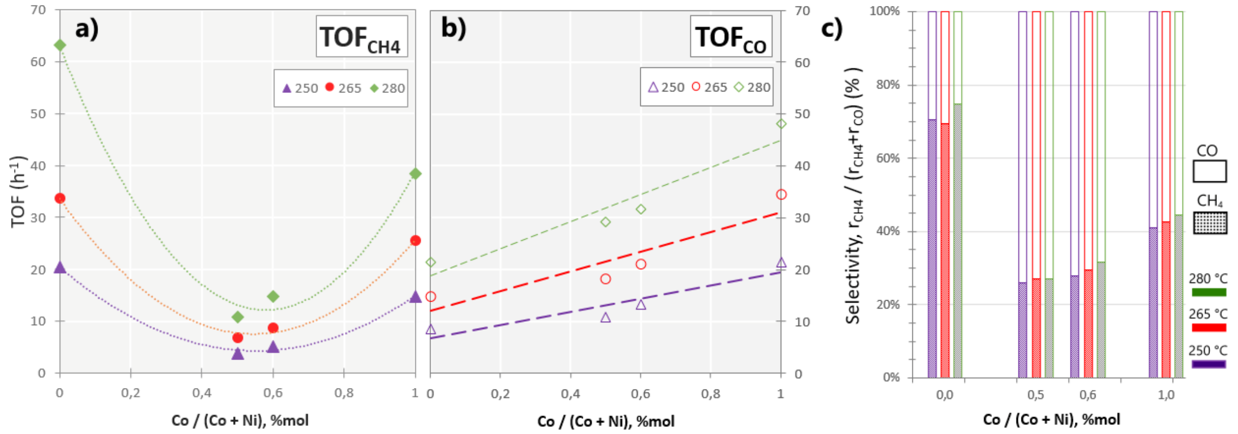

Fig. S5 Effect of the catalyst Ni-Co molar composition on the intrinsic reaction rates (TOF) for (a) $CH_{4(g)}$, (b) $CO_{(g)}$ formation and (c) their selectivities from 1 kPa $CO_{2(g)}$ + 15 kPa $H_{2(g)}$ (He balance for 1 atm) at 250 °C (purple), 265 °C (red) and 280 °C (green).

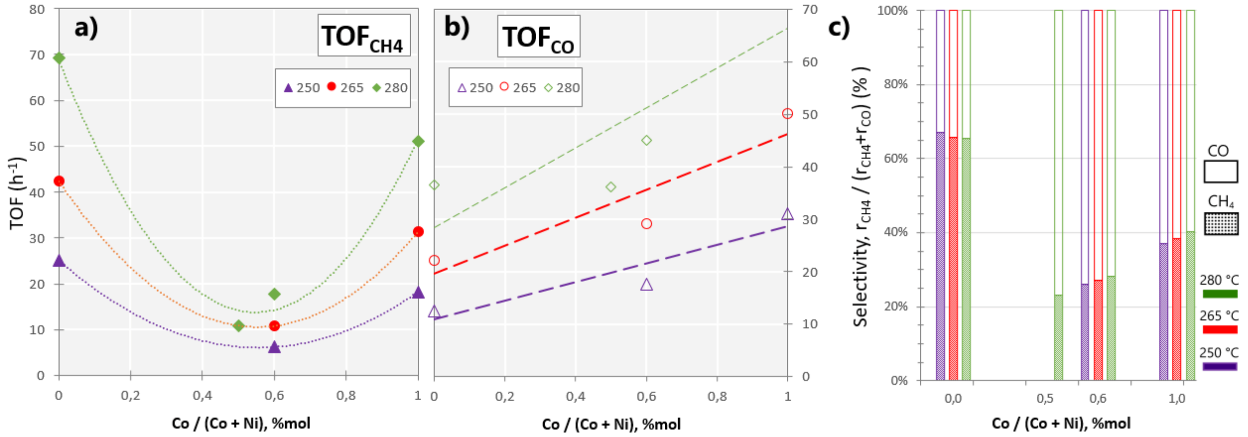

Fig. S6 Effect of the catalyst Ni-Co molar composition on the intrinsic reaction rates (TOF) for (a) $CH_{4(g)}$, (b) $CO_{(g)}$ formation and (c) their selectivities from 2 kPa $CO_{2(g)}$ + 25 kPa $H_{2(g)}$ (He balance for 1 atm) at 250 °C (purple), 265 °C (red) and 280 °C (green).

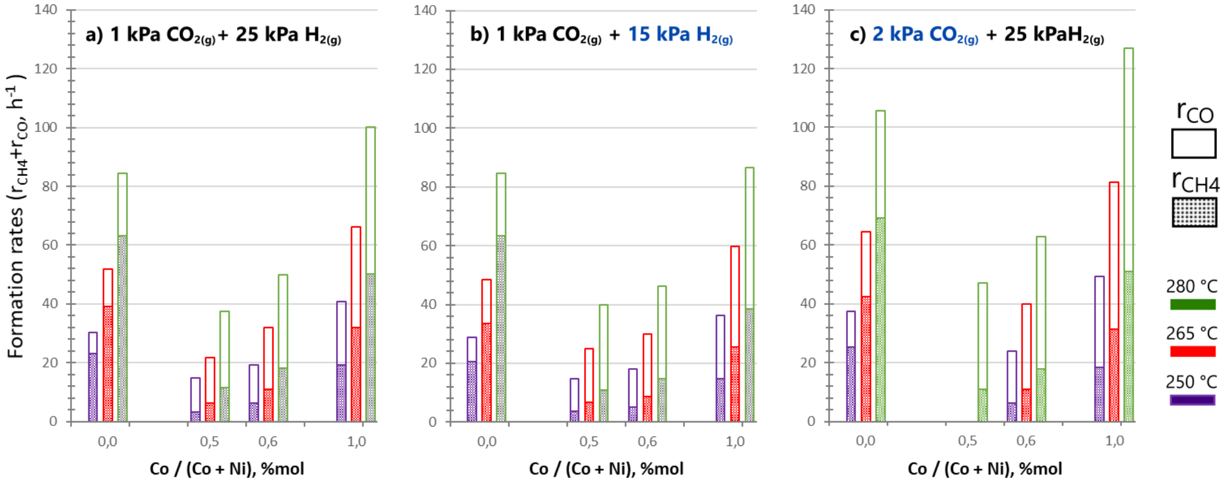

Fig. S7 Effect of catlysts Ni-Co molar composition on the combined formation rates of $CH_{4(g)}$ (patterned segments) and $CO_{(g)}$ (open segments) at different feed ratios: (a) $H_{2(g)}$:$CO_{2(5)}$=1:25, (b) $H_{2(g)}$:$CO_{2(5)}$=1:15 and (c) $H_{2(g)}$:$CO_{2(5)}$=2:25, and temperatures: purple: 250 °C, red: 265 °C and green: 280 °C.

A6 Geometries and properties of adsorbed models

Several possible geometries (orientation and binding points) were explored for each fragment and unique site with less precise methods (2×2×1 k-point mesh, 10^{-5}eV electronic precision). Some of these starting geometries dissociated or relaxed to other adsorbed geometries, only the models that relaxed to unique geometries were relaxed again as four-layer models with 4×4×1 k-point meshes until electronic energy varied less than 10^{-6}eV and all forces were under 0.02 eV/Å. Unless stated otherwise, all geometries presented bellow and in the main text correspond to these relaxed full precision four layer models. Electronic energies (eV) and main geometric parameters (distances d_{A-B} in Å, angles A_{ABC} in degrees) are included.

A6.1 CO

Site	Ni(100)/CO @ h	Ni(100)/CO @ b	Ni(100)/CO@ t	Co(100)/CO @ h	Co(100)/CO @ b	Co(100)/CO @ t
	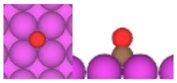	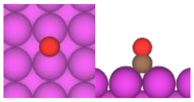	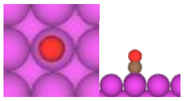	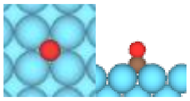	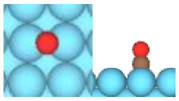	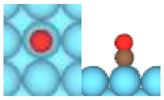
E0=	-307.88339326 $d_{C-O}=1.22$ $d_{C-Ni}=2.06/ 2.06/ 2.06/ 2.06$	-307.85799089 $d_{C-O}=1.19$ $d_{C-Ni}=1.89/1.89$	-307.71846790 $d_{C-O}=1.17$ $d_{C-Ni}=1.75$	-403.46091221 $d_{C-O}=1.23$ $d_{C-Co}=2.08/2.08/ 2.08/2.09$	-403.43876142 $d_{C-O}=1.19$ $d_{C-Co}=1.93/1.92$	-403.55846020 $d_{C-O}=1.18$ $d_{C-Co}=1.776$
Site	NiCo(100)/CO @ b_{CN}	Ni(100)/CO @ h_C	NiCo(100)/CO@ h_N	Co(100)/CO @ t_C	Co(100)/CO @ t_N	
	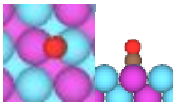	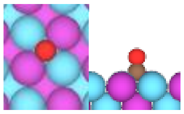	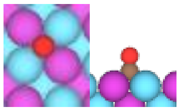	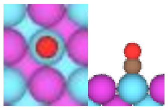	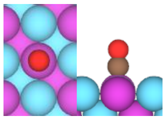	
E0=	-355.73821746 $d_{C-O}=1.19$, $d_{C-Ni}=2.05$, $d_{C-Co}=1.83$	-355.65074592 $d_{C-O}=1.22$ $d_{C-Ni}=2.08/2.09$, $d_{C-Co}=2.09/2.09$	-355.73933399 $d_{C-O}=1.22$ $d_{C-Ni}=2.08/2.08$, $d_{C-Co}=2.08/2.08$	-355.75919236 $d_{C-O}=1.17$, $d_{C-Co}=1.76$	-355.64619225 $d_{C-O}=1.17$, $d_{C-Ni}=1.76$	

Site	Ni(111)/CO @ hcp	Ni(111)/CO @ fcc	Ni(111)/CO@ b	Ni(111)/CO @ t	Co(111)/CO @ hcp	Co(111)/CO @ fcc
	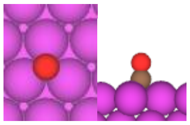	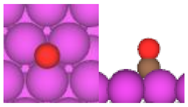	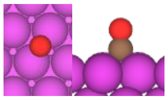	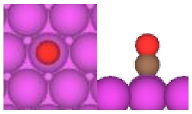	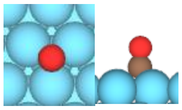	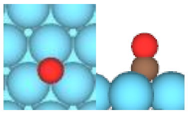
E0=	-314.28758633 $d_{C-O}=1.20$, $d_{C-Ni}=1.96/1.96/1.96$	-314.29380402 $d_{C-O}=1.20$, $d_{C-Ni}=1.96/1.96/1.97$	-314.18630213 $d_{C-O}=1.19$, $d_{C-Ni}=1.89/1.89$	-314.02531989 $d_{C-O}=1.17$, $d_{C-Ni}=1.75$	-411.69783090 $d_{C-O}=1.20$, $d_{C-Co}=2.00/2.01/1.97$	-411.71793530 $d_{C-O}=1.20$, $d_{C-Co}=2.00/2.00/1.99$
Site	Co(111)/CO @ b	Co(111)/CO @ t	NiCo(111)/CO @hcp_C	NiCo(111)/CO @hcp_N	NiCo(111)/CO @fcc_C	NiCo(111)/CO @fcc_N
	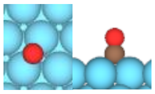	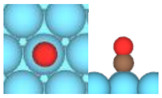	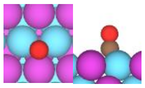	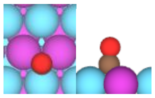	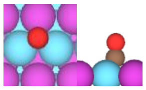	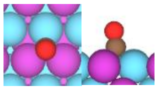
E0=	-411.67801789 $d_{C-O}=1.19$, $d_{C-Co}=1.91/1.93$	-411.76459288 $d_{C-O}=1.17$, $d_{C-Co}=1.76$	-362.92023855 $d_{C-O}=1.20$, $d_{C-Ni}=2.02$, $d_{C-Co}=1.97/1.97$,	-362.95466308 $d_{C-O}=1.20$, $d_{C-Co}=1.92$, $d_{C-Ni}=2.02/2.02$	-362.92192147 $d_{C-O}=1.20$, $d_{C-Ni}=2.01$, $d_{C-Co}=1.98/1.98$	-362.87350895 $d_{C-O}=1.20$, $d_{C-Co}=1.91$, $d_{C-Ni}=2.05/2.05$

Site	NiCo(111)/CO @b_C	NiCo(111)/CO @b_N	NiCo(111)/CO @b_{CN}	NiCo(111)/CO @t_C	NiCo(111)/CO @t_N	
	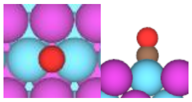	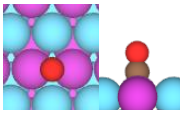	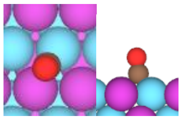	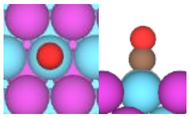	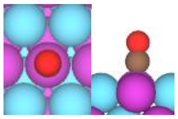	
E0=	-362.85270177 d_{C-O}=1.19, d_{C-Co}=1.92/1.92	-362.80194658 d_{C-O}=1.19, d_{C-Ni}=1.91/1.91	-362.85053318 d_{C-O}=1.19, d_{C-Co}=1.85, d_{C-Ni}=2.01	-362.95774413 d_{C-O}=1.17, d_{C-Co}=1.74	d_{C-O}=1.17, d_{C-Ni}=1.76	

A6.2 O and OH

O on (111) surfaces:

Site	Ni/O @ f	Ni/O @ h	Co/O @ f	Co/O @ h
	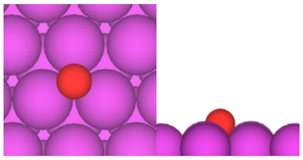	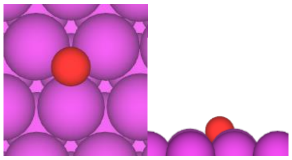	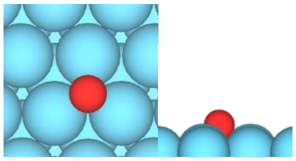	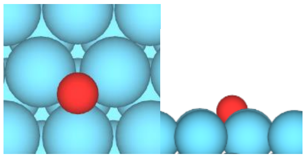
E0=	-305.20101543 d_{Ni-O}=1.85/1.86/1.85	-305.08966372 d_{Ni-O}=1.86/1.86/1.86	-403.03144089 d_{Co-O}=1.88/1.89/1.89	-403.11258927 d_{Co-O}=1.88/1.88/1.88
Site	NiCo/O @ f_C	NiCo/O @ f_N	NiCo/O @ h_C	NiCo/O @ h_N
	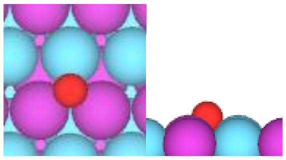	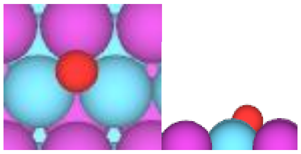		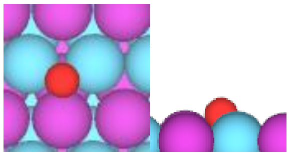
E0=	-353.97431097 d_{Co-O}=1.83, d_{Ni-O}=1.89/1.89	-354.19253323 d_{Co-O}=1.87/1.86, d_{Ni-O}=1.91	-353.96539566 d_{Co-O}=1.83, d_{Ni-O}=1.90/1.90	-354.22127059 d_{Co-O}=1.86/1.86, d_{Ni-O}=1.91

OH on (111) surfaces

Site	Ni/OH @ f	Ni/OH @ h	Co/OH @ f	Co/OH @ h
	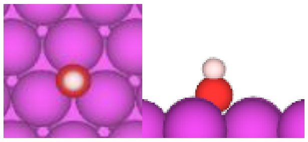	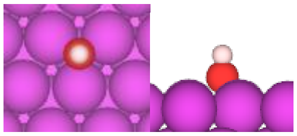	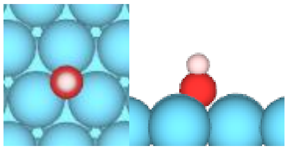	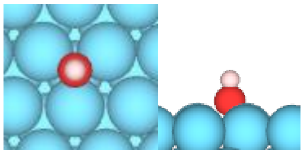
E0=	-308.93609818 d_{Ni-O}=2.00/2.00/2.00, d_{O-H}=0.97	-308.83120895 d_{Ni-O}=2.00/2.01/2.01, d_{O-H}=0.97	-406.75151055 d_{Co-O}=2.03/2.03/2.03, d_{O-H}=0.97	-406.79841419 d_{Co-O}=2.03/2.03/2.03, d_{O-H}=0.97
Site	NiCo/OH @ f_C	NiCo/OH @ f_N	NiCo/OH @ h_C	NiCo/OH @ h_N
	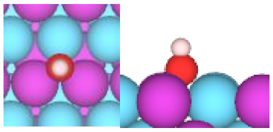	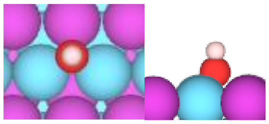	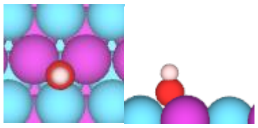	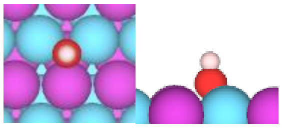
E0=	-357.68946125 d_{Co-O}=2.00, d_{Ni-O}=2.03/2.03, d_{O-H}=0.97	-357.91338314 d_{Co-O}=2.02/2.02, d_{Ni-O}=2.03, d_{O-H}=0.97	-357.67397336 d_{Co-O}=2.00, d_{Ni-O}=2.03/2.03, d_{O-H}=0.97	-357.90318490 d_{Co-O}=2.01/2.01, d_{Ni-O}=2.04, d_{O-H}=0.97

O on (100) surfaces

Site	Ni/O @ h	Co/O @ h	NiCo/O @ h_C	NiCo/O @ h_N
	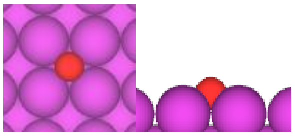	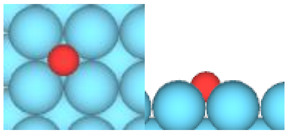	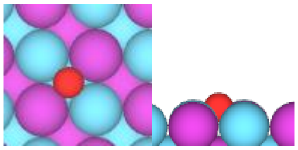	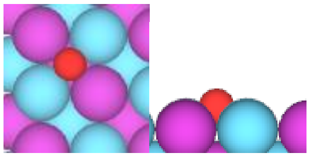
E0=	-299.01927037 d_{Ni-O}=1.97/1.97/1.97/1.97	-395.14438924 d_{Co-O}=2.00/2.00/2.00/2.00	-347.15010672 d_{Co-O}=1.97/1-97, d_{Ni-O}=2.01/2.01	-347.24324204 d_{Co-O}=1.97/1.97, d_{Ni-O}=2.02/2.03

OH on (100) surfaces

Site	Ni/OH @ h	Co/OH @ h	NiCo/OH @ h_C	NiCo/OH @ h_N
	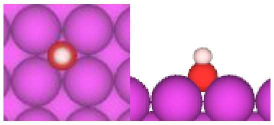	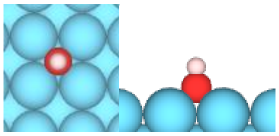	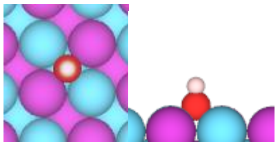	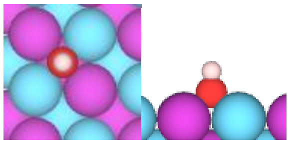
E0=	-302.67562576 d_{Ni-O}=2.15/2.15/2.14/2.14, d_{O-H}=0.98	-398.63656714 d_{Co-O}=2.18/2.19/2.17/2.18, d_{O-H}=0.98	-350.73724867 d_{Co-O}=2.17/2.15, d_{Ni-O}=2.17/2.19, d_{O-H}=0.98	-350.87233531 d_{Co-O}=2.15/2.16, d_{Ni-O}=2.19/2.18, d_{O-H}=0.98

A6.3 CO_3 species

The study of $^*CO_3$ species was initially considered from the observation of bands associated to carbonates appearing during the direct dissociation of $^*CO_2$ without H_2 feed (Fig. 31) and in comparison to the bands associated to bicarbonate in the dynamic and static FTIR studies under methanation conditions (Fig. 20). However, $^*CO_3$ species were not studied further considering their high surface recombination energies (eq. 4.9) compared with other surface species (Fig. 23) which suggests a favorable dissociation on the surface. Additionally, their experimental identification for Fig.31 (main text) may come from the interaction of $CO_{2(g)}$ and *O (from direct $^*CO_2$ dissociation) favored by the high $CO_{2(g)}$ partial pressure employed in that experiment, conditions vastly different from the studied methanation conditions. Furthermore, from a mechanistic perspective introducing a $^*CO_3$ intermediate derived from $CO_{2(g)}$ involves the counterintuitive oxygenation of a reactant that already has O for a reaction intended to produce a deoxygenated product ($CH_{4(g)}$). It is certainly possible to postulate reaction mechanisms involving $^*CO_3$, but it appears to significantly increase the complexity of the possible pathways and number of steps required while offering little advantage to break the initial C-O bonds for a consistent catalytic cycle leading from $CO_{2(g)}$ to the formation of $CH_{4(g)}$. This led to not study in more detail $^*CO_3$ (and bicarbonate) species in the presented work.

Regardless, stable configurations of surface $^*CO_3$ species binding bidentate (similar to HCOO**) with one O on top of a metal atom and other in a bridge position, effectively occupying a hollow site and as in Table S13. For Ni(111) a top-top position was also found and is included below, but was regarded less stable. On both (111) monometallic surfaces the main vibrational frequencies computed are close bands around 1700 cm^{-1} and 1080 cm^{-1} associated to the symmetric and asymmetric stretching of the *O-C bonds, respectively. For comparison, the higher frequencies are about >100 cm^{-1} above the bands associated to bicarbonate under methanation conditions (Fig. 20) and carbonate bands at high $CO_{2(g)}$ partial pressures (Fig. 31) which may suggest the observation of a preferred adsorption geometry different surface features such as steps, kinks or, for example, the metal-support interface.

Table S13 Example *CO_3 species

	Co(111)/CO_3	Ni(111)/$CO_{3\ (th)}$	Co(111)/$CO_{3\ (tt)}$
Configuration	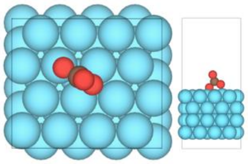 (top-bridge)	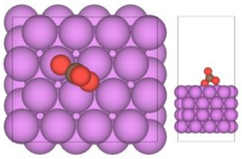 (top-bridge)	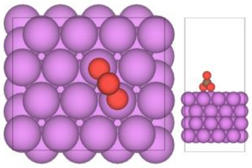 (top-top)
E_0 (eV)	-424.5844	-326.6505 (preferred)	-326.0523
Vibrational frequencies (cm^{-1})	1686.6 ; 1093.7 ; 732.1 ; 717.2 ; 617.4 ; 578.0 ; ... (< 500)	1710.9 ; 1070.0 ; 729.9 ; 724.2 ; 599.0 ; 571.5 ; ... (< 500)	-

A6.4 Bader charges of O on NiCo surfaces

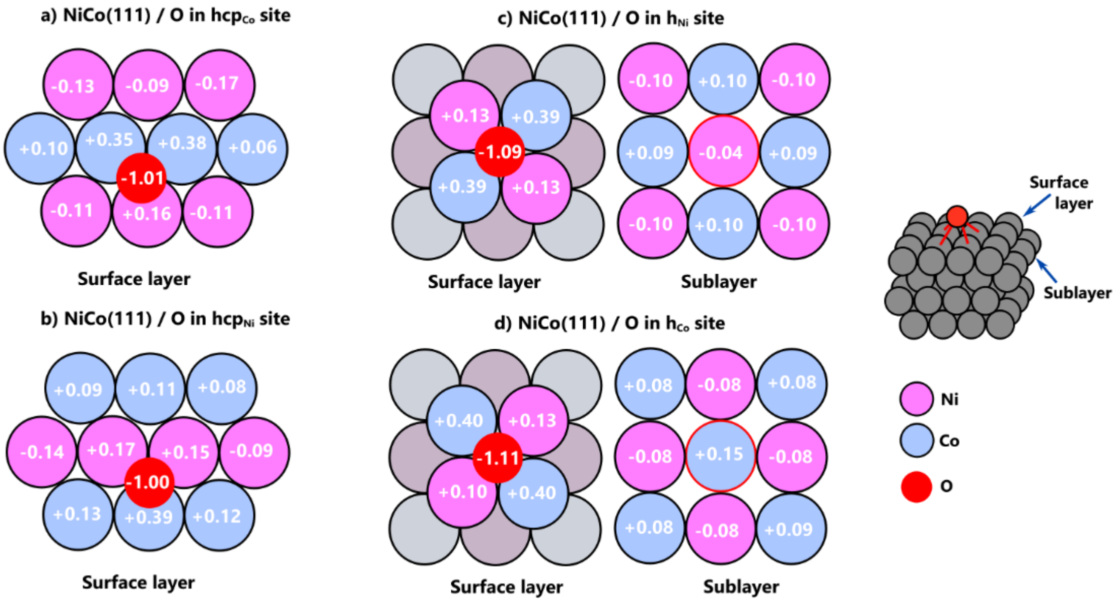

Fig. S8 Bader charges of surface models for O adsorbed on Co-rich (a,c) and Ni-rich (b,d) sites of NiCo (111) and (100) surfaces (respectively)

A6.5 H, C and CH_x species

H on (111) surfaces:

Site	Ni/H @ f	Ni/H @ h	Co/H @ f	Co/H @ h
	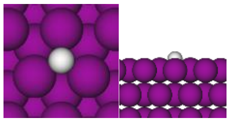	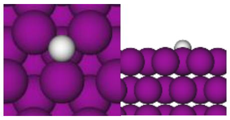	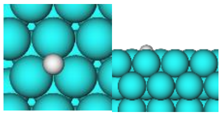	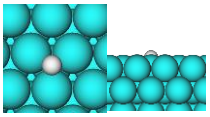
E0=	-302.20374172 $d_{\text{Ni-H}}$=1.72/1.72/1.72	-302.19008890 $d_{\text{Ni-H}}$=1.72/1.72/1.72	-399.86814225 $d_{\text{Co-H}}$=1.75/1.75/1.75	-399.83752437 $d_{\text{Co-H}}$=1.76/1.76/1.76
Site	NiCo/H @ f_C	NiCo/H @ f_N	NiCo/H @ h_C	NiCo/H @ h_N
	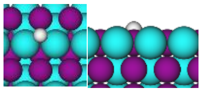	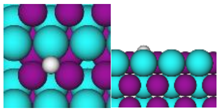	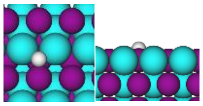	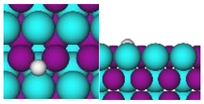
E0=	-350.96281044 $d_{\text{Ni-H}}$=1.72, $d_{\text{Co-H}}$=1.77/1.77	-350.95286606 $d_{\text{Ni-H}}$=1.72/1.72, $d_{\text{Co-H}}$=1.77	-350.95215547 $d_{\text{Ni-H}}$=1.72, $d_{\text{Co-H}}$=1.77/1.77	-350.94085674 $d_{\text{Ni-H}}$=1.73/1.73, $d_{\text{Co-H}}$=1.76

C on (111) surfaces

Site	Ni/C @ f	Ni/C @ h	Co/H @ f	Co/H @ h
	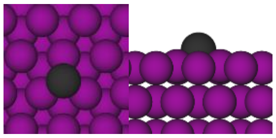	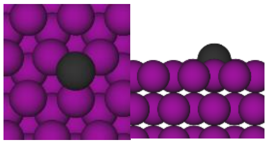	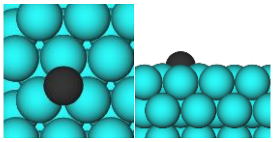	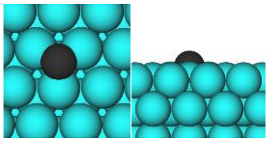
E0=	-306.01523836 $d_{\text{Ni-C}}$=1.78/1.78/1.78	-306.07358952 $d_{\text{Ni-C}}$=1.78/1.78/1.78	-403.48314760 $d_{\text{Co-C}}$=1.80/1.80/1.80	-403.74626185 $d_{\text{Co-C}}$=1.79/1.79/1.79

C on (111) surfaces

Site	NiCo/C @ f_C	NiCo/C @ f_N	NiCo/C @ h_C	NiCo/C @ h_N
	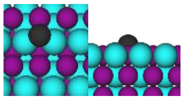	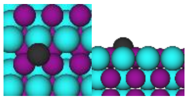	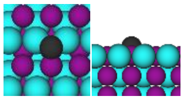	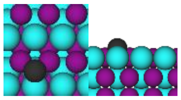
E0=	-354.72752759 $d_{\text{Ni-C}}$=1.85, $d_{\text{Co-C}}$=1.76/1.76	-354.58773653 $d_{\text{Ni-C}}$=1.82/1.82, $d_{\text{Co-C}}$=1.73	-354.87504482 $d_{\text{Ni-C}}$=1.84, $d_{\text{Co-C}}$=1.78/1.78	-354.76524594 $d_{\text{Ni-C}}$=1.81/1.81, $d_{\text{Co-C}}$=1.74

CH on (111) surfaces

Site	Ni/CH @ f	Ni/CH @ h	Co/CH @ f	Co/CH @ h
	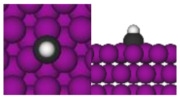	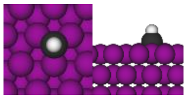	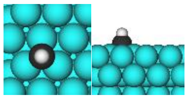	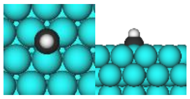
E0=	-310.42939000 $d_{\text{Ni-C}}$=1.85/1.85/1.85, $d_{\text{C-H}}$=1.10	-310.41135997 $d_{\text{Ni-C}}$=1.85/1.85/1.85, $d_{\text{C-H}}$=1.10	-407.88817465 $d_{\text{Co-C}}$=1.88/1.89/1.89, $d_{\text{C-H}}$=1.10	-407.98522612 $d_{\text{Co-C}}$=1.88/1.88/1.88, $d_{\text{C-H}}$=1.10
Side	NiCo/CH @ f_C	NiCo/CH @ f_N	NiCo/CH @ h_C	NiCo/CH @ h_N
	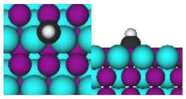	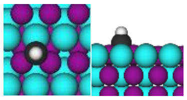	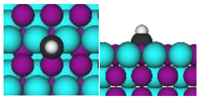	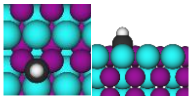
E0=	-359.13598665 $d_{\text{Ni-C}}$=1.90/$d_{\text{Co-C}}$=1.86, $d_{\text{C-H}}$=1.10	-358.99241918 $d_{\text{Ni-C}}$=1.89/1.89, $d_{\text{Co-C}}$=1.83, $d_{\text{C-H}}$=1.10	-359.15320011 $d_{\text{Ni-C}}$=1.90/$d_{\text{Co-C}}$=1.86/1.86, $d_{\text{C-H}}$=1.10	-359.07412897 $d_{\text{Ni-C}}$=1.89/1.89, $d_{\text{Co-C}}$=1.83, $d_{\text{C-H}}$=1.10

CH_2 at (111) surfaces

Site	Ni/CH_2 @ f	Ni/CH_2 @ h	Co/CH_2 @ f	Co/CH_2 @ h
	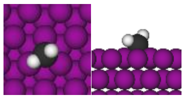	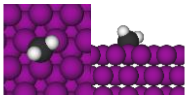	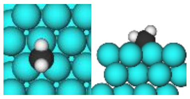	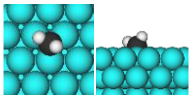
E0=	-313.99936531 d_{Ni-C}=1.93/1.93/2.00, d_{C-H}=1.16/1.10, d_{Ni-H}=1.77, A_{HCH}=101.78	-313.95288767 d_{Ni-C}=1.93/1.93/1.98, d_{C-H}=1.16/1.10, d_{Ni-H}=1.76, A_{HCH}=101.44	-411.58934904 d_{Co-C}=1.97/1.97/2.01, d_{C-H}=1.16/1.10, d_{Ni-H}=1.80, A_{HCH}=101.53	-411.57902745 d_{Co-C}=1.96/1.97/2.02, d_{C-H}=1.16/1.10, d_{Ni-H}=1.80, A_{HCH}=101.28
Side	NiCo/CH_2 @ f_C-Co	NiCo/CH_2 @ f_C-Ni	NiCo/CH_2 @ f_N-Co	NiCo/CH_2 @ f_N-Ni
	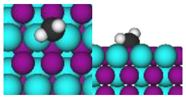	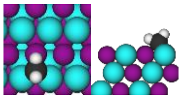	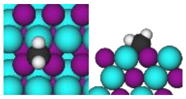	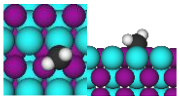
E0=	-362.80908028 d_{Co-C}=2.01/1.95, d_{Ni-C}=1.96, d_{C-H}=1.16/1.10, d_{Co-H}=1.79, A_{HCH}=101.43	-362.74613829 d_{Co-C}=1.96/1.96, d_{Ni-C}=2.02, d_{C-H}=1.16/1.10, d_{Ni-H}=1.79, A_{HCH}=101.63	-362.66878882 d_{Ni-C}=1.96/1.96, d_{Co-C}=1.97, d_{C-H}=1.16/1.10, d_{Co-H}=1.78, A_{HCH}=101.59	-362.61019705 d_{Ni-C}=2.02/1.97, d_{Co-C}=1.94, d_{C-H}=1.15/1.10, d_{Ni-H}=1.81, A_{HCH}=102.08
Side	NiCo/CH_2 @ h_C-Co	NiCo/CH_2 @ h_C-Ni	NiCo/CH_2 @ h_N-Co	NiCo/CH_2 @ h_N-Ni
	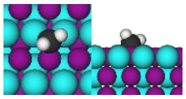	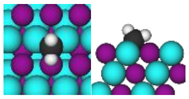	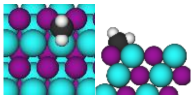	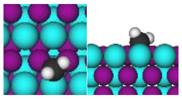
E0=	-362.78252335 d_{Co-C}=1.95/1.98, d_{Ni-C}=1.97, d_{C-H}=1.17/1.10, d_{Co-H}=1.76, A_{HCH}=100.93	-362.68844642 d_{Co-C}=1.96/1.96, d_{Ni-C}=2.01, d_{C-H}=1.16/1.10, d_{Ni-H}=1.77, A_{HCH}=101.14	-362.70426181 d_{Ni-C}=1.96/1.96, d_{Co-C}=1.96, d_{C-H}=1.17/1.10, d_{Co-H}=1.76, A_{HCH}=100.99	-362.65775192 d_{Ni-C}=1.96/2.01, d_{Co-C}=1.94, d_{C-H}=1.16/1.10, d_{Ni-H}=1.79, A_{HCH}=101.50

CH_3 on (111) surfaces

Site	Ni/CH_3 @ f	Ni/CH_3 @ h	Co/CH3 @ f	Co/CH3 @ h
	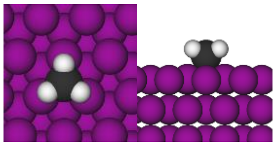	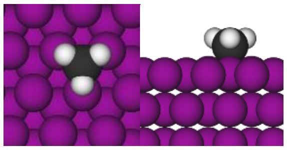	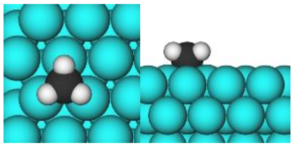	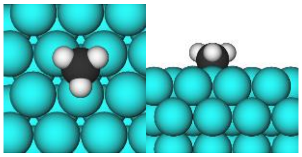
E0=	-318.03731865 d_{Ni-C}=2.15/2.15/2.15, d_{C-H}=1.12/1.12/1.12, d_{Ni-H}=2.05/2.06/2.07	-318.00638421 d_{Ni-C}=2.16/2.16/2.15, d_{C-H}=1.12/1.12/1.12, d_{Ni-H}=2.07/2.09/2.08	-415.77201200 d_{Co-C}=2.19/2.19/2.19, d_{C-H}=1.12/1.11/1.11, d_{Co-H}=2.11/2.12/2.12	-415.74789406 d_{Co-C}=2.20/2.21/2.20, d_{C-H}=1.11/1.11/1.11, d_{Co-H}=2.13/2.13/2.14
Site	NiCo/CH_3 @ f_C	NiCo/CH_3 @ f_N	NiCo/CH_3 @ h_C	NiCo/CH_3 @ h_N
	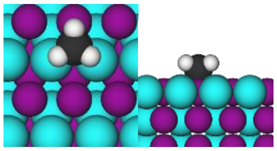	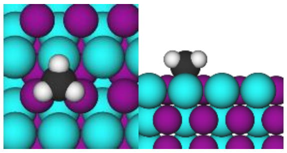	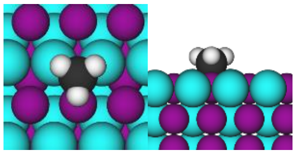	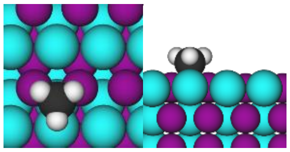
E0=	-366.89347546 d_{Ni-C}=2.15, d_{Co-C}=2.20/2.20, d_{C-H}=1.11/1.12/1.12, d_{Ni-H}=2.11, d_{Co-H}=2.11/2.10	-366.75762182 d_{Ni-C}=2.18/2.18, d_{Ni-C}=2.20, d_{C-H}=1.11/1.11/1.12, d_{Ni-H}=2.12/2.12, d_{Co-H}=2.10	-366.83746156 d_{Ni-C}=2.18, d_{Co-C}=2.19/2.19, d_{C-H}=1.11/1.12/1.12, d_{Ni-H}=2.12, d_{Co-H}=2.09/2.10	-366.78170284 d_{Ni-C}=2.18/2.18, d_{Co-C}=2.19, d_{C-H}=1.11/1.11/1.11, d_{Ni-H}=2.12/2.12, d_{Co-H}=2.13

H on (100) surfaces

Site	Ni/H @ h	Co/H @ h	NiCo/H @ h_C	NiCo/H @ h_N
	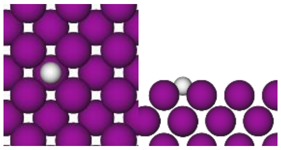	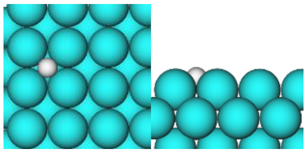	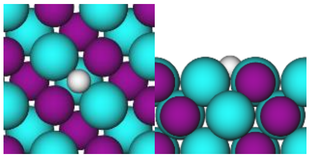	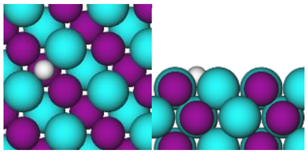
E0=	-295.70972902 d_{Ni-H}=1.86/1.86/1.86/1.86	-391.42238870 d_{Co-H}=1.90/1.90/1.90/1.90	-343.66270869 d_{Co-H}=1.90/1.90, d_{Ni-H}=1.87/1.87	-343.66953284 d_{Co-H}=1.90/1.90, d_{Ni-H}=1.87/1.87

C on (100) surfaces

Site	Ni/C @ h	Co/C @ h	NiCo/C @ h_C	NiCo/C @ h_N
	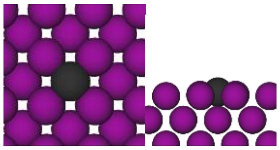	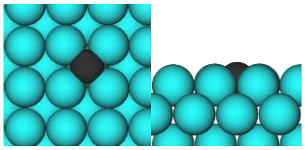	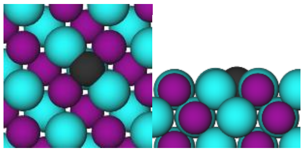	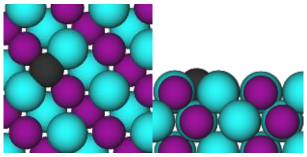
E0=	-300.94934499 d_{Ni-C}=1.85/1.85/1.85/1.85	-396.54758999 d_{Co-C}=1.88/1.88/1.88/1.88	-348.67742135 d_{Co-C}=1.86/1.86, d_{Ni-C}=1.87/1.87	-348.71392115 d_{Co-C}=1.85/1.85, d_{Ni-C}=1.88/1.88

CH on (100) surfaces

Site	Ni/CH @ h	Co/CH @ h	NiCo/CH @ h_C	NiCo/CH @ h_N
	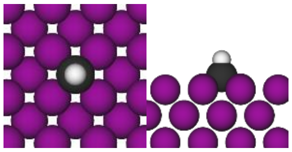	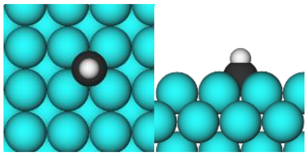	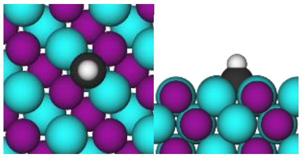	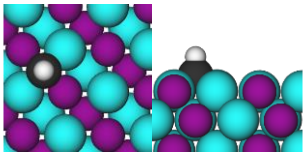
E0=	-304.61776645 d_{Ni-C}=1.94/1.94/1.94/1.94, d_{C-H}=1.11	-400.22081693 d_{Co-C}=1.97/1.97/1.97/1.97, d_{C-H}=1.11	-352.37142346 d_{Co-C}=1.95/1.95, d_{Ni-C}=1.96/1.96, d_{C-H}=1.11	-352.47777421 d_{Co-C}=1.96/1.96, d_{Ni-C}=1.97/1.97, d_{C-H}=1.11

CH_2 on (100) surfaces

Site	Ni/CH_2 @ h	Co/CH_2 @ h	NiCo/CH_2 @ h_C - bridge	NiCo/CH_2 @ h_N - bridge	NiCo/CH_2 @ h_N - Co
	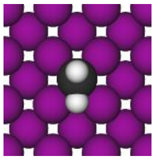 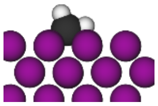	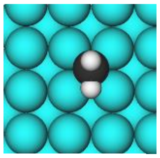 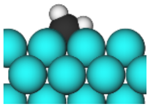	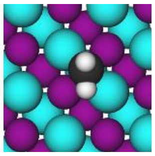 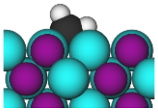	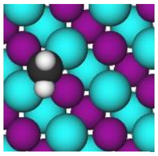 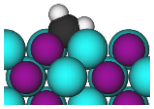	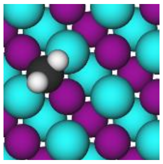 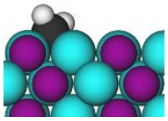
E0=	-307.84866428 d_{Ni-C}= 1.97/1.97/2.09/2.09, d_{C-H}=1.22/1.11, d_{Ni-H}=1.79/1.79, A_{HCH}=97.55	-403.50116730 d_{Co-C}= 2.02/2.02/2.16/2.16, d_{C-H}=1.18/1.11, d_{Co-H}=1.90/1.90, A_{HCH}=99.15	-355.65564461 d_{Co-C}=2.00/2.14, d_{Ni-C}=2.01/2.14, d_{C-H}=1.19/1.11, d_{Co-H}=1.88, d_{Ni-H}=1.89, A_{HCH}=98.75	-355.79405341 d_{Co-C}=2.00/2.16, d_{Ni-C}=2.00/2.15, d_{C-H}=1.19/1.11, d_{Co-H}=1.87, d_{Ni-H}=1.90, A_{HCH}=98.58	-355.78083907 d_{Co-C}=2.08/2.08, d_{Ni-C}=2.06/2.06, d_{C-H}=1.17/1.11, d_{Co-H}=1.77, A_{HCH}=96.54

CH_3 on (100) surfaces

Site	Ni/CH_2 @ b	Ni/CH_2 @ b (unstable)	Co/CH_3 @ h	NiCo/CH_3 @ b - Co	NiCo/CH_3 @ b - Ni
	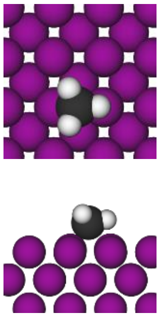	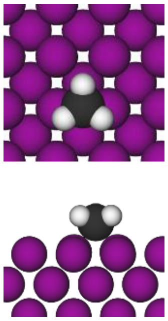	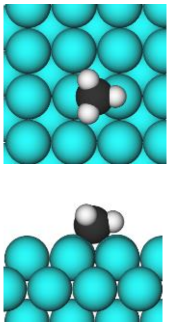	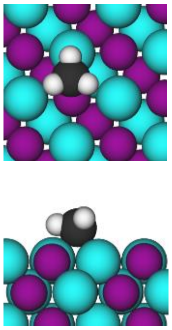	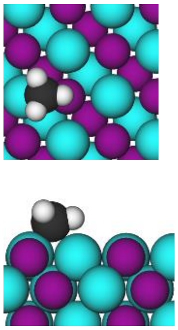
E0=	-311.61189387 $d_{Ni\text{-}C}$=2.02/2.16, $d_{C\text{-}H}$=1.14/1.10/1.10, $d_{Ni\text{-}H}$=1.88/2.50/2.50	-311.58176797 $d_{Ni\text{-}C}$=2.09/2.09, $d_{C\text{-}H}$=1.10/1.11/1.11, $d_{Ni\text{-}H1}$=2.72/2.72, $d_{Ni\text{-}H}$=2.11/2.13	-407.37304320 $d_{Co\text{-}C}$=2.07/2.22, $d_{C\text{-}H}$=1.13/1.10/1.10, $d_{Co\text{-}H}$=1.96/2.57/2.57	-359.62356230 $d_{Co\text{-}C}$=2.22, $d_{Ni\text{-}C}$=2.05, $d_{C\text{-}H}$=1.13/1.10/1.10, $d_{Co\text{-}H}$=1.94, $d_{Ni\text{-}H}$=2.55/2.54	-359.60463947 $d_{Co\text{-}C}$=2.07, $d_{Ni\text{-}C}$=2.19, $d_{C\text{-}H}$=1.13/1.10/1.10, $d_{Co\text{-}H}$=2.57/2.51, $d_{Ni\text{-}H}$=1.94

A6.6 Carbon chains

Reaction energies on Fig. 26 of the main text are computed $E_{Cn}+E_{sup}-E_{Cn\text{-}1}+E_C$ starting with E_C in one of the most stable C adsorption sites. Geometries, electronic energies (in eV) and main geometric distances ($d_{A\text{-}B}$ in Å, C in chains numbered from left to right) are presented below.

Table S14 Energies and geometric parameters of C_n species and chains on the model surfaces

Model	Co(111)/C1	Co(111)/C2	Co(111)/C3	Co(111)/C4	Co(111)/C5
	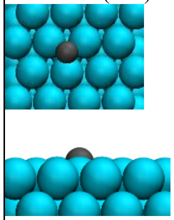	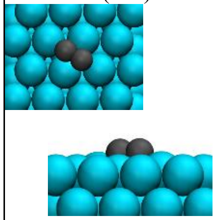	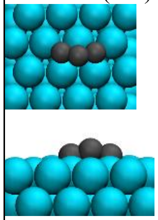	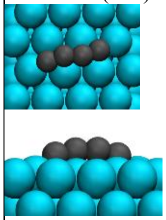	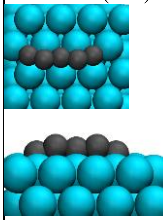
E0=	-403.74626185 $d_{Co\text{-}H}$=1.76/1.76/1.76	-412.02711286 $d_{C\text{-}C}$= 1.34, $d_{Co\text{-}C}$= 2.04/ 1.91/ 2.03, $d_{Co\text{-}C2}$= 2.04/ 2.04/ 1.90	-420.12877459 $d_{C\text{-}C}$= 1.36/ 1.37, $d_{Co\text{-}C1}$= 2.04/ 1.95/ 1.87, $d_{Co\text{-}C3}$= 2.03/ 1.95/ 1.86, $d_{Co\text{-}C2}$= 2.01/ 2.39/ 2.39	-428.30426440 $d_{C\text{-}C}$= 1.34/1.37/ 1.34, $d_{Co\text{-}C1}$= 2.02/ 2.08/ 1.89, $d_{Co\text{-}C4}$= 1.88/ 2.07/ 2.02	-436.38031157 $d_{C\text{-}C}$= 1.35/ 1.36/ 1.36/ 1.35, $d_{Co\text{-}C1}$= $d_{Co\text{-}C5}$= 2.04/ 1.87/ 1.96, $d_{Co\text{-}C3}$= 2.22/ 2.23/ 2.02

Table S14 (cont) Energies and geometric parameters of C_n species and chains on the model surfaces

Model	Ni(111)/C1	Ni(111)/C2	Ni(111)/C3	Ni(111)/C4	Ni(111)/C5
	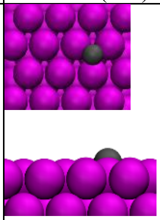	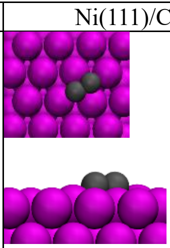	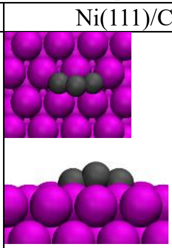	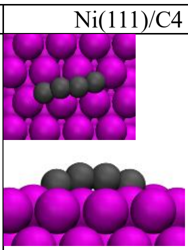	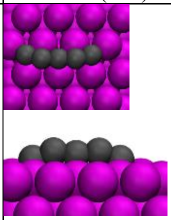
E0=	-306.07358952 d_{Ni-H}=1.72/1.72/1.72	-314.26031641 d_{C-C}= 1.34, d_{Ni-C1}= 2.02/ 2.02/ 1.87, d_{Ni-C2}= 2.01/ 2.01/ 1.87	-322.25405774 d_{C-C}= 1.36/ 1.36, d_{Ni-C1}=d_{Ni-C3}= 1.85/ 2.06/ 1.96, d_{Ni-C2}= 2.04/ 2.04/ 2.01	-330.47703184 d_{C-C}= 1.34/ 1.36/ 1.34, d_{Ni-C1}= 1.99/ 2.06/ 1.85, d_{Ni-C4}= 2.04/ 1.86/ 1.97	-338.45952531 d_{C-C}= 1.34/ 1.35/ 1.35/ 1.34, d_{Ni-C1}= 1.84/ 2.04/ 1.94, d_{Ni-C5}= 1.84/ 2.04/ 1.93, d_{Ni-C3}= 2.31/ 2.33/ 1.98

Table S14 (cont) Energies and geometric parameters of C_n species and chains on the model surfaces

Model	NiCo(111)/C1 –l	NiCo(111)/C2 -l	NiCo(111)/C3 -l	NiCo(111)/C4 -l	NiCo(111)/C5 -l
-l along Co/Ni lines	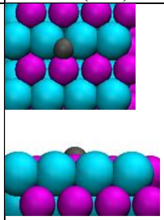	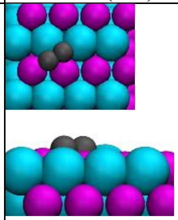	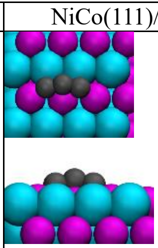	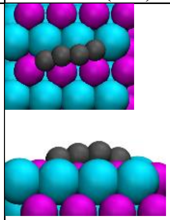	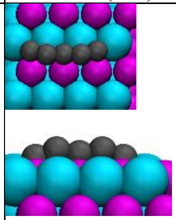
E0=	-354.87504482 d_{Ni-C}=1.84, d_{Co-Ni}=1.78/1.78	-363.04751038 d_{C-C}= 1.34, d_{Co-C1}= 1.90/ 2.04, d_{Ni-C1}= 2.04, d_{Co-C2}= 2.00, d_{Ni-C2}= 2.04/ 1.89	-370.81283375 d_{C-C}= 1.36/ 1.36, d_{Ni-C1}=d_{Ni-C3}=1.87/2.10, d_{Co-C1}=d_{Co-C3}=1.92, d_{Co-C2}=2.34/2.34, d_{Ni-C2}=2.01	-379.25555209 d_{C-C}= 1.34/ 1.36/ 1.33, d_{Ni-C1}= 1.89/ 2.07, d_{Co-C1}=1.97, d_{Ni-C4}=2.04, d_{Co-C4}= 1.87/ 2.05	-387.40543628 d_{C-C}= 1.34/ 1.36/1.36/ 1.34, d_{Co-C1}= 1.87/ 2.03, d_{Ni-C1}= 2.00, d_{Co-C5}=2.03/ 1.87, d_{Ni-C5}= 2.00

Table S14 (cont) Energies and geometric parameters of C_n species and chains on the model surfaces

Model	NiCo(111)/C1 -t	NiCo(111)/C2 -t	NiCo(111)/C3 -t	NiCo(111)/C4 -t	NiCo(111)/C5 -t
-t along Co/Ni lines	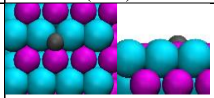	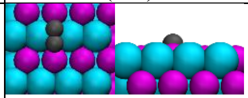	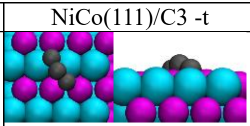	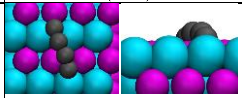	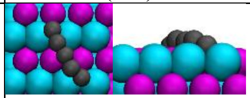
E0=	-354.87504482 d_{Ni-C}=1.84, d_{Co-Ni}=1.78/1.78	-363.14279503 d_{C-C}=1.34, d_{Co-C1}= d_{Co-C2}= 2.04/ 2.02, d_{Ni-C1}= d_{Ni-C2}= 1.98 (C-C in line in this view)	-371.02048088 dC-C= 1.36/ 1.36, dCo-C1=1.92/ 2.06, dNi-C1= 1.88, dNi-C2= 1.97/ 1.86, dCo-C2= 2.03	-379.26773842 d_{C-C}= 1.33/ 1.36/ 1.34, d_{Co-C1}= 1.99/ 2.08, d_{Ni-C}= 1.89, d_{Ni-C4}=2.06/ 2.01, d_{Co-C4}= 1.87	-387.31007518 d_{C-C}= 1.35/ 1.35/ 1.36/ 1.35, d_{Co-C1}= 2.02, d_{Ni-C1}=1.86/1.98, d_{Co-C5}=1.86, d_{Ni-C}= 2.29, d_{Ni-C5}=2.06/ 1.99, d_{Co-C3}=2.32/ 2.02,

Table S14 (cont) Energies and geometric parameters of C_n species and chains on the model surfaces

Model	Co(100)/C1	Co(100)/C2	Co(100)/C3	Co(100)/C4	Co(100)/C5
E0=	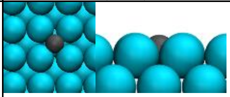 -396.54758999 d_{Co-C}= 1.88/ 1.88/ 1.88/ 1.88 (C in plane with surface)	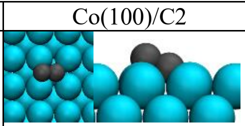 -403.71112218 d_{C-C}= 1.35, d_{Co-C1}= 1.94/ 1.94/ 2.18/ 2.18, d_{Co-C2}= 1.94/ 1.94	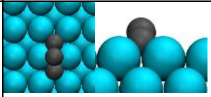 -412.78029716 d_{C-C}= 1.39/1.39, d_{Co-C1}= d_{Co-C1}= 1.99/1.99/ 2.08/ 2.08 (C-C-C in line)	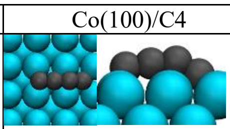 -420.29728414 d_{C-C}=1.35/ 1.34/ 1.34, d_{Co-C1}= 1.93/ 1.93/ 2.22/ 2.22, d_{Co-C4}= 1.91/ 1.91	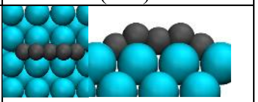 -429.41286208 d_{C-C}= 1.37/ 1.37/ 1.37/ 1.37, d_{Co-C1}= d_{Co-C2}= 1.98/ 1.98/ 2.10/ 2.10

Table S14 (cont) Energies and geometric parameters of C_n species and chains on the model surfaces

Model	Ni(100)/C1	Ni(100)/C2	Ni(100)/C3	Ni(100)/C3-2	Ni(100)/C4	Ni(100)/C5	Ni(100)/C5-2
E0=	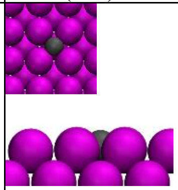 -300.94934499 d_{Ni-C}= 1.85/ 1.85/ 1.85/ 1.85 (C in plane with surface)	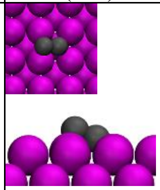 -307.92255416 d_{C-C}= 1.35, d_{Ni-C1}= 1.88/ 1.88/ 2.21/ 2.21, d_{Ni-C2}= 1.91/ 1.91	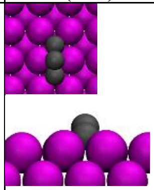 -317.08637608 d_{C-C}= 1.39/ 1.39, d_{Ni-C1}= d_{Ni-C3}= 1.93/ 1.93/ 2.10/ 2.10	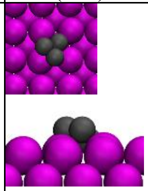 -314.54362074 d_{C-C}= 1.40/ 1.54/ 1.54, d_{Ni-C1}= 1.98/ 1.78/ 1.98/ 2.51, d_{Ni-C2}= d_{Ni-C3}= 2.03/ 1.93	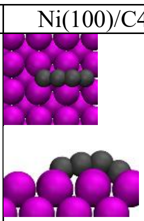 -324.57694819 d_{C-C}= 1.34/ 1.33/ 1.34, d_{Ni-C1}=1.85/1.85, d_{Ni-Cn}=1.86/1.86	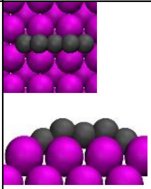 -333.65392743 d_{C-C}= 1.37/ 1.37/ 1.37/ 1.37, d_{Ni-C1}= d_{Ni-C5}= 1.93/ 1.93/ 2.09/ 2.09	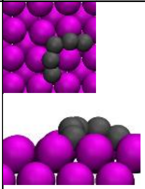 -332.65410396 d_{C-C}= 1.36/ 1.41/ 1.41/ 1.36, d_{Ni-C1}= 1.90/ 1.94/ 2.12/ 2.22, d_{Ni-Cn}= 1.89/ 1.94/ 2.12/ 2.22

Table S14 (cont) Energies and geometric parameters of C_n species and chains on the model surfaces

Model	NiCo(100)/C1	NiCo(100)/C2	NiCo(100)/C3	NiCo(100)/C4	NiCo(100)/C5
E0=	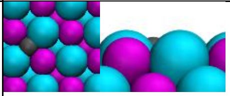 -348.71392115 d_{Co-H}=1.90/1.90, d_{Ni-H}=1.87/1.87 (C in plane with surface)	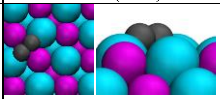 -356.17773423 d_{C-C}=1.32, d_{Ni-C1}= d_{Ni-C2}= 2.15/ 2.15, d_{Co-C1}= d_{Co-C2}=1.82	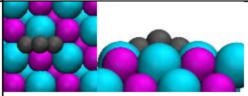 -364.90018887 d_{C-C}= 1.39/ 1.39, d_{Co-C1}= 2.08/ 1.98, d_{Ni-C1}=2.11/1.97, d_{Ni-C2}=2.12/1.97, d_{Co-C2}= 2.10/1.97, d_{Ni-C2}=2.02, d_{Co-C2}= 1.98	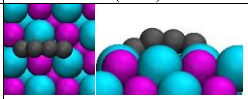 -372.40996148 d_{C-C}= 1.34/ 1.34/ 1.34, d_{Ni-C1}= 1.91/ 2.30, d_{Co-C1}= 2.29/ 1.90, d_{Ni-C4}=1.92, d_{Co-C4}=1.87	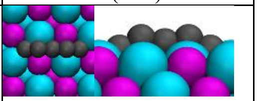 -381.49634639 d_{C-C}=1.37/1.37/1.37/1.37, d_{Ni-C1}= 1.97/ 2.12, d_{Co-C1}= 2.10/ 1.96, d_{Co-C5}=2.11/1.96, d_{Ni-C5}= 2.11/ 1.97, d_{Ni-C3}=2.27/2.27, d_{Co-C3}= 2.25/ 2.25

A6.7 *C as descriptor of CH_x binding strength

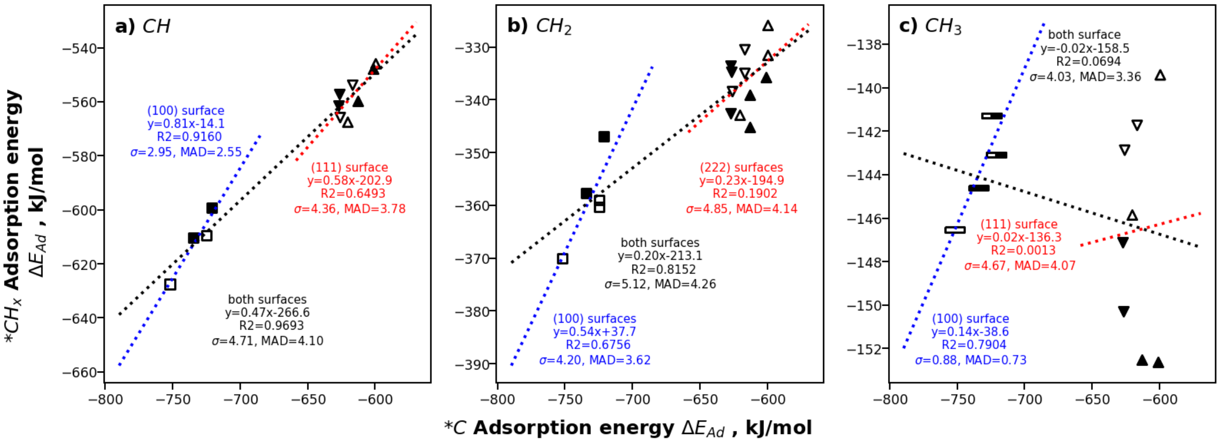

Fig. S9 Adsorption energy of *C to simultaneously describe adsorption of CHx species on (111) and (100) surfaces

A6.8 *C and *O describe some $*CO_xH_y$ binding strengths

Following the descriptor analysis, Fig. S10 shows the ability of *C and *O to describe the adsorption strength of some $*CO_xH_y$ species. In particular, the *HCOH on (111) surfaces bind closer to bridge sites but blocking a three-fold sites, which explains its poorer description from three-fold *C binding energies.

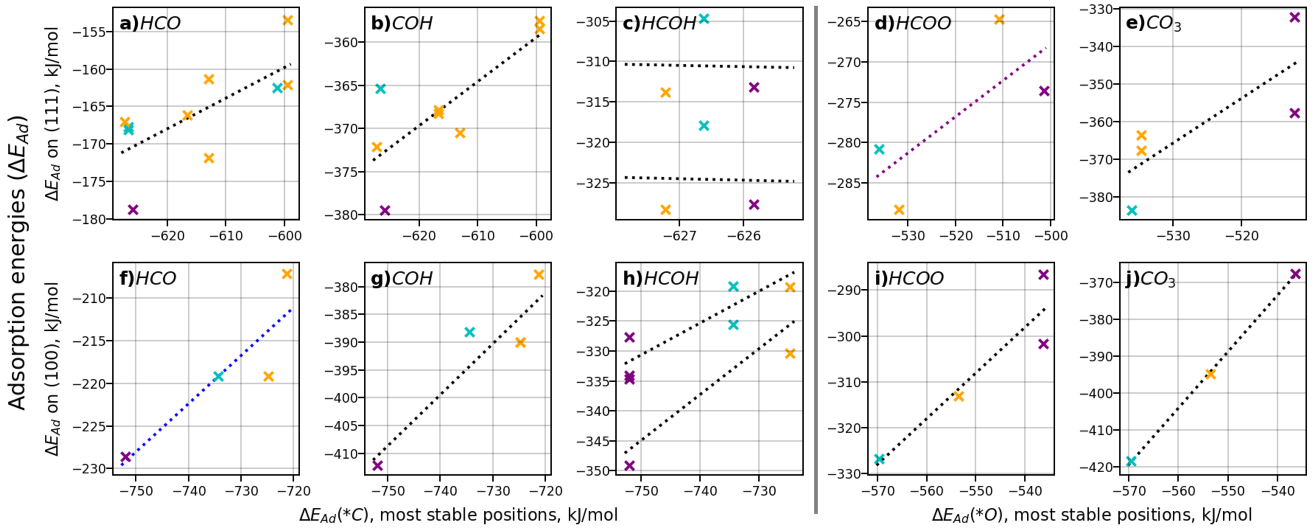

Fig. S10 *C as descriptor for the adsorption strength of (a,f) HCO, (b,g) COH and (c,h) HCOH. *O as descriptor for the binding strength of (d,i) HCOO and (e,j) CO_3

A7 Reaction profiles

A7.1 Construction of reaction profiles

The detailed sequence of reaction steps used for the construction of the reaction profiles included in the main text are detailed in Scheme S1. The nomenclature is as follows: {*A+*B} represent the slab model with *A and *B co-adsorbed, {} is an empty slab, {C} would be the cell with C physisorbed on a clean slab and (C) is C as gas in an empty cubic cell. TS denotes reactive steps for which transition states were computed, other steps correspond to migrations and reconfigurations for which the activation energies are considered not relevant in comparison. Merging points for the profile sections are denoted by numbers in parenthesis.

Scheme S1 Reaction steps for the construction of energy profiles. {*A} for surface models with adsorbed A, {} for empty surface models and (G) for gas models.

CO_2 dissociation		
	$(CO_2)+\{\} \rightarrow \{*CO_2\}$	Chemisorption
→(1)	$\{*CO_2\}\rightarrow \{*CO+*O\}$	Direct dissociation
Direct dissociation		
(1) → (2)	$\{*CO+*O\}+\frac{1}{2}(H_2)+\{\} ->\{*CO\}+\{*O+*H\}$	Separation + H_2 dissociative adsorption
	$\{*CO\}\rightarrow \{*C+*O\}$	Direct carbonyl dissociation
→ (3), (2)	$\{*C+*O\}+\frac{1}{2}(H_2)+\{\}\rightarrow \{*C\}+\{*O+*H\}$	Separation + H_2 dissociative adsorption
HCO route		
(1) → (2)	$\{*CO+*O\}+(H_2)+\{\} \rightarrow \{*CO+*H\}+\{*O+*H\}$	Separation + H_2 dissociative adsorption
	$\{*CO+*H\}\rightarrow \{*HCO\}$	*HCO formation
	$\{*HCO\}\rightarrow \{*CH+*O\}$	*HCO dissociation
→ (4), (2)	$\{*CH+*O\}+\frac{1}{2}(H_2)\rightarrow \{*CH\}+\{*O+*H\}$	Separation + H_2 dissociative adsorption
COH route		
(1) → (2)	$\{*CO+*O\}+(H_2)+\{\} \rightarrow \{*CO+*H\}+\{*O+*H\}$	Separation + H_2 dissociative adsorption
	$\{*CO+*H\}\rightarrow \{*COH\}$	*COH formation
	$\{*COH\}\rightarrow \{*C+*OH\}$	*COH dissociation
→ (5), (2)	$\{*C+*OH\}+\{\}\rightarrow \{*C\}+\{*OH\}$	Separation by hydroxyl migration
O elimination		
(2) →	$\{*O+*H\}\rightarrow \{*OH\}$	Hydroxyl formation
(5) →	$\{*OH\}+\frac{1}{2}(H_2)\rightarrow\{*OH+*H\}$	H_2 dissociative adsorption
	$\{*OH+*H\}\rightarrow \{H_2O\}$	Formation of adsorbed water
	$\{H_2O\} \rightarrow (H_2O) + \{\}$	H_2O release
CH_x hydrogenation		
(3) →	$\{*C\}+\frac{1}{2}(H_2)->\{*C+*H\}$	H_2 dissociative adsorption
	$\{*C+*H\}\rightarrow \{*CH\}$	*CH formation
(4) →	$\{*CH\}+\frac{1}{2}(H_2)->\{*CH+*H\}$	H_2 dissociative adsorption
	$\{*CH+*H\}\rightarrow \{*CH_2\}$	$*CH_2$ formation
	$\{*CH_2\}+\frac{1}{2}(H_2)->\{*CH_2+*H\}$	H_2 dissociative adsorption
	$\{*CH_2+*H\}\rightarrow \{*CH_3\}$	$*CH_3$ formation
	$\{*CH_3\}+\frac{1}{2}(H_2)\rightarrow \{*CH_3+*H\}$	H_2 dissociative adsorption
	$\{*CH_3+*H\}\rightarrow \{CH_{4(gas)}\}$	Physisorbed CH_4 formation
	$\{CH_{4(gas)}\}\rightarrow \{\} + (CH_{4(gas)})$	CH_4 release

A7.2 PDOS of the activation of CO_2

The activation of CO_2 was studied though the DOS of free gas phase $CO_{2(g)}$ (Fig. S11a-c) and on metallic surfaces using the Ni(100) surface as example (Fig. S11d-f). For the relaxed models

Fig. S11a show similar contributions of both O atoms to the $2\Sigma_u$ (and other) molecular orbitals (MO), bending and extending (Fig. S11b) one C-O bond moves the $2\Sigma_u$ MO close to the fermi level and the $4\Sigma_g$ MO to lower energies, also splitting the degenerate $2\Sigma g$, $1\Pi_u$ and the $1\Pi_u$ MO. PDOS contributions to the activated $CO_{(2)}$-$O_{(1)}$ geometry shows the $2\Sigma_u$ has a mayor contribution of the leaving $O_{(1)}$ atom and the lower part of the split $3\Sigma_g$ still interacting with the C and other O atom. The Fig. S11d,f shows the displacement of a DOS peak at an equivalent position of the $2\Sigma_u$ between the initial and final geometries of the *CO_2 activation on Ni(100). PDOS contributions on Fig. S11e for the transition state shows that this peak is mostly formed by the leaving $O_{(1)}$ atom. As discussed by Vogt et al.[26], the activation of this peak is considered a relevant part of the dissociation of chemisorbed CO_2.

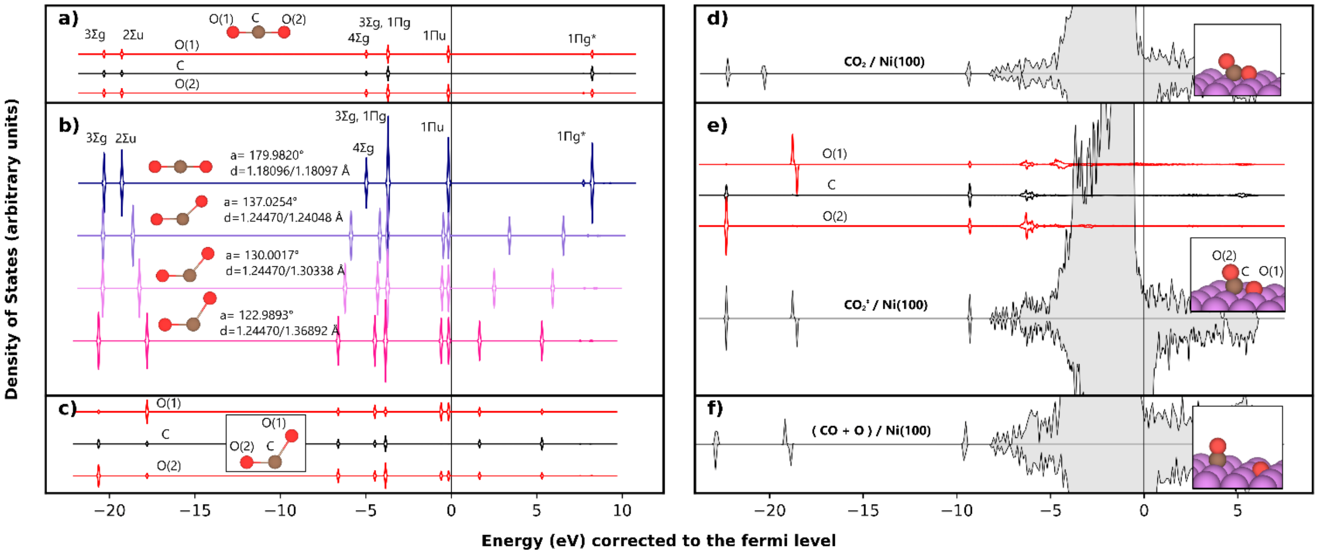

Fig. S11 DOS for the activation of CO_2. In gas phase: (a) PDOS contributions of the relaxed molecule, (b) DOS bending and extending one C-O bond and (c) PDOS contributions for the activated geometry. On Ni(100): (d) initial DOS, (e) PDOS and DOS of the transition state, (f) final DOS.

A7.3 High coverage CO_2 activation

Adsorption and activation of $CO_{2(g)}$ was studied in surfaces pre-covered with six co-adsorbed *CO (Fig. S12) to assess the electronic effect of the surfaces also donating charge to spectator species[52], Fig. S12 shows the surface configurations,

Table S16 details energetics of the adsorption and reactive step. Test at higher coverages desorbed the CO_2 molecule, six *CO were used since on-surface comparisons are desirable and coverages around ½ ML (7-9 *CO total) are reasonable experimentally. To maintain a reasonable

---

[52] Long range interactions also are expected play a role when the coverage is increased. The contribution of these interactions to the differences from the low coverage results is not properly accounted and underrepresented by DFT-RPBE. Moreover, classic dispersion corrections depend only on the geometry, thus their effect is considered mostly systematic and independent of the electronic nature of the surfaces. Therefore, the effects discussed are more representative of the electronic effect of the surface also donating electronic charge to nearby spectators.

computational cost a 3x3x1 k-point mesh was employed[53] (Table S15 shows a negligible effect), electronic convergence criteria was increased to 10^{-6} eV, the two topmost layers and all surface species were relaxed until forces were below 0.05 eV/Å. Frequency calculations considered only the reactive species. A few arrangements of the co-adsorbed *CO were tested looking for more stable configurations where these spectators did not significantly change their adsorption mode through the reaction, this way energy differences in the main text (Fig. 35) represent only the adsorption and reaction under study. Bader charges of the initial models confirm that spectator *CO species draw electron density from the surfaces the reaction takes place in (Co(111):2.78e, Ni(111):2.87e, Co(100):2.41, NiCo(100):2.15e, Ni(100):2.91e), specific values will depend on the configuration and adsorption modes includes but results from systems in Fig. S12 (Fig. 35) provide some insight on the general effect of the coverage.

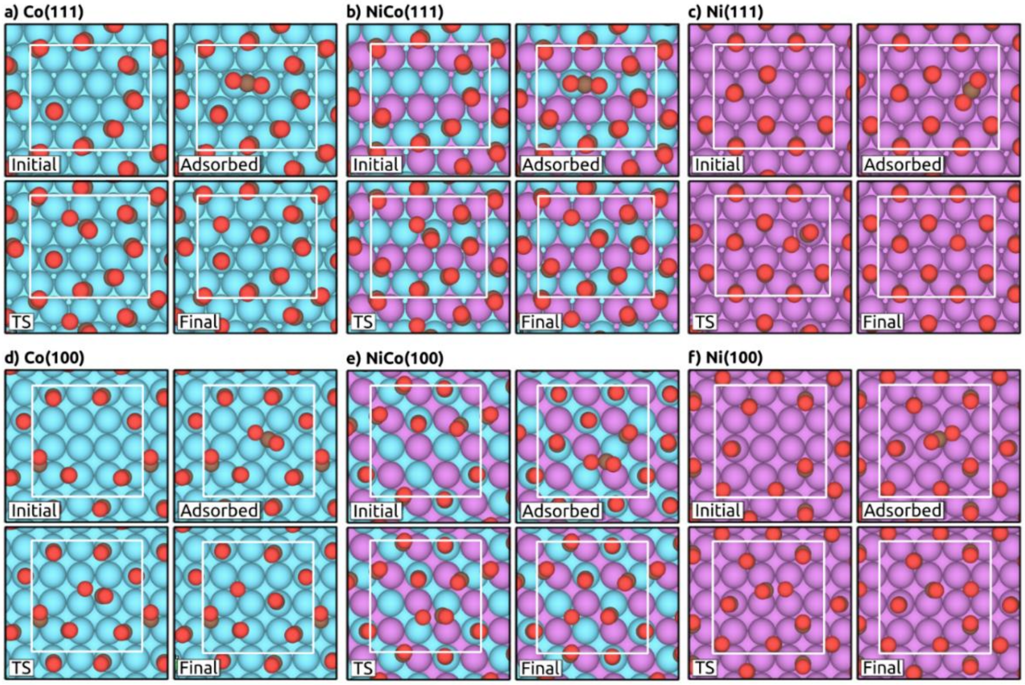

Fig. S12 $CO_{2(g)}$ adsorption and activation on Co (a,d), NiCo(b,e) and Ni (c,f), (111) and (100) surfaces (respectively) precovered with six *CO. White square demarks the unit cell.

Table S15 Comparison of reaction (ΔE_{rx}) and activation (E_a) electronic energies with reduced k-point mesh, energies in eV (kJ/mol in parentheses).

	{*CO_2}	Transition state	{CO+O}	ΔE_{rx}	E_a(f)
3x3x1	-368,8325631	-368,5873187	-369,6761974	-0,84363427	0,24524445
4x4x1	-368,8943048	-368,6581389	-369,7373097	-0,84300486	0,23616586
Diff.				0,00062941 (0.06 kJ/mol)	-0,00907859 (-0,88 kJ/mol)

---

[53] This reduced the number of k-points from 8 in the standard 4x4x1 k-point meshes to 5 with the 3x3x1 k-point mesh (all these for spin up and down, non-symmetrized calculations).

Table S16 $CO_{2(g)}$ adsorption (ΔG_{ads}), $*CO_2$ activation (ΔG_a) and dissociation (ΔG_{rx}) free energies (kJ/mol) on clean surfaces and coadsorbed with six *CO spectators.

Surface	Co		NiCo		Ni	
	ΔG_{ads}	ΔG_a (ΔG_{rx})	ΔG_{ads}	ΔG_a (ΔG_{rx})	ΔG_{ads}	ΔG_a (ΔG_{rx})
(111) -clean	111	25.97(-99.72)	108	24.15(-77.53)	111	52.93(-74.65)
(111) -$(CO)_6$	136	51.50(-64.79)	124	57.32(-21.95)	139	62.62(-67.40)
(100) -clean	69	26.02(-112.72)	70	27.40(-82.62)	74	32.23(-87.81)
(100) -$(CO)_6$	84	33.75(-96.91)	100	29.27(-83.08)	106	42.20(-78.77)

A8 Kinetic Isotopic effect

Table S17 extends Table 10 including KIE values for the H_2/D_2 exchange at higher temperatures, the discussion from the main text holds for the Ni/SiO_2 and $Ni_{0.5}Co_{0.5}/SiO_2$ catalysts and is expected to be also valid for the Co/SiO_2.

Table S17 Experimental KIE (1kPa $CO_{2(g)}$, 25 kPa $H_{2(g)}$, He balance)

	Co/SiO_2	$Ni_{0.5}Co_{0.5}/SiO_2$			Ni/SiO_2		
	250°C	250°C	265°C	280°C	250°C	265°C	280°C
KIE - $CO_{(g)}$	1.01	1.06	0.94	0.95	1.02	1.00	0.97
KIE - $CH_{4(g)}$	0.79	0.90	0.77	0.80	0.79	0.77	0.77

A8.1 C-O bond breaking steps

This section details the bond breaking steps discussed in sec. 8.3 of the main text. Fig. S13 - Fig. S16 show the geometries of the reaction steps included in Fig. 36 of the main text.

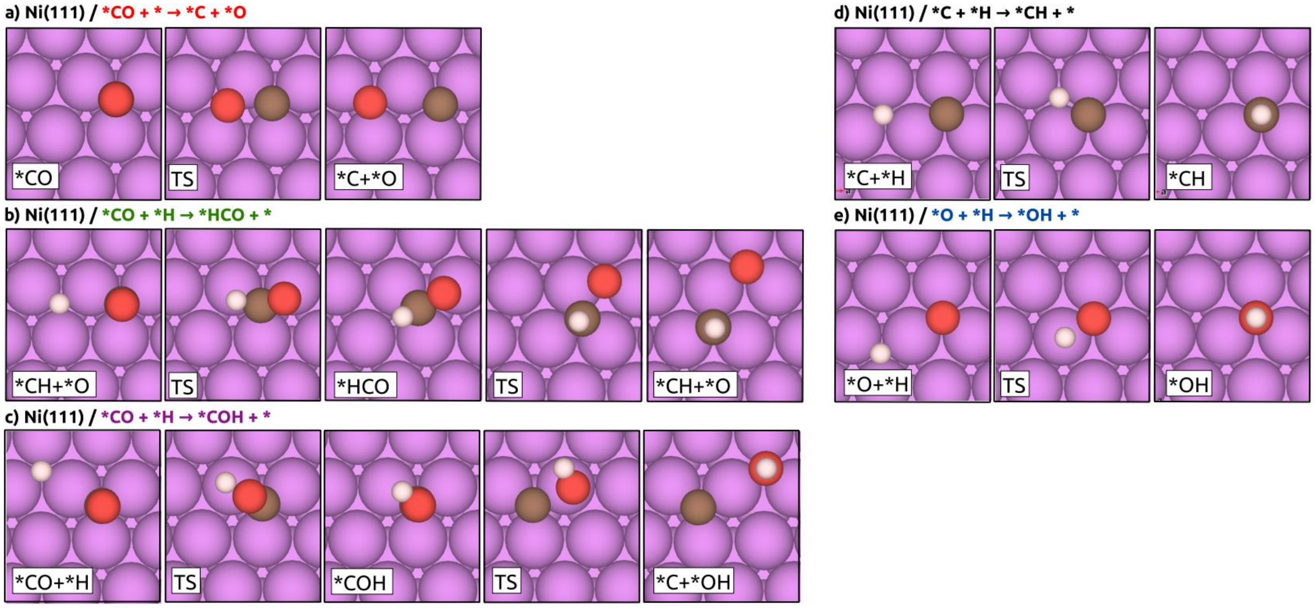

Fig. S13 *C-O breaking routes on Ni(111): a) direct, b) H-assisted HCO, c) H-assisted COH and associated steps (d,e) included in Fig. 36 of the main text. Colors are purple: Ni, red: O, white: H.

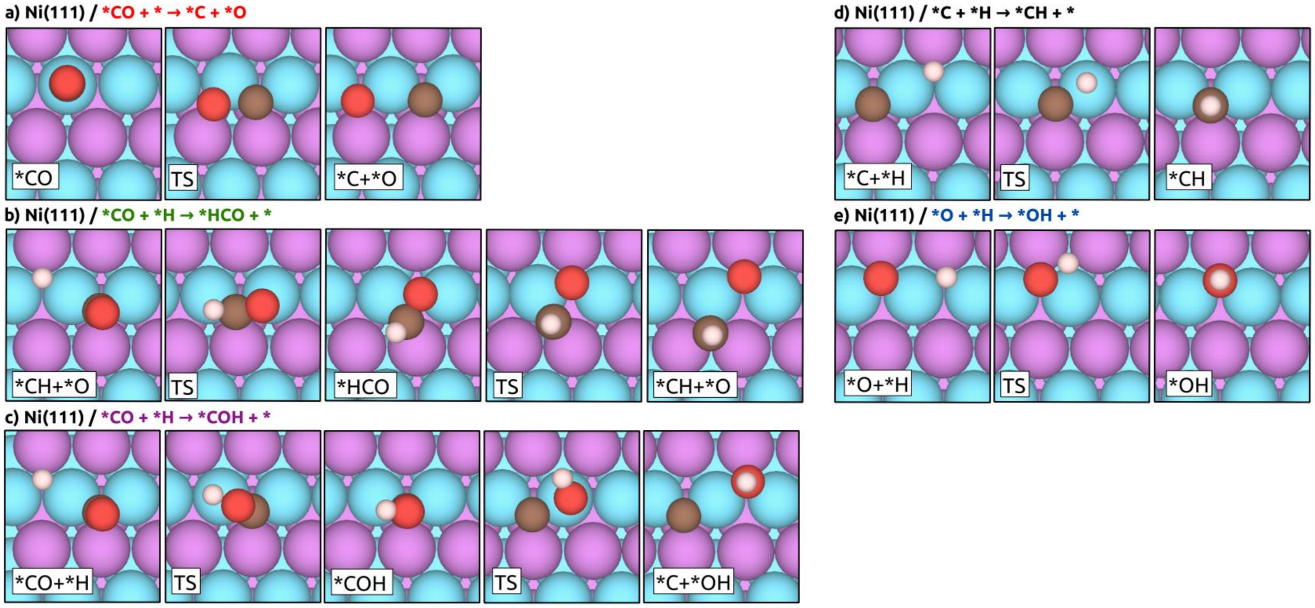

Fig. S14 *C-O breaking routes on NiCo(111): a) direct, b) H-assisted HCO, c) H-assisted COH and associated steps (d,e) included in Fig. 36 of the main text. Colors are purple: Ni, cyan: Co, red: O, white: H.

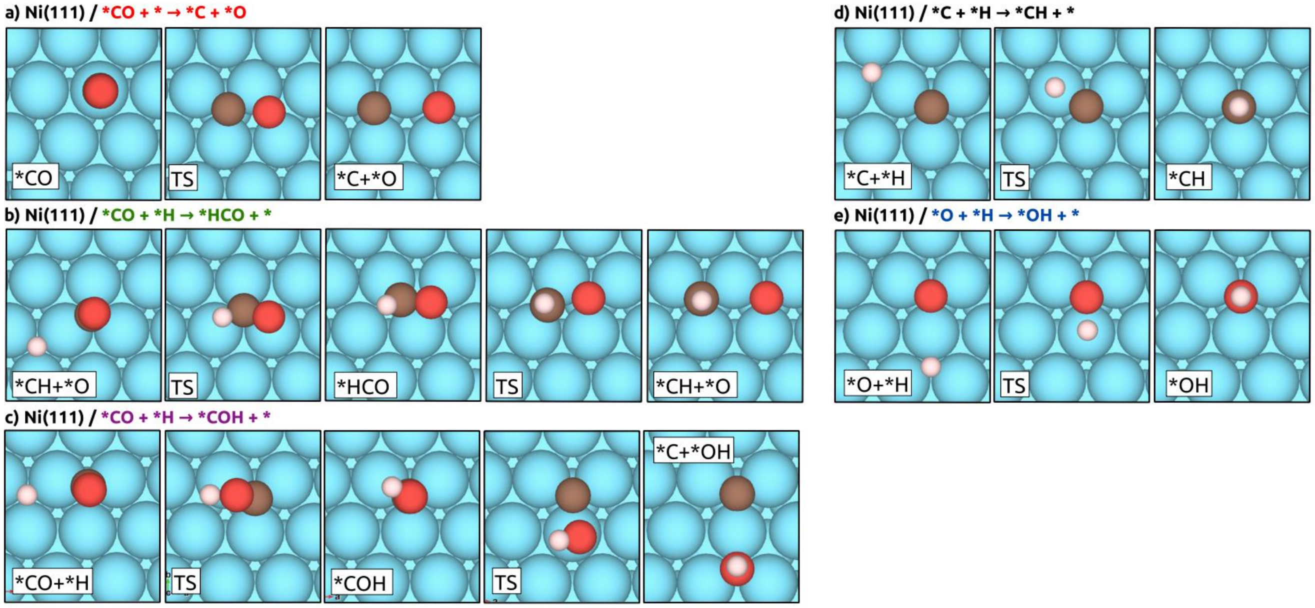

Fig. S15 *C-O breaking routes on Co(111): a) direct, b) H-assisted HCO, c) H-assisted COH and associated steps (d,e) included in Fig. 36 of the main text. Colors are cyan: Co, red: O, white: H.

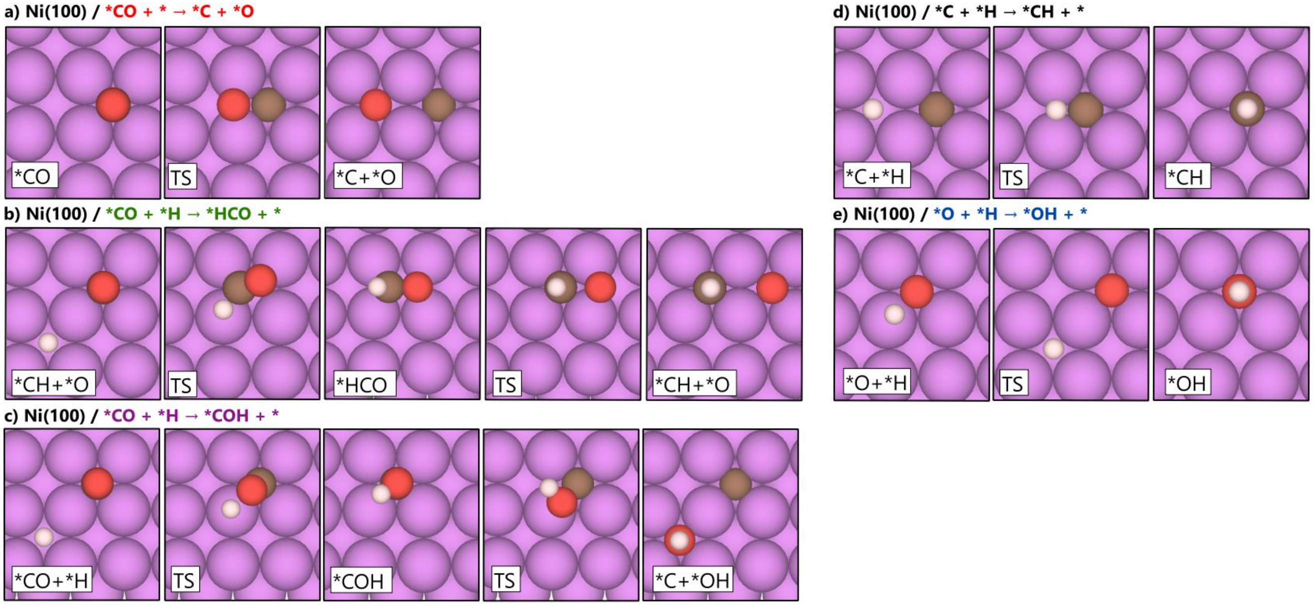

Fig. S16 *C-O breaking routes on Ni(100): a) direct, b) H-assisted HCO, c) H-assisted COH and associated steps (d,e) included in Fig. 36 of the main text. Colors are purple: Ni, red: O, white: H.

A8.2 Alternative reaction routes to break the second C-O bond

It should be noted that the reaction may proceed through a different mechanism with step combinations not included in Fig. 36, additional steps were only briefly explored[54]. It should be considered first that the presented work focusses on the comparison of catalysts for which different surface compositions and geometries are considered. This translated in the six surface models employed on which any reaction step under consideration had to be studied separately. For this multiplicity and the computational cost of using large models with high precision and thigh convergence parameters (compared to similar studies) an even more cautious selection of a limited number of possible pathways to explore was compulsory. To this end, the in-situ FTIR results provided valuable insight on the identity and abundance of surface intermediates, kinetic and isotopic experiments clarified the involvement of H in kinetically relevant steps. Published theoretical studies involving reaction mechanisms for the CO and CO_2 activation and methanation, and dry reforming of methane and even Fischer Tropsch Synthesis processes on Ni, Co and other transition metal surfaces were thoughtfully considered to identify possible reaction pathways from CO_2 to CH_4 and the steps most often reported as the preferred routes. This constant process of search, contrast with experimental results led to the routes presented in the main text, though several other possible pathways were sketched or briefly tested.

In particular, the routes proposed by the reviewer are chemically consistent and deserve individual discussions:

---

[54] Keep in mind that each new step required the lengthy identification of 6 transition states through neb, dimer and frequency calculations. Adding reaction routes to the study becomes prohibitive when six surfaces are simultaneously under consideration.

(1) A *COOH intermediate could be initially formed from CO2(g)/*CO2 +*H in a similar fashion that the formate intermediate (*HCOO), however no experimental evidence of a COOH intermediate was identified from the FTIR in-situ results to initially justify the study of its formation or dissociation towards methanation intermediates. The absence of recognizable COOH species also suggest routes directly derived are not probable, such as HCOOH. In contrast, the FTIR identification of stable formate intermediates should be considered. In their case, the dynamic evolution of HCOO surface populations (area under the curve *in lieu* of coverage) is not consistent with the evolution of products, hence their direct participation on the reaction mechanism was ruled out.

(2) Experimentally, methanol is reportedly not formed on Ni or Co catalyst and no experimental evidence indicating the formation of CH_3OH was observed in the presented work (e.g., unexpected peaks in the Gas Chromatography during the kinetic study) for any of the studied catalysts. Adding the lack of FTIR indicators for methanol-related intermediates such H_2COH and H_3COH and sounding signals in the GC and Mass spectrometry the inclusion of such species and their formation/dissociation steps that may led to the from the simpler and more commonly proposed methane intermediates (*CO, *HCO, *COH and *CHx). It is recognized, however, that the contribution of early methanol related steps (e.g. involving surface HCOH) may not be evident from the experimental evidence analyzed. In particular, the lower second barrier of the COH path is attributed to a weaker bond between C-O since O has now sp_3 hybridization forming the O-H bond, consequently, a second hydrogenation of HCO was also tested (following[55] *HCO+*H→**HCOH→*CH+*OH), but the *HO-OH* resulted in higher barriers[56] in agreement other studies[76].

(3) The suggested *HCO ↔ *COH interconversion is particularly interesting considering the C-O splitting profiles on (100) surfaces (Chapter 8.3, Fig. 36 d-f in the main text). These activation steps shows lower formation barriers for *HCO than *COH (from *CO+*H) but lower dissociation barriers for *COH+*→*C+*OH than for *HCO→*O+*CH. Thus, an HCO→COH step with a moderate barrier would connect the lower barriers of both routes. The study of an *HCO↔*COH interconversion was considered and neb paths were proposed but their initial relaxations showed a significant energy decrease mid-path. These initial calculations suggested that approaching the required configuration for an *HCO↔*COH interconversion favored the interaction of the migrating *H with the surface promoting the dissociation to stable co-adsorbed *CO+*H. This suggested that the interconversion most favorably occurs via a stable intermediate *CO+*H (i.e., COH -> CO+H -> HCO) which is already represented in the profiles (Fig 36, main text). Additionally, other studies[1], [3] did not show such interconversion, supporting the decision to prioritize the inclusion of other steps in this work.

---

[55] Cis-bidentate HCOH was considered for geometric consistency and to maximize interaction with the surface, promoting CH and OH binding to separate sites.

[56] Note that the **HCOH intermediate may help connecting *HCO and *COH species[113], complexing more the explored pathways.

Therefore, based on the experimental observations, previous studies and chemical consistency the studied routes were considered the most probable to have a significant contribution to the overall reaction rate for the studied surfaces that justified their study. Conversely, it is expected that the disregarded pathways do not contribute significantly, though should be remembered that the possibility of not considering a more favorable route is unavoidable in the current approach to surface reaction studies.

A8.3 Reaction energies

Table S18 Activation and reaction energies for the simulated steps (265 °C)

Surface		(111)			(100)	
	Co	NiCo	Ni	Co	NiCo	Ni
$*CO_2 \rightarrow *CO + *O$	26 (-100)	24 (-76)	53 (-74)	26 (-113)	27 (-83)	32 (-88)
$*CO \rightarrow *C + *O$	243 (115)	266 (125)	292 (177)	156 (-8)	178 (24)	192 (25)
$*CO + *H \rightarrow *HCO$	139 (124)	136 (127)	140 (127)	100 (78)	124 (79)	136 (96)
$*HCO \rightarrow *CH + *O$	70 (-41)	84 (-12)	102 (-11)	93 (-102)	110 (-42)	116 (-43)
$*CO + *H \rightarrow *COH$	177 (90)	188 (103)	192 (108)	169 (76)	174 (76)	172 (80)
$*COH \rightarrow *C + *OH$	146 (34)	159 (40)	180 (68)	76 (-81)	96 (-63)	92 (-57)
$*C + *H \rightarrow *CH$	65 (-30)	58 (-33)	55 (-53)	66 (17)	62 (6)	72 (24)
$*CH + *H \rightarrow *CH_2$	50 (30)	45 (27)	57 (31)	58 (46)	54 (41)	64 (60)
$*CH_2 + *H \rightarrow *CH_3$	44 (-18)	37 (-18)	47 (-11)	72 (5)	76 (10)	78 (22)
$*CH_3 + *H \rightarrow *CH_{4(g)}$	75 (-37)	67 (-41)	57 (-45)	61 (-41)	53 (-46)	56 (-32)
$*O + *H \rightarrow *OH$	117 (18)	95 (9)	113 (14)	137 (32)	134 (22)	140 (31)
$*OH + *H \rightarrow *H_2O$	123 (34)	118 (28)	104 (17)	129 (47)	121 (36)	123 (34)

A8.4 Additional reaction profiles

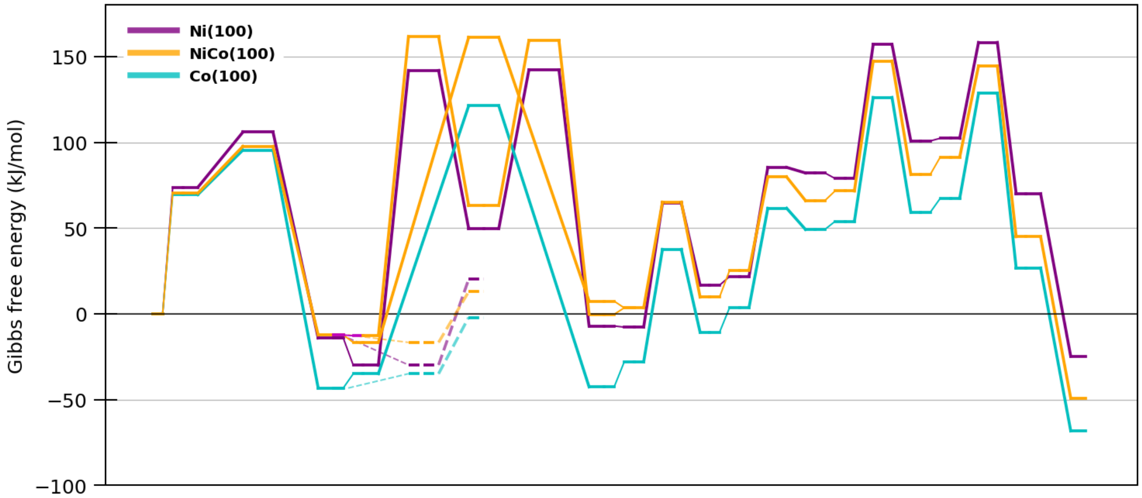

Fig. S17 Gibbs free energy profile on the (100) surfaces including direct CO dissociation and COH routes for NiCo(100).

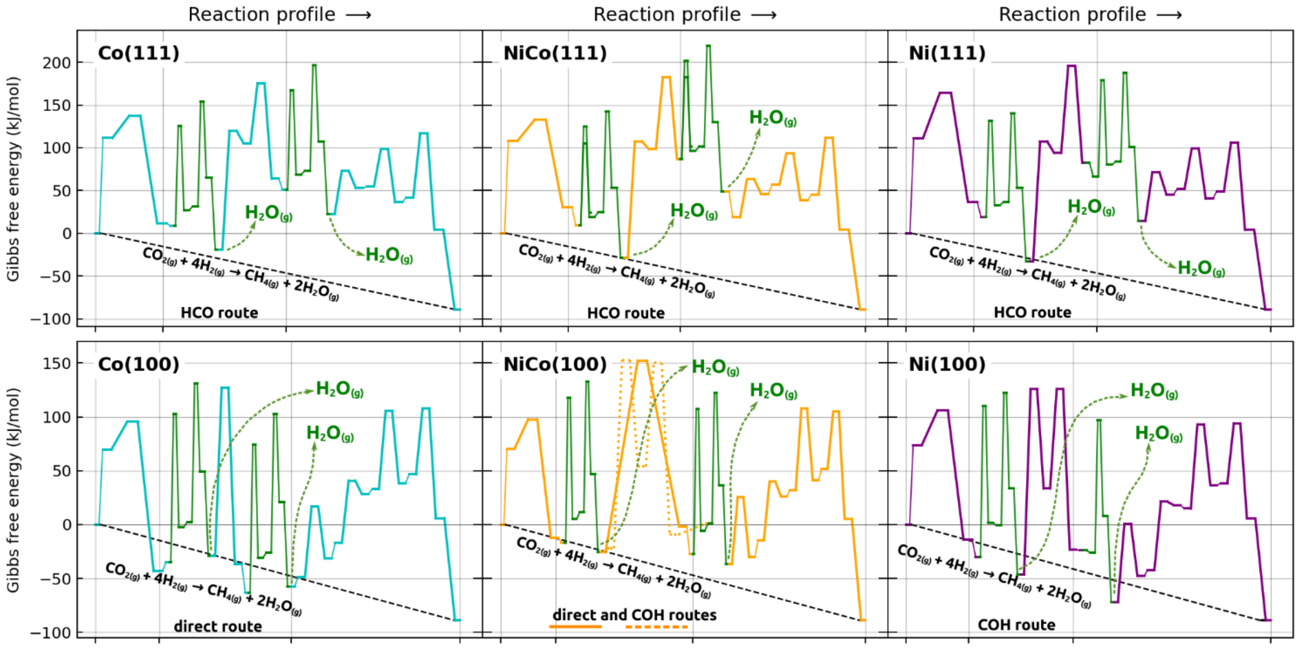

Fig. S18 Gibbs free energy profiles for the complete reaction including *O elimination steps (green lines), consistent with the gas phase reaction energetics (dashd black lines).

A9 Main geometric parameters during surface reactions

Following tables include some relevant geometric parameters. VASP geometry files (and all simulation files) are available in the digital repository of the Carbon and Catalysis Laboratory (CarboCat), University of Concepción.

A9.1 CH$_x$ hydrogenation geometries

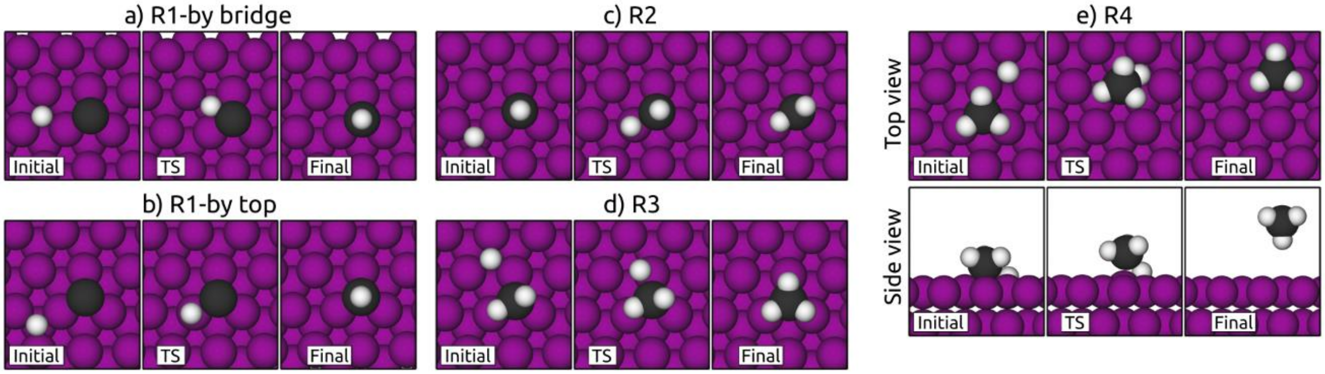

Fig. S19 *C hydrogenation towards CH$_{4(g)}$ (Scheme 2, sec. 8.4) on Ni(111). (a,b) show two converged routes for the first hydrogenation step.

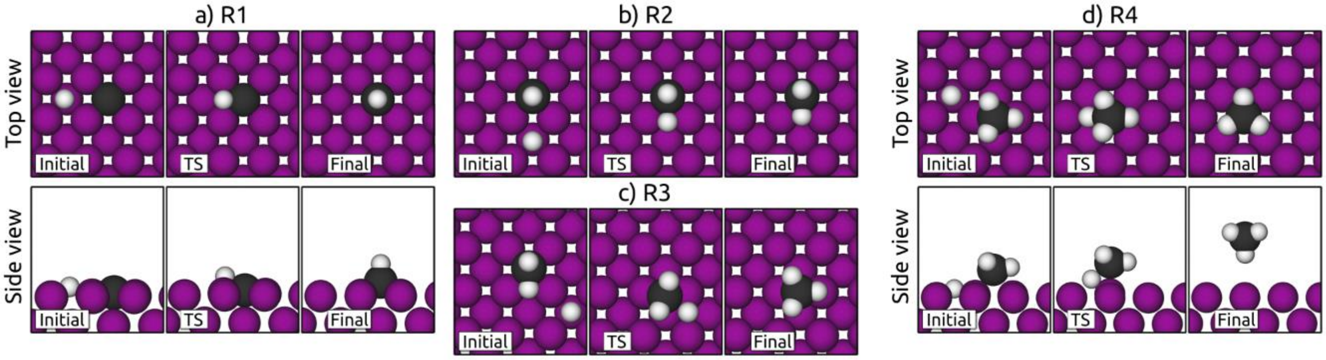

Fig. S20 *C hydrogenation towards $CH_{4(g)}$ (Scheme 2, sec. 8.4) on Ni(100).

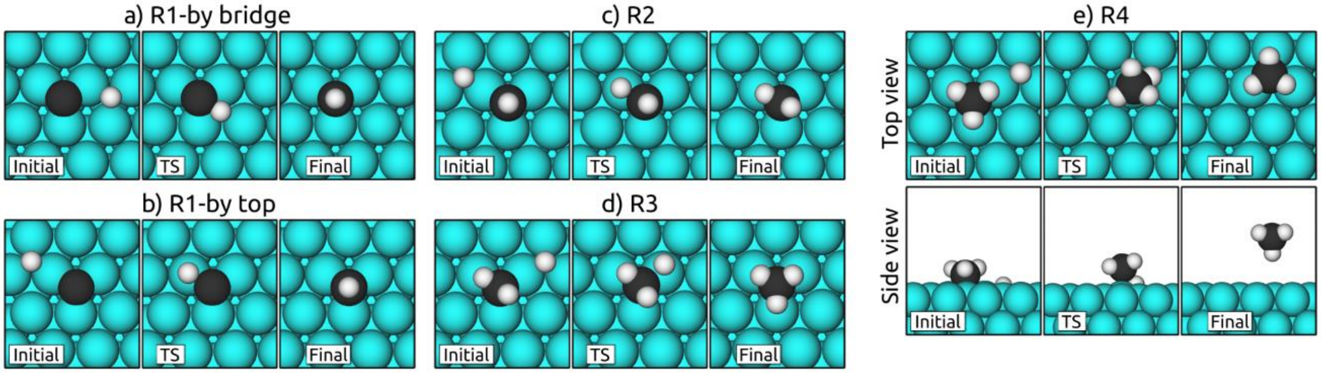

Fig. S21 *C hydrogenation towards $CH_{4(g)}$ (Scheme 2, sec. 8.4) on Co(111). (a,b) show two converged routes for the first hydrogenation step.

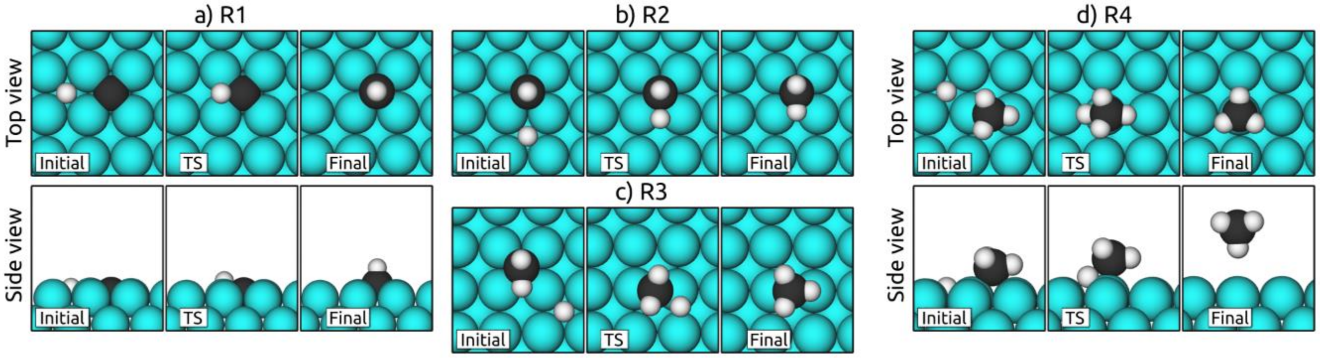

Fig. S22 *C hydrogenation towards $CH_{4(g)}$ (Scheme 2, sec. 8.4) on Co(100).

A9.2 CH_x hydrogenation reactions

Table S19 Relevant geometric parameters of the *C hydrogenation steps (H* reactive) on (100) surfaces.

Ni(100)			
	initial	TS	final
R1	d_{Ni-H*}=1.78/1.78/ 1.94/ 1.94, d_{Ni-C}=1.84/ 1.84/ 1.86/ 1.86, d_{C-H*}=2.72	d_{Ni-H*}=1.69/1.69, d_{C-H*}=1.52, d_{Ni-C}=1.85/1.85/1.87/1.87	d_{Ni-C}=1.94/1.94/1.94/1.94, d_{C-H}=1.11
R2	d_{Ni-H*}=1.78/1.78/ 1.91/ 1.91, d_{Ni-C}=1.92/ 1.92/ 1.95/ 1.95, d_{C-H}=1.11, d_{C-H*}=2.70, A_{HCH}=97.09	d_{Ni-H*}=1.66/ 1.66, d_{Ni-C}=1.95/ 1.95/ 2.01/ 2.01, d_{C-H}=1.11, d_{C-H*}=1.52, A_{HCH}=92.69	d_{Ni-C}= 1.97/1.97/2.09/2.09, d_{C-H}=1.22/1.11, d_{Ni-H}=1.79/1.79, A_{HCH}=97.55
R3	d_{Ni-H*}=1.79/1.88/1.86/1.88, d_{C-H*}=3.61, d_{Ni-H}= 1.77/1.78, d_{C-H}=1.23/1.11, A_{HCH}=97.34, d_{Ni-C}=2.08/2.08/1.97/1.97	d_{Ni-H*}=1.56/ 1.83, d_{Ni-C}=1.94/ 1.92, d_{C-H}=1.10/ 1.10, d_{C-H*}= 1.72	d_{Ni-C}=2.02/2.16, d_{C-H}=1.14/1.10/1.10, d_{Ni-H}=1.88/2.50/2.50
R4	d_{Ni-H*}=1.79/ 1.91/ 1.80/ 1.91, d_{Ni-C}=2.04/ 2.13, d_{Ni-H}= 1.87, d_{C-H}= 1.14/ 1.10/ 1.10, d_{C-H}=3.11	d_{Ni-H*}=1.77/ 1.54, d_{Ni-C}=2.05, d_{C-H}= 1.10/ 1.10/ 1.10, d_{C-H*}=1.65	d_{Ni-C}=3.96, d_{C-H}=1.10/ 1.10/ 1.10/ 1.10, d_{Ni-H*}=2.86
Co(100)			
	initial	TS	final
R1	d_{Co-H*}= 1.86/ 1.86/ 1.90/ 1.90, d_{Co-C}= 1.87/ 1.87/ 1.88/ 1.88, d_{C-H*}=2.64	d_{Co-H*}=1.73/ 1.73, d_{C-H*}=1.53 d_{Co-C}=1.90/ 1.90/ 1.90/ 1.90,	d_{Co-C}=1.97/1.97/1.97/1.97, d_{C-H}=1.11
R2	d_{Co-H*}=1.83/ 1.83/ 1.92/ 1.92, d_{Co-C}=1.95/ 1.95/ 1.99/ 1.99, d_{C-H}=1.11, d_{C-H*}=2.67, A_{HCH}=96.80	d_{Co-H*}=1.70/ 1.70, d_{C-H}=1.11, d_{Co-C}= 1.90/ 1.90/ 2.04/ 2.04, d_{C-H*}=1.56, A_{HCH}=92.35	d_{Co-C}= 2.02/2.02/2.16/2.16, d_{C-H}=1.18/1.11, d_{Co-H}=1.90/1.90, A_{HCH}=99.15
R3	d_{Co-H*}=1.85/ 1.91/ 1.91/ 1.89, d_{Co-C}= 2.02/ 2.01/ 2.15/ 2.16, d_{C-H}=1.18/ 1.11, d_{C-H*}= 3.62, A_{HCH}=98.91	d_{Co-H*}= 1.56/ 2.01, d_{Co-C}= 1.97/ 1.97, d_{C-H}= 1.11/ 1.11, d_{C-H*}= 1.75	d_{Co-C}=2.07/2.22, d_{C-H}=1.13/1.10/1.10, d_{Co-H}=1.96/2.57/2.57
R4	d_{Co-H*}= 1.83/ 1.91/ 1.86/ 1.99, d_{Co-C}=2.09/ 2.21, d_{C-H}=1.13/ 1.10/ 1.10, d_{Co-H}=1.96, d_{C-H*}=3.11	d_{Co-H*}= 1.87/ 1.55, d_{Co-C}=2.11, d_{C-H}=1.10/ 1.10/ 1.10, d_{C-H*}=1.64	d_{Co-C}=3.97, d_{Co-H*}=2.87, d_{C-H}=1.10/1.10/1.10/1.10
NiCo(100)			
	initial	TS	final
R1	d_{Co-H*}=1.97/1.90, d_{Ni-H*}= 1.94/1.77, d_{Co-C}= 1.84/ 1.84, d_{Ni-C}=1.86/ 1.89, d_{C-H*}= 2.65	d_{Co-H*}=1.67, d_{Ni-H*}=1.74, d_{Co-C}=1.86/ 1.85, d_{Ni-C}=1.91/1.87, d_{C-H*}=1.55	d_{Co-C}=1.96/1.96, d_{Ni-C}=1.97/1.97, d_{C-H*}=1.11
R2	d_{Co-H*}=1.89/ 1.86, d_{Ni-H*}= 1.94/ 1.76, d_{Ni-C}=1.99/ 1.95, d_{Co-C}= 1.97/ 1.94, d_{C-H}=1.11, d_{C-H*}=2.68, A_{HCH}=97.57	d_{Co-H*}=1.68, d_{Ni-H*}=1.69, d_{Ni-C}=2.04/1.98, d_{Co-C}=2.01/1.98, d_{C-H}= 1.11, d_{C-H*}=1.58, A_{HCH}=91.82	d_{Co-C}=2.00/2.16, d_{Co-H}=1.87, d_{Ni-C}=2.00/2.15, d_{Ni-H}=1.90, d_{C-H}=1.19/1.11, A_{HCH}=98.58
R3 -Co	d_{Co-H*}=1.83/1.93, d_{Ni-H*}=1.89/1.86, d_{Ni-C}=2.14/2.01, d_{Co-C}=2.00/2.14, d_{C-H}=1.19/1.11, A_{HCH}=98.25, d_{C-H*}=3.61	d_{Co-H*}=1.57, d_{Ni-H*}=1.93, d_{Co-C}=1.94, d_{Ni-C}=1.97, d_{C-H}=1.11/1.11, d_{C-H*}=1.72	d_{Co-C}=2.22, d_{Ni-C}=2.05, d_{C-H*}=1.13/1.10/1.10, d_{Co-H*}=1.94, d_{Ni-H}=2.55/2.54
R3 -Ni	d_{Co-H*}=1.92/1.91, d_{Ni-H*}=1.82/1.88, d_{Ni-C}=2.15/2.01, d_{Co-C}=2.00/2.16, d_{C-H}=1.19/1.11, A_{HCH}=98.36, d_{C-H*}=3.64	d_{Co-H*}=2.41, d_{Ni-H*}=1.50, d_{Co-C}=1.97, d_{Ni-C}=1.93, d_{C-H}=1.10/1.10, d_{C-H*}=1.86	d_{Co-C}=2.07, d_{Ni-C}=2.19, d_{C-H*}=1.13/1.10/1.10, d_{Co-H}=2.57/2.51, d_{Ni-H*}=1.94
R4 -t_{Co}	d_{Co-H*}=1.94/1.81, d_{Co-H*}=1.82/1.96, d_{Ni-C}=2.17, d_{Co-C}=2.09, d_{C-H}=1.11/1.10/1.13, d_{C-H*}=3.11	d_{Ni-H*}=1.76, d_{Co-H}=1.57, d_{Co-C}=2.10, d_{C-H}=1.10/1.10/1.11, d_{C-H*}=1.68	d_{C-H}= 1.10/ 1.10/ 1.10/ 1.10, d_{Co-H*}=3.25, d_{Ni-H*}=3.21
R4 -t_{Ni}	d_{Co-H*}=1.96/1.87, d_{Co-H*}=1.77/1.95, d_{Ni-C}=2.07, d_{Co-C}=2.20, d_{C-H}=1.13/1.10/1.10, d_{C-H*}=3.11	d_{Ni-H*}=1.53, d_{Co-H}=1.84, d_{Ni-C}=2.08, d_{C-H}=1.10/1.10/1.11, d_{C-H*}=1.68	d_{C-H}=1.10/1.10/1.10/1.10, d_{Co-H*}=3.25, d_{Ni-H*}=3.21

Table S20 Relevant geometric parameters of the *C hydrogenation steps (H* reactive) on (111) surfaces.

Ni(111)			
	initial	TS	final
R1 -b	d_{Ni-C}=1.76/ 1.77/ 1.80, d_{Ni-H*}=1.74/1.67/1.72, d_{C-H*}=2.73	d_{Ni-C}=1.82/1.79/1.82, d_{Ni-H*}=1.80/1.80/1.86, d_{C-H*}=1.47	d_{Ni-C}=1.85/1.85/1.85, d_{C-H*}=1.10
R1 - top	d_{Ni-C}=1.77/1.77/1.78, d_{Ni-H*}=1.71/1.72/1.71, d_{C-H*}=3.06	d_{Ni-C}=1.79/1.79/1.80, d_{Ni-H*}=1.50, d_{C-H*}=1.77	d_{Ni-C}=1.85/1.85/1.85, d_{C-H*}=1.10
R2	d_{Ni-H*}=1.72/1.72/1.71, d_{Ni-C}=1.84/1.84/1.86, d_{C-H}=1.10, d_{C-H*}=3.01, A_{HCH}=97.42	d_{Ni-H*}=1.49, d_{Ni-C}=1.88/1.88/1.86, d_{C-H}=1.10, d_{C-H*}=1.70, A_{HCH}=89.34	d_{Ni-C}=1.93/1.93/2.00, d_{C-H}=1.16/1.10, d_{Ni-H}=1.77, A_{HCH}=101.78
R3	d_{Ni-H*}=1.68/1.75/1.71, d_{Ni-C}=1.94/1.91/2.00, d_{C-H}=1.16/1.10, d_{Ni-H}=1.78, A_{HCH}=102.00, d_{C-H*}=2.70	d_{Ni-H*}=1.51/2.43, d_{Ni-H}=1.88, d_{C-H*}=1.74 d_{C-H}=1.10/1.14, d_{Ni-C}=1.93/1.99/2.07,	d_{Ni-C}=2.15/2.15/2.15, d_{C-H}=1.12/1.12/1.12, d_{Ni-H}=2.05/2.06/2.07
R4	d_{Ni-H*}=1.67/1.71/1.76, d_{Ni-C}=2.21/2.22/2.11, d_{C-H}=1.11/1.12/1.12, d_{C-H*}=2.86	d_{Ni-H*}=1.95/1.94/1.57, d_{Ni-C}=2.10, d_{C-H}=1.10/1.10/1.10, d_{C-H*}=1.61	d_{Ni-H*}=3.55/4.36/3.56, d_{Ni-C}=4.57/4.59/5.21, d_{C-H}=1.10/1.10/1.10, d_{C-H*}=1.10
Co(111)			
	initial	TS	final
R1 -b	d_{Co-C}=1.80/1.78/1.77, d_{Co-H*}=1.73/1.82/1.69, d_{C-H*}=2.68	d_{Co-H*}=1.90/1.82/1.77, d_{Co-C}=1.78/1.83/1.83, d_{C-H*}=1.45	d_{Co-C}=1.88/1.88/1.88, d_{C-H*}=1.10
R1 - top	d_{Co-C}=1.78/1.78/1.78, d_{Co-H*}=1.76/1.76/1.70, d_{C-H*}=2.99	d_{Co-H*}=1.52, d_{Co-C}=1.81/1.81/1.78, d_{C-H*}=1.68	d_{Co-C}=1.88/1.88/1.88, d_{C-H*}=1.10
R2	d_{Co-H*}=1.77/1.77/1.71, d_{Co-C}=1.88/1.88/1.87, d_{C-H}=1.10, A_{HCH}=95.17, d_{C-H*}=2.92	d_{Co-H*}=1.51, d_{C-H}=1.10, d_{Co-C}=1.92/1.92/1.86, A_{HCH}=90.47, d_{C-H*}=1.62	d_{Co-C}=1.96/1.97/2.02, d_{C-H}=1.16/1.10, d_{Ni-H}=1.80, A_{HCH}=101.28
R3	d_{Co-H*}=1.76/1.76/1.72, d_{Co-C}=2.01/1.96/1.96, d_{C-H}=1.16/1.10, d_{Co-H}=1.79, d_{C-H*}=2.97	d_{Co-H*}=1.53, d_{Co-C}=2.05/2.10/1.94, d_{C-H}=1.13/1.10, d_{C-H*}=1.74	d_{Co-C}=2.20/2.21/2.20, d_{C-H}=1.11/1.11/1.11, d_{Co-H}=2.13/2.13/2.14
R4	d_{Co-H*}=1.74/1.74/1.77, d_{Co-C}=2.19/2.19/2.27, d_{C-H}=1.11/1.11/1.11, d_{C-H*}=3.17	d_{Co-H*}=1.98/1.98/1.58, d_{Co-C}=2.16, d_{C-H}=1.10/1.10/1.10, d_{C-H*}=1.62	d_{Co-H*}=3.63/3.55/3.67, d_{Co-C}=4.67/4.58/4.69, d_{C-H}=1.10/1.10/1.10, d_{C-H*}=1.10
NiCo(111)			
	initial	TS	final
R1 -b	d_{Ni-H*}=1.76, d_{Co-H*}=1.71/1.72, d_{Ni-C}=1.84, d_{Co-C}=1.75/1.76, d_{C-H*}=1.67	d_{Ni-H*}=1.90/1.85, d_{Co-H*}=1.73, d_{Ni-C}=1.89, d_{Co-C}=1.77/1.79, d_{C-H*}=1.47	d_{Ni-C}=1.90/d_{Co-C}=1.86/1.86, d_{C-H*}=1.10
R1 - t_{Ni}	d_{Ni-H*}=1.70, d_{Ni-C}=1.85, d_{C-H*}=3.14, d_{Co-H*}=1.76/1.76, d_{Co-C}=1.76/1.76	d_{Ni-H*}=1.51, d_{Co-C}=1.79/1.79, d_{Ni-C}=1.84, d_{C-H*}=1.76	d_{Ni-C}=1.90/d_{Co-C}=1.86/1.86, d_{C-H*}=1.10
R1 - t_{Co}	d_{Ni-H*}=1.73, d_{Co-H*}=1.78/1.69, d_{Ni-C}=1.83, d_{Co-C}=1.76/1.76, d_{C-H*}=2.92	d_{Co-H*}=1.52, d_{Co-C}=1.78/1.76, d_{Ni-C}=1.85, d_{C-H*}=1.68	d_{Ni-C}=1.90/d_{Co-C}=1.86/1.86, d_{C-H*}=1.10
R2	d_{Ni-H*}=1.74, d_{Co-H*}=1.79/1.70, d_{Co-C}=1.86/1.84, d_{Ni-C}=1.91, d_{C-H}=1.10, A_{HCH}=96.33, d_{C-H*}=2.87	d_{Co-H*}=1.50, d_{Co-C}=1.90/1.84, d_{Ni-C}=1.95, d_{C-H}=1.10, A_{HCH}=91.05, d_{C-H*}=1.63	d_{Co-C}=1.95/1.98, d_{Ni-C}=1.97, d_{C-H}=1.17/1.10, d_{Co-H}=1.76, A_{HCH}=100.93
R3	d_{Ni-H*}=1.70/1.79, d_{Co-H*}=1.69, d_{Co-C}=2.00/1.94, d_{Ni-C}=1.95, d_{C-H}=1.16/1.10, d_{Co-H}=1.78, d_{C-H*}=2.59	d_{Co-H*}=1.52, d_{Co-C}=2.07/1.92, d_{Ni-C}=2.02, d_{C-H}=1.10/1.15, d_{Co-H}=1.85, d_{C-H*}=1.71	d_{Ni-C}=2.18, d_{Co-C}=2.19/2.19, d_{C-H}=1.11/1.12/1.12, d_{Ni-H}=2.12, d_{Co-H}=2.09/2.10
R4 - t_{Ni}	d_{Ni-H*}=1.74, d_{Co-H*}=1.74/1.74, d_{Co-C}=2.18/2.18, d_{Ni-C}=2.22, d_{C-H}=1.12/1.12/1.11, d_{C-H*}=3.14	d_{Ni-H*}=1.56, d_{Co-H*}=2.00/2.00, d_{Ni-C}=2.11, d_{C-H}=1.10/1.10/1.10, d_{C-H*}=1.62	d_{Ni-H*}=3.61, d_{Co-H*}=3.60/3.61, d_{Ni-C}=4.65, d_{Co-C}=4.62/4.64, d_{C-H}=1.10/1.10/1.10, d_{C-H*}=1.10
R4 - t_{Co}	d_{Ni-H*}=1.70, d_{Co-H*}=1.75/1.77, d_{Co-C}=2.17/2.25, d_{Ni-C}=2.16, d_{C-H}=1.11/1.12/1.11, d_{C-H*}=3.17	d_{Co-H*}=1.58, d_{Co-C}=2.14, d_{C-H}=1.10/1.10/1.10, d_{C-H*}=1.62	d_{Ni-H*}=3.61, d_{Co-H*}=3.60/3.61, d_{Ni-C}=4.65, d_{Co-C}=4.62/4.64, d_{C-H}=1.10/1.10/1.10, d_{C-H*}=1.10